Scour around Offshore Wind Turbine Foundations

Petersen, Thor Ugelvig

Publication date:
2014

Document Version
Publisher's PDF, also known as Version of record

I

Scour around Offshore Wind Turbine Foundations

Thor Ugelvig Petersen

June 2014

Ph.D. thesis
Section for Fluid Mechanics, Coastal and Maritime Engineering
Department of Mechanical Engineering
Technical University of Denmark
Kgs. Lyngby, Denmark

Published in Denmark by
Technical University of Denmark

Section for Fluid Mechanics, Coastal and Maritime Engineering
Department of Mechanical Engineering
Technical University of Denmark
Nils Koppels Alle, Building 403, DK-2800 Kgs. Lyngby, Denmark
Phone +45 4525 4150, Mob +45 2682 3935
E-mail: info.skk@mek.dtu.dk
http://www.mek.dtu.dk/

Publication Reference Data

Petersen, T. U.
Scour around Offshore Wind Turbine Foundations
PhD Thesis
Technical University of Denmark, Department of Mechanical Engineering
June 2014.
Keywords: Edge scour, cover stones, scour protection, backfill, time scale, steady current, waves, offshore wind farms, monopiles, tidal current.

Contents

Nomenclature

Greek Characters:

α	Side-slope of the stone layer
β	Angle to the right downstream centerline, Chapter 3.
γ	Specific weight of water
γ_s	Specific weight of soil grains
δ	Boundary layer thickness
κ	Karman constant
θ	Shields parameter
θ_{cr}	Critical Shields parameter for initiation of motion on bed
θ_f	Shields parameter corresponding to the wave which backfills, Chapter 4.
σ_g	Geometric standard deviation of particle size distribution
σ_U	R.M.S. value of U , calculated from the spectrum function S_U , $\sigma_U{}^2 = \int_0^\infty S_U(f)\, df$
τ_0	Bed shear stress
ν	Kinematic viscosity
τ_b	Instantaneous bed shear stress
τ_∞	Undisturbed bed shear stress
ω	Angular frequency of the tidal flow, Chapter 3
ω_x	x-directional vorticity, Chapter 3.

Roman Characters

A	Empirical coefficient
A_r	Aspect ratio by B/h
B	Empirical coefficient
B	Channel width, Chapter 2 and Appendix A.
C	Empirical coefficient
d	Grain size
d_{13}	Particle size at which 13% of soil is finer
d_{50}	Particle size at which 50% of soil is finer
d_{84}	Particle size at which 84% of soil is finer
D	Stone diameter, Chapter 2
D	Pile diameter, Chapter 4.
D_c	Mean size of cover/armour stones
D_f	Mean size of filter stones
D_p	Pile diameter
D_s	Stone size, Appendix A
F	Free-board height
f	Frequency
f	Friction factor
f_p	Peak frequency of waves
f_w	Wave friction coefficient
g	Gravitational acceleration
h	Water depth at measurement section
h_b	Berm height
h_s	Height of stone layer, Appendix A.
KC	Keulegan-Carpenter number,
KC_f	Keulegan-Carpenter number corresponding to the wave which backfills, Chapter 4.

KC_i	Keulegan-Carpenter number corresponding to the wave which generates initial scour hole to be subjected to backfilling subsequently, Chapter 4.
k	Turbulent kinetic energy
L	Wave length
L_f	Length of exposed filter layer
L_s	Length of scour hole
N	Number of stone layers
R	Hydraulic radius
Re	Reynolds number
RE	Wave boundary layer Reynolds number
Re_{D_p}	Pile Reynolds number
Re_d	Grain Reynolds number
Re_δ	Bed boundary layer Reynolds number
S_c	Scour depth in the case of current alone, Chapter 4 and Chapter 5.
S	Edge scour alongside berm (corresponding to the equilibrium stage), Chapter 2, Chapter 3 and Appendix A.
S	Scour depth by scour/backfilled scour hole (corresponding to the equilibrium state), or depth of scour hole generated by scour process (again, corresponding to the equilibrium state)
S_i	Initial depth of scour hole (at the beginning of backfilling), see Fig. 6
St	Strouhal number
S_t	Scour depth over time
$S(f)$	Spectrum function
S_0	Equilibrium scour depth
s	Specific weight of sediment (= γ_s/γ)
t	time
T	Time scale of scour process
t_c	Thickness of armour layer
t_f	Thickness of filter layer
T^*	Time scale of scour/backfilling (normalized)
T_p	Wave period, corresponding to the peak frequency
T_{tidal}	Period over which the sediment is mobilized during a tidal period

T_w	Wave period, corresponding to regular waves
U	Orbital (horizontal) velocity at the bottom
U_c	Current velocity
U_{cw}	Current-velocity-to-wave-velocity ratio
U_s	Secondary current velocity (= $\sqrt{v^2 + w^2}$)
U_f	Undisturbed friction velocity in current
U_{fm}	Undisturbed friction velocity in waves
U_m	$U_m = \sqrt{2}\,\sigma_U$. This quantity becomes identical to the maximum value of the bottom orbital velocity in the case of small-amplitude sinusoidal waves
U_{max}	Maximum velocity in current, Chapter 2.
u, v, w	Streamwise, vertical, and lateral components of velocity
u', v', w'	Fluctuating Streamwise, vertical, and lateral velocities
V	Depth-averaged-velocity
V_t	Time series of the depth-averaged-current velocity in tidal flow
w_b	Width (diameter) of berm, Chapter 3.
x, y, z	Cartesian coordinates
y^+	Dimensionless distance from bed, Chapter 2
$\bar{}$ =	Time averaging

Preface

The present Ph.D. thesis is submitted as one of the requirements for obtaining the Ph.D. degree at the Technical University of Denmark. The Ph.D. study was carried out at the Section for Fluid mechanics, Coastal and Maritime Engineering in the Department of Mechanical Engineering.

Professor B. Mutlu Sumer has acted as the main supervisor during this study, and the author is indebted to him for his unfettered patience, valuable discussions and encouraging spirit throughout the study.

I also wish to thank my co-supervisors: Associate Professor David R. Fuhrman for the guidance in relation to the CFD work, Professor Jørgen Fredsøe for valuable discussions and insightfulness and Professor Erik D. Christensen.

A special attention is also addressed to Jan-Joost Schouten and Tim Raaijmakers for a fruitful collaboration and for hosting me during my stay at Deltares. My attention and gratitude also goes to the staff in the section of Fluid mechanics, Coastal and Maritime Engineering for assistance and discussions: Associate Professor Knud Erik Meyer, for providing the PIV equipment and supervising the measurements. I will also give thanks to Luca Lucatelli, Jon Bøgelund Bruun, Asli Yazici, Magnus Woxholtt-Jensen, Thomas Probst, Pierre Breard, Kristine Pilegaard, Jacob Elholm and Zahra Waisi who have conducted parts of the experiments reported in this thesis. I will also thank the Ph.D.-students and Post docs. in the coastal group: Ph.D. Anders Wedel Nielsen, PhD. Nilas Mandrup Hansen, Karsten Lindegård Jensen, Post doc Cüneyt Baykal, Ph.D. Niels Gjøl Jacobsen, Ph.D. Sten Esbjørn Kristensen, Ph.D. Sina Saremi, Ph.D Bjarne Jensen, Ph.D. Kasper H. Kærgaard, the staff in the laboratory Jan Justesen, Henning Jespersen, Jan Larson, Poul-Erik Hyldbo and Claus Grølsted, and the draftsman Liselotte Norup for preparing some of the figures. Acknowledgement are directed to (1) Danish GTS-university-cooperation project “Future Marine Structures”; (2) the Danish Council for Strategic Research (DSF)/Energy and Environment Program "Seabed Wind Farm Interaction"; (3) FP7-project, MERMAID 28870; and (4) Statkraft through Statkraft Ocean Energy Research Program (SOERP)(Norway) for the financial support.

Finally, I would like to thank Line for her support and patience during the project, and looking after our two sons Carl and Johan during busy times.

1st of June 2014, Kgs. Lyngby

_____

Thor Ugelvig Petersen

Abstract

Scour around Offshore Wind Turbine Foundations

Over the last decades several offshore wind farms have been installed and commissioned in the European waters. Typically the foundations of the wind turbines are protected against scour at the base by installing scour protection with rock dump. The Egmond aan Zee offshore wind farm located about 10 – 18 km off the coast of the Netherlands constructed in 2006, utilized such a scour protection system to prevent removal of the sediment base. Following the installation of the scour protection system and subsequently on a yearly basis an extensive survey campaign has been carried out, to evaluate the performance (stability) of the scour protection and to quantify the edge scour development at the circumference of the scour protection. The survey campaign showed considerable edge scour of up to 2.7 m, which was expected from design considerations. However, no clear information exists on the mechanisms causing the edge scour development around scour protections at offshore wind turbine foundations. The purpose of the present thesis is to investigate and explain the development of the edge scour in such applications, and describe the flow mechanism causing the scour.

Furthermore, the dissertation also focuses on the case where the foundation is placed without scour protection. Here the continuously changing flow climate, comprising currents, waves and combined waves and current forces the scour depth around the foundation to change over time experiencing scour and backfill in an alternating fashion. The scour mechanism and the time development of a scour process in waves, current and steady current has received a vast amount of research over the last decades revealing various features of scour processes. While the scour process seems well documented, relatively few studies have been reported on backfilling and to the authors knowledge no study is yet available, investigating in a systematic manner the backfilling process around monopiles. The thesis therefore also aims at explaining the mechanism and time development of backfill.

In Chapter 2, flow and edge scour adjacent to stone covers in steady current propagating in-line with a stone cover layer is studied. The results indicate that the exposure to steady current scours the bed at the side edge of the cover structure, the edge scour. The model tests show that the edge scour is caused by the combined action of the following two effects: (1) Primary flow; and (2) Secondary flow. The primary flow stirs up the sediment and entrains the sediment into the main body of the flow by, and the secondary flow carries the sediment away from the junction between the sediment bed and the cover stones, resulting in the edge scour. With this, stones at the edge of the cover structure are “undermined”, and as a result, slump down into the scour hole. The maximum scour is about 0.8 times the equivalent stone diameter.

In Chapter 3, flow and edge scour around scour protections at offshore wind turbine foundations are studied by means of particle image velocimetry, hot-film measurements and actual scour tests. The experimental results are supported by a field investigation of edge scour at the offshore wind park Egmond aan Zee and Scroby Sands offshore wind farm. It is found that the edge scour is caused by the local increase in the hydrodynamic field leading to increased sediment transport and scour. The governing flow processes are the horseshoe vortex generated in front of the scour protection berm, the contraction and acceleration flow at the side edge of the scour protection, and a pair of counter-rotating vortices emerging in the near bed wake region of the pile and scour protection. The latter mentioned flow features show a significant potential to scour the adjacent sea bed, and in turn cause loss of stability of the scour protection. Design guidelines are provided to determine the equilibrium stage scour in current, tidal current and combined waves and current.

In Chapter 4, a description of the backfilling process around both slender and large piles exposed to waves and combined waves and current, is given, based on results of physical model tests. Using the results it is possible to numerically model and estimate the changing scour depth over time. It is shown that the scour depth corresponding to the equilibrium stage of the backfilling process is the same as that corresponding to the equilibrium stage of the scour process for the same wave or combined waves and current climate. The time scale of the backfilling process has been determined as a function of three parameters namely: (1) the Keulegan-Carpenter number of the initial wave or the current (which generate the initial scour hole); (2) that of the subsequent wave which backfills the scour hole; and (3) the Shields parameter associated with the latter wave for live-bed conditions. In the case of combined waves and current, the current-to-wave-velocity ratio is also involved. The time scale of the backfilling process is completely different from that of scour. The time scale of backfilling is much larger than that of scour when the Keulegan-Carpenter number associated with the backfilling is $KC_f < O(10)$ (typical wind farm application), while the trend is opposite when $KC_f \gg O(10)$.

In Chapter 5, the time scale of scour around a slender vertical pile in combined waves and current is studied. The time scale of scour in combined waves and current is found to depend on three parameters: (1) the Keulegan-Carpenter number; (2) the Shields parameters of the wave component of the flow; and (3) the current-to-wave-velocity ratio. The study indicates that the time scale of scour increase significantly when superimposing even a slight current on a wave. The results further show that the time scale of scour approaches the wave-alone time scale in the wave-dominated regime, and it approaches the current values in the current-dominated regime, as anticipated.

Resumé

Erosion omkring Havvindmøllers Fundamenter

Gennem de sidste årtier er mange havvindmølleparker i de Europæiske farvande blevet bygget og taget i brug. Typisk bliver vindmøllernes fundamenter beskyttet mod udvaskning af havbundens sediment, ved at installere en erosionsbeskyttelse ved en stenkastning. Havvindmølleparken Egmond aan Zee, der er bygget omkring 10 - 18 km fra Hollands kyst i 2006, udnytter en sådan stenkastning, for at forebygge fjernelse af sedimentet omkring fundamentets fod. I forlængelse af stenkastningernes installering og efterfølgende i årlige intervaller, er der foretaget omfattende opmålinger og inspektion af deres virke og udvikling af rand erosion langs kanten af stenkastningerne. Opmålingerne viste væsentlig erosionsudvikling omkring randen af stenkastningerne på op til 2.7 m, hvilket var forudset fra det indledende design arbejde. Imidlertid, findes der ingen konkret information og forklaring på mekanismerne, der forårsager denne rand erosion ved stenkastningerne omkring havvindmøllernes fundamenter. Formålet med denne afhandling er at undersøge og forklare erosionsudviklingen samt beskrive processerne, der fører til den type erosion.

Ydermere, fokuserer afhandlingen også på erosionsudviklingen omkring et ubeskyttet fundament. I dette tilfælde vil den stadig skiftende miljøpåvirkning, i form af strøm, bølger og kombinerede bølger og strøm, forårsage en varierende erosionsdybde omkring fundamentet i et vekslende samspil mellem erosion og tilbagefyldning af sediment. Der er forsket en del i erosionsmekanismerne og tidsudviklingen af erosion omkring fundamentet, og de markante processer er klarlagt. Dette er dog ikke tilfældet ved tilbagefyldning af sediment i erosionshullerne omkring de ubeskyttede fundamenter. Afhandlingen fokuseres derfor også på at klarlægge processerne og tidsudviklingen af tilbagefyldning.

I Kapitel 2, er der undersøgt rand erosion ved en stenkastning i en langsgående strømning. Resultaterne indikerer at sedimentet langs randen af stenene bliver fjernet og rand erosion opstår. De fysiske model forsøg viser, at randerosionen er forårsaget i kombination af (1) primær strømninger, og (2) sekundær strømninger. Primær strømningen bringer sedimentet i bevægelse og løfter det fra bunden, derefter bærer sekundær strømmen sedimentet væk fra foden af stenlaget og rand erosion opstår. Randerosionen forårsager sætninger i stenlaget, når de yderste sten falder ned i erosionshullet. Den største erosion er fundet til at være omkring 0.8 gange stenens ækvivalente diameter.

I kapitel 3, er strømninger og erosion omkring stenkastninger ved havvindmøller undersøgt ved hjælp af particle image velocimetry, hot-film målinger og egentlige erosionsforsøg. De fysiske forsøg er understøttet af feltmålinger af rand erosion ved havvindmølleparkerne Egmond aan Zee og Scroby Sands. Det er fundet, at rand

erosionen er forårsaget af lokalt øgede strømningsfelter, der skaber forøget sediment transport og erosion. De dominerende processer er hestesko hvirvlen dannet foran stenkastningen, acceleration og kontraktion af strømningen på siden af stenkastningen, og et sæt modsat roterende hvirvler i monopælens og erosionsbeskyttelsens slipstrøm. De nævnte processer viste et markant potentiale for at erodere den omkringliggende havbund og forårsage stabilitetsproblemer for stenkastningen. Retningslinjer er præsenteret for bestemmelse af erosionsudvikling i strøm, tidevandsstrøm og kombineret bølger og strøm.

I kapitel 4, beskrives tilbagefyldningsprocessen omkring både slanke- og tykke pæle ved fysiske model forsøg i bølger og kombinerede bølger og strøm. Ved hjælp af resultaterne er det muligt at udføre numerisk modellering og forudsige erosionsudviklingen over tid. Det er vist, at ligevægtsniveauet for tilbagefyldningsprocessen er lig med ligevægtsniveauet for erosionsprocessen, når ens bølge- eller kombinerede bølge og strøm klimaer tages i betragtning. Tidsskalaer for tilbagefyldningsprocessen er bestemt som funktion af tre parametre, henholdsvis: (1) Keulegan-Carpenter-tallet for den indledende bølge eller strøm (som genererer erosionshullet); (2) Keulegan-Carpenter-tallet for den bølge, der efterfølgende tilbagefylder erosionshullet; og (3) Shields parameteren tilhørende den sidstnævnte bølge for live-bed betingelser. I tilfældet af kombinerede bølger og strøm må parameteren for forholdet imellem bølge- og strømhastighed også tages i betragtning. Tidsskalaen af tilbagefyldning er fuldstændig anderledes end den for erosion. Tidsskalaen for tilbagefyldningen er langt større end for erosion, når Keulegan-Carpenter-tallet for tilbagefyldningsprocessen er $KC_f < O(10)$ (typisk i forbindelse med havvindmøller), og omvendt når $KC_f \gg O(10)$.

I Kapitel 5, undersøges tidsskalaen for erosion omkring en slank vertikal pæl udsat for kombinerede bølger og strøm. Det vises at tidsskalaen i kombinerede bølger og strøm afhænger af tre parametre: (1) Keulegan-Carpenter-tallet; (2) Shields parameteren tilhørende bølgedelen af det samlede strømning; og (3) hastighedsforholdet imellem bølger og strøm. Studiet indikerer at tidsskalaen for erosion stiger markant når bare en mild strømning lægges ovenpå en bølge. Resultaterne viser også tidsskalaen for erosion antager værdien for tidsskalaer i bølger i bølgedominerede forhold, og nærmer sig værdierne for erosion i strøm i strømdominerende situationer.

Chapter 1

Introduction

During the last decades the offshore wind industry has grown to become an important source of energy supply. Most of the offshore wind farms are located in the North Western Europe, primarily in Denmark, the United Kingdom, the Netherlands, Sweden and Germany, but over the recent years the offshore wind power industry is growing all over the world (Offshore Center Danmark, 2010 and 2012; 4coffshore.com, 2014). Denmark has a long experience in wind power and the development began in the early 1980's and has experienced a rapid growth over the last 10-15 years. The first offshore wind farm (OWF) Vindeby was erected in 1991 north of Lolland in the Great Belt of Denmark. OWF Vindeby consists of 11 turbines placed in shallow waters, with a total capacity of 5 MW. Since the construction of Vindeby larger offshore wind farms with more advanced technologies have been erected. Today the largest OWF in Denmark is Anholt which deploy 111 turbines with a total capacity of 399.6 MW.

An offshore wind turbine (OWT) consists of four main parts: Foundation, tower, nacelle and rotor. The design basis of these parts is shared with a land based wind turbine, but one of the characteristic differences is the foundation principle. For a land based wind turbine the tower is usually grouted in place and the cost of the foundation is about 10% of the overall costs. For OWT the foundation design is more comprehensive and the total costs amounts to 30 – 40% depending on the water depth, metocean- and soil conditions, to mention a few.

For offshore wind farms there are typically four types of foundation structures: monopiles, tripods, jackets and gravity based. Traditionally OWT have been erected in shallow waters (< 25m), and for these conditions monopiles or gravity-based foundations are the preferred design principle in Denmark (Offshore Center Danmark, 2012). For larger water depth jacket type or even floating platforms may be used as foundations.

The foundations are often erected in harsh hydrodynamic environments, exposed to strong tidal currents and large waves individually and in combination. It is essential to have a detailed understanding of how these hydrodynamic environments affects the structures as a whole; including the foundation and the interaction between flow, structure and sea bed (Sumer, 2014).

The considerations in regards to the flow, structure and seabed interaction encompass several physical aspects, such as water depth, significant wave heights and peak periods, tidal current speeds and return periods, seabed material (e.g. sand, silt and clay), stratified

sea beds, degradation of the general sea bed level, the migration of large bed forms (e.g. ripples, mega-ripples, dunes and sand waves), and the local scour around the foundations.

Clearly, the above mentioned aspects can singlehandedly or jointly pose a threat to the stability of the foundation, if they are not considered in the design and countermeasures are taken. Therefore scour protection with rock armour are almost invariably installed at offshore wind turbine foundations as armouring to protect these structures against scour and unfavorable effects of migrating sand waves; Horns Rev 1 OWF (Hansen et al., 2007), Egmond aan Zee OWF (Raaijmakers et al., 2007 and Louwersheimer et al., 2009), Scroby Sands OWF and Arklow Bank OWF (Whitehouse et al., 2011) to mention a few examples. We may note an unprotected installation with no rock protection is also a viable option (as will be detailed later, Wittrup, 2012).

Scour around unprotected monopiles have received a vast amount of attention over the last decades, with a detailed account on the topic given in the books of Breusers and Raudkivi (1991), Hoffmans and Verheij (1997), Whitehouse (1998), Melville and Coleman (2000) and Sumer and Fredsøe (2002); and more recently in numerical studies by Roulund et al. (2005), Liu and Garcia (2008) , Zhao et al. (2010) and Khosronejad et al. (2012) and experimental studies on scour and backfilling of scour holes around piles by Sumer et al. (2013). The information rendered in the latter works has also made it possible for establishing long-term numerical models to estimate the time development of the scour depth around mono-piles with the changing sea climate (Nielsen and Hansen, 2007; Raaijmakers and Rudolph, 2008; and Harris et al. 2010). More recently, such models were applied over larger areas to study at which locations allowing free scour development (i.e. leaving out the scour protection and adjusting the monopile design) would be more cost-efficient compared to installing scour protections (e.g. Raaijmakers et al, 2013).

Following the studies on scour around unprotected monopiles few investigations have been presented on flow and scour mechanisms with the scour protection installed at the base of the monopile by Chiew (1995), Chiew and Lim (2000), Lauchlan and Melville (2001), Vos et al. (2011,2012), Nielsen et al. (2011,2013) and Sumer and Nielsen (2013).

1.1. Edge Scour around Scour Protections

The field surveys reported by Raaijmakers (2010, 2011), Whitehouse et al. (2011) and Hansen, et al. (2007) of scour protections around OWT foundations show deformations of the stone layer comprising both sinking of the stone layer and considerable edge scour. The design principles and considerations of scour protection systems does in fact comprise edge scour, but so far the mechanisms causing edge scour have not been fully established. One of the important failure mechanisms of a stone layer involves failure of the edge material at the toe of the stone layer. The failure can be caused the combined action of soil failure and the edge scour generated either by current or waves. The hydrodynamics and soil mechanics of the above mentioned failure mechanisms are, today, poorly understood. The industry needs this knowledge in order to design these structures to ensure the safety operation of OWTs, considering that these protection structures involve significant sums with regard to installation. Therefore following issues needs to be addressed:

1. Differentiation of the failure mechanisms at the edge of the rock protection.
2. Critical conditions beyond which stability and integrity of the stone layer is lost.
3. Quantification of the additional rock to be used as counter measures, if a so-called falling apron concept is adopted, to offset the unwanted effect of the edge failure.

This thesis presents results of detailed measurements in an experimental campaign covering the flow adjacent to a stone cover placed on the sea bed. These results form the basis of a detailed description of the mechanisms causing the edge scour observed at the offshore wind parks Egmond aan Zee and Scroby Sands, as will be detailed in Chapter 3. Equilibrium stage scour depth as well as time scale of the edge scour process is found experimentally for various flow conditions comprising waves and current presented in design diagrams.

1.1.1. Offshore Wind Park Egmond aan Zee

Through this PhD project an attempt was also given to investigate the existence of edge scour at stone covers and the implications in the field. To address this issue a study on the offshore wind park Egmond ann Zee (OWEZ) in collaboration with the company Deltares was initiated. Deltares were formerly managing an extensive survey programme of the sea bed bathymetry over the entire OWF (see Raaijmakers et al, 2009). This section provides the basic information on Egmond Aan Zee OWF and the technical details on the foundation principle and the scour protection system.

1.1.2. Scour protection at Egmond ann Zee OWF

Several studies, such as Raaijmakers et al. (2007), Raaijmakers et al. (2010) and Whitehouse et al (2011), have reported on scour development at the Offshore Windpark Egmond aan Zee (OWEZ), and this section describes the local conditions, installed scour protections and the edge scour development in the period 2006-2013.

OWEZ is the first offshore wind farm in The Netherlands constructed in 2006, located about 10 to 18 km off the coast of Egmond aan Zee. OWEZ consists of 36 wind turbines with a distance in between from 140 D_p to 220 D_p (Simoons, 2012), and with a water depth range of 16 m to 21 m over the site. The turbines are founded on monopiles with a diameter D_p = 4.6 m, driven into the seabed consisting of fine sands with d_{50} = 0.25 mm. The scour protection comprise two layers of stone material; (1) a filter layer with a thickness of 0.4 m consisting of stones the size $D_{f,50}$ = 0.05 m; and (2) an amour layer on top of the filter layer with a minimum thickness of 1.4 m comprising cover stones the size $D_{c,50}$ = 0.4 m. From design the filter layer was installed in a circular shape with a berm width (expressed as diameter) $w_b \sim 5.2D_p$, subsequently the monopile was driven through the filter layer and lastly the armour layer was applied by a grab crane to a berm width $w_b \sim 4D_p$ (measured at the top).

Since edge scour development is obviously not dependent on the design of the scour protection, but on the actual as-built scour protection, the presently available layout of the scour protection is plotted in Fig. 3.29 (Chapter 3). This figure shows that the present

scour protection still meets the design requirements (while a gradual degradation of the scour protection each year was accounted for in design). The average armour layer thickness is estimated at 0.40-0.45D_p and the average filter layer thickness at 0.1D_p.

The environmental conditions at OWEZ are dominated by tidal current with a main tidal direction of north-northeast (23˚N) during flood and south-southwest (203˚N) during ebb, see the actual tidal current rose for OWEZ in Fig. 3.30 (Chapter 3). The tide is characterized by a tidal asymmetry with a mean depth-averaged amplitude of the flood velocity of about 0.5m/s against an ebb velocity of 0.43 m/s, resulting in a tidal asymmetry factor of 1.15. The maximum recorded amplitude of the depth-averaged velocity in the direction of the flood current is 1.31m/s against 0.91m/s in the direction of the ebb current, resulting in a factor of 1.44.

1.1.3. Edge Scour Development at OWEZ

Before, during and after the construction of OWEZ bathymetrical surveys were conducted to accurately determine the as-built layouts. Since construction annual surveys were performed to evaluate the performance of the scour protection and to quantify the edge scour development. At present, the survey database contains a total of 403 surveys. The present section only details the average bed level changes around the scour protection (edge scour) over the aforementioned survey campaign running from 2006 - 2013.

The edge scour development will be described in reference to Fig. 1.2, which displays a sequence of the average bed level change following the installation of the armour layer in successive order. In this figure, the results of the 6th to 13th survey campaign are incorporated. The previous surveys (1st to 5th) were made before and during the construction phase of OWEZ, and the description of these surveys are indicated in Table 1.1. Returning to Fig. 1.2, each subplot is computed by translating the horizontal survey

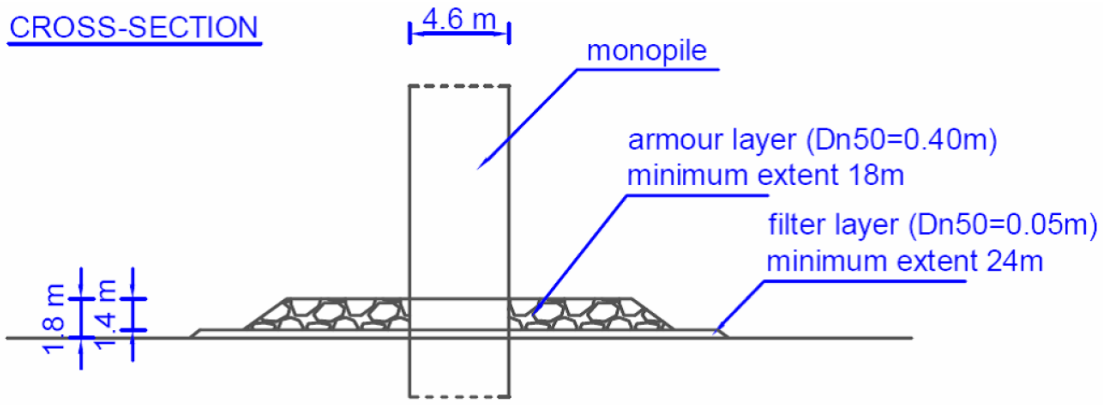

Figure 1.1. Design sketch of the scour protection system of OWEZ.

Survey No.	Description	Execution date
SU01	Initial sea bed	2006 May
SU02	Post filter installation	2006 June
SU03	Control survey	2006 June
SU04	In survey armour	2006 July
SU05	Out survey armour	2006 October
SU06	Control survey	2007 June

Table 1.1. Initial surveys during the construction phase of OWEZ, indices of survey number, description and execution date are given.

coordinates to the pile centre and the vertical coordinates to the initial seabed level for each individual survey. Subsequently, the 36 surveys are normalized by dividing by the pile diameter and averaged, resulting in an average edge scour pattern for each year. In these figures downward movement (scour) is indicated by positive values. Note that the negative values close to the pile centre (within a circle of $3D_p$) represent the installed scour protections. The average number of days between pile installation and the survey is indicated in the title of each subplot Fig 1.2a-h.

The edge scour development around the perimeter of the scour protection is clearly visible in Fig. 1.2a-h in the region outside $3D_p$, and shows the following three distinct

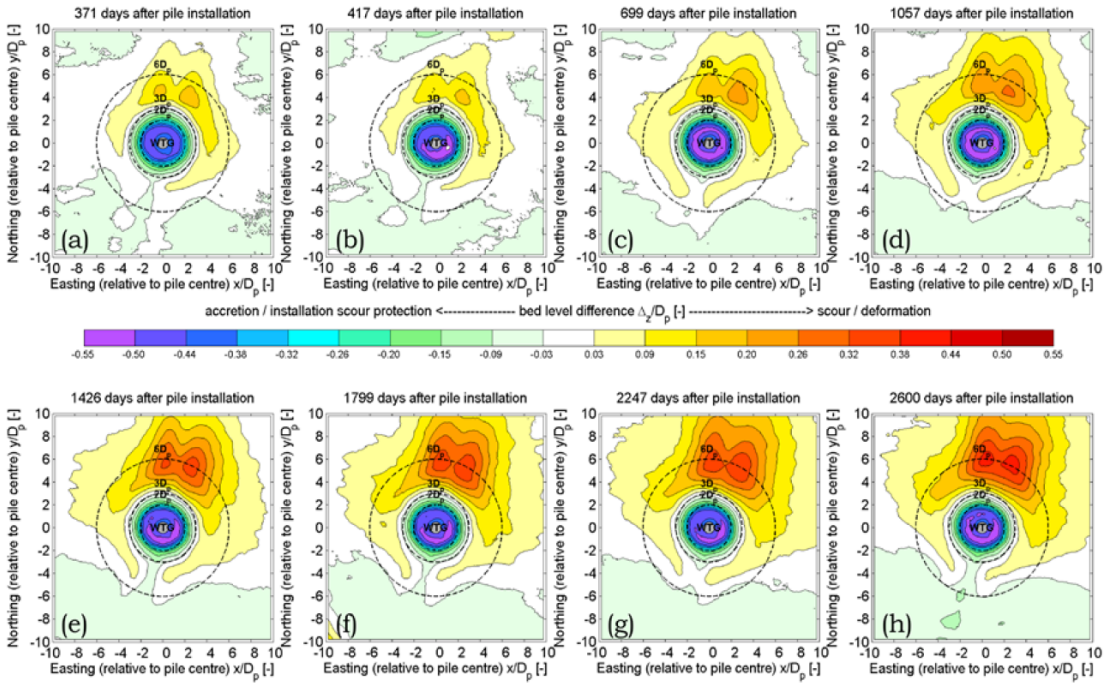

Figure 1.2. A filled contour plot of the average bed level change between 2006 and 2013, illustrating the developing edge scour (on average) through image a-h. Courtesy of Nordzeewind, a 50/50 joint venture of Shell and NUON.

features, described below. (Note that these averaged plots clearly illustrate the patterns, but do not provide information on the edge scour distribution over the individual monopiles. Besides, the deepest edge scour depths are leveled out:

(1) Edge scour happens from the upstream point to the transverse sides of the scour protection relative to the main tide direction (flood). Here the maximum edge scour depth is about 0.6 – 1.6 m. The actual current rose showing the tidal directions ebb and flood is shown in Fig. 3.30 (Chapter 3), and the individual measurements for each turbine are presented and discussed in connection with Fig. 3.32 (Chapter 3)

(2) A "two-legged" scour hole forms downstream to the main tide direction (flood) originating from the transverse sides of the scour protection. The deepest part of the (averaged) edge scour hole in Fig. 1.2h reaches 1.6 – 2.8 m. Note, that the individual measurements for each turbine are shown and discussed in conjunction with Fig. 3.33 (Chapter 3).

(3) A ridge forms in the downstream (flood) edge scour hole, and shows in Fig. 1.2a-h as an elevated area in the scour hole along the right downstream centerline (flood). Note, that the sequence of images in Fig. 1.2a-h displays the average bed displacement over the ensemble of 36 wind turbines, and the indication of the ridge is somewhat leveled out for that reason. Therefore, also the three-dimensional bathymetry is plotted for an individual monopile in Fig. 1.3 which shows a typical edge scour pattern observed at OWEZ, and here the ridge is clearly visible on both sides of the scour protection.

The reason for the developing edge scour around the scour protections in OWEZ could be caused by various hydrodynamic conditions: (1) tidal current, (2) waves; or (3) combined waves and current. Simoons (2012) suggest the lee-wake vortices appearing downstream of the dominant tidal direction as the possible cause of the two scour holes, and hereby points options one or three as the possible hydrodynamic condition responsible.

All three hydrodynamic conditions and their effect on the edge scour patterns observed in Figs. 1.2 – 1.3, are considered and discussed in this thesis; Chapter 2, 3 and Appendix A describes the effect of steady current and tidal current; whereas Chapter 3 also includes the effect of combined waves and current.

1.2. The Time Development of Scour and Backfill

Applying a stone cover as protective measures against scour can be expensive and e.g. for OWT it could be relevant to install the monopile foundations partially or fully unprotected (Wittrup, 2012) omitting the rock dump to reduce the overall installation costs. To accommodate an unprotected OWT foundation design and installation, varies scour mechanisms and the corresponding hydrodynamics needs to be examined.

The sea bed around an unprotected OWT foundation continuously experiences scour and backfilling in an alternating fashion under the ever changing wave and current climate. Here the scour and the backfilling process come into focus when the time variation of scour depth in a continuously changing flow climate (currents, waves, and combined waves and current) is considered. Observations and previous experimental campaigns

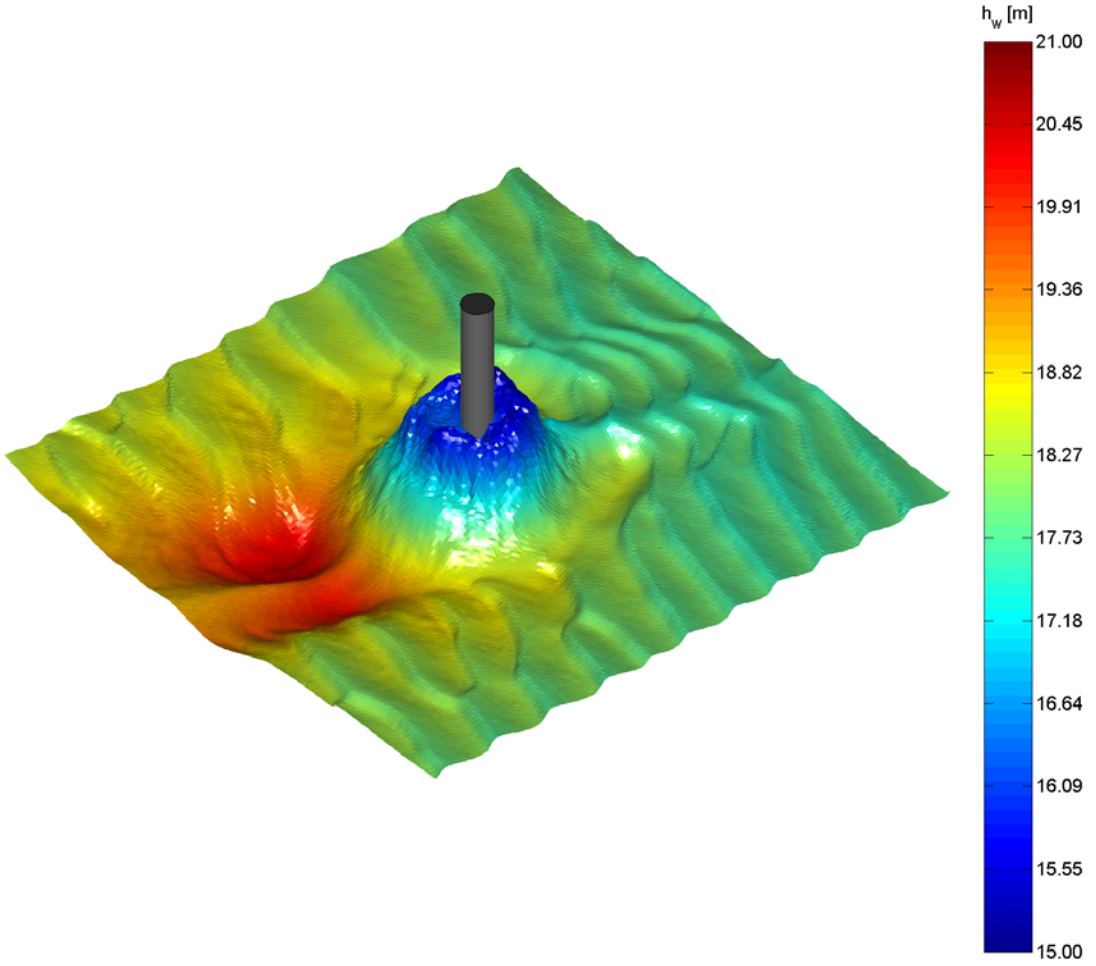

Figure 1.3. 3D-bathymetry around an individual monopile in OWEZ. The color scheme shows the water depth obtained with multibeam measurements. In order to more clearly show the bed level elevations, the vertical scale is grossly exaggerated relative to the horizontal axis. Courtesy of Nordzeewind, a 50/50 joint venture of Shell and NUON.

show that if suitable flow conditions exist, a previously generated scour hole around a pile may be backfilled, e.g. a scour hole generated by steady current is backfilled when the flow conditions change from: (1) steady current to waves; (2) wave to a milder wave climate; and (3) steady current to combined waves and current.

1.2.1. The backfilling Process

As opposed to the vast amount of studies in relation to the scour process around a pile, relatively few studies have been reported on backfilling. Fredsøe et al. (1992) studied backfilling in the case of a pipeline in a limited experimental program. Likewise, Hartvig et al. (2010) studied backfilling in the case of a pile, again, with a limited coverage. Both studies focused on backfilling of previously generated scour holes with limited data, and no clear description or understanding of the backfilling process was offered.

Engineering models have been developed with the purpose of predicting the time history of scour and backfilling for large times (weeks, months, or years) given the site specific flow climate changes, Nielsen and Hansen (2007), Raaijmakers and Rudolph (2008 a and b), and Harris et al. (2010). These models have essentially two components: scour and backfilling. The existing information on scour has been successfully incorporated in the models. This is not so, however, for the backfilling because of the lack of knowledge in this topic. To the authors' knowledge, no study is yet available investigating, in a systematic manner, backfilling around structures.

The present thesis therefore also focuses on flow and scour measurements for an unprotected mono pile. A detailed description of the backfilling process is given. Equilibrium scour depth and the time scale in a backfilling process are determined experimentally for various flow conditions comprising: steady current, waves and combined waves and current. Empirical expressions for the time scale of the backfilling process is offered, which enables an implementation of the present results in the previously mentioned engineering models.

1.2.2. The scour process in combined waves and current

The present study also focuses on scour characteristics in a flow environment where waves and current are present concurrently. Although previous work reveals various features of scour processes (such as the scour depth) in combined waves-and-current environment (Sumer and Fredsøe, 2001a, Raaijmakers and Rudolph, 2008a, 2008b), no study is yet available, investigating in a systematic manner the time scale of the scour process, an important quantity needed to develop the previously mentioned engineering models to predict scour history around piles for large times (months, years). To this end, an experimental program of physical model tests has been carried out, and design diagrams are offered.

The results show that the time scale of scour increases significantly when superimposing even a slight current on a wave flow regime. The results further show that the time scale of scour approaches the wave-alone time scale in the wave-dominated regime, and it approaches the current values in the current-dominated regime.

1.3. Outline

The present thesis is compiled of articles published, accepted, submitted or to be submitted to journals or conferences. The particular statuses about the individual papers are stated in the beginning of each specific chapter.

Chapter 2 presents results of physical model experiments where the scour adjacent to a stone cover in current is investigated. The chapter includes detailed flow measurements by particle image velocimetry in a stereoscopic setup resolving the three-component velocity and turbulence intensity field at the junction between the stone layer (acting as a rough surface) and the sand (acting as a hydraulically smooth surface). Various stone sizes, berm heights and side slopes of the covers have been used in a parametric study to find the equilibrium scour depth and the time scale of the scour process. This chapter is an extended version of a conference paper Petersen et al. (2012a), see Appendix A

Chapter 3 presents results of an extensive physical model tests campaign and field investigation of flow and edge scour around scour protections at offshore wind turbine foundations. The physical model tests encompass particle image velocimetry of the three-dimensional flow in the wake region of the pile and scour protection. The observations made in the flow experiments are supported by hot-film measurements of the bed shear stress made at the upstream-, transverse- and downstream side of the scour protection. The knowledge obtained through the latter mentioned experiments formed the basis when performing the actual scour tests. It is shown that scour happens alongside the periphery of the scour protection from the upstream- to the transverse sides, caused by the combined effect of the horseshoe vortex generated in front of the berm, and acceleration and contraction of the flow at the side edge of the scour protection. In the downstream near bed wake region a pair of counter-rotating vortices scoured the sea bed, and the experiments showed scour depth of up till 1.1 times the pile diameter. Clearly, the observed edge scour patterns, observed around the scour protection, depends heavily on the pile diameter, and the height and width of the scour protection. The experimental results seem to conform very well to the edge scour patterns observed in the field at OWEZ described in Section 1.1.

Chapter 4 presents the results of physical model tests of scour and backfill around both slender and large unprotected monopiles exposed to current, waves and combined waves and current. The results show the scour depth corresponding to the equilibrium stage of the backfilling process is the same as that corresponding to the equilibrium stage of the scour process for the same wave or combined waves and current climate. The time scale of the backfilling process has been determined as a function of three parameters namely: (1) the Keulegan-Carpenter number of the initial wave or the current (which generate the initial scour hole); (2) that of the subsequent wave which backfills the scour hole; and (3) the Shields parameter associated with the latter wave for live-bed conditions. In the case of combined waves and current, the current-to-wave-velocity ratio is also involved. During the experimental campaign it was decided to measure the time development of backfill by exploiting depth from stereo video sequences. The three-dimensional images, obtained by this technique, showing the bathymetry of the scour hole during the backfilling process are included in the paper. The procedure to obtain the images and further details are included in the conference paper in Appendix B.

In Chapter 5 the time scale of scour around a slender vertical pile in combined waves and current is studied. It is found that the time scale of scour in combined waves and current depends on three governing parameters, namely: (1) the Keulegan-Carpenter number; (2) the Shields parameters of the wave component of the flow; and (3) the current-to-wave-velocity ratio. It is possible to estimate the time scale of scour using the design guidelines provided in the chapter.

In Appendix C the sinking of the scour protections at Horns Rev 1 are studied based on physical model tests of sinking of scour protections adjacent to monopiles under the effect of waves and combined waves and current. The tests were performed during a master study supervised by the author in collaboration with PhD Anders Wedel Nielsen and Professor B. Mutlu Sumer. The extended version of the paper is in preparation.

1.4. Linking Chapters

The present results, detailed in Chapters 2 and 3, show that the failure of the edge material of scour protections or stone covers are heavily influenced by the edge scour. Alongside the edge of the scour protection sediment is removed and with this the stones at the edge are "undermined", and in turn the stones slump into the scour hole. The edge scour was found to be caused mainly by changes in the immediate hydrodynamic field in steady current or tidal current, where secondary currents, horseshoe vortices, contraction and acceleration of the flow or counter-rotating vortices were observed to scour the adjacent sea bed. The present experimental findings are supported by the observations of edge scour at the offshore wind farms Egmond aan Zee and Scroby Sands, where tidal currents scours the upstream-, transverse- and downstream sides of the scour protections, as will be detailed in the thesis (Chapter 3). It should be noted that waves also causes edge scour, but the scour is expected to be significantly smaller in magnitude for the wave climates experienced for offshore wind farm applications, the specific effect of waves on edge scour have not been studied in the present thesis. Edge scour in combined waves and current have been studied, and the results show that superposition of waves onto a current flow climate reduces the edge scour and, from the knowledge gained in Chapter 5 in conjunction with scour around a pile in combined waves and current, it is expected that the time scale of the scour increases (Chapter 3).

It should be noted that for the present campaign of edge scour experiments in current, tidal current and combined waves and current the edge scour process reached equilibrium, where the stones at the edge of the berm had fallen into the scour hole forming a protective slope. Therefore the stability and integrity of the overall stone covers remained intact even though the edge material failed. This trend was observed for both the edge scour adjacent to stone covers and scour protections around offshore wind farms respectively (Chapters 2 and 3).

It is shown that the edge scour can effectively be reduced by applying a falling apron as counter measures by a two-fold reason: (1) the stones in the falling apron covers and protects the previously erodible sea bed; and (2) the erodible part of the sea bed are located further away from the pile and scour protection where the scour potential is less pronounced. Fig. 3.27 in Chapter 3 can be used to determine the required length and/or volume of a falling apron to achieve a certain reduction in the edge scour depth.

As mentioned previously, the sea bed around an unprotected monopile experiences scour and backfill in an alternating fashion with the changing wave and current climate. With the information on the equilibrium stage scour depth and the time development of scour and backfill in current, waves or combined waves and current given in Chapters 4 and 5, it is now possible to better estimate the time variation of scour and backfill for longer time spans (weeks, months or years). If the predicted scour depth is small, it might be relevant to simply extent the monopile further into the sea bed omitting the scour protection system.

Similar analysis is relevant in the case where the stones of the scour protection system are to be placed in a previously generated scour hole (as is discussed in Chapters 2 and 3). Here, the time variation of scour and backfill (presented in Chapters 4 and 5) is needed to estimate the relevant time over which the monopile should be left unprotected before the stones are installed.

Chapter 2

Experimental investigation of flow and edge scour in current adjacent to stone covers

This chapter is submitted to and under review in Journal of Waterway, Port, Coastal and Ocean Engineering, ASCE.

T. U. Petersen[1], B. M. Sumer[2] J. Bøgelund[3], A. Yazici[4],
J. Fredsøe[5] & K. E. Meyer[6]

[1]Ph.D. – candidate, [2]Professor, [5]Professor, [6]Associate Professor, Technical University of Denmark. Section for Fluid Mechanics, Coastal and Maritime Engineering. Kgs. Lyngby, Denmark.

[3,4]M.Sc, Rambøll Oil & Gas, Formerly Technical University of Denmark, DTU Mekanik, Section of Coastal, Maritime & Structural Engineering.

Abstract: This paper presents the results of an experimental investigation on edge scour adjacent to a stone cover laid on a sandy bed. The three-dimensional flow over the edge of the stone layer has been investigated by the use of Particle Image Velocimetry. The flow measurements show a significant amount of turbulence in the primary flow near the junction between the stone layer and the sand bed, and formation of complex secondary flow structures. The results show that the flow and the edge scour process in a steady current is governed by the size of the roughness elements and to some extent the side slope of the berm. The edge scour is caused by the combined action of the primary flow and the secondary flow. The primary flow stirs up the sediment and puts it into suspension, and the secondary flow carries it away from the junction between the stone layer and the sand bed, resulting in a scour hole forming adjacent to the toe of the stone layer. The measured scour depth attained a constant level of about 1 times the stone size in the live-bed regime, further the scour depth showed a slight decrease when the side slope of the berm was increased. Design diagrams are presented for the scour depth and the time scale of the scour process.

Keywords. Edge scour, cover stones, steady current, scour protection, coastal structures, offshore structures, scour, offshore wind farm, secondary scour.

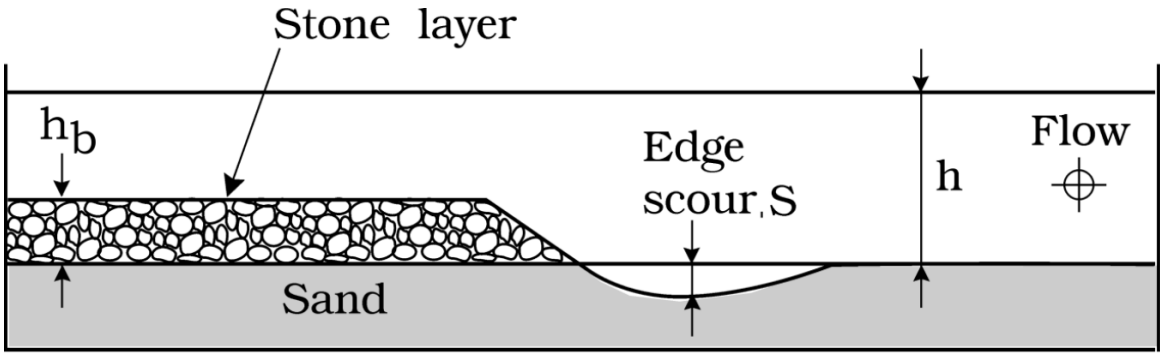

Figure 2.1. Definition sketch (schematic). Edge scour adjacent to stone cover.

2.1. Introduction

One of the methods widely used as scour protection at marine structures is rock dumping on a sandy bed. Such structures may be falling aprons used for toe protection, or they may be revetments and even breakwaters (surface piercing structures). When this structure (see the definition sketch in Fig. 2.1 for a falling apron or a berm) is exposed to current, the sand at the edge of the berm is agitated by the turbulence in the primary flow and the motion of the secondary current. When the flow reaches a critical value the sand at the side will be put into suspension and the secondary current redistributes it, and as a results of this mechanism a scour hole forms adjacent to the edge of the stone layer (Fig. 2.1).

With this, stones at the edge of the cover stones are “undermined”, and as a result slump down into the scour hole. The stone layer needs to be designed considering the edge scour such that no extensive damage to the cover occurs. Field studies by Raaijmakers et al. (2007), Raaijmakers et al. (2010) and Whitehouse et al. (2011) reveals the edge scour and the need for detailed studies on the account.

The edge-scour process and, in turn, the stability of the stone cover is affected by the three-dimensional flow over the edge of the berm. Truelsen et al. (2005) studied the flow and scour around a single stone, and in a follow-up study Dixen et al. (2013) concentrated on the scour around a half-buried sphere. The latter authors focused on the interaction of a single stone with the primary flow, whereas the present study comprises a surface of roughness elements interacting with the flow over a sand bed, considering turbulence and secondary currents generated by the presence of a stone layer.

Secondary flow structures in the case of a transition in the surface roughness and/or abrupt changes of curvature have received extensive amounts of attention. Müller and Studerus (1979), Nakagawa et al. (1981), McLean (1981) and Studerus (1982) showed that a sudden change in surface-roughness can force a secondary motion of the fluid directly over the rough section into the smooth section. Concurrent studies by Perkins (1970), Naot and Rodi (1982), Nezu and Rodi (1985) and Tominaga et al. (1989) concerned with corner induced secondary currents, where the secondary motion goes from the main body of the flow towards corners. The latter two types of secondary currents are turbulence driven, and a thorough account of the topic is given in the book of Nezu and Nakagawa (1993).

To the authors knowledge no study is yet available investigating in a systematic manner the three-dimensional flow (streamwise- and secondary flow) and the resulting edge scour

adjacent to stone layers in current. The scour at the edge of a stone layer has been studied in a limited experimental study by Fredsøe et al. (2001). The investigation consisted of one setup with a surface-piercing berm simulating a rip-rap revetment structure. The results indicated that the size of the roughness elements had an important effect on the edge scour process. Horseshoe-vortices, contraction of streamlines and lee-wake flow generated around the individual stones were observed to play a significant role in the scour process. More recently Petersen et al. (2012a) was able to measure the secondary current over the edge of a stone layer by Particle Image Velocimetry (PIV). The information rendered by the latter two studies has been included in the present investigation.

The purpose of the present investigation is to study the process of edge scour alongside the toe of a stone layer, and the study has a two-fold focus. One is to investigate the mechanisms responsible for the scour process, critical conditions for scour and the implications on the stone layer. The second purpose is to collect data for various characteristics of the edge scour process, including governing parameters and the time scale of scour. Data is collected for the purpose of establishing design diagrams.

Preliminary experimental results from the current investigation may be found in Petersen et al. (2012a, and Appendix A) which was presented at the 6th International Conference on Scour and Erosion in 2012.

2.2. Experimental Setup

Two kinds of experiments were carried out: (1) Scour experiments where the scour process adjacent to the berm was monitored in the live-bed regime ($\theta > \theta_{cr}$) with sediment transport prevailing over the entire sediment bed, revealed by the presence of sediment ripples on the bed; and (2) Velocity measurements by Particle Image Velocimetry (PIV) mapping the flow field at the toe of the berm in the clear-water regime ($\theta < \theta_{cr}$), with no ripples present. Here θ is the undisturbed Shields parameter defined by

$$\theta = \frac{U_f^2}{g(s-1)d_{50}} \tag{2.1}$$

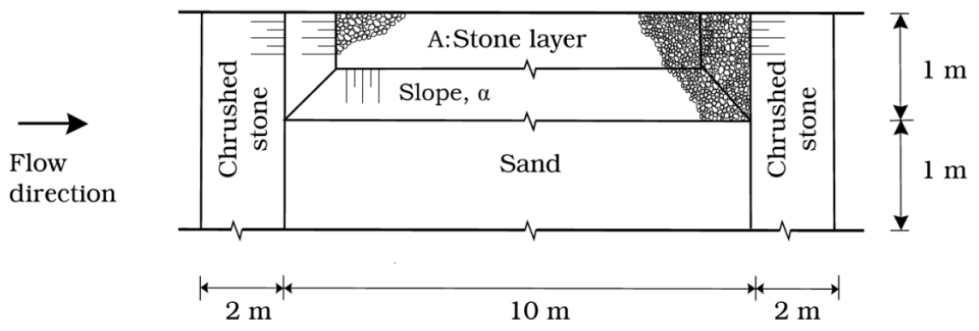

Fig. 2.2. Experimental setup, plan-view.

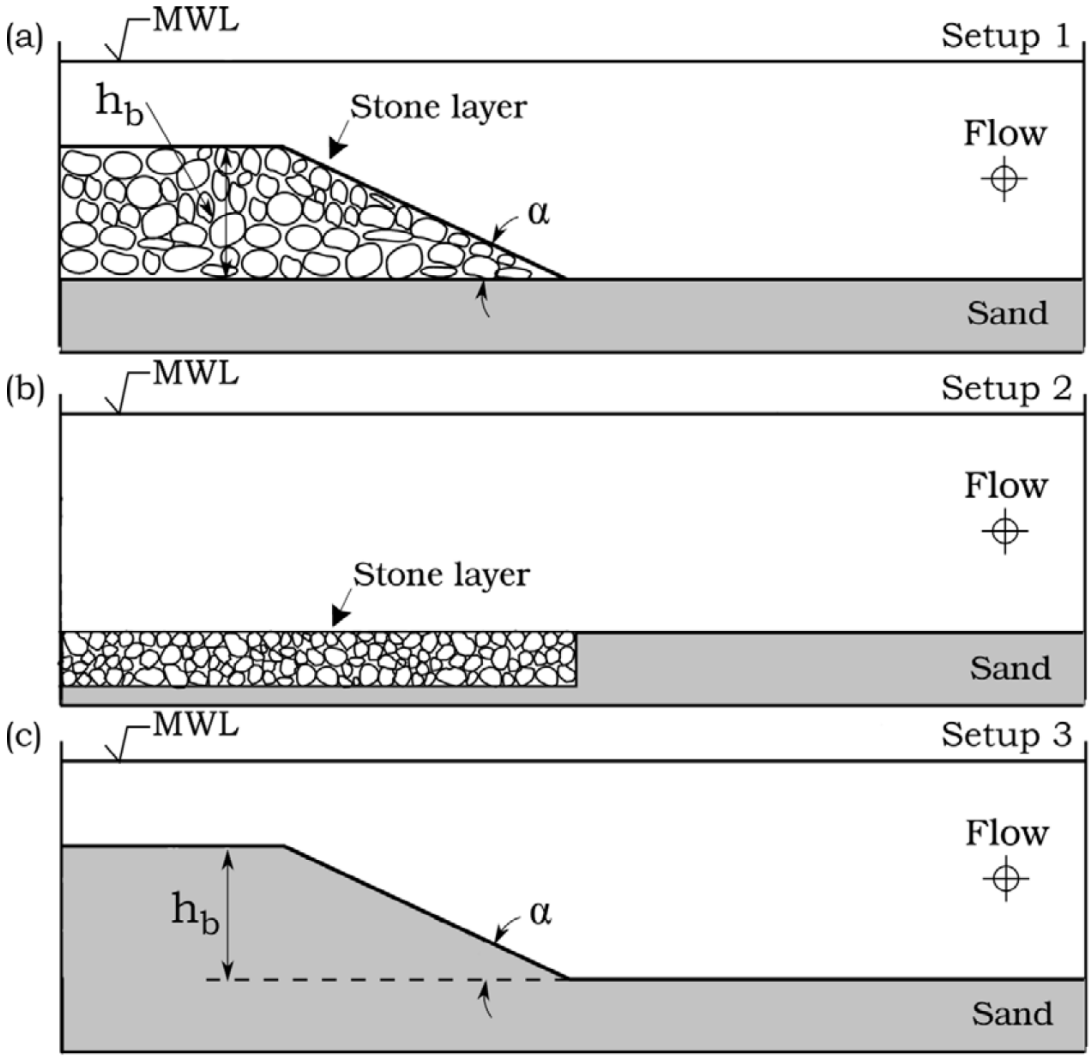

Figure 2.3. Three test setups for the measurements.

in which U_f is the bed friction velocity, g is the gravitational acceleration, s the specific gravity of the sediment grains (=2.65) and d_{50} is the sediment size. θ_{cr} is the critical value of the Shields parameter corresponding to the initiation of sediment motion at the bed.

2.2.1. Scour Experiments

The experiments were carried out in a current flume. The flume was 2.0 m wide, 0.5 m deep and 28 m long. The water depth was h = 30 cm. The current was achieved by recirculating water in the flume.

A sediment section in the form of a sand pit with two ramps at the two ends was formed in the flume. The sand pit was 2 m wide, 0.15 m deep and 10 m long (see Fig. 2.2), the distance from the upstream end of the sand pit to the inlet section being 7.5 m. The two end ramps (with 1:15 slope) were made from round stones with a 4 cm diameter. The grain

size of the sediment (fine sand) used in the experiments was d_{50} = 0.17 mm with a geometric standard deviation of $\sigma_g = d_{84}/d_{50}$ = 1.3.

A stone layer was placed on top of the sand (A in Fig. 2.2, and Fig. 2.3a) covering half of the flume width in the transverse direction, extending over the entire length of the sand pit. Two kinds of side slopes were adopted in the experiments α = 1:1 and α = 1:3

The stone layer was made of crushed angular stones with sizes of D = 1.1 cm, 2.4 cm and 3.8 cm (Fig. 2.4), each with a geometric standard deviation σ_g ~ 1.2. The stone size was measured as the diameter in all three directions, recalculated to an equivalent sphere diameter. The experiments were conducted with a stone layer thicknesses h_b = 6 cm, 10 cm and 18 cm.

Some supplementary tests were conducted with the stone layer embedded flush with the sand bed (see Setup 2, Fig. 2.3b). The thickness of the stone layer in these experiments was h_b = 3D, in which D is the stone size 2.4 cm. In the setup of these latter tests, the initial sand level was such that it was at the same level as the theoretical bottom corresponding to the stone roughness in the stone layer. The theoretical bottom is assumed to lie at 0.25 D below the top of the stones (Bayazit, 1976 and 1983).

A mini underwater video camera monitored the overall time development of the scour process at the toe of stone layer. Here measuring vertical pins (3.0 mm diameter) with distance markers were placed in order to resolve the time development of the scour process. Each of the pins was placed with a distance of 5 cm in between them. The movement of the sand grains in the video recordings acted as flow tracers, visualizing the flow structures alongside the toe of the stone layer and the individual stones.

The experiments were run for sufficiently long period of time for the scour process to reach its equilibrium stage. Subsequently, the scour profiles in the cross-flow direction were measured by a laser rangefinder (leicaDisto™ D3a) with a vertical precision of 1 mm and this operation was performed at 10 sections (about 10 cm apart) along the length of the working section.

The velocity profile across the water depth over the sand section was measured, using a Laser Doppler Anemometer (LDA), a Dantec 2D LDA system (Dantec Dynamics, Denmark) comprising a 14 mm “pen-size” submersible probe shooting horizontally, the measurements being conducted in the back-scatter mode. The measurement vertical was located 7 m away from the inlet section of the sand pit and at 0.5 m distance from the side wall. The system was equipped with a BSA F60 Flow Processor and the data was logged in BSA Flow Software v4.50. The data was logged in burst mode which meant the sampling frequency ranged between 90 – 300 Hz.

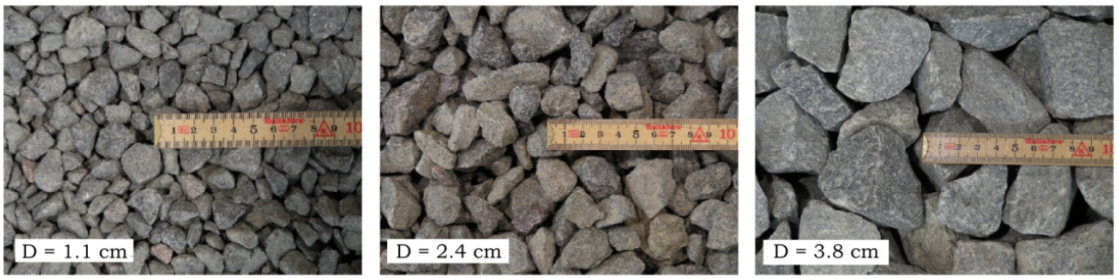

Fig. 2.4. Stones.

The current velocity was constantly monitored at y = 0.37 h corresponding to the depth averaged velocity during the course of each and every test. The latter velocity measurements were carried out, using the LDA equipment for Test 4 - 9, and an OTT propeller (the size 2.5 cm) for Tests 10 - 22. This was because the LDA was not available for the latter tests.

The procedure used in the scour tests was as follows:

1. Remove the stone layer;
2. Level off the sand bed;
3. Apply the stone layer on top of the sand;
4. Run the steady current until the scour process has reached its equilibrium stage;
5. Drain the water in flume, and measure the scour profile; and
6. Repeat Steps 1-5 until the test matrix is exhausted.

2.2.2. PIV Experiments

PIV measurements were made to investigate the three-dimensional flow in cross-sectional plane at the junction between the sand and the stone layer. The objectives of the PIV study were twofold: to obtain the secondary currents, and to estimate the turbulence intensity field over the sand and the stone layer. Three kinds of setups were tested: (1) A berm made of the same sand as the bed (Fig. 2.3c); (2) A stone layer embedded flush with the sand bed (Fig. 2.3b); and (3) A stone layer placed on the sand bed with the same side slope α as in Setup 1 (Fig. 2.3a). These setups are designated as Setup 3, Setup 2 and Setup 1. The side slope in Setups 1 and 3 was α = 1:3, and the berm height was h_b = 18 cm.

The measurements were made with a PIV system from Dantec Dynamics; the system consisted of two four megapixel cameras, double pulsed (1200 mJ/pulse) Nd:Yag laser, a synchronizer to facilitate system timing and frame grabbers to facilitate image acquisition. The PIV data logging was made in Dynamic Studio v3.30. As shown in Fig. 2.5a the two cameras were mounted alongside the flume side wall viewing the measurement volume at a 45° angle. On the glass side wall for each camera a water prism with an orientation of 45° was mounted in order to eliminate refraction. The laser light sheet was also introduced from the flume side wall aimed directly at the measurement volume. Silver-coated hollow glass-spheres the size 10 μm were used as seeding particles to obtain optimal reflection.

The PIV measurements were made in the clear-water regime, where no sediment transport occurred (not even adjacent to the stone cover), as mentioned earlier. This ensured that the sediment bed would not change during the execution time, and that larger sediment particles suspended from the bed would not disturb the data collection. This further allowed acquisition of large ensembles of data. The setup was prepared with a flat

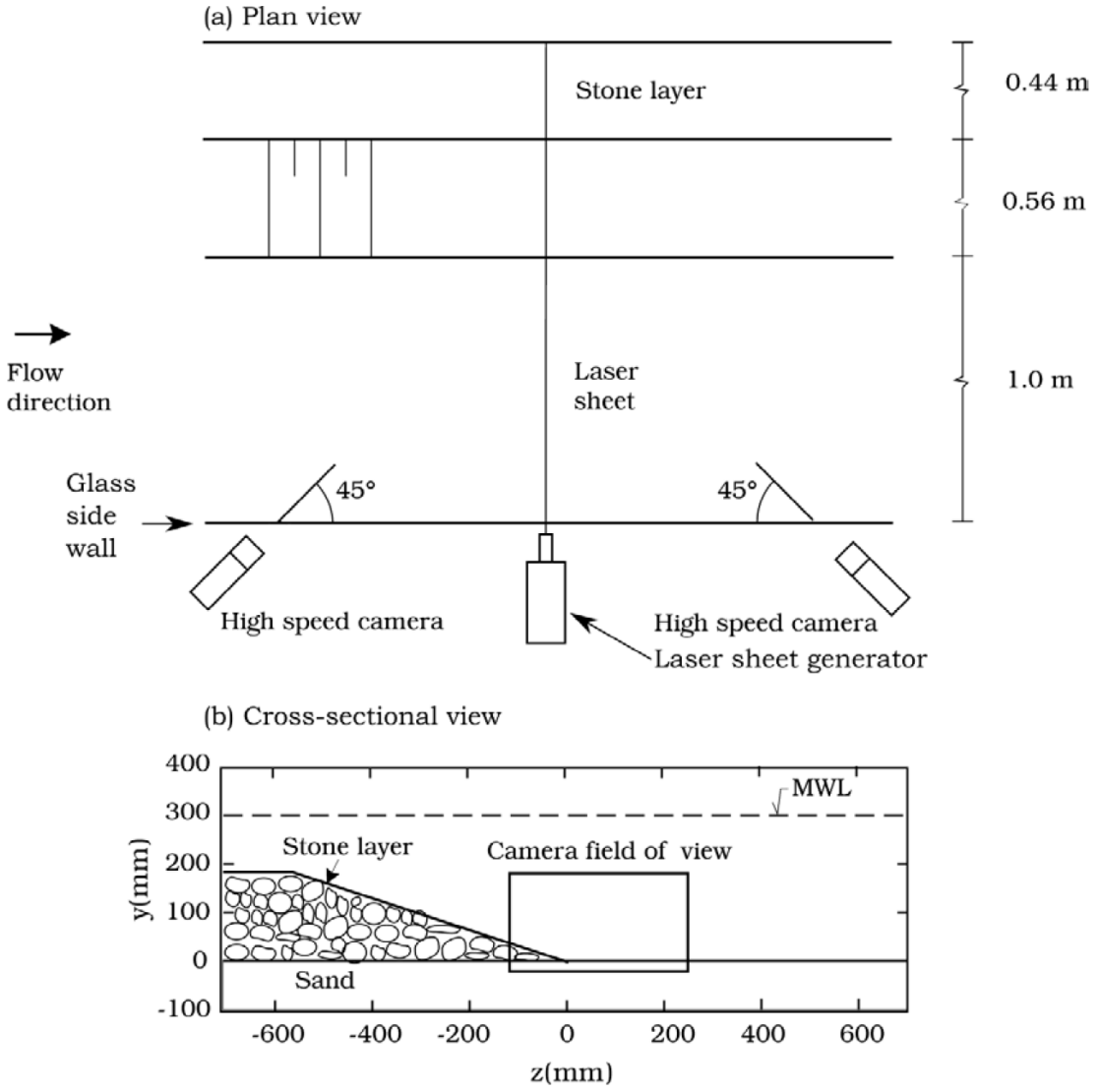

Fig. 2.5. (a) Experimental setup PIV experiments, plan-view. (b) Camera Field of View (PIV) to scale, cross-sectional view.

sediment bed and the experiment was carried out in the clear water regime, and no change in the bed morphology was observed.

For the given Setups 1, 2 and 3, the specific experimental conditions are given in Section 2.3. For each setup, a specific camera field of view (CFV) was measured, so that the flow in the vicinity of the stone layer toe was covered, a typical CFV to scale is illustrated in Fig. 2.5b. The calibration images for the specific field of view were used to provide the dimensional position for the field of view in laboratory coordinates.

At the frame position ensembles of 2800 - 5400 image pairs were obtained. The image pairs were subsequently analyzed and interrogated using the Dynamic Studio v3.30. Images were interrogated with 32 x 32 windows, using a 50 % overlap. Typical vector removal rates ranged from 2 to 4 % with the bulk of removed vectors near the sediment bed and the stone layer. In both cases the moderate scattering of laser light from the sediment grains and the stones were responsible for the removal of vectors. This effect

was inevitable despite the effort to minimize it with flat black paint applied to the surface of the stones.

2.3. Test Conditions

Table 2.1 summarizes the test conditions. In the table N is the number of stone layers obtained from

$$N = \frac{h_b}{D} \tag{2.2}$$

The quantity V is the depth averaged current velocity associated with the far field conditions measured at y = 0.37 h. The quantity U_f denotes the bed friction velocity determined in the following two ways: (1) from the familiar log-fit exercise using the measured velocity profiles from the PIV measurements; (2) from the flow resistance relation

$$U_f = \sqrt{f/2}\,V \tag{2.3}$$

in which f is calculated from the Colebrook-White formula (e.g. Schlichting, 1979) and V was obtained from the LDA or OTT propeller measurements described in the previous section. From Eq. (2.3) and the listed values for V in Table 2.1 Test 1 – 3 the obtained values of the friction velocity are 0.44 cm/s, 0.33 cm/s and 0.37 cm/s respectively. These results compare well with the listed values in Table 2.1 for the friction velocity obtained through the log fit exercise. This gives confidence in the PIV measurements, and the boundary layer profile and turbulence quantities are further discussed later in conjunction with Figs. 2.6 and 2.7.

In the table, the quantity S is the scour depth corresponding to the equilibrium stage of the scour process (Figure 2.1) while the quantity T is the time scale of the scour process, and T^* the non-dimensional time scale defined by

$$T^* = \frac{\left(g(s-1)d_{50}^3\right)^{1/2}}{D^2}\,T \tag{2.4}$$

As mentioned earlier the time scale is normalized in analogy to the time scale of scour around e.g. pipelines (Fredsøe et al., 1992), piles (Sumer et al., 1992) and spherical bodies (Truelsen et al., 2005). See also Sumer and Fredsøe (2002).

Test Number	Test Setup	Stone Size D [cm]	Number Stone Layers N [-]	Slope of the Stone Layer Toe α [-]	Berm Height h_b [cm]	Rougness Ratio d50/D [-]	Depth Averaged Current Velocity V [cm/s]	Friction Velocity in Steady Surrent U_f [cm/s]	Shields Parameter θ [-]	Measured Equilibrium Scour Depth S [mm]	Timescale T [s]	Norm. Timescale T* [-]
PIV Tests												
1	1	2,4	9	1:3	18	0,007	10,3	0,45	0.006	-	-	-
2	2	2,4	3	-	0	0,007	7,5	0,36	0.005	-	-	-
3	3	-	-	1:3	18	1,000	8,5	0,40	0.006	-	-	-
Scour Tests												
4	1	2,4	3	1:3	6	0,007	34,1	1,5	0,08	15	2150	33,3
5	1	2,4	3	1:3	6	0,007	42,1	1,9	0,12	16	1320	20,4
6	1	2,4	3	1:3	6	0,007	56,9	2,5	0,23	-	740	6,0
7	1	2,4	3	1:3	6	0,007	39,6	1,7	0,11	12	960	14,9
8	1	2,4	9	1:3	18	0,007	43,0	1,9	0,13	15	1350	20,9
9	1	2,4	9	1:3	18	0,007	30,5	1,3	0,06	8	1655	25,6
10	1	2,4	9	1:3	18	0,007	30,2	1,3	0,06	10	1820	28,2
11	1	2,4	9	1:3	18	0,007	30,0	1,3	0,06	6	3570	55,3
12	1	2,4	9	1:3	18	0,007	39,0	1,7	0,11	12	1980	30,7
13	1	2,4	9	1:3	18	0,007	50,0	2,2	0,18	15	2320	35,9
14	2	2,4	3	-	0	0,007	39,0	1,7	0,11	11	2650	41
15	2	2,4	3	-	0	0,007	49,0	2,2	0,17	25	2160	33,4
16	2	2,4	3	-	0	0,007	42,0	1,8	0,12	18	2620	40,6
17	2	2,4	3	-	0	0,007	48,0	2,1	0,16	19	2040	31,6
11	1	1,1	18	1:3	18	0,016	38,0	1,6	0,10	7	2855	210,4
12	1	1,1	18	1:3	18	0,016	43,0	1,8	0,12	9	2110	155,5
13	1	1,1	18	1:3	18	0,016	45,0	1,9	0,14	7	1380	101,7
14	1	2,4	4	1:1	10	0,007	39,0	1,7	0,11	10	3950	61,2
15	1	2,4	4	1:1	10	0,007	45,0	2,0	0,14	12	3450	53,4
16	1	2,4	4	1:1	10	0,007	48,0	2,1	0,16	22	560	8,7
17	1	2,4	4	1:1	10	0,007	43,0	1,9	0,13	12	3450	53,4
18	1	3,8	5	1:3	18	0,0045	38,7	1,6	0,10	19	790	4,9
19	1	3,8	5	1:3	18	0,0045	42,9	1,9	0,13	20	540	3,3
20	1	3,8	5	1:3	18	0,0045	33,1	1,4	0,07	10	980	6,1
21	1	3,8	5	1:3	18	0,0045	32,2	1,4	0,07	10	655	4
22	1	3,8	5	1:3	18	0,0045	29,5	1,3	0,06	5	750	4,6

Table 2.1. Test Conditions: Particle Image Velocimetry measurements and scour experiments.

2.4. Results and Discussion

2.4.1. Flow from PIV measurements

Fig. 2.6 shows the mean velocity distribution obtained from the PIV measurements. The velocity and the distance from the bed are normalized by the inner flow parameters (namely U_f, the bed friction velocity and ν, the kinematic viscosity). The measurements presented in Fig. 2.6 corresponds to the far field, at the spanwise distance z = 200 mm from the toe (Test 1, Fig. 2.3a). Line a in Fig. 2.6 represents the van Driest (1956) velocity profile defined by:

$$\bar{u} = 2U_f \int_0^{y^+} \frac{dy^+}{1+\left\{1+4\kappa^2 y^{+2}\left[1-exp\left(-\frac{y^+}{A_d}\right)\right]^2\right\}^{1/2}} \tag{2.5}$$

in which $\bar{u}$ is time averaged streamwise velocity. Here y^+ is

$$y^+ = \frac{yU_f}{\upsilon} \tag{2.6}$$

κ is the von Karman constant (=0.4) and A_d the damping coefficient (=25). Line b in Fig. 2.6 represents the logarithmic law for flow over a hydraulically smooth bed defined by:

$$\bar{u} = U_f\,(2.5\,ln\,y^+ + 5.1) \tag{2.7}$$

Fig. 2.7, on the other hand, shows the distribution of the turbulence quantities $\left(\sqrt{\overline{u'^2}}, \sqrt{\overline{v'^2}}, \sqrt{\overline{w'^2}}\right)$ normalized in the same way at the same location. u' is the fluctuating component of the streamwise velocity, $u' = u - \bar{u}$, v' is the fluctuating component of the vertical velocity, $v' = v - \bar{v}$ and w' is the fluctuating component of the lateral velocity, $w' = w - \overline{w}$.

The solid lines in Fig. 2.7 are reproduced from Monin and Yaglom (1973, Fig. 26 p. 280), corresponding to the smooth-wall, fully developed turbulent boundary layers. We note that the grain Reynolds number (in Test 1) is k_S^+ = 1.7 < 5 (in which k_s^+ is $k_s U_f/\nu$, k_s is Nikuradse's equivalent sand roughness, taken as $k_s = 2.5d_{50}$), and therefore the bed in this experiment acted as a hydraulically smooth wall (Nezu and Nakagawa, 1993). Figs. 2.6 and Fig. 2.7 indicate that the present far-field data agree quite well with the classic smooth-wall boundary layer

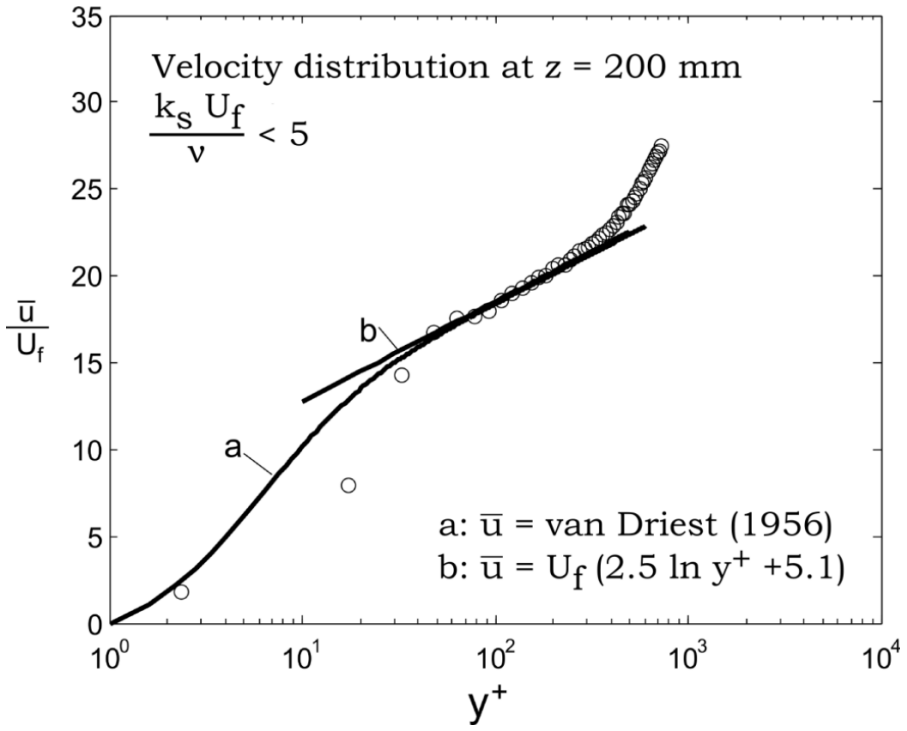

Fig. 2.6. Semilogarithmic plot of time-averaged velocity profile at z = 200 mm from the toe of the stone layer (Test 1).

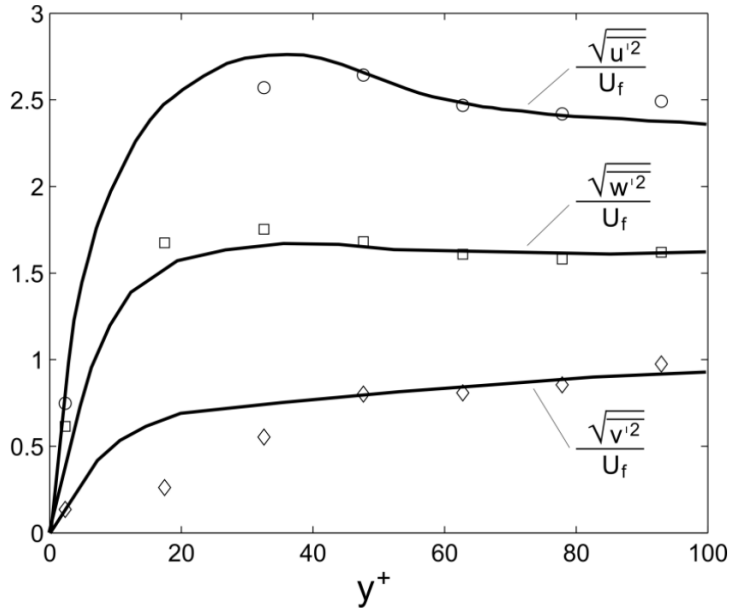

Fig. 2.7. Turbulence quantities near the bed at z = 200 mm from the stone layer (Test 1), solid lines taken from Monin and Yaglom (1973).

data, and therefore this gives confidence in the use of the present PIV results with regard to the flow quantities measured in the near-field, such as the mean flow, turbulence and secondary flows.

Fig. 2.8a shows the contour plot of the mean streamwise component of the flow velocity $\bar{u}(y,z)$, while Fig. 2.8b shows the contour plot of the turbulent kinetic energy $k(y,z)$ in Test 1 with Setup 1 (Fig. 2.3a). Here k is defined by

$$k = \frac{1}{2}\left(\overline{u'^2} + \overline{v'^2} + \overline{w'^2}\right) \tag{2.8}$$

The results obtained for Setups 2 and 3 are not presented here for reasons of space. Nevertheless, the picture regarding both $\bar{u}$ and k is much the same in the qualitative sense.

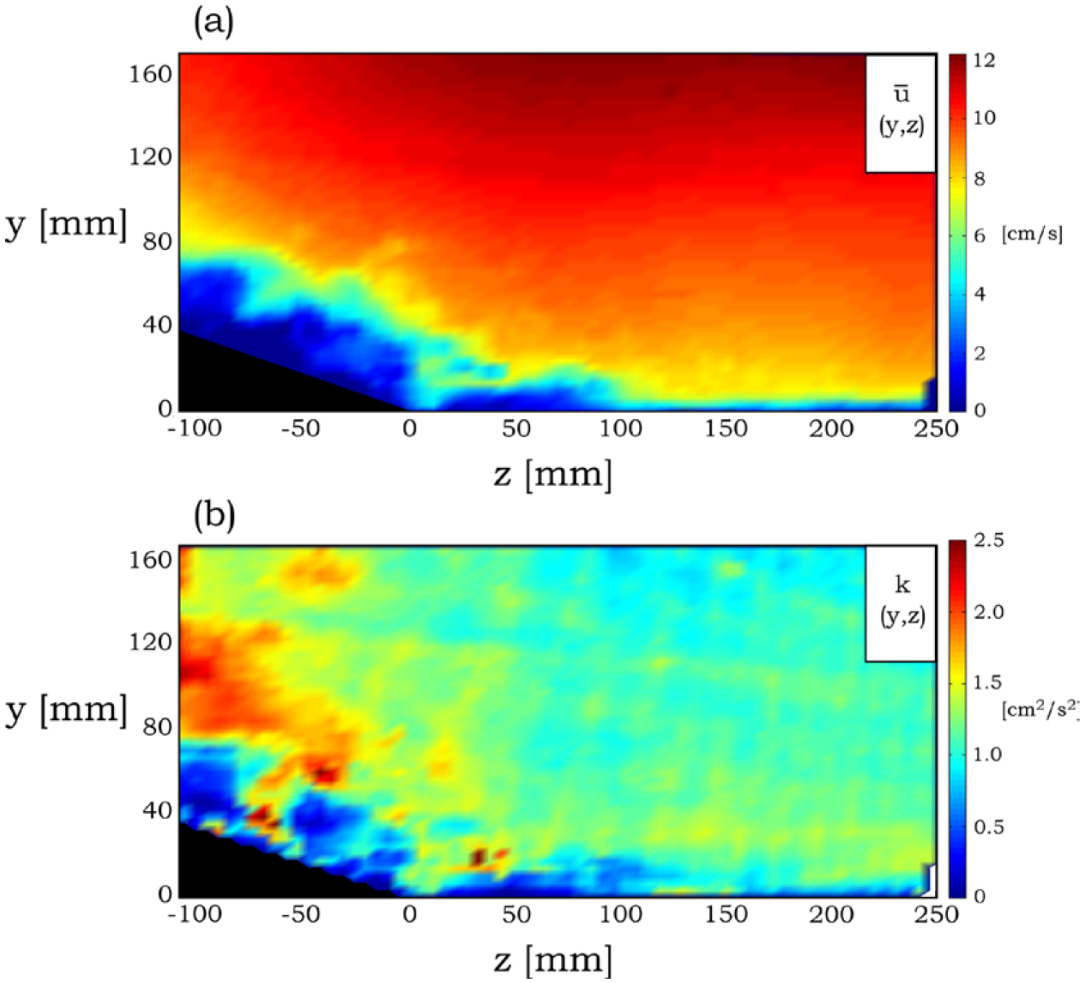

Figure 2.8. (a) Contour plot of mean streamwise velocity $\bar{u}(y,z)$ in Camera Field of View (Test 1). (b) Contour plot of turbulent kinetic energy $k(y,z)$ in Camera Field of View (Test 1), with k defined by Eq. (2.8).

Fig. 2.9 displays the secondary currents obtained by the present PIV measurements for the three cases studied, namely Setup 1, Setup 2 and Setup 3 (see, Fig. 2.3) (it is important to notice that the scales in the three panels of Fig. 2.9 are kept different for illustration purposes). The PIV vector diagrams in Fig. 2.9 are accompanied with the sketches displayed in Fig. 2.10 to help recognize the longitudinal vortices marked N and M.

The secondary flow picture in Fig. 2.9c (or Fig. 2.10c) resembles what is known as corner flows, and has been reported by earlier researchers, notably Perkins (1970), Naot and Rodi (1982), Nezu and Rodi (1985) and Tominaga et al. (1989) among others. This corner-induced secondary flow is mainly caused by the anisotropic wall turbulence; the velocity fluctuations tangential to the isovel lines of the primary flow exceeds those perpendicular to the isovel, forming a source of vorticity. The motion of the secondary currents is therefore towards any isovel curvature. The magnitude of the secondary flow velocity U_s is $\frac{U_s}{V} = 0.01 - 0.012$ and $\frac{U_s}{U_f} = 0.25 - 0.32$, in which U_s is defined by

$$U_s = \sqrt{\overline{v^2} + \overline{w^2}} \tag{2.9}$$

The latter values agrees well with the findings of Nezu and Nakagawa (1993) and Melling and Whitelaw (1976) which states $U_s/U_{max} \cong 0.015$ and $U_s/U_f \cong 0.3$.

The secondary flow in the case with a sudden change in surface roughness (Fig. 2.9b) is similarly turbulence driven. Here the gradients of $\overline{v^2}$, $\overline{w^2}$ and $\overline{vw}$ are generated due to the non-homogeneity of the bed shear stress and in turn the anisotropy of turbulence (Nezu and Nakagawa, 1993). The bed shear stress τ_0 over the rough section is greater than over the smooth generating anisotropy between v' and w' constituting a source of streamwise vorticity and cellular secondary currents. The gradients of v' and w' forces the secondary motion from the rough patch of the bed towards the smoother part (Fig. 2.10b), as revealed by studies of Müller and Studerus (1979), Nakagawa et al. (1981), McLean (1981) Studerus (1982) and more recently by Fredsøe et al. (1993) and Fuhrman et al. (2011) in the case of wave boundary layers. From Fig. 2.9 (b), it can be seen that the magnitude of roughness-induced secondary currents, near the bottom, is $U_s/V \cong 0.045$ and $U_s/U_f \cong 1$. These values are in remarkably good agreement with those obtained by Fuhrman et al. (2011) from a CFD exercise carried out for oscillatory flow with similar roughness ratio $\left(\frac{d_{50}}{D}\right)$ and those obtained experimentally and analytically by Wang and Cheng (2005, 2006) for current flow over varying rough and smooth bed strips.

Clearly, with the superposition of the two previous cases a more complex secondary flow will be obtained (Fig. 2.9a). The side-wall roughness case, forming the combined case of the latter two secondary flow scenarios (corner- and roughness induced secondary currents), has been studied numerically Naot (1984) and experimentally by Tominaga and Nezu (1986), Hayashi (1985) and Tominaga et al. (1989). The latter works revealed that an increase in side-wall roughness produced slightly stronger secondary currents. The present study shows the same effect going from about $U_s/V \cong 0.01$ in the corner region of the uniform roughness case, to about $U_s/V \cong 0.03$ in the side-wall roughness case shown in Fig. 2.9a.

From the traces of the secondary current patterns shown in Fig 2.9 and Fig. 2.10 it is clear that both types of turbulence-induced secondary currents at the toe of the berm have cross-flow motion over the sand bed directed away from the berm. When comparing the strength of the secondary flow the transition in surface roughness forces a motion which is several times stronger than in the corner-flow case. This indicates that the roughness ratio d_{50}/D between the sand- and the stone layer has the most significant effect on the formation of the secondary flow components and the magnitude of the velocity U_s. When increasing the slope α of the berm the strength of the secondary current is expected to decrease even with a side-wall roughness applied and this trend is clearly observed in the present data. The effect of the pattern and strength of the secondary currents in relation to the scour process will be detailed in the following sections.

Fig. 2.11 illustrates the way in which the turbulent kinetic energy varies with respect to the spanwise direction for the three cases, Setup 1, Setup 2 and Setup 3 (Fig. 2.3). The following conclusions can be drawn from Fig. 2.11:

1. Let us start with the corner-induce secondary flow case, namely Fig. 2.11c shows that the turbulence near the bed increases as z approaches to zero ($z \to 0$). This is linked to the secondary flow; the secondary flow directed towards the corner brings turbulence rich fluid from the main body (outer region) of the flow into the corner area, and therefore the turbulence is increased here. Clearly, this effect is reduced as one moves away from the corner.

2. Regarding the case of the sudden change in the roughness (see the inset in Fig. 2.11b). The figure indicates that; (1) a significant amount of turbulence is generated over the rough section; and (2) this turbulence is evidently transported towards the far field by the secondary flow previously described in conjunction with Fig. 2.9b (or Fig. 2.10b). Obviously, one expects that the level of turbulence will undergo a certain amount of decay with the distance from the toe, as revealed by Fig. 2.11b.

3. As for the case with the roughness change combined with the sloping side wall (Fig. 2.11a) the distinct difference in the turbulence level in Fig. 2.11b (Setup 2, Fig. 2.3) and in Fig. 2.11a (Setup 1, Fig. 2.3) is linked to the bed shear stress associated with the main flow over the rough boundary. The bed shear stress over the free-board is, for the present setup (Setup 1, Fig. 2.3), $\mathrm{O}\left(\frac{1}{2}\tau_{toe}\right)$ in which τ_{toe} is the bed shear stress at the toe of the rough side-wall, and O means order of magnitude. The latter is due to the small flow velocity over the free-board. As the turbulence is directly proportional with τ_0, namely $k \sim \frac{\tau_0}{\rho}$, then the turbulence generated in the case of Setup 1 will be smaller than that generated in Setup 2, as revealed by Fig. 2.11b and Fig. 2.11a. Obviously this turbulence is subject to decay with increasing z, until it reaches the level associated with the sand bed, as indicated in Fig. 2.11a.

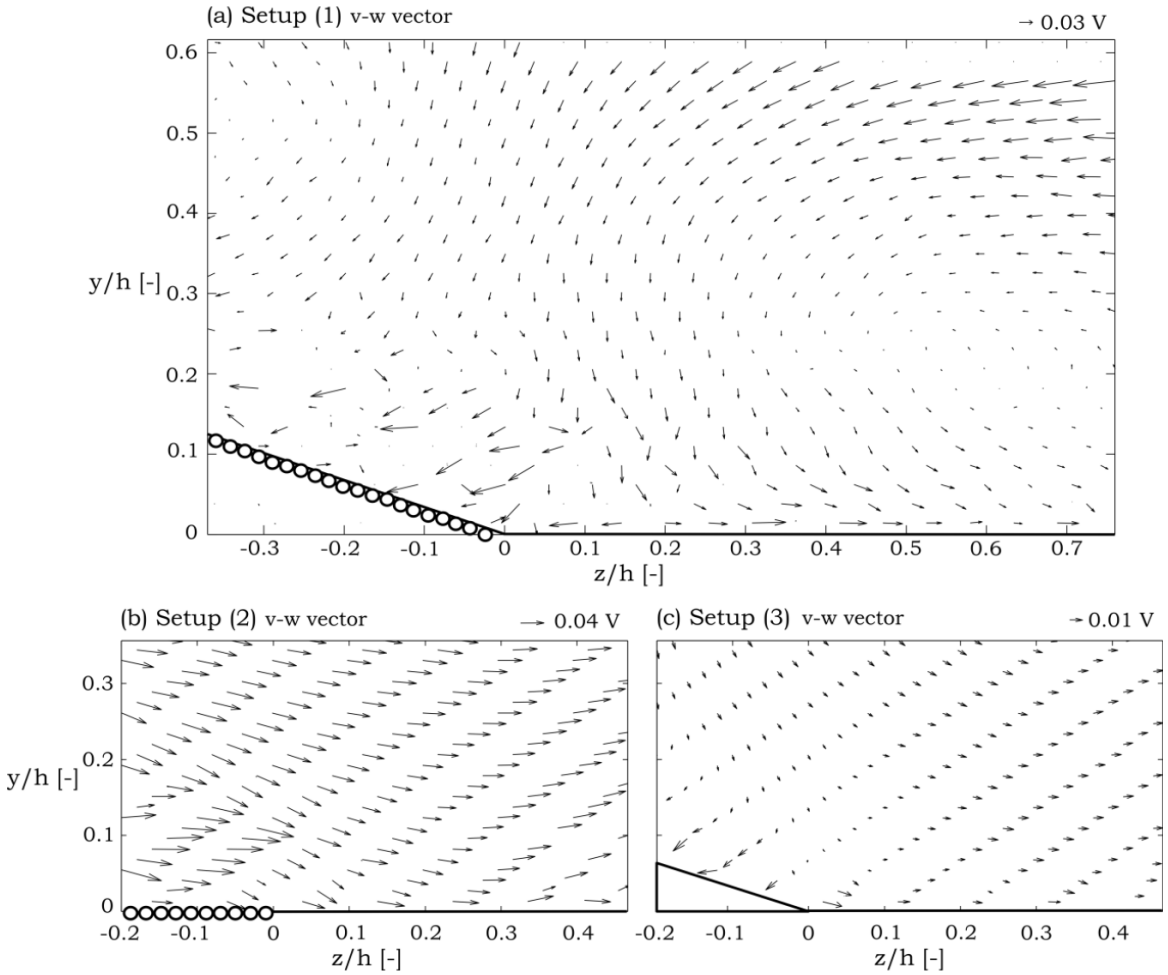

Figure 2.9. Vector description (v, w) of cellular secondary currents in: (a) Setup 1, (b) Setup 2 and (c) Setup 3, according to the definition in Fig. 2.3.

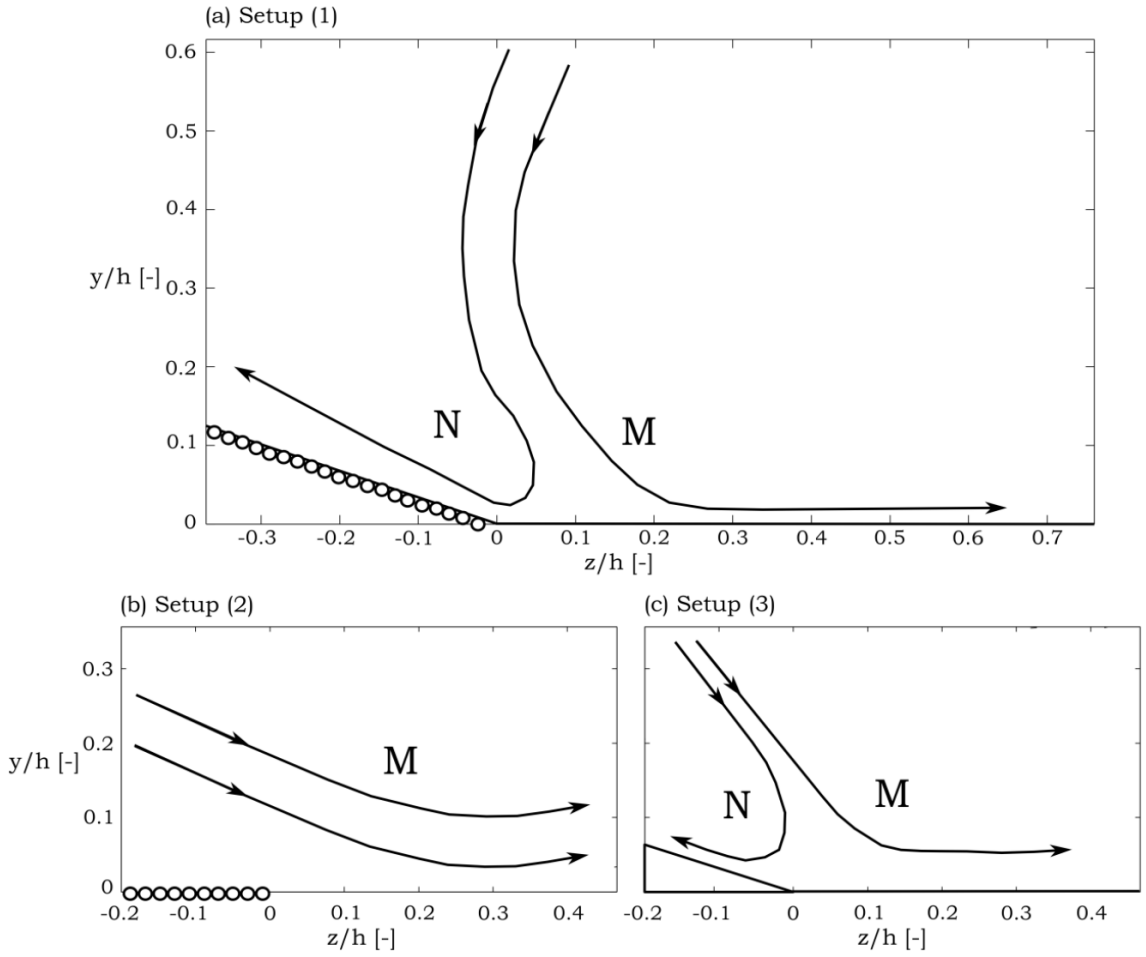

Figure 2.10. Secondary current patterns observed in Setup 1, Setup 2 and Setup 3 presented in Fig. 2.9.

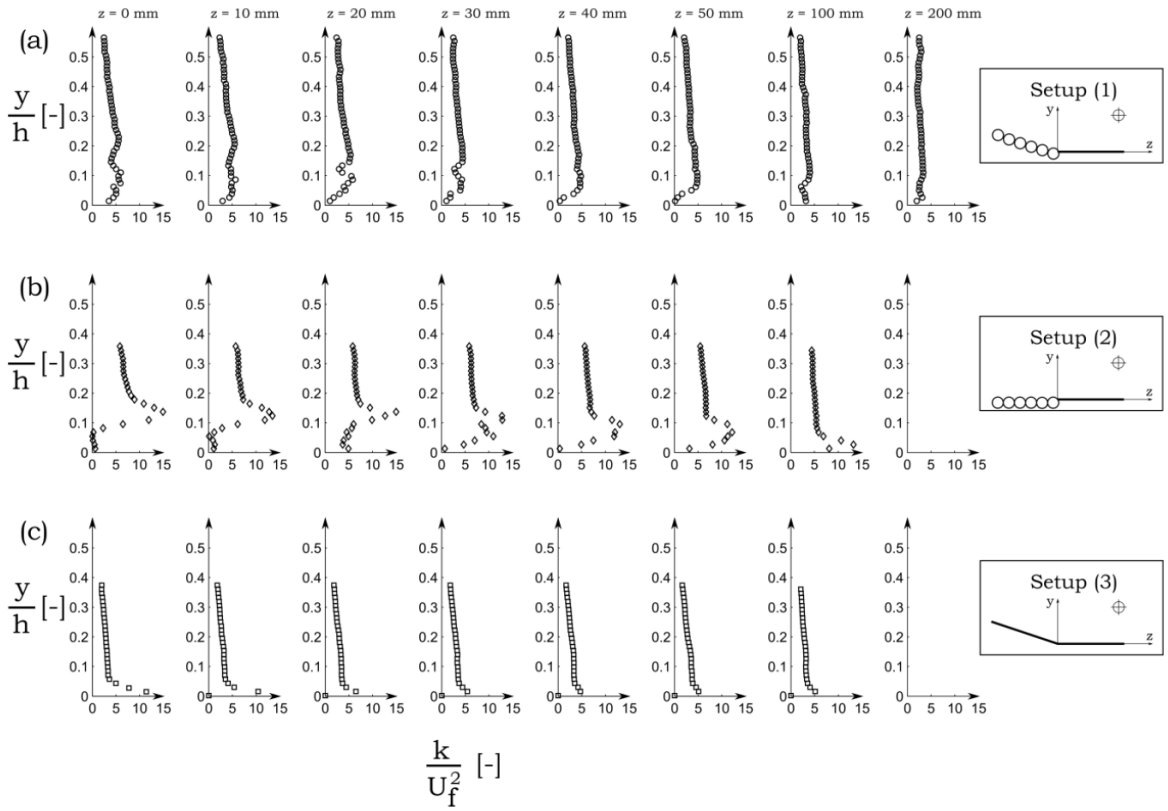

Figure 2.11. Turbulent kinetic energy in the spanwise direction z over the smooth section in (a) Setup 1, (b) Setup 2 and (c) Setup 3 (see the definition sketch in Fig. 2.3).

2.4.2. Mechanism of edge scour

Fig. 2.12 shows the cross flow bed profiles measured at ten sections corresponding to the equilibrium stage of the scour process in Test 9. The results show considerable scatter and this is due to the ripples, which extend over the entire sediment bed. Fig. 2.13 displays the "space-averaged" cross-flow bed profile (solid line), averaged over the ten profiles given in Fig. 2.12. Fig. 2.13 also includes the "time-averaged" profile (dashed line), obtained at the last section (x = 900 mm, see Fig. 2.12). As expected, the mean profile obtained by space averaging and that obtained by time averaging practically collapse on a single curve (save the far-field end of the scour profiles). Despite the scatter Fig. 2.12 and Fig. 2.13 show the following pattern:

1. Scour occurs at the edge of the stone layer (Area B)
2. Deposition occurs inside the toe of the stone layer (Area A)
3. A slight deposition also occurs outside area B (Area C), although the space-averaged profile does not display this feature.

As indicated in Fig. 2.13 and observed through the remaining tests in Table 2.1, about 2/3 of the scoured sediment is transported with the primary flow out of the measurement section, and about 1/3 of the sediment is transported laterally into the stone layer.

Fig. 2.9a, Fig. 2.10a, Fig. 2.11a, Fig. 2.12 and Fig. 2.13 suggest the following mechanism of edge scour (or toe scour): Sediment is stirred up by the main (primary) flow and entrained into the main body of the flow, and the secondary current M in Fig. 2.9a and Fig. 2.10a carries the sediment away from the toe towards the sand section, resulting in a scour hole marked B in Fig. 2.13. Clearly the additional amount of turbulence brought into the toe area from the rough section (Fig. 2.11a) will enhance the entrainment of sediment into the main body of the flow. It may be noted that the previously mentioned additional field of turbulence also includes flow features such as horseshoe vortices and lee-wake vortices formed around individual stones.

Now, as seen in Fig. 2.9a and Fig. 2.10a, the other branch of the secondary flow near the toe, marked N in Fig. 2.10a, will carry the sediment entrained into the flow, away from the toe penetrating inside the stone layer, and therefore will cause a deposition there marked A in Fig. 2.13.

Returning back to the scour process. With the scour, stones at the edge of the berm are "undermined", and as result slump down into the scour hole, forming a protective cover. In some cases the latter process was accompanied by sinking of the stones caused by shear failure of the sand beneath the stones. Here the sand loses its bearing capacity and the stones sink into the sediment bed. The displacement and sinking of the stones at the toe causes some portion of the upper stones layers to "avalanche" en masse over the sloping surface of the stone layer. As a result the surface of the sloping stone layer

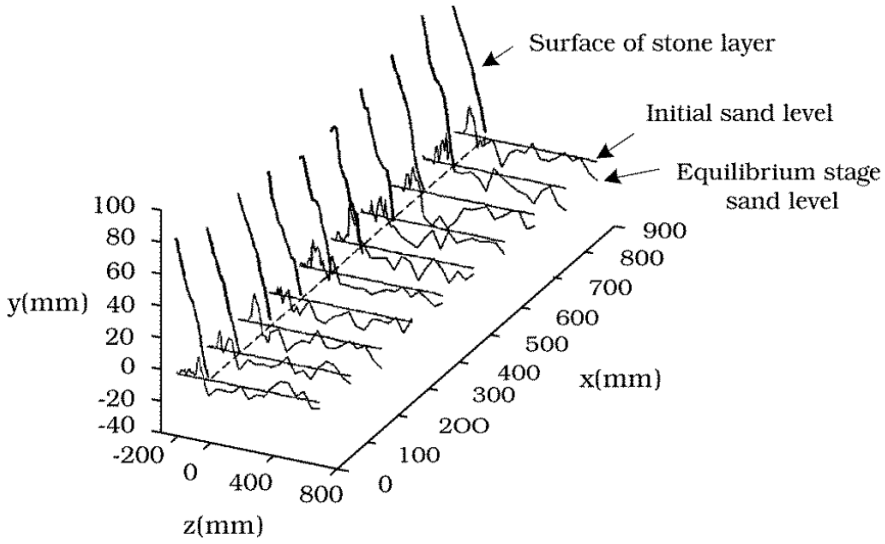

Figure 2.12. Bed profiles measured at 10 sections across the longitudinal direction. The length of the working section was 1 m. Live-bed ($\theta > \theta_{cr}$). Test 9. Vertical scale is grossly exaggerated.

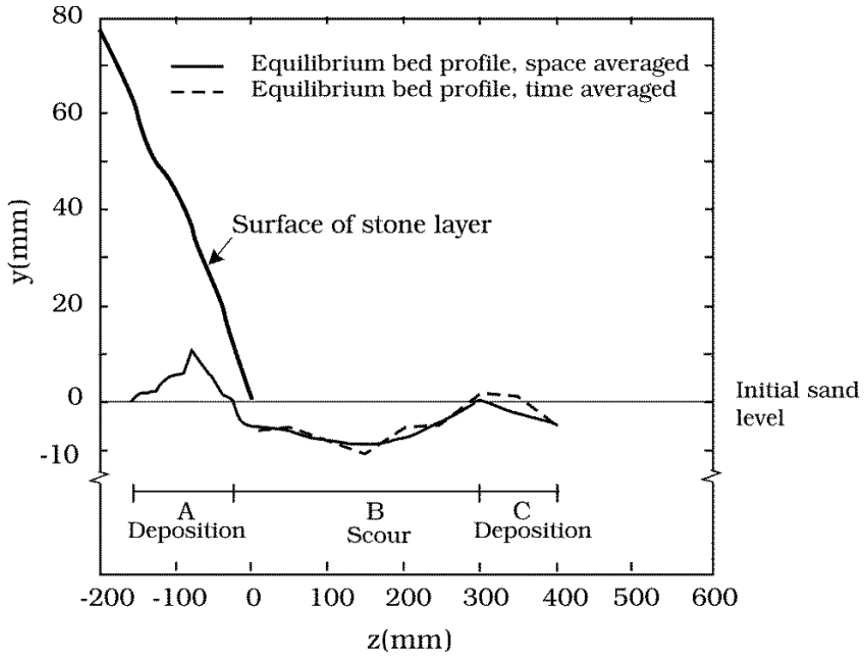

Figure 2.13. Mean bed profile, space- and time averaged in cross-flow direction. Sketch of scour and deposition pattern. Live-bed ($\theta > \theta_{cr}$). Test 9. Vertical scale is grossly exaggerated.

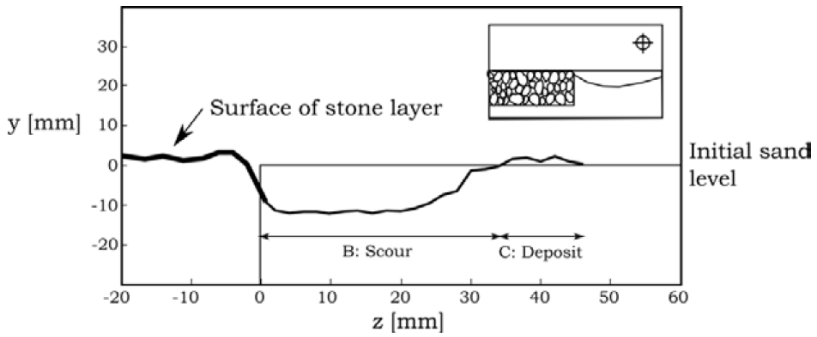

Figure 2.14. Mean bed profile, space averaged in cross-flow direction. Sketch of scour and deposition pattern. Live-bed ($\theta > \theta_{cr}$). Test 14. Vertical scale is grossly exaggerated.

stretches and settles. The observed displacements of the stone layer surface is O(0.3 – 0.5D) in the vertical and O(2 – 3D) in the horizontal on average.

Figure 2.14 displays the scour profile obtained in the case where the stones in three layers were embedded flush with the sand bed (Test 14, Setup 2 Fig. 2.3). It is clearly seen that there is a distinct scour hole forming adjacent to the junction between the stone section and the sand bed. This scour hole can be explained in exactly the same way as in the previous case (Setup 1, Fig. 2.3). Namely the scour is caused by the combined effect of the primary- and the secondary flow (Fig. 2.9b). In this case, as no second branch of the secondary current (like N in Fig 2.10), there will be no sand transport into the stone section, as clearly revealed in Fig. 2.14.

2.4.3. Scour depth

On dimensional grounds, the equilibrium stage of the edge scour process, where the sediment is removed from the side of the berm, can be described by the following relationship of the governing parameters in non-dimensional form:

$$\frac{S}{D} = f\left(\theta, \frac{d_{50}}{D}, \frac{F}{h}, \alpha\right) \tag{2.10}$$

in which S is the equilibrium scour depth here normalized by the stone size D, θ is the Shields parameter, $\frac{d_{50}}{D}$ is the roughness ratio between the sand and the stone layer, F/h is the free-board-to-water-depth ratio and α the slope of the toe of the berm.

Regarding the independent variables in Eq. (2.10):

1. θ is involved because it controls the sediment transport in the scour process.
2. $\frac{d_{50}}{D}$ is involved as it controls the magnitude of U_s.
3. F/h is involved as it controls the magnitude of U_s.

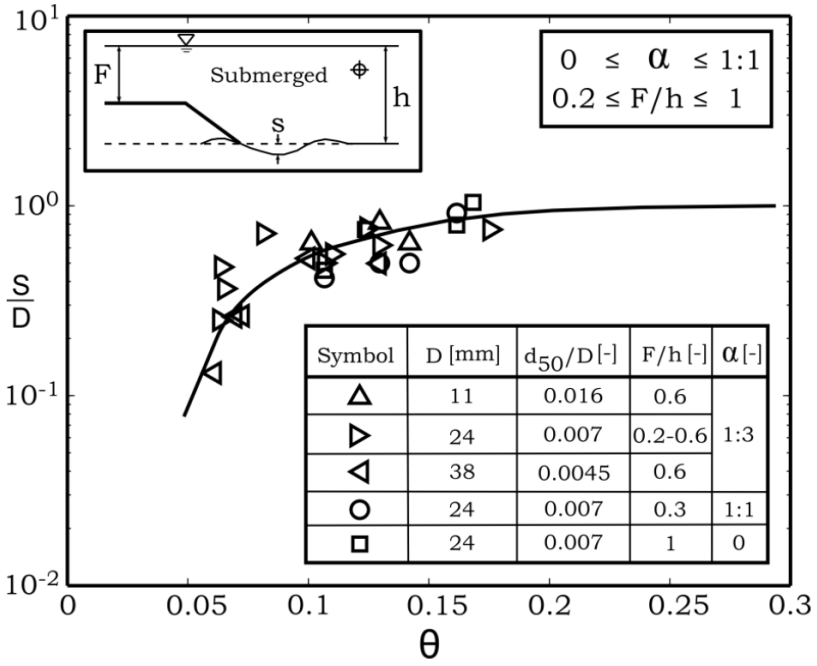

Figure 2.15. Equilibrium scour depth. Live-bed ($\theta > \theta_{cr}$).

4. α is involved because it affects the magnitude of U_s and the pattern of the secondary flow structures, and hereby the redistribution of sediment in the scour process

Now, the equilibrium scour depth S normalized by the stone size D is grouped according to $\frac{d_{50}}{D}$, $\frac{F}{h}$ and the α value and plotted against the Shields parameter in Fig. 2.15.

Fig. 2.15 shows the following:

1. It is seen that the scour depth correlates well with the stone size D, and D is involved because it represents the change in surface roughness from the stone layer to the sand bed. The roughness change induces a significant secondary current, as was discussed in conjunction with Fig. 2.9a and Fig. 2.9b.

2. The data reveals that there is correlation between the equilibrium scour depth S/D and the Shields parameter. With increasing Shields parameter the scour depth increases until it attains a constant level $S/D \to 1$, while S/D decreases with decreasing θ. The latter behavior is expected as the sediment transport is significantly decreased approaching the critical Shields parameter, even with some amplification of θ close the stone layer. The dependence of the equilibrium scour depth to the Shields parameter is in accord with previous results in relation scour around stones by Truelsen et al. (2005) and Dixen et al. (2013).

3. For the tested ranges of $d_{50}/D = 0.0045 - 0.016$ no clear effect on the scour depth is observed. This may be linked with the relatively narrow range of this parameter for the data plotted in the figure. Clearly caution must be observed when the field value of d_{50}/D is outside the present range.

4. From the present data the effect of α on S/D is not evident. For the tested ranges of α it seems the effect of the stone size D is dominating, both with respect to the strength of the secondary currents and the magnitude of S/D. This is in conjunction with Fig. 2.15 and the previous discussed secondary current patterns presented in Fig. 2.9.

Fig. 2.16 compares the present data with those of Fredsøe et al. (2001). The setup for the latter comprised an emerged berm, i.e. $h_s \geq h$, F/h = 0 and α = 1:1 simulating a revetment structure. Fig. 2.16 shows that the present non-dimensional scour depth is slightly larger than the results of Fredsøe et al. (2001) and can be explained as follows. The free-board-to-water-depht ratio F/h is greater in the present case than in Fredsøe et al. (2001) for the same side slope. The greater the value of the F/h parameter, the greater the magnitude of the secondary flow, and therefore the scour depth should be larger in the present case.

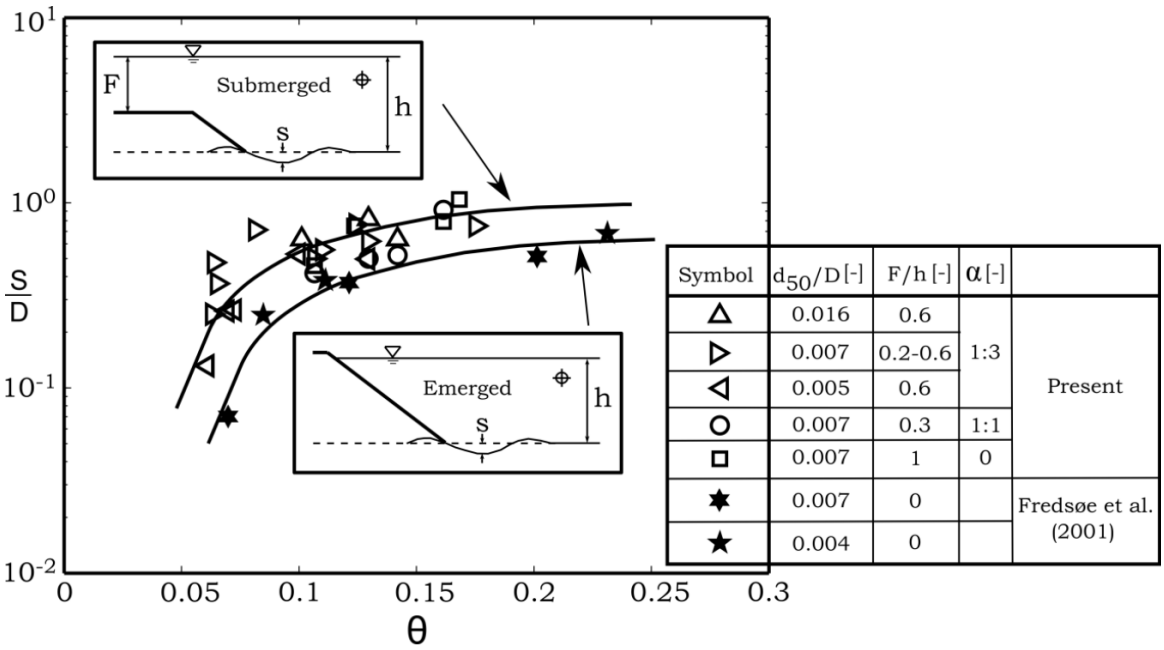

Figure 2.16. Equilibrium scour depth. Empty symbols: From present scour experiments for submerged stone layers. Filled symbols: data from Fredsøe et al. (2001) for emerged stone layers.

2.4.4. Time scale of the scour process

The scour adjacent to the stone cover develops towards the equilibrium stage through a transitional period. Fig. 2.17 gives two examples illustrating how the scour depth develops during this period. Typically the migration of ripples over the measurement area, as mentioned previously, cause fluctuations as the scour process develops towards the equilibrium stage, where the fluctuations continue. In 80 % of the scour experiments the time development of the scour process showed this behavior as displayed in Fig. 2.17a (Test 4). For the remaining 20 % the scour development showed fewer and smaller size fluctuations, as displayed in Fig. 2.17b (Test 16). The varying fluctuation size was predominantly caused by movement of either the entire stone layer surface or individual stones into the measurement section. An implication of this was a reduction in the ripple amplitude and, in turn, the fluctuations of the scour-depth-verus-time curve in Fig. 2.17a. It is seen that the time variation of the scour depth can be approximated by:

$$S_t = S_0 \left(1 - exp\left(\frac{-t}{T}\right)\right) \tag{2.11}$$

The quantity T is the time scale of the scour process and represents the time over which a substantial amount of scour takes place. The present treatment of the time development of scour expressed in Eq. (2.11) adopts the procedure of previous studies in relation to scour (Sumer and Fredsøe, 2002; Sumer et al. 1992, Truelsen et al. 2005; and Petersen et al., 2012b).

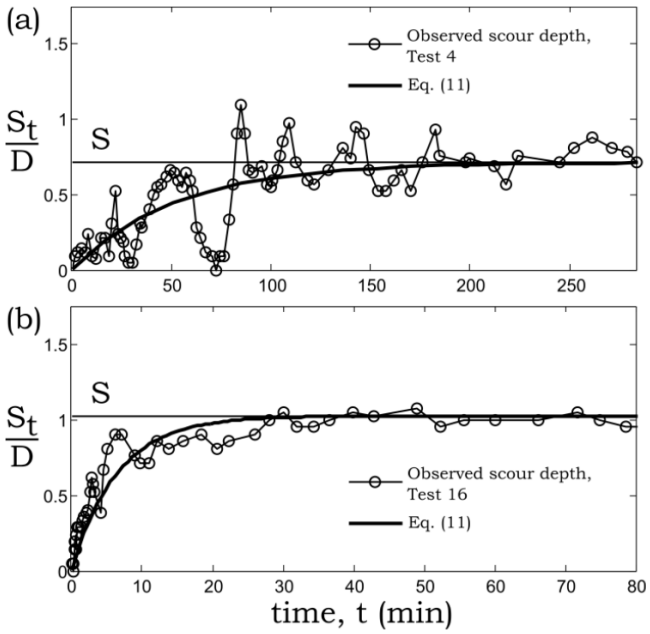

Figure 2.17. Time series of the depth of the scour hole monitored 5 cm of the edge of the stone layer in (a) Test 4. and (b) Test 16.

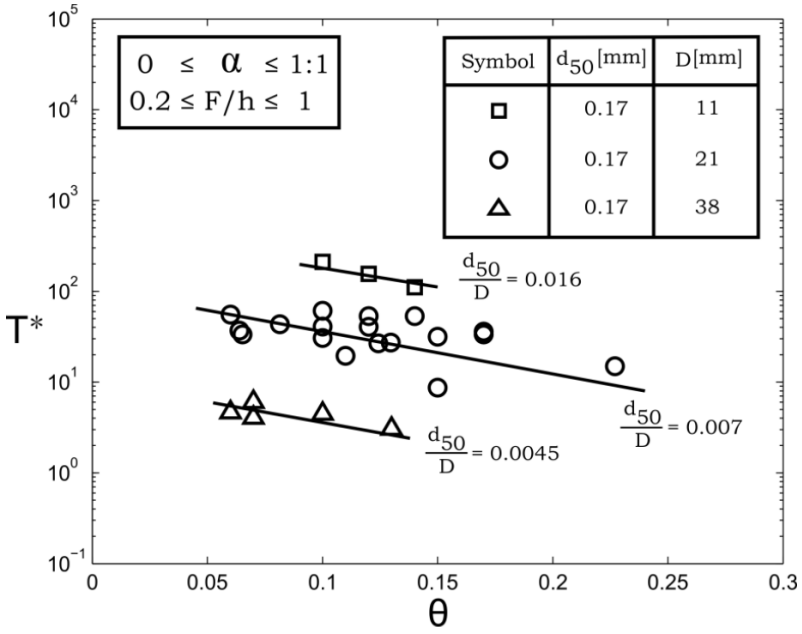

Figure 2.18. Normalized time scale of scour. Live-bed ($\theta > \theta_{cr}$).

The time scale T may be defined by following equation:

$$T = \frac{1}{S} \int_0^{\infty} (S - S_t)\, dt \tag{2.12}$$

For Eq. (2.12) to provide reasonable results a standard Savitzky-Golay filter (Savitzky and Golay, 1967) is applied to the scour-depth-versus-time curve before integration.

On dimensional grounds, the time scale can be written in the following functional form, similar to Eq. (2.10):

$$T^* = T^* \left(\theta, \frac{d_{50}}{D}, \frac{F}{h}, \alpha\right) \tag{2.13}$$

in which T^* is the normalized time scale (Fredsøe et al., 1992, Sumer et al. 2002) defined by Eq. (2.3).

Fig. 2.18 shows the normalized time scale plotted against the Shields parameter. As expected the time scale decreases with increasing θ. The sediment transport occurs at a higher rate with increasing θ, and therefore the scour process will be faster. This result is consistent with similar results obtained for scour around spheres (Truelsen et al., 2005), pipelines (Fredsøe et al., 1992) and piles (Sumer et al., 1992, 1993).

Fig. 2.18 further shows that the time scale decreases with decreasing d_{50}/D. This is because the smaller the value of d_{50}/D the larger the secondary currents which are responsible for the redistribution of sediment.

Although limited, the data displayed in Fig. 2.16 can be implemented for practical situations such as falling aprons($F/h \neq 0$), including the stone protection at the foundations of wind turbines (exposed to currents), and breakwaters and revetments ($F/h = 0$) (exposed to shore-parallel currents). Caution must be observed with regards to the ranges of the governing parameters employed in the present experiments and those encountered in practice.

2.5. Remarks on practical applications

As previously mentioned Naot (1984), Hayashi et al. (1985), Nezu et al. (1985), Nezu and Rodi (1985) Tominaga and Nezu (1986), Tominaga et al. (1989) studied primary and secondary flow structures in open-channel flows. The latter works point out the importance of the aspect ratio on the formation of the secondary flow patterns. The present work has a fixed aspect ratio of $A_r = B/h$ = 6.7 which falls right at the limit between narrow and wide open channels (Nezu and Nakagawa, 1993). Therefore effects from both regimes can be considered for the distribution of secondary current over the entire cross-section. Since the present study focuses on the local change in the secondary currents right at the edge of a stone layer only small changes with respect to the secondary flow pattern and strength are expected with a variation in A_r.

The present study comprises a range for the Shields parameter of $\theta = 0.06 - 0.23$ and the sediment transport is mainly considered where bed load is dominant. Clearly for larger values of the Shields parameter caution must be exercised when extrapolating the data.

Small scale ripples were present throughout the live-bed test series, and the ripple size relative to the scour hole dimensions is obviously an order of magnitude larger than encountered in practice. The ripple size observed in the present study was about 1 – 1.5 cm in height and ~10 cm in length. The effect of this is mainly observed in the time development of the edge scour hole, and the implication is discussed in the section regarding time scale of scour.

Finally, Fig. 2.16 predicts the edge scour as a lowering of the averaged bed level covered with ripples. It is therefore recommended that, as a conservative approach, the bed-form amplitude (from ripples or dunes) should be added to the scour depth plotted in Fig. 2.16, to accommodate the effect of bed forms in scour predictions.

2.6. Conclusion

The present results show that the size of the roughness elements, and to some extent the side-slope, are the governing parameters in controlling the three-dimensional flow field in regards to both turbulence and secondary currents adjacent to a cover stone layer. The generated turbulence laterally diffuses from the rough section over the stones into the smoother sand section on the side of the berm. It is shown that secondary current patterns form either originating from transition in surface roughness or corner effects. The transition in surface roughness generates the strongest secondary currents over the sand

bed. When increasing the slope of the berm the strength of the secondary current decreases.

The mechanism causing edge scour adjacent to the stone cover has been identified as the combined action of two effects; (1) Primary flow and (2) Secondary flow. Sediment is stirred up by the turbulence generated by the primary flow and brought up into suspension, and the secondary flow carries the sediment away from the junction between the bed and the stones, resulting in the edge scour. As a result of this mechanism the sediment is deposited outside the scour hole as shown in Figs. 2.13 and Fig. 2.14. The primary findings of the present investigation are:

(a) It was found that the scour depth attains a constant level at high values of the Shields parameter. The maximum scour depth was found to be about 1 times the stone size

(b) An increased value of the slope of the berm will decrease the scour depth relative to a berm with a milder slope with the same stone size. For lower values of the free-board-to-water depth ratio the scour depth is reduced to about 0.6 times the stone size.

Acknowledgement. This study is supported partially by (1) Danish GTS-university-cooperation project “Future Marine Structures”; (2) the Danish Council for Strategic Research (DSF)/Energy and Environment Program "Seabed Wind Farm Interaction"; (3) EU FP7-project, MERMAID 28870; and (4) Statkraft through: Statkraft Ocean Energy Research Program (SOERP)(Norway).

Chapter 3

Experimental and field investigation of flow and edge scour around scour protections at offshore wind turbine foundations

This chapter is to be submitted to Coastal Engineering, Elsevier.

T. U. Petersen[1], B. M. Sumer[2], J. Fredsøe[3], T. C. Raaijmakers[4] & J. Schouten[5]

[1]Ph.D. – candidate, [2]Professor, [3]Professor, Technical University of Denmark. Section for Fluid Mechanics, Coastal and Maritime Engineering. Kgs. Lyngby, Denmark.

[4]Researcher/advisor, [5]Offshore Engineer, Deltares│Delft Hydraulics, Rotterdamseweg 185, 2629 HD Delft, P.O. Box 177, 2600 MH Delft.

Abstract: When building offshore wind turbines with monopile foundations, scour protection typically is placed to avoid scouring of the soil close to the monopile. An important aspect is that the scour protection itself causes erosion, inflicted by the local increase in current and/or wave velocities and in turn increased bed shear stresses. Scour of the edge material alongside the scour protection may cause deformations and failure of the scour protection of offshore wind turbine foundations. This can reduce the stability of the stone layer and cause exposure of cables running between the monopiles where they go from buried to the transition piece on the foundation. Although much information is available on the design of scour protection systems around monopiles, little is known on the mechanisms causing edge scour and the equilibrium stages of the edge scour process in steady current, waves and combined waves and current.

This paper presents an extensive experimental campaign to explain the edge sour process in current, tidal current and combined waves and current. The three-dimensional flow field around the pile and scour protection is resolved by particle image velocimetry and bed shear stress measurements, showing a local increase in the hydrodynamic field leading to increased sediment transport and scour. The governing process in steady current is a pair of symmetrical counter-rotative vortices emerging in the near bed wake region of the pile and scour protection, causing a significant downstream scour hole. It is found that the equilibrium scour hole depth and length scales with the pile diameter and the ratio between the thickness- and the width of the scour protection.

In the second part of the present paper, the results from the experimental campaign are compared with the edge scour experienced in practice, outlined by a survey programme of

the offshore wind park Egmond Aan Zee and a published field investigation of Scroby Sands OWF by Whitehouse et al. (2011).

Keywords. Edge scour, cover stones, steady current, scour protection, coastal structures, offshore structures, scour, offshore wind farm, secondary scour.

3.1. Introduction

Over the last two decades the offshore wind industry has grown, with more and more offshore wind farms erected. The first larger offshore wind farm (OWF) in the North Sea off the Dutch coast is the offshore windpark Egmond aan Zee (OWEZ), located in shallow waters (16 – 21 m water (MSL)) 10 – 18 km off the coast at the city of Egmond Aan Zee. This location is exposed to strong tidal currents (up to 1.3 m/s) and large waves from the North Sea. The wind turbines are founded on mono-piles with a typical scour protection system with rock dump around the base of the mono-pile. The wind park was installed through May to October 2006, and a survey program running from 2006 – 2013 showed considerable edge scour developing outside the cover stone area of up to 2.7 m (Raaijmakers et al, 2010, Louwersheimer et al., 2009 and Raaijmakers et al., 2007). The edge scour development over the survey campaign shall be displayed and discussed in the second part of this paper. The edge scour was in fact taken into account in the design, which included physical model tests, and sufficient filter material was installed at the edges of the scour protection. This filter material acting as a falling apron, meaning that the stones in the filter layer are allowed to slump into the edge scour hole as it develops, thereby protecting the slope and bottom of the edge scour hole, and in turn preventing the edge scour hole from causing damage to the armour layer.

Whitehouse et al. (2011) compiled data in relation to and discussed the development of edge scour (termed secondary scour) around scour protections at offshore wind turbine foundations at several locations, such as Scroby Sands OWF, Arklow Bank OWF and Horns Rev 1 OWF. The latter study reports edge scour predominantly in the range of 0.2 – 1.2 D_p (with D_p = pile diameter), noticeably in the same range as for scour around an unprotected mono-pile (see Fig. 12 and Fig. 17 in Whitehouse et al., 2011).

Scour around unprotected monopiles have received a vast amount of attention over the last decades, with a detailed account on the topic given in the books of Breusers and Raudkivi (1991), Hoffmans and Verheij (1997), Whitehouse (1998), Melville and Coleman (2000) and Sumer and Fredsøe (2002); and more recently in numerical studies by Roulund et al. (2005), Liu and Garcia (2008) , Zhao et al. (2010) and Khosronejad et al. (2012) and experimental studies on scour and backfilling of scour holes around piles by Sumer et al. (2013). The information rendered in the latter works has also made it possible for establishing long-term numerical models to estimate the time development of the scour depth around mono-piles with the changing sea climate (Nielsen and Hansen, 2007; Raaijmakers and Rudolph, 2008; and Harris et al. 2010). More recently, such models were applied over larger areas to study at which locations allowing free scour development (i.e. leaving out the scour protection and adjusting the monopile design) would be more cost-efficient compared to installing scour protections (e.g. Raaijmakers et al, 2013).

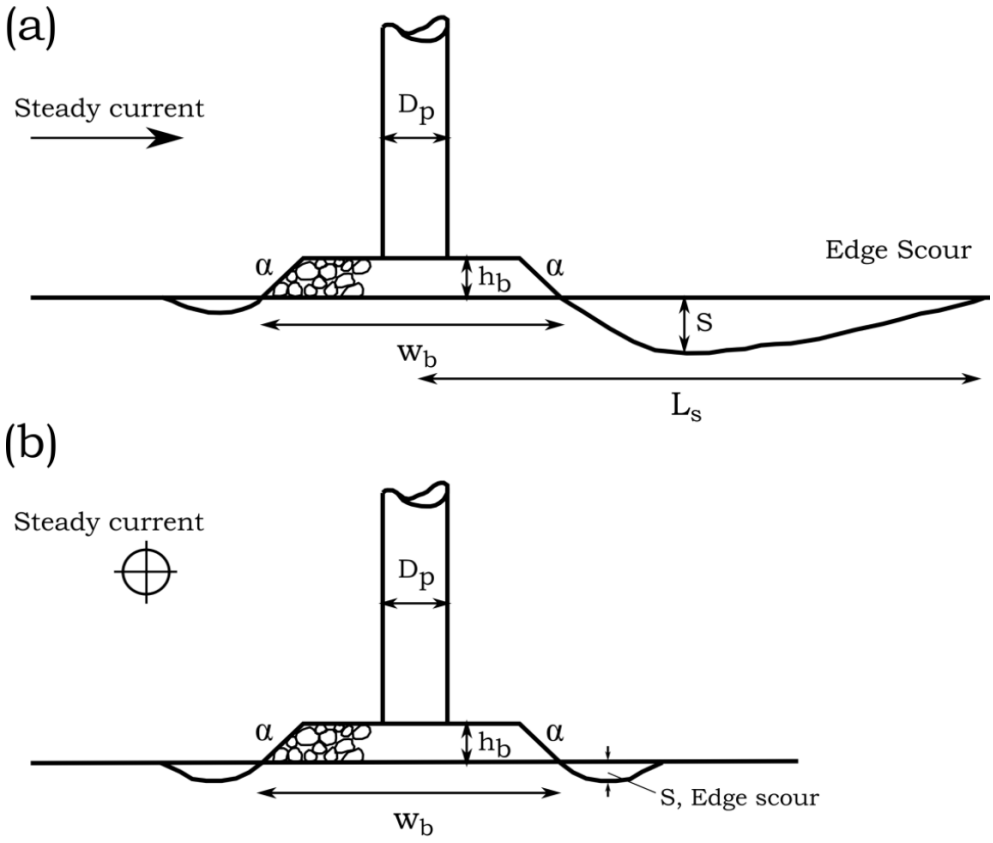

Figure 3.1. Definition sketch (schematic). (a) scour hole generated by current downstream of scour protection; (b) scour generated by current at the transverse section of the scour protection.

Following the studies on scour around unprotected monopiles few investigations have been presented on flow and scour mechanisms with the scour protection installed at the base of the monopile by Chiew (1995), Chiew and Lim (2000), Lauchlan and Melville (2001), Chiew (2002), Vos et al. (2011,2012), Nielsen et al. (2011,2013) and Sumer and Nielsen (2013). Some results have also been collected with respect to scour alongside riprap berms in steady current by Fredsøe et al. (2001), Petersen et al. (2012a, 2014), and these studies show that the combined effect of primary flow, secondary flow and turbulence generated around the individual stones at the edge of the berm scours the adjacent sea bed, and as result the stones slump in to the scour hole. In waves Sumer et al. (2005) showed that scour at the edge of submerged berms is caused by steady streaming. However, to the authors' knowledge no study is yet available investigating, in a systematic manner, the edge scour developing around scour protections at monopiles in current and combined waves and current. The development of edge scour is important for the structural stability of the stone cover, as well as to counteract free-span of cable ties where they go from buried to the transition piece (Whitehouse et al., 2011; Hansen and Gislason, 2005).

The present study aims to understand the mechanisms that cause the edge scour at the perimeter of the scour protection and the subsequent failure of the stone layer in accordance with the definition sketch (schematic) in Fig. 3.1. To this end, an extensive programme of physical model scour tests with steady current, combined waves and

current; and simulated tidal current has been carried out, supported by three-component flow measurements via particle image velocimetry (PIV) and measurements of the bed shear stress. This study shows that in steady current edge scour happens in the near-field domain of the scour protection and in the farther downstream area, caused by the following two mechanisms, respectively: (1) the horseshoe-vortex generated in front of the scour protection and the deviation and acceleration of flow at the transverse sides of the scour protection scours the neighboring sea bed; (2) a pair of symmetrical counter-rotating vortices generated downstream of the monopile and scour protection, suspends the sediment and scours the wake area downstream.

To enhance the understanding of the flow and improve the design criteria, this study investigates the flow field, velocity distributions, coherent turbulent flow structures and the bed shear stress around scour protections at circular monopiles in steady current, combined waves and current and simulated tidal current, using physical model tests. To further support the findings in the experimental campaign, a field investigation of edge scour development is made for two offshore wind farms where scour protection is installed. It is found that the observed edge scour development and the measured equilibrium edge scour depth in the physical model tests agrees well with the edge scour experienced in practice at OWF Egmond Aan Zee and Scroby Sands OWF.

3.2. Experimental Setup

Three kinds of experiments were carried out: (1) Velocity measurements by Particle Image Velocimetry (PIV) mapping the flow field from the pile section until $7D_p$ in the downstream direction, in steady current conditions; (2) measurements of the bed shear stress, again, in steady current conditions, and (3) Scour experiments where the scour process adjacent to the berm was monitored in the live-bed regime in steady current, combined waves and current and tidal current conditions. All the measurements were for the most part conducted with a monopile and a scour protection system with several layers of cover stones. Some flow visualization with dye added to the water was made to visualize the flow structures, as will be detailed in Section 3.4

3.2.1. Scour Experiments

3.2.1.1. Scour Experiments in Steady Current

These experiments were carried out in two different current and wave/current flumes respectively: (1) a 2.0 m wide, 28 m long and 0.5 m deep and the water depth was h = 30 cm, displayed in Fig. 3.2 (schematic); and (2) a 4.0 m wide, 28 m long and 1.0 m deep and the water depths in this flume ranged from h = 0.4 and 0.5 m, illustrated in Figs. 3.2 – 3.3 (schematic). The current was achieved by recirculating water in the flumes.

In the case of the 2 m wide flume a sediment section in the form of a sand pit with two ramps at the two ends was formed in the flume. The sand pit was 2 m wide, 0.15 m deep and 11 m long (see Fig. 3.2), the distance from the upstream end of the sand pit to the inlet section being 10 m. The two end ramps (with 1:15 slope) were made from round stones the size 4 cm. The grain size of the sediment (fine sand) used in the experiments was d_{50} = 0.17 mm with a geometric standard deviation of $\sigma_g = d_{84}/d_{50}$ = 1.3. A

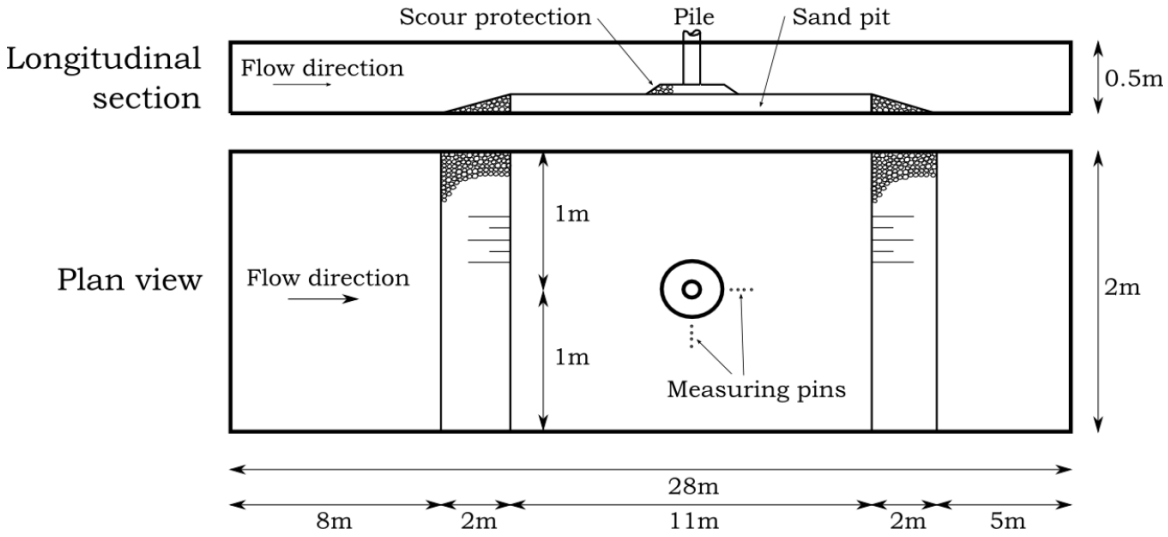

Figure 3.2. Test setup for the scour and PIV experiments in the 2-meter wide flume, section and plan view.

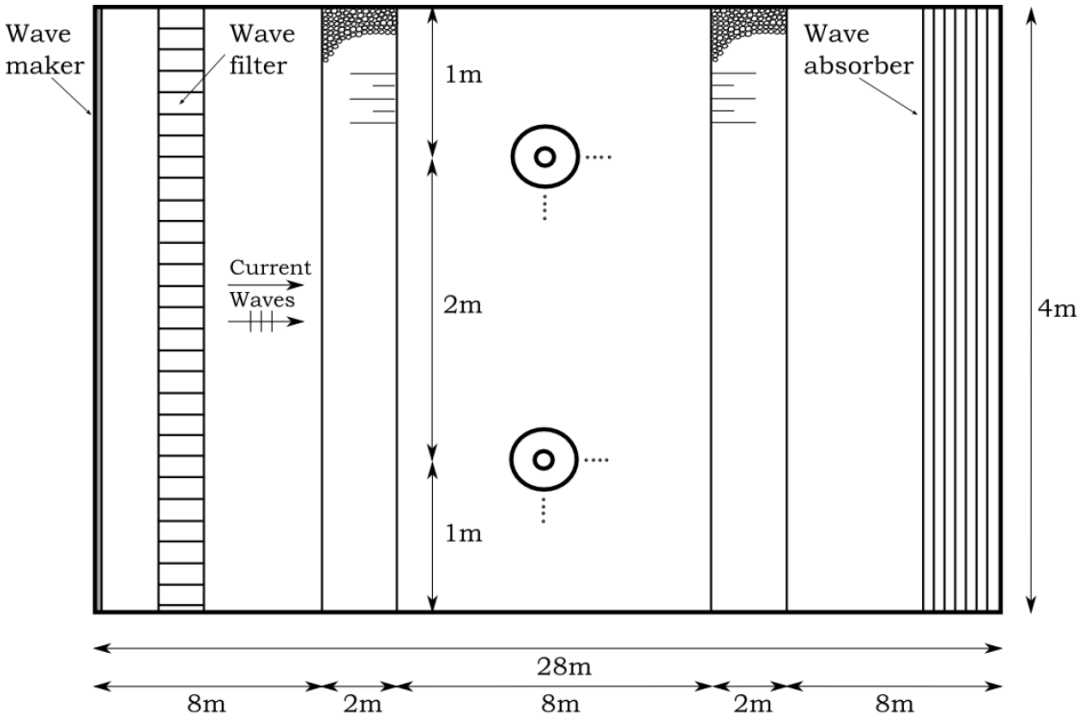

Figure 3.3. Test setup for the scour experiments in the 4-meter wide flume, plan view.

model pile was placed 7 m from the beginning of the sand section at the centerline of the flume.

In the case of the 4 m wide flume the sand section was 4 m wide, 0.15 m deep and 8 m long. The distance from the offshore end of the sand section to the inlet/wave generator was 10 m. The two end ramps were made from crushed stones the size of 2 cm with a core of concrete blocks with a slope of 1:15. Two model piles were tested at the same time in order to save time. The piles were each placed in the middle of the sand section and the distance between the piles were 2.0 m, which ensured no interference between the two setups.

The model piles were embedded vertically in the sediment bed, extending to the base bottom of the flume and rigidly fixed at the top of the flume. Model piles with diameters of D_p = 5.0, 7.0, 7.5 and 10.0 cm were implemented in the tests. This range of pile diameters were selected to adjust the range of the boundary-layer-to-pile-size ratio δ/D to attain values of 3 – 5. The equilibrium scour depth S around an unprotected pile should be uninfluenced by this parameter when $\delta/D \gtrsim 4$ (Melville and Sutherland, 1988; Sumer and Fredsøe, 2002). Similarly the range of the model piles in the combined waves and current experiments enabled a variety of Keulegan-Carpenter (KC) numbers within the range encountered in offshore wind farm applications.

Scour protection with stones was placed on top of the sand covering a circle around the pile. The stone layer was made of crushed angular stones with sizes of D_c = 0.7, 1.1 and 2.1 cm (see Fig. 3.4a-c). Each of the stone layers utilized in the experiments had a geometric standard deviation $\sigma_g \sim 1.2$. The experiments were conducted with a stone layer height above sea bed h_b = 0, 3, 3.5 and 5 cm. For the h_b = 0 setup a stone layer of about five stones were installed so the top of the stones were flush with the initial sand level. This range of berm heights were chosen to ensure values of berm-height-to-pile-size ratio $h_b/D_p \simeq 0 – 0.5$. The width of the berm w_b = 20, 28, 30, 35, 37.5, 40, 44, 46 and 50 cm (measured as the diameter of the scour protection berm as indicated in Fig. 3.1) enabled the berm-width-to-pile-size ratio to range $w_b/D_p \simeq 2 – 5$. At the perimeter of the scour protection side slopes α = 1:2, 1:3 and 0 were applied, see Fig. 3.1 (Note that $\alpha = 0$ corresponds to the setup with the stone layer installed flush with the initial sand level). The range of the latter parameters h_b/D_p, w_b/D_p and α were chosen according to the ranges encountered in practice.

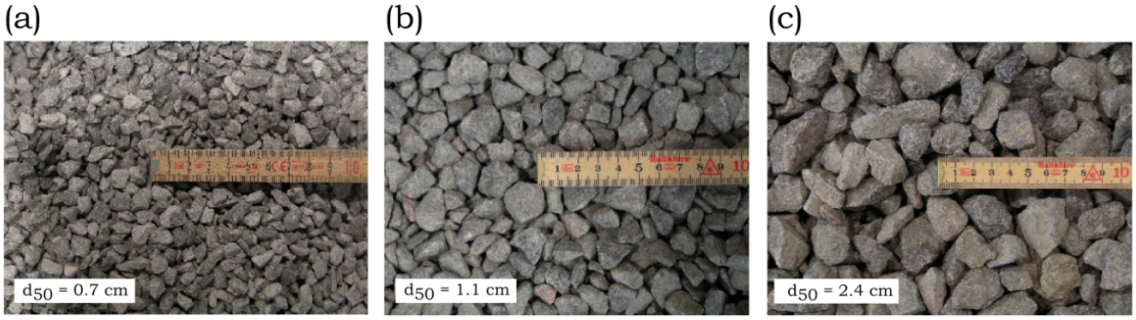

Figure 3.4. Stones used in the scour experiments: a, b and c. Stones used in the PIV measurements: b. Stones used in the bed shear stress measurements: a.

With these setups, the time development of the scour process was monitored by two mini underwater video cameras facing the onshore- and the offshore side of the scour protection. Here measuring vertical pins (3.0 mm diameter) with distance markers were placed in order to resolve the time development of the scour process (Fig. 3.2 and Fig. 3.3). Each of the pins was placed with a distance of 5 cm in between them. The movement of the sand grains in the video recordings acted as flow tracers, visualizing the flow structures downstream of the pile section. To further enhance the flow visualization dye was added at various locations alongside the periphery of the scour protection. The cameras had a viewing area of about 100° in plan view and a time resolution of 1/25 s.

The experiments were run for sufficiently long period of time for the scour process at the downstream side to reach its equilibrium stage. The equilibrium stage of the scour process at the transverse part of the setup was achieved in approximately half the time, mostly due to the relatively lower scour depth observed in this area, as will be detailed later. Subsequently, the scour profiles were measured with a bed-profiler in a 2 by 2 cm grid covering the entire extent of the setup and the downstream scour hole. The bed profiler consisted of a laser rangefinder mounted on a carriage over the flume. A software specifically for the purpose of traversing the laser over the bed and generating 3D plots was developed. The laser rangefinder had a vertical precision of 1 mm. Following the bed-profiling of the scour hole the individual stones around the pile were removed carefully without disturbing the sediment at the base of the stone layer and the pile. Thereafter the bed-profiling was made again over the part previously covered by stones in a 1 by 1 cm grid.

In the current tests the velocity profile across the water depth over the sand section was measured, using a Laser Doppler Anemometer (LDA), a Dantec 2D LDA system (Dantec Dynamics, Denmark) comprising a 14 mm “pen-size” submersible probe, the measurements being conducted in the back-scatter mode. The focal length of the pen-size probe was 8 cm. The measurement point was located 7 m away from the beginning of the sand pool and at 0.5 m distance from the side wall. The system was equipped with a BSA F60 Flow Processor and the data was logged in BSA Flow Software v4.50. The data collected was used to determine the velocity to calculate the quantities such as the depth-averaged current velocity and the bed friction velocity. The steady current velocity was continuously monitored by a small scale OTT propeller (3 cm diameter) during the course of the experiment.

3.2.1.2. Scour Experiments in Combined Waves and Current

These experiments were conducted in the previously mentioned 4 m wide wave/current flume (Fig. 3.3). The flume was equipped with Active Wave Absorption Control System (AWACS) and DHI Wave Synthesizer 2.40 (Schäffer et al., 1994). This system renders simultaneous generation of desired incident waves and absorption of reflected waves. To further reduce reflecting a wave absorber, made of perforated plastic plates with an archshaped cross-sectional profile, was placed at the far onshore-end of the flume.

A honeycomb type of wave filter, 0.6 m in length and extending over the entire width and depth of the flume was installed 3 m from the paddle-front of the wave generator. This ensured alignment of the waves and that unevenness of the surface elevation across the width of the flume were avoided.

The waves were generated by a piston-type wave generator. Irregular waves were used to avoid bed undulations associated with large time series in regular waves, which were observed in test durations longer then O(2 hours). This effect is discussed in Petersen et al. (2012b) and Sumer et al. (2013) which involved experiments with similar setups. A measured in-situ water elevation spectrum for North Sea storm conditions was used as the control spectrum to generate a displacement signal for the wave generator. The spectrum was well described by the JONSWAP spectrum.

The water depth in the combined wave and current scour experiments was maintained at h = 40 cm at the pile section. In the case of combined waves and current the initial water level was adjusted to a smaller value (5 – 15 % of 40 cm) depending on the current velocity. With the introduction of the current the water level increased to 40 cm.

In the case of combined waves and current the bed orbital velocity was measured using a similar LDA setup as mentioned for current-alone tests. Here the system was equipped with a Dantec 9055N0124 frequency shifter and a Dantec 9055N0214 frequency tracker. The measurement point was located at the pile section 7 cm from the bed and 20 cm from the side wall. The bed orbital velocity was monitored during the entire course of the experiments, and the data collected were used to calculate the spectrum for the horizontal orbital velocity. The latter spectrum was to determine the maximum orbital velocity at the bed according to Eq. (3.8) and (3.9). The sampling frequency for the combined waves and current experiments was set to 140 Hz.

3.2.1.3. Scour Experiments in Simulated Tidal Current

The purpose of the presently simulated tidal current scour tests were to extend the investigation for the previously mentioned steady current case (unidirectional) to the case where the flow direction reverses periodically (two-directional). The undisturbed tidal current flow pattern can be expressed by

$$V_t = \bar{V}\ \cos(\omega t) \tag{3.1}$$

in which t is the time, $\bar{V}$ is the maximum depth-averaged-velocity and ω is the angular tidal frequency, defined by $\omega = 2\pi f$, where f is the tidal frequency. Given the time series of the V_t velocity described by Eq. (3.1), the actual deployed velocity signal could be simplified to the model shown in Fig. 3.5 and Fig. 3.6. The tidal period T_{tidal} is defined as the time over which the sediment in the far field is mobilized, ie. the interval when the mean velocity is bigger than U_{cr} (~30.5 cm/s in the 2m wide flume) in a period (see the definition sketch in Fig. 3.5). Fig. 3.6 displays a typical velocity record measured at y = 0.37h (11.1cm) above the bed (here $\bar{u}$ = V) in Test 77.

The experiments were carried out in the 2m wide flume mentioned in relation to the scour tests in steady current (Fig. 3.2), since the current flow direction could be reversed by

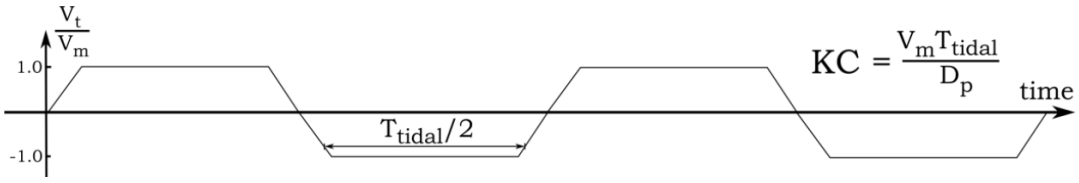

Figure 3.5. Definition sketch (schematic) of the tidal current flow pattern in the 2m wide flume (see Fig. 3.2).

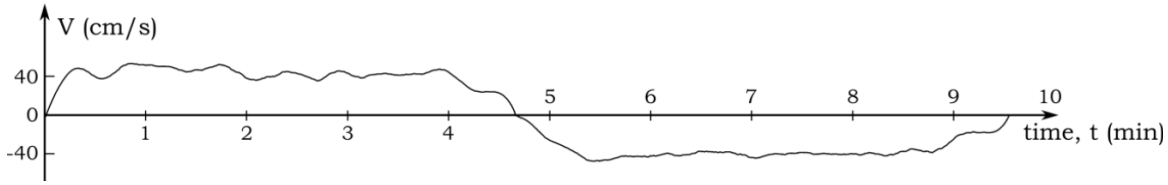

Figure 3.6. A typical velocity record for the simulated two-directional tidal current in the 2m wide flume (Fig. 3.2). Test 77, Table 3.3.

changing the blade pitch of the pump. The experimental setup for the remaining part was similar to the scour tests in steady current.

3.2.1.4. Scour Experiments in Steady Current with Filter Layer

The purpose of the present experiments with a filter layer installed immediately beneath the armour layer (or cover stones) is to investigate the effect of applying a falling apron on the downstream scour hole. In practical applications extending the filter layer beyond the edge of the cover stones is a well-known principle for controlling the development of the edge scour. As the edge scour develops the stones in the exposed part of the filter layer slump into the scour hole and forms a protective slope, the falling apron principle. For design considerations it is relevant to estimate the volume of the falling apron (length of the exposed filter layer L_f times the thickness of the filter layer t_f) to attain a certain reduction in the edge scour depth, and in turn a more stable scour protection system.

In the present setup the elliptical plan view extent of the filter layer were implemented with a fixed exposure length for the upstream- and transverse sides of the scour protection, while the downstream exposure length of the filter layer varied over the campaign in accord with the definition sketch in Fig. 3.7. The exposure length downstream of the armour layer in the present test series was $L_f = 0$, 6, 8.5 and 20 cm, and at the transverse sides $L_f \sim 1.2h_b$ or $2D_c$.

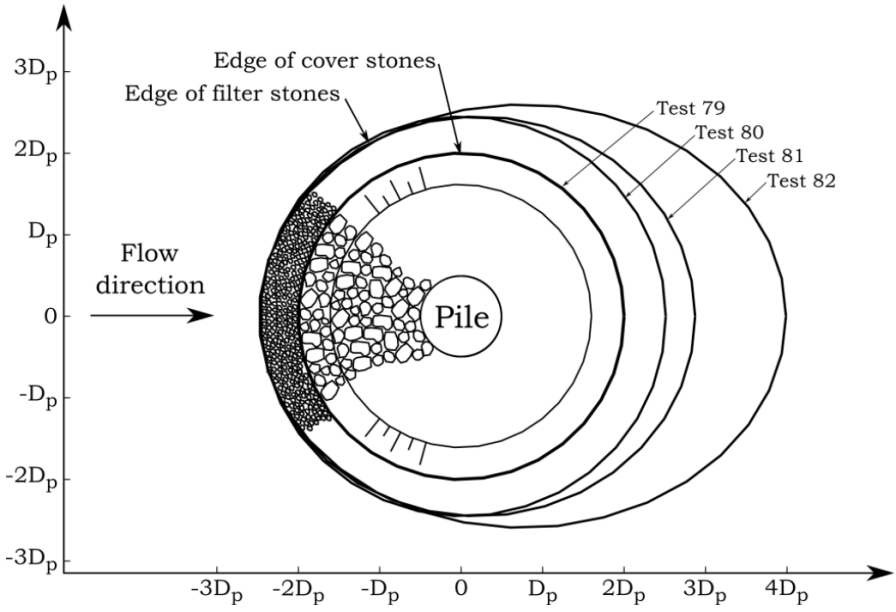

Figure 3.7. Definition sketch (to scale) of the bottom-mounted piles with cover stone and filter layer applied.

3.2.1.5. Test Procedure in the Scour Tests

The procedure used in the scour tests was typically as follows:

1. Level of the sand bed around the pile
2. Apply the stone layers around the pile
3. Run the desired steady current, combined waves and current or tidal current until the scour process has reached its equilibrium stage
4. Drain the water in the flume
5. Measure the bed-profile; identify the equilibrium scour depth and the length of the scour hole directly from the measured bed-profile.
6. Remove the scour protection.
7. Measure the bed-profile beneath the scour protection.
8. Repeat Steps 1-7 until the test matrix is exhausted.

3.2.2. Velocity Measurements by PIV

Particle Image Velocimetry (PIV) measurements were made to investigate the three-dimensional flow field in planes from the pile section and downstream. The objectives of the PIV study were three-fold: (1) to obtain the streamwise, vertical and lateral velocity components (u, v, w); (2) to estimate the turbulence intensity field and the decay

downstream of the fluctuating components of the flow (u', v', w') and (3) to resolve the streamwise vorticity downstream of the pile setup.

The setup for the PIV measurements shown in Fig. 3.8a, consisted of a transparent monopile with a scour protection system at the base, in which h_b/D_p = 0.35, w_b/D_p = 4, α = 1:2 and stones the size D_c = 1.1 cm (see Fig. 3.4b). The individual stones in the scour protection system and the pile were glued together with the industrial product Elastocoast® from BASF (Elastocoast, 2014). The Elastocoast® material is made for riprap revetments and dikes as a bonding material that reinforces hydraulic gravel at their contact interfaces permanently by means of a two-component plastic polyurethane. By applying this material the stone layer acted as a rigid body while the porosity remained intact, and hereby the structure could be moved as one unit.

The measurements were made with a PIV system from Dantec Dynamics; the system consisted of two four megapixel cameras, double pulsed (1200 mJ/pulse) Nd:Yag laser, a synchronizer to facilitate system timing and frame grabbers to facilitate image acquisition. The PIV data logging was made in Dynamic Studio v3.30. The two cameras were mounted alongside the flume side wall viewing the measurement volume at a 45° angle, see Fig. 3.8a. On the glass side wall for each camera a water prism with an orientation of 45° was mounted in order to eliminate refraction. The laser light sheet was also introduced from the flume side wall aimed directly at the measurement volume. Silver-coated hollow glass-spheres the size 10 μm were used as seeding particles to obtain optimal reflection, a detailed account on the setup is given in Petersen et al. (2012a and 2014) which for the most part utilized a similar setup.

The PIV measurements were made in the clear-water regime and no sediment transport occurred, not even adjacent to the structure where increased bed shear stress is expected. This ensured that the bed level of the sediment around the scour protection would not change during execution of the tests, which allowed acquisition of large ensembles of data. Further to this any suspended sediment particles would also disturb the data collection. The setup was prepared with a flat sediment bed for each of the measurements performed in the PIV measurement campaign.

For the given setup the camera field of view (CFV) remained constant, while moving the structure upstream in steps, see the definition sketch in Fig. 3.8b. Hereby measuring the velocity time series in CFV planes in steps downstream of the structure. In total the PIV measurements were carried out in 7 specific x-planes downstream of the pile as illustrated in Fig. 3.8b:

$$x = [0\ 2\ 3\ 4\ 5\ 6\ 7] \cdot D_p \tag{3.2}$$

in which x = 0 corresponds to the center of the pile as shown in Fig. 3.8b, and D_p = 10 cm.

The calibration images for the CFV were used to provide the dimensional position for the field of view in laboratory coordinates. During post-processing, as the CFV could not be placed symmetrically over the x-axis, the measured velocity field was mirrored to the uncovered part to attain symmetry (see Fig. 3.8b).

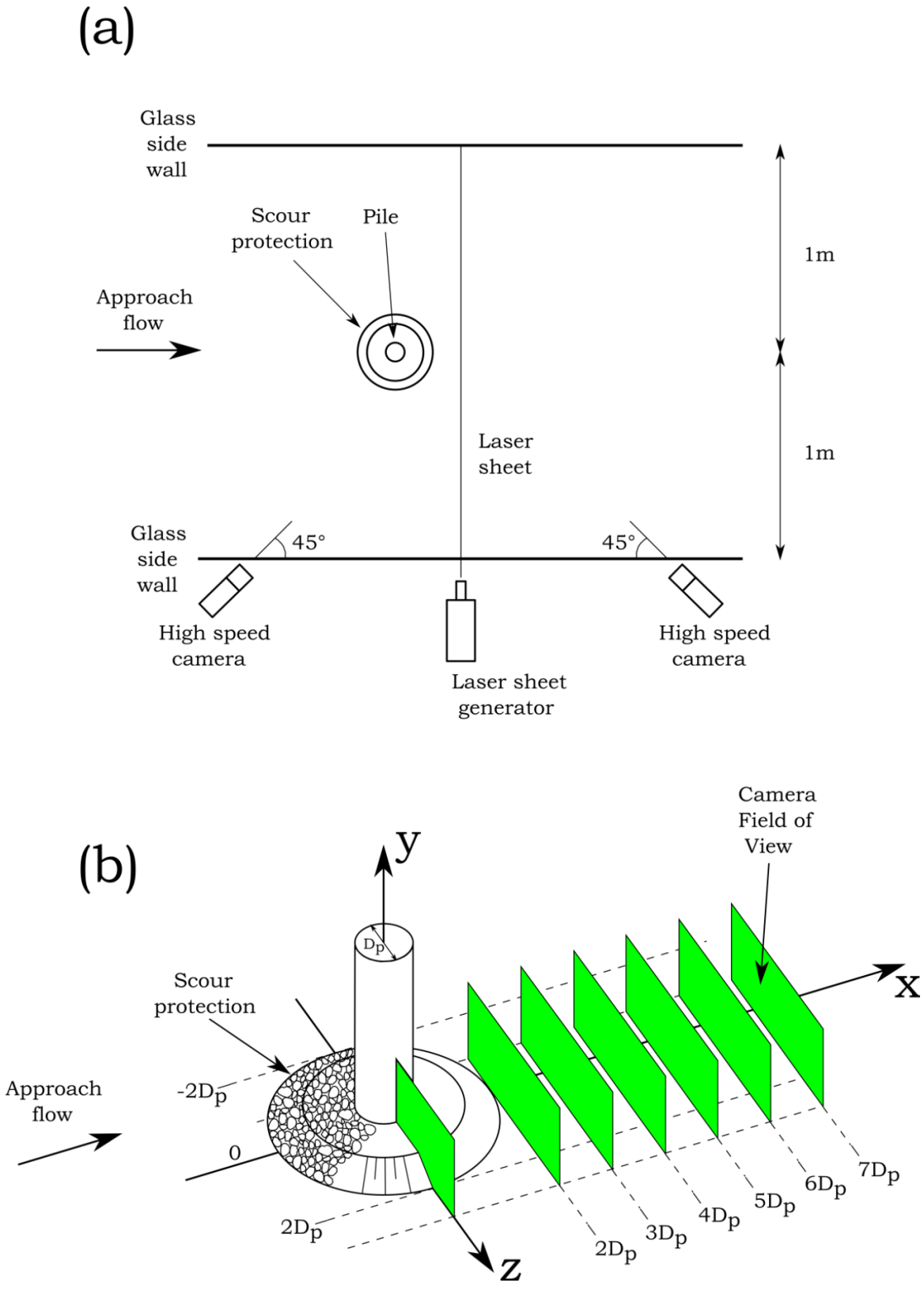

Figure 3.8. Test setup for the Particle Image Velocimetry (PIV) measurements in 2-meter wide flume, see Fig. 3.2. (a) Plan view; (b) side view close up with Camera Field of View (CFV) to scale with pile diameter D_p.

At each frame position ensembles of 1000 image pairs were obtained at a frequency of 6 Hz and a time between the two frames Δt = 1500μs. The image pairs were subsequently analyzed and interrogated using the Dynamic Studio v3.30. Images were interrogated with 32 x 32 windows, using a 50 % overlap. Typical vector removal rates ranged from 2 to 4 % with the bulk of removed vectors near the sediment bed and the stone layer and the pile surface. In both cases the moderate scattering of laser light from the sediment grains, the stones and the surface of the pile were responsible, despite the effort to remove this with flat black paint.

3.2.2.1. Test Procedure in the PIV tests

The procedure used in the PIV tests was typically as follows:

1. Place the pile and scour protection at the specific location and level off the bed
2. Run the steady current
3. Initiate the PIV system and sample 1000 images.

Repeat steps 1 - 3 until the CFV positions downstream of the setup given in Fig. 3.8b and Eq. (3.2) has been measured.

3.2.3. Bed Shear Stress Measurements with Hot-film Probe

The main purpose of this campaign was to measure the instantaneous bed shear stress τ_b and the corresponding time averaged component $\overline{\tau_b}$ upstream-, transversal- and downstream side of the scour protection; and relate this to the undisturbed bed shear stress $\overline{\tau_\infty}$. In which $\overline{\tau_\infty}$ is measured in the absence of the pile and scour protection setup. Further to correlate and substantiate the knowledge gained through the PIV measurements of the wake flow downstream of the pile setup.

The tests to measure the bed shear stress outside the scour protection area were conducted in a 0.6 m wide, 0.8 m deep and 26 m long flume, see Fig. 3.9. An artificial bed of 6mm PVC plates was installed in the flume raising the flume floor by 5 cm. This procedure enabled installation of the hot-film probe beneath the artificial bed allowing cables to run from the probe without disturbing the flow. The current was achieved by recirculating water in the flume.

A pile with diameter D_p = 4 cm was mounted in the flume resting on the bottom and fixed rigidly at the top. Around the pile a scour protection system was applied with the stone size D_c = 0.7 cm extending in a circle around the pile with a berm width w_b = 8, 12 and 16 cm and with a fixed berm height h_b = 2cm.

The bed shear stress measurements were made in the plane of symmetry upstream, downstream and at the transverse side of the pile as illustrated in Fig. 3.10. The bed shear stress was measured by a 1-component hot-film probe measuring τ_b in the streamwise direction. The hot-film was placed in a Brass-housing in the middle of the flume mounted flush with the smooth flume bed (see Fig. 3.9). The probe was calibrated in position, using a small three sided calibration channel of 1mm in depth and 30mm in width, which

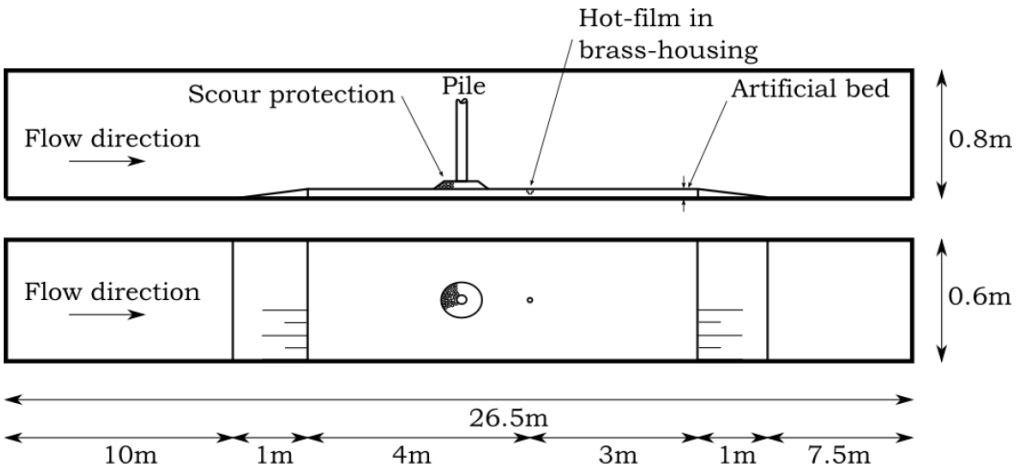

Figure 3.9. Test setup for the bed shear stress experiments in the 0.6m wide flume, section and plan view.

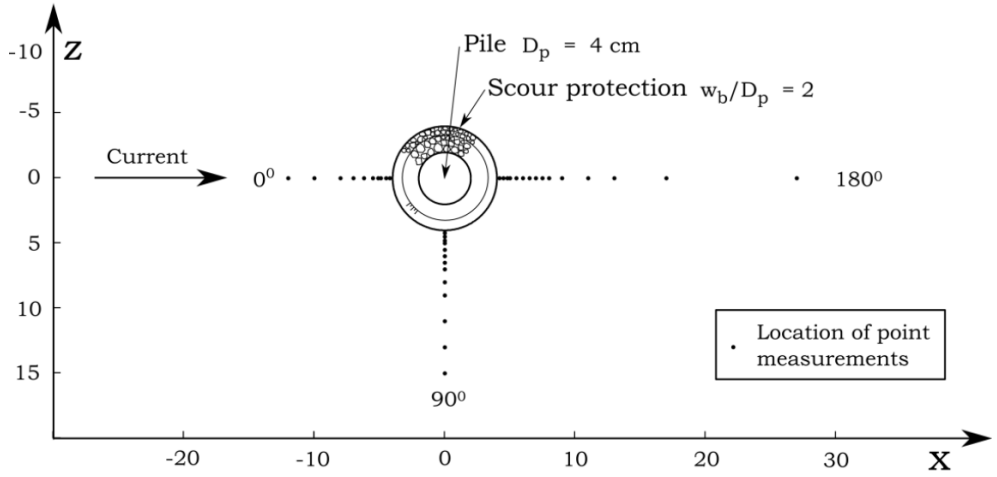

Figure 3.10. Location of point measurements of bed shear stress around the bottom-mounted cylinder with/without scour protection. Test 84.

was placed over the probe. The calibration procedure and additional information can be found in Sumer et al. (1993).

The hot-film probe yields no information whether the direction of the bed shear stress is positive or negative with respect to the streamwise direction. For this purpose simultaneous measurement of the streamwise velocity has been conducted by a Laser Doppler Anemometer (LDA) focused 0.4 mm right above the position of the hot-film probe. The LDA system is similar to the system utilized in the 2m wide flume for the scour experiments, but the probe was replaced with 310 mm focal length probe mounted outside the flume. The sign of the velocity is used to decide the longitudinal direction of τ_b. The LDA is also used to provide measurements of the depth-averaged-velocity V. The velocity V was obtained from integration of the measured velocity profile over the depth of the water column in the bed shear stress tests.

3.2.3.1. Test Procedure in the Bed Shear Stress tests

The procedure used in the bed shear stress tests was typically as follows:

1. Place the pile and scour protection at the specific location
2. Run the steady current and measure the bed shear stress over a period of 180s.
3. Repeat steps 1 -2 until every point measurement upstream, downstream and at the transverse side has been completed. Typical locations of the point measurements with the hot-film probe and the LDA are shown in Fig. 3.10 for Test 84.

3.3. Test Conditions

Tables 3.1, 3.2, 3.3 and 3.4 summarize the test conditions for the scour tests. Table 3.1 for scour tests in current, Table 3.2 for scour tests in combined waves and current, Table 3.3 for scour tests in simulated tidal current and Table 3.4 for scour tests in current with filter layer installed. Table 3.5 on the other hand summarizes the test conditions for the PIV- and the bed shear stress tests.

3.3.1. Test Conditions for the Scour Tests

In Table 3.1, summarizing the scour experiments in steady current, N is the number of stone layers obtained from

$$N = \frac{h_b}{D_c} \tag{3.3}$$

The aspect ratio A_r between the berm height h_b and the berm width w_b

$$A_r = \frac{h_b}{w_b} \tag{3.4}$$

The quantity V is the depth averaged current velocity associated with far field conditions obtained by two different approaches: (1) single point measurements at y = 0.37h where $\bar{u}$ = V, considering a fully developed turbulent boundary layer, and (2) integrating the measured velocity distribution over the water depth by LDA.

The quantity U_f denotes the bed friction velocity determined in the following two ways: (1) from the familiar log-fit exercise using the measured velocity profiles; (2) from the flow resistance relation

$$U_f = \sqrt{f/2}\,V \tag{3.5}$$

in which f is calculated from the Colebrook-White formula (e.g. Schlichting, 1979), and V was obtained from the LDA or OTT propeller measurements described in the previous section.

The Shields parameter θ in the table is defined by

$$\theta = \frac{U_f^2}{g(s-1)d_{50}} \tag{3.6}$$

in which g is the gravitational acceleration, s the specific gravity of the sediment grains (=2.65). Note that the Shields parameter is calculated based on the grain roughness rather than the ripple roughness. This is in accord with Sumer et al. (1993), Sumer and Fredsøe (2001b), Fredsøe et al. (1992) and Sumer and Fredsøe (2002).

The equilibrium scour depths normalized by the pile diameter are also indicated in Table 3.1, where S/D_p corresponds to the near field scour depths obtained at the transverse side of the scour protection and S_d/D_p is the maximum scour depth downstream of the pile as shown in Fig. 3.1a. Indicated in the table is also the length of the downstream scour hole L_s (see Fig. 3.1a). The quantity T is the time scale of the scour process, and T^* is the nondimensional time scale defined by

$$T^* = \frac{\left(g(s-1)d_{50}^3\right)^{1/2}}{D_p^2}\,T \tag{3.7}$$

The time scale is normalized in the same manner as previous works on pile generated scour (Sumer and Fredsøe 2002). Note that Table 3.1 summarizes tests carried out in both the 2-meter wide and the 4-meter wide flumes, as indicated in the table.

In Table 3.2 which summarizes the test conditions for the combined waves and current conditions, the quantities listed correspond to the two fundamental cases, that is the wave-alone and the current-alone case. In combination they form the corresponding combined waves and current climate. In the table U_m is the maximum value of the bed orbital velocity calculated from the spectrum function of U

$$U_m = \sqrt{2}\,\sigma_U \tag{3.8}$$

with σ_U

$$\sigma_U^2 = \int_0^\infty S_U(f)\, df \tag{3.9}$$

in which $S_U(f)$ is the spectrum function of the measured orbital velocity at the bed U and f is the frequency. Note that $U_m = \sqrt{2}\,\sigma_U$ is identical to the maximum value of the bed orbital velocity in the case of small-amplitude linear waves and is adopted in accord with Sumer and Fredsøe (2001a), Petersen et al. (2012a) and Sumer et al. (2013). The quantity U_{fm} in the table is the undisturbed friction velocity in waves calculated from

$$U_{fm} = \sqrt{\frac{f_w}{2}}\, U_m \tag{3.10}$$

here f_w is the wave friction factor. The friction factor f_w is calculated based on the bed behaving as hydraulically smooth (with $d_{50}U_{fm}/\nu < 5$) and the wave boundary layer Reynolds number $RE < 1.5 \cdot 10^5$. The wave boundary layer was hence in the laminar regime where $f_w = 2/\sqrt{RE}$ (Fredsøe and Deigaard, 1992). The Shields parameter in Table 3.2 is defined in the same manner as in Eq. (3.6), with U_f replaced by U_{fm}. The KC number in Table 3.2 is defined by

$$KC = \frac{U_m T_p}{D_p} \tag{3.11}$$

in which T_p is the peak period of the waves corresponding to the peak frequency f_p of the waves

$$T_p = \frac{1}{f_p} \tag{3.12}$$

The quantity U_{cw} in Table 3.2 is defined by

$$U_{cw} = \frac{U_c}{U_c + U_m} \tag{3.13}$$

in which U_c is the current velocity at D/2 from the bed in the current-alone fundamental case (in analogy with Sumer and Fredsøe 2001a, Petersen et al. (2012a) and Sumer et al. 2013), and U_m is the bed orbital velocity defined by Eq. (3.8) in the wave-alone case. In

accord with Table 1, the measured equilibrium scour depths normalized by the pile diameter are also given in Table 3.2. Note that Table 3.2 summarizes tests carried out in the 4-meter wide flume.

In Table 3.3, where the test conditions are summarized for the simulated tidal current, T_{tidal} defines the tidal period over which the current is reversed periodically. The Keulegan-Carpenter number in Table 3.3 is defined by

$$KC = \frac{\bar{V}\, T_{tidal}}{D_p} \tag{3.14}$$

in which $\bar{V}$ the time averaged component of the measured streamwise velocity V_t. In accord with Table 3.1 and Table 3.2, the measured equilibrium scour depths normalized by the pile diameter and the scour hole length are also given in Table 3.3. Note that Table 3.3 summarizes tests carried out in the 2-meter wide flume.

Table 3.4 gives the test conditions for the scour tests with a filter layer installed immediately beneath the armour layer (cover stones with the size D_c) with the stone size D_f. In the table distinction is also made between the thickness of the filter layer t_f and the thickness of the armour layer t_c ($h_b = t_f + t_c$). The length of the downstream exposed filter layer L_f in the table, together with h_f defines the volume of stones in the falling apron, as previously mentioned. A definition sketch of L_f is given in Fig. 3.7.

In conjunction with Tables 3.1 - 3.3, the measured equilibrium scour depths normalized by the pile diameter and the scour hole length are also given in Table 3.4. Note that Table 3.4 summarizes tests carried out in the 2-meter wide flume.

Note that the Shields parameter in all the scour experiments (current, combined waves and current, and tidal current) was larger than the critical value ($\theta > \theta_{cr}$) corresponding to initiation of motion at the bed, meaning that the scour experiments were conducted in the live-bed regime. The live-bed regime was also revealed by the appearance of ripples on the sediment bed in the far field of the structure in every scour test.

3.3.2. Test Conditions for the PIV Tests

As discussed in the previous section a series of PIV measurements were performed in planes downstream of the pile. Given the appreciable data storage and processing requirements of the PIV measurements, it was decided to focus on a single current flow velocity. Table 3.5 gives the test conditions for the PIV experiments, and the notations are similar to Table 3.1 – 3.4. Note that the Shields parameter in the PIV experiments was lower than the critical value and no motion on the bed was observed.

3.3.3. Test Conditions for the Bed Shear Stress Tests

Table 3.5 also contains the test conditions for the bed shear stress tests performed in the 0.6m wide flume. Given in the table is the thickness of the boundary layer δ (= $1.5D_p$) taken from the measured velocity profile, and the pile Reynolds number Re_{D_p} defined

$$Re_{D_p} = \frac{VD_p}{\nu} \tag{3.15}$$

in which ν is the kinematic viscosity, and the bed-boundary-layer Reynolds number

$$Re_{\delta} = \frac{V\delta}{\nu} \tag{3.16}$$

Note that the bed friction velocity U_f indicated in Table 3.5 was obtained through the familiar log-fit exercise of the measured streamwise velocity profile. With the hot-film probe installed and calibrated the undisturbed bed shear stress measured in absence of the pile and scour protection relates to the bed friction velocity in the following manner

$$U_f = \sqrt{\frac{\tau_0}{\rho}} \tag{3.17}$$

From the measurements through Test 84 – 86 (same flow climate) and Eq. (3.17) U_f = 1.45 cm/s, which agrees very well with the U_f indicated in Table 3.5. Further the bed friction velocity is also checked against the prediction from the Darcy-Weisbach equation

$$U_f = \sqrt{\frac{f}{2}}V \tag{3.18}$$

where f is the friction coefficient, and is calculated from the Blasius formula

$$f = \frac{0.0557}{Re^{0.25}} \tag{3.19}$$

In which $Re = RV/\nu$, R is the hydraulic radius and ν is the kinematic viscosity. From Eq. (3.18) the bed friction velocity is estimated $U_f = 1.46$ cm/s. The agreement between the measured bed shear stress, bed friction velocity obtained from the log-fit exercise and the estimate from Eq. (3.18) gives confidence in the hot-film probe measurements.

Test No.	Test setup	Water depth	Cover stone size	No. stone layers	Berm height	Berm width	Aspect ratio	Pile diameter	Berm-width-to-pile-size ratio	Depth Averaged Current Velocity	Friction velocity in steady current	Shields Parameter	Measured Equilibrium Scour Depth	Measured Equilibrium Scour Depth	Measured scour hole length	Time scale of far field scour	Norm. Timescale
		h	D_c	N	h_b	w_b	A_r	D_p	w_b / D_p	V	U_f	θ	S	S_d	L_S	T	T^*
[-]	[-]	[m]	[cm]	[-]	[cm]	[cm]	[-]	[cm]	[-]	[cm/s]	[cm/s]	[-]	[cm]	[cm]	[cm]	[s]	[-]
1	2m wide	0,3	1,1	3	3	40	0,075	10	4	35,6	1.57	0,089	2,3	3,7	97,5	-	-
2	2m wide	0,3	1,1	3	3	40	0,075	10	4	43,3	1.90	0.13	2.7	6,1	128	3750	3,34
3	2m wide	0,3	1,1	3	3	40	0,075	10	4	39,0	1.71	0,11	2,5	4,2	113	2355	2,10
4	2m wide	0,3	2,1	2	3,5	40	0,0875	10	4	34,9	1,53	0,085	1.9	2,1	95	-	-
5	4m wide	0,4	1,1	3	3	40	0,075	10	4	37,1	1,58	0,091	2.5	3,4	114	2350	2,10
6	4m wide	0,4	2,1	2	3,5	40	0,0875	10	4	37,1	1,58	0,091	2.4	3,1	105	2550	2,27
7	2m wide	0,3	2,1	2	3,5	40	0,0875	10	4	35,8	1,57	0,089	1.7	2	102	1750	1,56
8	2m wide	0,3	1,1	3	3	40	0,075	10	4	45,7	2,01	0,15	2.4	6,2	144	1625	1,45
9	4m wide	0,5	1,1	3	3	40	0,075	10	4	42,9	1,79	0,12	2,5	6,5	126	-	-
10	2m wide	0,3	1,1	3	3	37,5	0,080	7,5	5	37,5	1,65	0,099	2,5	1,9	108	-	-
11	2m wide	0,3	1,1	3	3	37,5	0,080	7,5	5	42,6	1,87	0,13	2.2	3	125	1620	2,57
12	2m wide	0,3	1,1	3	3	30	0,100	10	3	38,1	1,67	0,101	2,8	6,1	82	2650	4,20
13	2m wide	0,3	1,1	3	3	30	0,100	10	3	31,2	1,37	0,068	1.5	2,7	68	4625	4,12
14	2m wide	0,3	1,1	3	3	30	0,100	10	3	32,8	1,44	0,075	1.9	5,5	79	7250	6,47
15	2m wide	0,3	1,1	3	3	30	0,100	10	3	40,5	1,78	0.115	2.9	7,9	94	3140	2,80
16	2m wide	0,3	1,1	3	3	20	0,150	10	2	39,5	1.67	0.102	3.3	4,8	57	8355	7,45
17	2m wide	0,3	1,1	4	0	40	0	10	4	33,1	1,45	0,077	0.8	1,6	64	2520	2,25
18	2m wide	0,3	1,1	4	0	40	0	10	4	40,7	1,79	0,116	0.9	1,7	87	4660	4,16
19	2m wide	0,3	1,1	4	0	40	0	10	4	44,6	1,96	0,139	0.8	2,6	101	1045	0,93
20	4m wide	0,4	1,1	5	5	40	0,125	10	4	35,5	1,51	0,083	3,2	8,2	90	8560	7,63
21	4m wide	0,4	1,1	5	5	50	0,100	10	5	35,5	1,51	0,083	2,2	4,1	130	2265	2,02
22	2m wide	0,3	2,1	3	0	40	0	10	4	38,3	1,68	0,103	2.2	1,8	74	2080	1,85
23	2m wide	0,3	1.1	3	3	40	0,075	10	4	43,1	1,89	0,13	2.35	6,1	132	3570	3,18
24	4m wide	0,4	1.1	5	5	40	0,125	10	4	39,26	1,67	0,102	3.6	7,5	109	-	-
25	4m wide	0,4	1.1	5	5	50	0,1	10	5	39,3	1,67	0,102	3.2	5,4	145	2640	2,35
26	4m wide	0,4	1,1	5	5	40	0,125	10	4	31,1	1.32	0,064	1.3	6,9	91	2425	2,16
27	4m wide	0,4	1,1	5	5	50	0,1	10	5	31,1	1.32	0,064	0.75	4,7	111	2965	2,64
28	4m wide	0,4	1,1	5	5	40	0,125	10	4	43,1	1.84	0.123	-	11,7	125	1710	1,52
29	4m wide	0,4	1,1	5	5	50	0,1	10	5	43,1	1.84	0.123	-	7,6	165	2540	2,27
30	4m wide	0,4	0,7	3	1,5	20	0,075	5	4	40,0	1,7	0,102	-	2,7	61	-	-
31	4m wide	0,4	0,7	4	2,1	28	0,075	7	4	40,0	1,7	0,102	-	3,9	81	-	-
32	2m wide	0,3	1.1	3	3	30	0,100	7,5	4	44,4	1.93	0.128	2,2	6,2	96	2255	4,10
33	2m wide	0,3	2.1	2	3	35	0,086	7,5	4,7	44,5	1.94	0.129	2.2	2,9	98	-	-
34	2m wide	0,3	2.1	2	3	35	0,086	7,5	4,7	46,1	2.00	0.138	2.7	3,1	101	910	1,44
35	2m wide	0,3	0,7	5	3	35	0,086	7,5	4,7	39,7	1.73	0.103	-	1,5	92.5	2690	4,26
36	2m wide	0,3	0,7	5	3	35	0,086	7,5	4,7	33,5	1.46	0.073	0,5	1,5	72	4359	6,91
37	2m wide	0,3	1.1	3	3	44	0,068	10	4,4	50,0	2.18	0.163	2,6	4,6	139	1990	3,15

38	2m wide	0,3	1,1	4	0	46	0,000	10	4,6	50,7	2.21	0.167	0.6	3,7	70	870	0,78
39	2m wide	0,3	1.1	2	2	44	0,045	10	4,4	40,1	1.74	0.105	1,3	2,5	123	2265	2,02
40	2m wide	0,3	1.1	3	3	40	0,075	10	4	40,1	1.74	0.105	1,9	3,9	110	1828	1,63
41	2m wide	0,3	1.1	3	3	40	0,075	10	4	50,1	2.18	0.163	2,5	6,7	138	740	0,66
42	2m wide	0,3	1.1	3	3	30	0,100	10	3	45,6	1.99	0.136	2,7	6,7	97	1637	1,46
43	2m wide	0,3	1.1	3	3	30	0,100	10	3	50,2	2.19	0.164	2,8	7,1	96	897	0,80
44	2m wide	0,3	1.1	4	4	30	0,133	10	3	46,1	2.01	0.138	2,9	9	105	1491	1,33
45	2m wide	0,3	1.1	4	4	30	0,133	10	3	50,1	2.18	0.163	2,8	9,8	95	863	0,77
46	2m wide	0,3	1.1	4	4	30	0,133	10	3	48,1	2.10	0.151	3.0	9,3	109	1133	1,01
47	2m wide	0,3	1.1	4	4	30	0,133	10	3	41,7	1.81	0.113	3.4	10,3	98	2781	2,48
48	2m wide	0,3	1.1	4	4	30	0,133	10	3	37,7	1.64	0.092	2,9	10	95	3958	3,53
49	2m wide	0,3	1.1	4	4	30	0,133	10	3	34	1.48	0.075	2,7	5,9	77	5160	4,60
50	2m wide	0,3	1.1	4	0	46	0,000	10	4,6	39,2	1.7	0.100	0.4	2,6	76	3476	3,10
51	2m wide	0,3	1.1	4	0	40	0,000	10	4	36,2	1.57	0.085	1.2	2,7	69	3588	3,20
52	2m wide	0,3	1.1	4	0	46	0,000	10	4,6	32,4	1.41	0.068	1.4	1,3	47	4037	3,60
53	2m wide	0,3	1.1	4	0	40	0,000	10	4	44,1	1.92	0.126	0.5	2,5	75	1817	1,62
54	2m wide	0,3	1.1	3	3	30	0,100	10	3	48,1	2.09	0.151	2.5	6,7	110	1270	1,13
55	2m wide	0,3	1,1	4	0	30	0	7,5	4	50,7	2,2	0,167	-	-	-	-	-

Table 3.1. Edge scour in steady current. Live-bed ($\theta > \theta_{cr}$).

Test No.	Test setup	Water depth h	Cover stone size D_c	No. stone layers N	Berm height h_b	Berm width w_b	Aspect ratio A_r	Pile diameter D_p	Berm-width-to-pile-size ratio w_b / D_p	Peak frequency of waves f_p	Maximum orbital velocity at the bed U_m	Bed friction velocity in waves U_{fm}	Keulegan-Carpenter number KC	Shields parameter in waves θ	Depth averaged current velocity V	Unidsturbed current velocity at D/2 U_c	Velocity ratio U_{cw}	Measured equilibrium scour depth downstream S/ D_p
[-]	[-]	[m]	[cm]	[-]	[cm]	[cm]	[-]	[cm]	[-]	[Hz]	[cm/s]	[cm/s]	[-]	[-]	[cm/s]	[cm/s]	[-]	[-]
56	4m	40	1,1	-	-	-	-	10	4	0,67	24,4	1,9	4	0,127	15,6	13,6	0,36	0,13
57	4m	40	1,1	4	5	40	0,125	10	4	0,67	24,4	1,9	4	0,127	15,6	13,6	0,36	0,24
58	4m	40	1,1	-	-	-	-	10	4	0,67	24,4	1,9	4	0,127	26,5	22,8	0,48	0,55
59	4m	40	1,1	4	5	40	0,125	10	4	0,67	24,4	1,9	4	0,127	26,5	22,8	0,48	0,34
60	4m	40	1,1	-	-	-	-	10	4	0,67	24,4	1,9	4	0,127	40,0	31,6	0,56	0,86
61	4m	40	1,1	4	5	40	0,125	10	4	0,67	24,4	1,9	4	0,127	40,0	31,6	0,56	0,45
62	4m	40	1,1	2	3	40	0,075	10	4	0,67	24,4	1,9	4	0,127	15,6	13,6	0,36	0,23
63	4m	40	1,1	1	1,5	40	0,0375	10	4	0,67	24,4	1,9	4	0,127	15,6	13,6	0,36	0,25
64	4m	40	1,1	2	3	40	0,075	10	4	0,67	24,4	1,9	4	0,127	26,5	22,8	0,48	0,29
65	4m	40	1,1	1	1,5	40	0,0375	10	4	0,67	24,4	1,9	4	0,127	26,5	22,8	0,48	0,33
66	4m	40	1,1	2	3	40	0,075	10	4	0,67	24,4	1,9	4	0,127	40,0	31,6	0,56	0,35
67	4m	40	1,1	1	1,5	40	0,0375	10	4	0,67	24,4	1,9	4	0,127	40,0	31,6	0,56	0,35
68	4m	40	1,1	4	5	40	0,125	10	4	0,67	24,4	1,9	4	0,127	72,9	56,6	0,70	0,6
69	4m	40	1,1	2	3	40	0,075	10	4	0,67	24,4	1,9	4	0,127	72,9	56,6	0,70	0,53
70	4m	40	1,1	4	3,5	28	0,125	7	4	0,33	24,5	1,7	11	0,103	15,6	12,5	0,34	0,46
71	4m	40	1,1	2	2,1	28	0,075	7	4	0,33	24,5	1,7	11	0,103	15,6	12,5	0,34	0,41
72	4m	40	1,1	4	3,5	28	0,125	7	4	0,33	24,5	1,7	11	0,103	26,5	21,6	0,47	0,53
73	4m	40	1,1	2	2,1	28	0,075	7	4	0,33	24,5	1,7	11	0,103	26,5	21,6	0,47	0,47
74	4m	40	1,1	4	3,5	28	0,125	7	4	0,33	24,5	1,7	11	0,103	72,9	53,6	0,69	0,79
75	4m	40	1,1	2	2,1	28	0,075	7	4	0,33	24,5	1,7	11	0,103	72,9	53,6	0,69	0,66

Table 3.2. Edge scour in combined current and waves. Live bed ($\theta > \theta_{cr}$).

Test No.	Test setup	Water depth	Stone size	No. Stone Layers	Berm Height	Berm Width	Aspect Ratio	Pile diameter	Berm-width-to-pile-size ratio	Depth Averaged Current Velocity	Friction velocity in steady current	Shields Parameter	Tidal period	Keulegan-Carpenter number	Froude number	Measured Equilibrium Scour Depth	Measured scour hole length	Norm. Timescale
		h	D_c	N	h_b	w_b	A_r	D_p	w_b / D_p	V	U_f	θ	T_{tidal}	KC ($=VT_{tidal}/D_P$)	Fr	S_d	L_S	T*
[-]	[-]	[m]	[cm]	[-]	[cm]	[cm]	[-]	[cm]	[-]	[cm/s]	[cm/s]	[-]	[s]	[-]	[-]	[cm]	[cm]	[-]
76	2m	0,3	1,1	3	3	40	0,075	10	4	39	1,65	0,101	960	3744	0,20	4,9	80	3,4
77	2m	0,3	1,1	3	3	40	0,075	10	4	39	1,65	0,101	360	1404	0,20	4,9	110	5,1
78	2m	0,3	1,1	3	3	40	0,075	10	4	39	1,65	0,101	120	468	0,20	4,7	95	3,4

Table 3.3. Edge scour in tidal current. Live bed ($\theta > \theta_{cr}$).

Test No.	Test setup	Water depth	Cover stone size	Filter stone size	Height of armour layer	Height of filter layer	Berm width	Aspect ratio	Pile diameter	Berm-width-to-pile-size ratio	Length of filter layer	Depth Averaged Current Velocity	Friction velocity in steady current	Shields Parameter	Measured Equilibrium Scour Depth	Measured scour hole length
		h	D_c	D_f	h_c	h_f	w_b	A_r	D_p	w_b / D_p	L_f	V	U_f	θ	S_f	L_S
[-]	[-]	[m]	[cm]	[cm]	[cm]	[cm]	[cm]	[-]	[cm]	[-]	[cm]	[cm/s]	[cm/s]	[-]	[cm]	[cm]
79	2m wide	0,3	2,1	0,7	3	1,2	40	0,11	10	4	6	44,5	1,94	0,129	2,4	130
80	2m wide	0,3	2,1	0,7	3	1,2	40	0,11	10	4	8,5	44,6	1,94	0,13	2,5	120
81	2m wide	0,3	2,1	0,7	3	1,2	40	0,11	10	4	20	44,6	1,94	0,13	1,1	-
82	2m wide	0,3	2,1	0,7	3	1,2	40	0,11	10	4	0	44,6	1,94	0,13	9,4	127

Table 3.4. Edge scour in steady current with filter layer. Live bed ($\theta > \theta_{cr}$).

Test No.	Test setup	Water depth	Cover stone size	No. stone layers	Berm height	Berm width	Aspect ratio	Pile diameter	Berm-width-to-pile-size ratio	Depth Averaged Current Velocity	Undisturbed friction velocity in steady current	Boundary layer thickness	Boundary layer Reynolds numder	Pile Reynolds number
		h	D_c	N	h_b	w_b	A_r	D_p	w_b / D_p	V	$U_{f,\infty}$	δ	Re_δ	Re_{Dp}
[-]	[-]	[m]	[cm]	[-]	[cm]	[cm]	[-]	[cm]	[-]	[cm/s]	[cm/s]	[cm]	[-]	[-]
PIV tests														
83	2m wide	0.3	1,1	3	3.5	40	0,087	10	40	18,1	0,8	30	$3{,}0 \cdot 10^4$	$1{,}8 \cdot 10^4$
Bed Shear Stress tests														
84	0.6m wide	0,3	0,7	3	2	8	0,25	4	2	35,3	1,44	6	$2{,}0 \cdot 10^4$	$1{,}4 \cdot 10^4$
85	0.6m wide	0,3	0,7	3	2	12	0,17	4	3	35,3	1,44	6	$2{,}0 \cdot 10^4$	$1{,}4 \cdot 10^4$
86	0.6m wide	0,3	0,7	3	2	16	0,13	4	4	35,3	1,44	6	$2{,}0 \cdot 10^4$	$1{,}4 \cdot 10^4$

Table 3.5. Test conditions PIV- and bed shear stress tests

3.4. Results and Discussion

3.4.1. Flow from PIV and Bed Shear Stress Measurements

The flow around the pile and the scour protection in steady current was investigated by means of flow visualizations, mapping the three-dimensional velocity field (PIV measurements) and bed shear stress tests (hot-film measurements).

The flow visualizations were made by injecting blue and green dye at the upstream-, transverse- and downstream side of the scour protection and also upstream of the pile. Further to this the suspended sediment alongside the perimeter and downstream of the scour protection acted as ideal flow tracers in the video recordings made in each individual test.

The flow visualizations showed that the flow around the scour protection from the far upstream point to the centre of the pile is well described by Nielsen et al. (2011) and the following description of the upstream flow patterns is given in accord with this study. From the transverse side of the scour protection and further downstream the present flow visualizations and velocity measurements show different flow structures which will be detailed in the following section (see Fig. 3.11).

Around the pile the flow structures resemble the patterns observed for an unprotected pile, well described in Sumer and Fredsøe (2002), Roulund (2005) and Nielsen et al. (2011). Here the most dominant flow pattern is the horeshoe-vortex generated by the downflow in front of the pile (see Fig. 3.11), infiltrating the scour protection at the pile base and exfiltrating upstream into the main flow at a distance of about $1.0 - 1.2 \cdot D_p$ measured from the pile centre.

By adding dye to the upstream side of the scour protection the horseshoe-vortex in front of the scour protection and the infiltration of water into the porous stone layer was visualized, as sketched in Fig. 3.11.

Flow visualizations from the upstream point of the scour protection and alongside the perimeter to the transverse side showed contraction of streamlines and acceleration of the flow at the transverse sides. This effect was also observed in the case of a half-buried sphere (see Fig. 1 in Dixen et al., 2013) and in the case of an oblong stockpile (see Fig. 7 in Furieri et al., 2012). Further to this the flow around the individual stones at the perimeter of the scour protection was visualized by the sediment acting as flow tracers on the video recordings, the flow patterns observed here is well described by Petersen et al.(2014) and Fredsøe et al.(2001) and will be discussed in the section on scour in steady current.

As mentioned previously the downstream flow visualizations made from the transverse- to the far downstream side of the scour protection by Nielsen et al. (2011) reveals the vortex shedding in Fig. 3.11 as the most important flow feature. The present flow visualizations however show that the downstream flow in the near bed wake area has a significant effect on the scour protection, as will be detailed in the following. By adding dye at the downstream side at the perimeter of the scour protection and observing the sediment motion an important flow pattern was disclosed: two counter-rotating vortices were generated in the lee-zone of

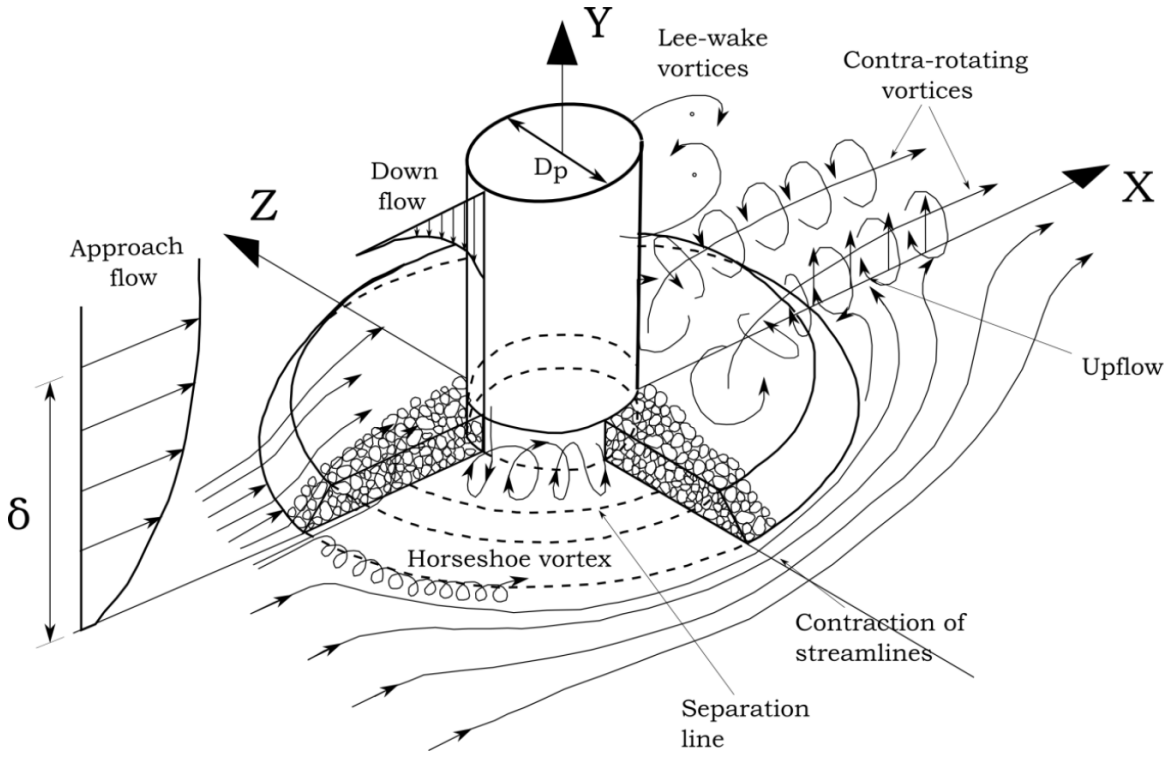

Figure 3.11. Definition sketch. Steady flow around a bottom-mounted vertical cylinder with scour protection installed.

the pile and scour protection (as sketched in Fig. 3.11). The dye and sediment at the downstream centerline was partially transported upstream into and over the scour protection reaching the base of the pile and partially removed downstream, swept into the two counter-rotating vortices. Both the dye and the sediment swept away by the vortices showed two important flow motions; (1) a continues streaming motion from the transverse side of the pile and scour protection towards to centerline (x-axis in Fig 3.11); and (2) a periodic vortex shedding of the counter-rotating vortex pair. The following paragraphs on the PIV measurements and the bed shear stress will further deal with disclosing the motion of the downstream flow and vortex system.

Now, Fig. 3.12a-c show the time averaged velocity components $\overline{u}, \overline{v}, \overline{w}$ obtained by PIV measurements and the individual CFV planes are tiled together into a composite image of the entire mean flow field. Obviously the incoming flow is greatly disturbed by the bottom-mounted pile and scour protection. From an overall qualitative analysis in Fig. 3.12a three different flow features are revealed:

(1) as expected, a wake zone (zone 1 in Fig. 3.12a) is noticed downstream of the pile and scour protection, characterized by negative time averaged streamwise velocities along the centerline close to the pile from about $0 - 2.5\ D_p$, and a recovering flow further downstream with positive time averaged streamwise velocities from about $2.5D_p$ and further downstream. The same kind of wake zone is noticed in Fig. 3.12b and Fig 3.12c for the vertical and lateral velocities respectively. Fig 3.12b shows the vertical velocity with an upwards directed

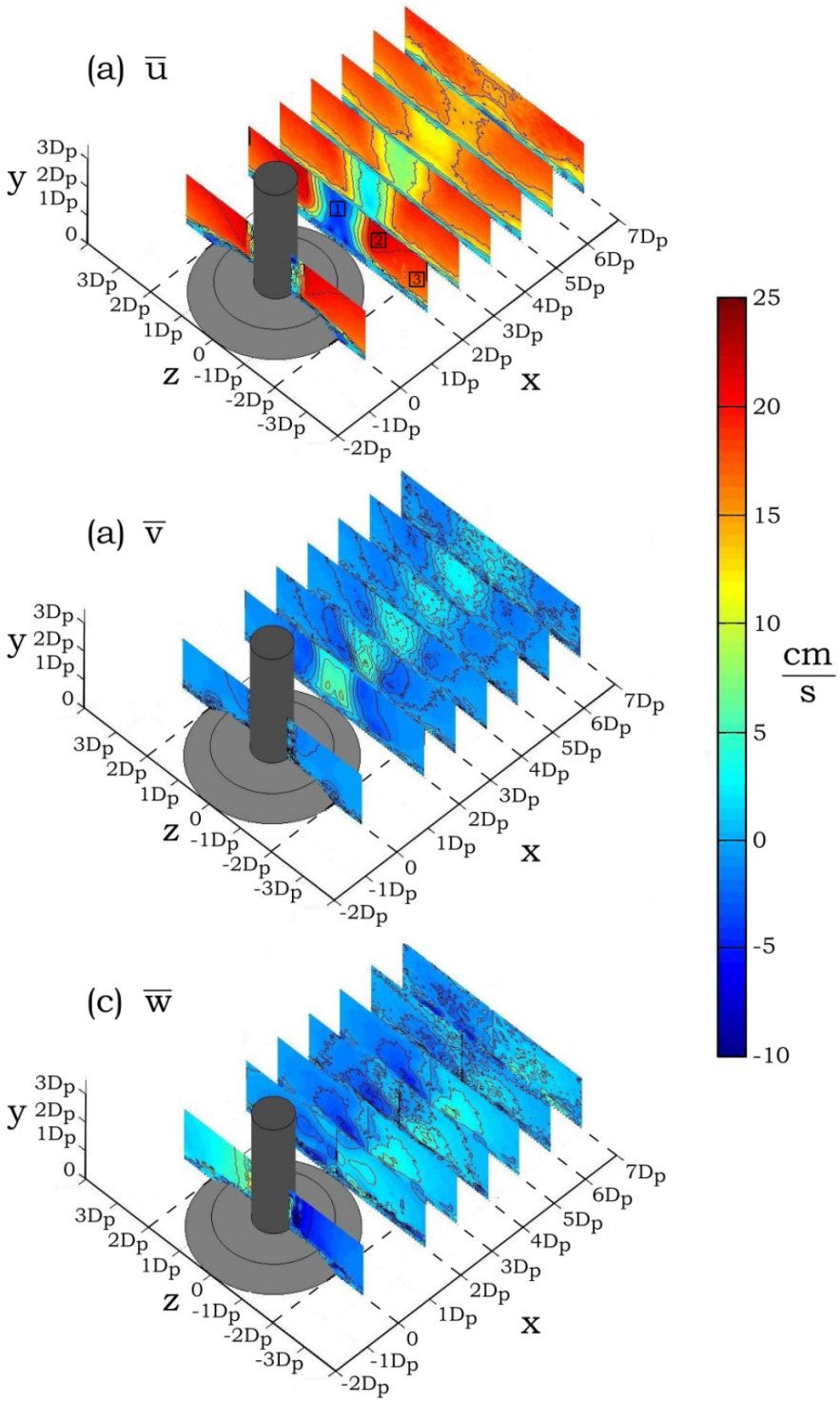

Figure 3.12. Measured mean velocity field downstream of bottom-mounted vertical cylinder with scour protection. Sandy bed with $d_{50} = 0.00017$ mm. Depth averaged current velocity for the undisturbed flow V = 18.3 $\frac{cm}{s}$. Clear water ($\theta < \theta_{cr}$). (a) Mean streamwise velocity $\bar{u}$; (b) mean vertical velocity $\bar{v}$; and (3) mean lateral velocity $\bar{w}$.

motion along the centerline of up till $\bar{v} = 0.35$V at $2D_p$. Notice that at both z = D_p to $2D_p$ and z = $-D_p$ to $-2D_p$ the vertical velocity is negative, enforcing a large vorticity in the streamwise-direction, which will be detailed later in conjunction with Fig. 3.13 in the following section. In Fig. 3.12c the lateral velocity $\bar{w}$ show the converging flow towards the centerline building up in magnitude with maximum of $\bar{v} = 0.42$V at about $4D_p$ and decaying further downstream. It applies to all velocity components in the wake zone in Fig. 3.12a-c that the flow is recovering downstream as the flow patterns in the wake area enforced by the pile and scour protection dissolves.

(2) Contraction and acceleration of the flow takes place at the transverse side of the pile and scour protection identified as zones 2 and 3 in Fig. 3.12a. The highest streamwise velocities ($\bar{u} = 1.23V$ or 22.2 cm/s) are found on each side of the pile owing to the diverging flow around the pile and scour protection, whose effect extends over several D_p downstream. The contraction and acceleration of the flow immediately at the transverse edge of the scour protection will be detailed in the following section on the results of the bed shear stress measurements.

(3) Finally, a pair of symmetrical counter-rotative vortices are identified as zones 4 and 5 in Fig. 3.13. The streamwise vorticity plotted in Fig. 3.13 are defined by the following:

$$\omega_x = \frac{dv}{dy} - \frac{dw}{dz} \tag{3.20}$$

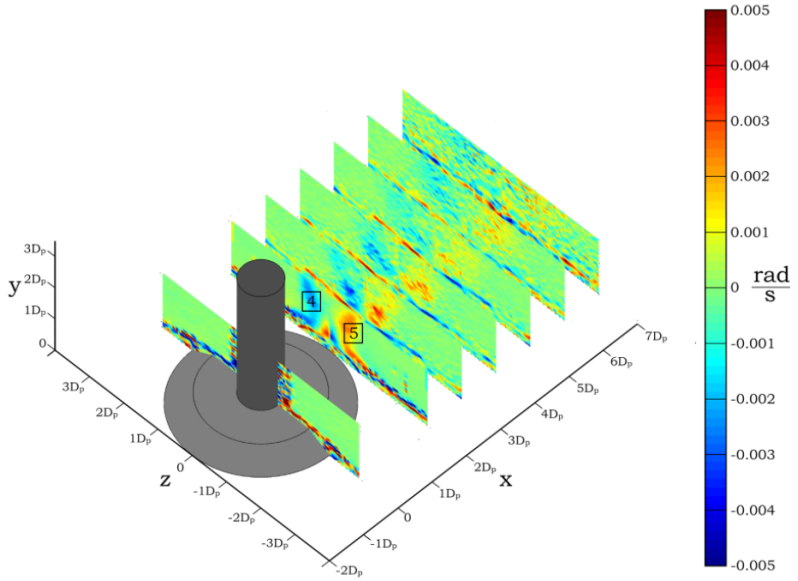

Figure 3.13. x-directional vorticity (ω_x by Eq. (3.20)) field downstream of bottom-mounted vertical cylinder with scour protection. Derived from velocity fields of ($\bar{u}, \bar{v}, \bar{w}$) displayed in Fig. 3.12.

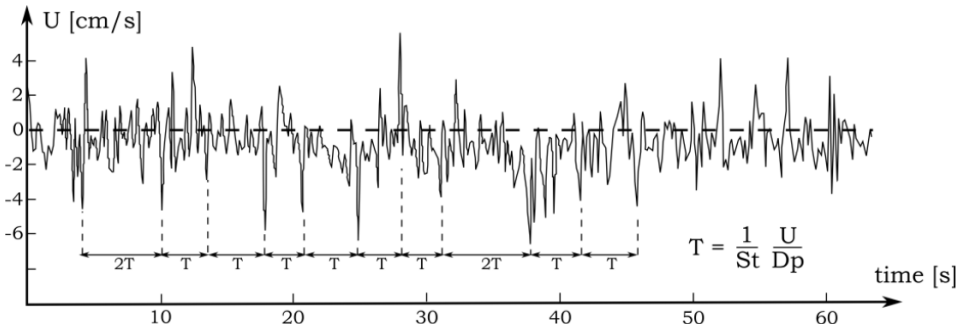

Figure 3.14. Time series of the stream wise velocity u measured at $(x, y, z) = (2D_p, 0.5D_p, 0)$ ie. a measurement point in CFV-plane $2D_p$ downstream in correspondence with Fig. 3.8a and Fig. 3.12.

In Fig. 3.13 the warm red-yellow colors corresponds to clock-wise rotation and the cold blue color to anti-clock-wise rotation. These vortices are due to the converging flow in the near-bed downstream region, which generate a pressure maximum at the centerline where the converging flow reattaches. This regions forms a source of vorticity as the pressure drives the flow upwards in a continuous manner. At further distances from the bed the vortex-shedding from the pile is dominant. Fig. 3.14 shows a time series of the streamwise velocity component u monitored at the far downstream point of the scour protection at x = $2D_p$ and y = $0.5D_p$ above the bed. Also indicated in Fig. 3.14 is the period T between the peaks of the signal, defined in the following way:

$$T = \frac{1}{St}\frac{D}{U} \tag{3.21}$$

in which St is the normalized vortex-shedding frequency, namely the Strouhal number (see Williamson, 1989; Roshko, 1961 and Schewe, 1983). The following two effects are visible in the figure: (1) the mean streamwise velocity $\bar{u}$ is negative, in accord with the velocity field of $\bar{u}$ given in Fig. 3.12a for the given location (x,y,z); (2) the velocity u is fluctuating with a frequency relative to the Strouhal number in a quasi-cyclic manner. In some intervals the peaks of u are periodic with T defined from Eq. (3.21), whereas in other intervals the periods resemble 2T. One can also notice that most peaks are of negative velocity, while few are positive, owing to the nature of the vortex-shedding, which at the location should be predominantly of negative values. Note that the location of the measurement point dictates that it is only the counter-rotating vortices and the streaming which is visible in the time series, the regular vortex-shedding from the pile is suppressed at this distance to the bed.

Now, the bed shear stress was measured at upstream-, downstream- and the transverse sides of the scour protection. Fig. 3.15 displays $\overline{\tau_b}/\overline{\tau_\infty}$ (the amplification in the bed shear stress) over the upstream- and downstream centerline in the proximity of the scour protection

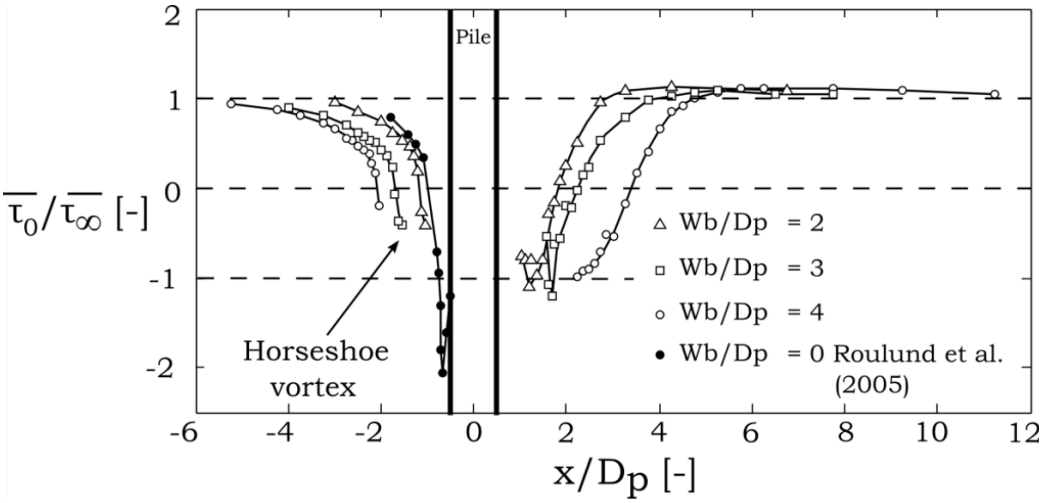

Figure 3.15. Amplification of the bed shear stress at the upstream and downstream side of the bottom-mounted vertical cylinder with scour protection. D = 4 cm, V = 35.3 cm/s, δ = 6 cm, $\frac{\delta}{d_p}$= 1.5, $Re_D = 1.36 \cdot 10^4$. Measured in Test 84 – 86, Table 3.5.

grouped according to the w_b/D_p ratio. Also indicated in Fig. 3.15 are the bed shear stress measurements of Roulund et al. (2005) for a bottom-mounted unprotected pile (w_b/D_p = 0) on a rigid bed. Firstly, the negative values for the upstream $\bar{\tau}$ are the footprint of the horse-shoe vortex generated by the adverse pressure gradient inflicted by the berm. This forces motion in the opposing flow direction right upstream of stagnation point. The amplification curves of the present measurements collocated with the Roulund et al. (2005) seems sensitive with respect to shape and appearance, but shows lower negative amplifications as expected. The adverse pressure gradient generated by the berm is lower; firstly because of the low berm height relative to the pile diameter, and secondly the berm is a porous medium allowing some part of the approach flow to penetrate the surface.

The downstream part of the $\bar{\tau}$ amplification curves in Fig. 3.15 is described below. Immediately of the edge of the scour protection the direction of the bed shear stress is negative, showing a time averaged motion of the fluid over the bed in the direction opposite to the streamwise direction. Noticeably the amplification curves of the bed shear stress, for each of the w_b/D_p respectively, reaches the value of the undisturbed bed shears stress as $\bar{\tau} \to -\overline{\tau_\infty}$ when $x/D_p \to w_b/D_p$ (see Fig 3.15). From Fig. 3.12a the time averaged streamwise velocity $\bar{u}$ in this region is < O(0.5V), and O means order of magnitude. Therefore, the observed amplification must be caused by the combined action of the following two effects: (1) the time-averaged opposed streamwise flow observed in Fig 3.12a. (2) the turbulent flow structures in the near bed region in the wake of the pile and scour protection, ie. the counter-rotating vortices as previously described and illustrated in conjunction with Fig. 3.11 and Fig. 3.13. As x/D_p is increased from this point the bed shear stress increases as $\bar{\tau} \to 0$. This behaviour is supported by the traces of the streamwise velocity previously mentioned in concurrence with Fig. 3.12a. Further downstream as x/D_p increases the bed shear stress attends the undisturbed value $\bar{\tau} \to \overline{\tau_\infty}$.

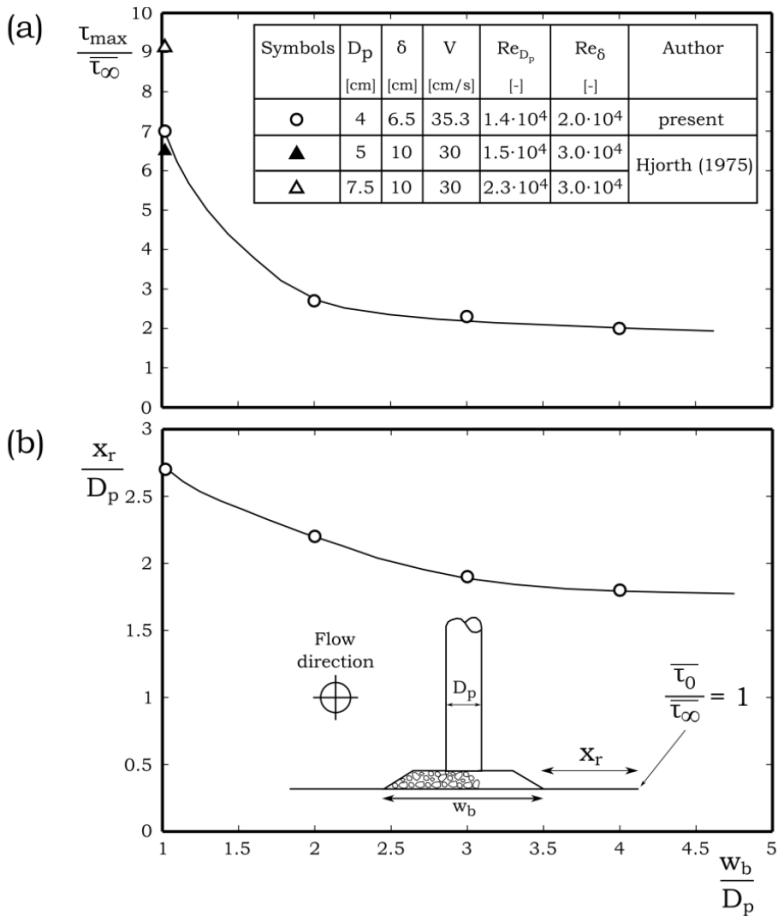

Figure 3.16. (a) Maximum amplification of the bed shear stress at the transverse side of the scour protection. D = 4 cm, V = 34 cm/s, δ = 6 cm, δ/D_p= 1.5, $Re_D = 1.36 \cdot 10^4$; (b) re-attachment length x_r (ie. $\overline{\tau_0}/\overline{\tau_\infty} = 1$). Measured in Test 84 – 86, Table 3.5.

Illustrated in Fig. 3.16a is the maximum amplification of $\bar{\tau}$ at the transverse side of the scour protection. The figure shows a drastic increase in the amplification as w_b/D_p is decreased, and a decreasing asymptotic behavior in the amplification as w_b/D_p is increased. From the studies of Hjorth (1975), Baker (1979), Sumer et al. (1997) and Roulund et al. (2005) the amplification in the bed shear stress can reach values of ~5-9 on the transverse sides of the unprotected pile depending on the value of Re_{D_p} and δ/D_p. Obviously, for low values of the w_b/D_p the increased hydrodynamic field, and in turn the amplification of the bed shear stress around the pile itself, will influence the flow at the side edge of the berm. From Fig. 3.16a it seems that this effect disappears for values of w_b/D_p > 2.5 - 3. A similar trend is observed in Fig. 3.16b where the re-attachment length x_r (where $\overline{\tau_0}/\overline{\tau_\infty} = 1$) shows an asymptotic behavior when $w_b/D_p \gtrsim 3$.

Obviously, the above mentioned increase in the bed shear stress would induce a certain amount of sediment transport in front and at the side edges of the scour protection, which will lead to the formation of a scour hole around the edge of the scour protection in a period

of time, when the bed is erodible. Further, some parts of the agitated sediment in the neighboring downstream area of the scour protection will be transported backwards in to the scour protection, and some parts will be eroded downstream. The further details of the scour process are given in the following sections.

3.4.2. Edge Scour Process

3.4.2.1. Mechanism of Edge Scour in Current-alone

With the information rendered through the PIV and bed shear stress measurement campaign displayed in Figs. 3.11 – 3.16, the scour process in steady current will be described in reference to Fig. 3.17, Fig. 3.18 and Fig. 3.19. Fig. 3.17 displays a sequence of three-dimensional images of the bed morphology obtained in Test no. 23 measured by the previously mentioned bed-profiler system. Fig. 3.17a shows the pile and scour protection setup with the initial flat sediment bed around at $t = 0$. At $t = 0$ the current is switched on, and with this the edge scour develops around and downstream of the structure, with Fig. 3.17b - d illustrating the time evolution of the scour process. The treatment of the edge scour process in current will be divided into two parts: (1) edge scour in the near field of the structure, observed from the far upstream point to the transverse side of the scour protection; and (2) edge scour in the downstream field is observed from the transverse side and downstream of the structure, which will be detailed in the following section.

Returning to Fig. 3.17d showing the equilibrium stage of the scour process and Fig. 3.18 showing an image taken at the equilibrium stage of test no. 23 with the water drained from the flume. The view is taken from the downstream centerline in upstream direction towards the scour protection. Following three distinct areas of interest can be identified in Fig. 3.17 and Fig. 3.18: (1) edge scour happens alongside the perimeter from the far upstream point to the transverse side of the scour protection, marked by zone 1 in Fig. 3.17(d); (2) a two-legged scour hole forms downstream of the structure, originating from the transverse sides of the scour protection, marked by zone 2 in Fig. 3.17(d) and clearly visible in Fig. 3.18; and (3) a ridge forms between the two legs of the scour hole, starting at the pile base extending downstream into the scour hole, marked by zone 3 in Fig. 3.17(d) and shown in Fig. 3.18.

With the information obtained from the results of the PIV and bed shear stress measurement campaigns given in Figs. 3.11 – 3.16 collocated with the bed morphology images presented in Fig. 3.17 – 3.18 the edge scour mechanisms for (1) the near- and (2) downstream case are respectively as follows:

(1) In the near field case the horseshoe-vortex generated in front of the berm (see Fig. 3.11) is key to the scour process, together with the contraction of streamlines and the acceleration of flow at the side edge of the berm, sediment is removed alongside the perimeter of the scour protection. The horseshoe-vortex and the accelerated flow at the edge of the berm agitate and suspend the adjacent sediment and the streamwise flow carries the sediment away downstream. In addition to these processes the flow and turbulence around the individual stones, in the form of horseshoe-vortices and lee-wake flow, described by Petersen et al. (2014) and Fredsøe et al. (2001), enhance the local sediment transport and hereby supports

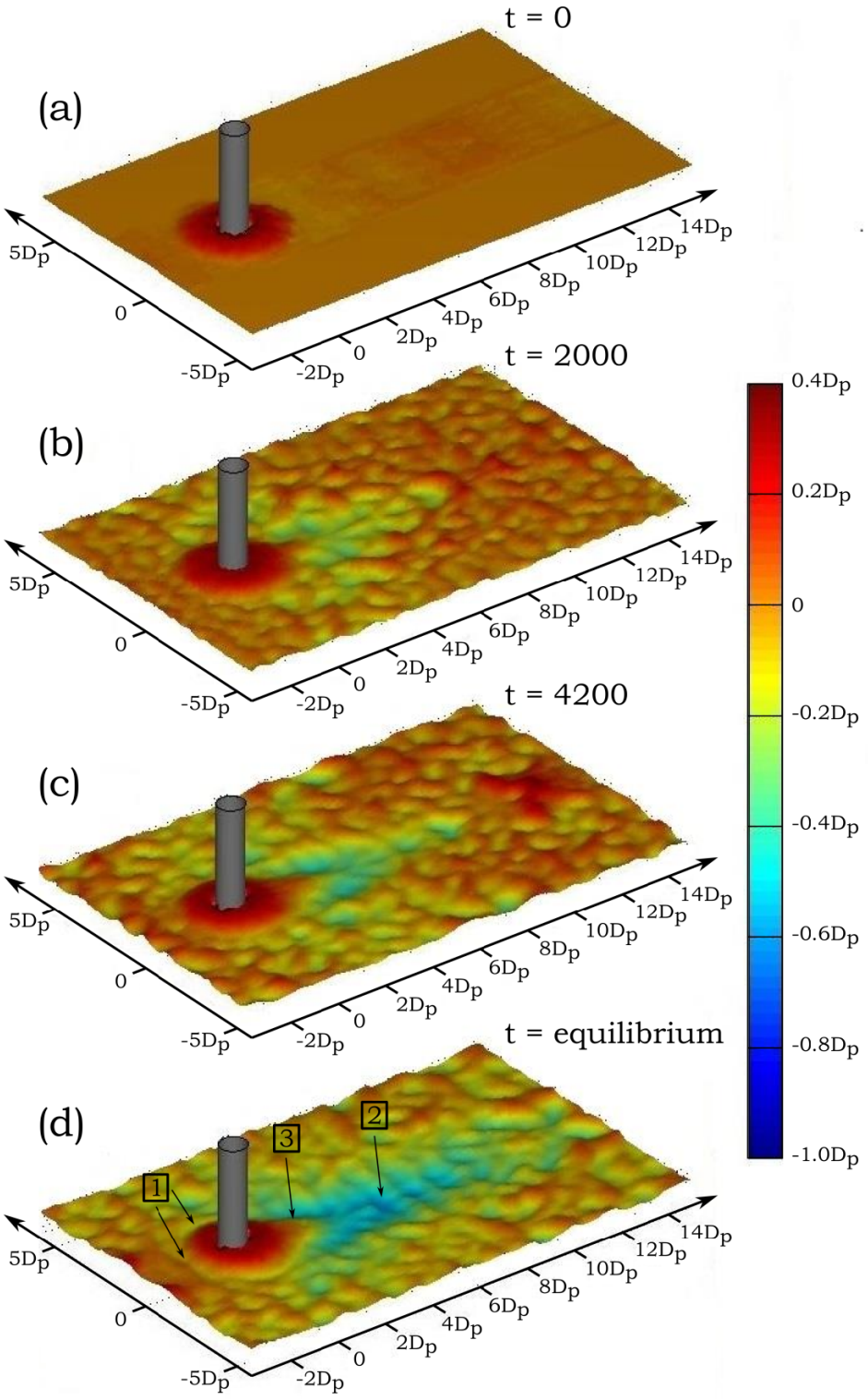

Figure 3.17. Sequence of three-dimensional pictures illustrating the time evolution of edge scour around the scour protection (measured in Test 23, Table 3.11.); (a) t = 0s; (b) t = 2000s; (c) t = 4200; and (d) t = equilibrium. Note that the time scale of scour in Test 23 is T = 3570 not far from the bed profile given in (c).

Figure 3.18. Image taken downstream of the bottom-mounted cylinder with scour protection, facing upstream (Test 23, Table 3.1).

the overall scour mechanism at the sides of the scour protection. As the scour continues and the latter processes remove sediment beneath the stones, stability is lost and the stones at the edge of the berm slump into the scour hole. In most cases the latter process was accompanied by sinking of the stones caused by shear failure of the sand beneath, resulting in the sand losing its bearing capacity. Obviously some portion of the scoured sediment is brought into the stone layer by the streamwise flow penetrating the porous scour protection, where it is deposited. This deposition will be discussed in the following paragraphs.

(2) The pairing counter-rotating vortices (see Fig. 3.11) are the key element in the downstream scour process, combined with the deviation and acceleration of the flow over the sides of the pile and the berm, these vortices can erode a significant amount of sediment away from the edge of the scour protection. The scour hole emerges from the transverse side of the scour protection where the streamlines of the primary flow starts to converge (see Fig. 24 and Fig 25 in Roulund et al., 2005 for converging streamlines downstream of a pile), and from here the streamwise and lateral velocity (Figs. 3.12a and 3.12c) and the counter-rotating vortices drive the sediment transport downstream and towards the centerline, where the counter-rotating vortices in a periodic manner sweeps the sediment into suspension. At some downstream distance of the scour protection the streamwise velocity $\bar{u}$ and the bed shear stress $\bar{\tau}$ is positive (see the downstream flow field of $\bar{u}$ in Fig. 3.12a and the bed shear stress $\bar{\tau}$ in Fig. 3.15), and the suspended sediment is scoured away downstream, leaving the footprint of the pairing counter-rotating vortices visible as the two-legged scour hole converging downstream, visible in Fig. 3.17 and Fig. 3.18. The scour hole ends where the longitudinal turbulent vortex structures downstream dissolves, as mentioned in the previous section on flow, resulting in a finite scour hole length.

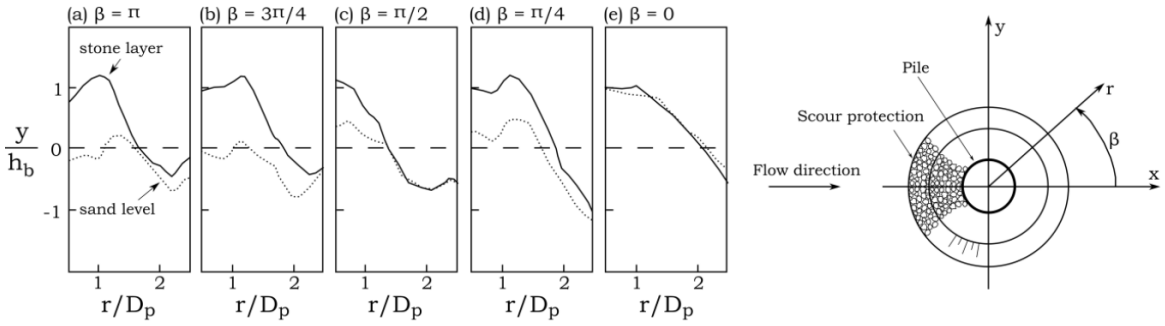

Figure 3.19. Sand deposit within scour protection at the equilibrium stage of Test 23 (see Table 3.1).

Immediately downstream of the berm the streamwise velocity $\bar{u}$ (see Fig. 3.12a) and the bed shear stress is negative (Fig. 3.15) and the suspended sediment is brought backwards into the porous stone layer where it is deposited. Fig. 3.19 shows the surface of the stone layer and the corresponding deposition level of the sand within at the equilibrium stage of Test no. 23, with Fig. 3.19a–e illustrating the deposition in the radial distance from the perimeter of pile (see the definition sketch in Fig. 3.19). From the far upstream point at $\beta = \pi$ to $\beta = 3\pi/4$ the sediment at the pile base is removed by the horseshoe-vortex generated in front of the pile penetrating the scour protection, as described by Nielsen et al. (2011) and further detailed in Nielsen et al. (2013). As $\beta = \pi/2 \rightarrow \pi$ in Fig. 3.19c - e the sediment deposition level increases generating the center of the ridge at $\beta = 0$, where the sediment level is flush with the surface of the scour protection, also seen in Fig. 3.19e. The winnowing/deposition pattern inside the scour protection shown in Fig. 3.19 is practically symmetric around the pile as $\beta = \pi \rightarrow 2\pi$. Note that the sinking of the scour protection at the equilibrium stage was measured during the entire current scour test campaign reported in Table 3.1, and the results agree well with the findings of Nielsen et al. (2011) and more recently in Sumer and Nielsen (2013).

The latter mentioned ridge is present from the pile base extending through the scour protection into the downstream scour hole. In Fig. 3.17 and Fig. 3.18 the small scale ripples alongside the ridge is observed, with the ripple crest bending towards the ridge, showing the sediment transport direction in the downstream scour hole as previously described. The formation of small scale ripples developing in the downstream scour hole was also observed and described in the case of an unprotected bottom-mounted pile and is clearly visible in Fig. 32 in Roulund et al. (2005). The ripples show the same formation patterns as in the present study and also a somewhat smaller ridge at the downstream centerline is visible from this figure. Observing Fig. 31a-g in the latter mentioned study, the formation of the ridge and the suspension of the scoured sediment at the downstream centerline along the crest of the ridge is visible, which is in accord the with description of the scour process in the present study.

3.4.2.2. Equilibrium Scour Depth in Steady Current

On dimensional grounds the equilibrium scour depth in the edge scour process in the near-field the scour protection, where sediment is removed from the upstream- to the transverse side of the berm, can be described by the following non-dimensional relation of the governing parameters:

$$\frac{S}{h_b} = f\left(\theta, \frac{w_b}{D_p}, \frac{h_b}{D_p}, \frac{h_b}{D_c}\right) \tag{3.22}$$

in which S is the near-field equilibrium scour depth here normalized by the berm height h_b, θ the Shields parameter, h_b/D_p is the berm-height-to-pile-size ratio and h_b/D_c is the berm-height-to-stone-size ratio, which in the present treatment corresponds to a surface roughness of the berm and the number of cover stone layers N or N_c in accord with previous works dealing with scour protections around OWT foundations (Nielsen et al (2013) and Nielsen et al. 2011).

Regarding the independent variables in Eq. (3.22):

1. θ is involved since it controls the sediment transport rate in the scour process
2. w_b/D_p is involved since it controls the width of the scour protection and thus the obstruction to the flow.
3. h_b/D_p is involved as it controls how much obstacle the berm is to the flow
4. h_b/D_c is involved in its function as a scalar for the surface roughness of the berm

Now, the equilibrium near field scour depth S (measured in zone 1 in Fig. 3.17 at the transverse side of the scour protection) normalized by the berm height h_b is grouped according to the berm-width-to-pile-size ratio w_b/D_p and plotted against the Shields parameter in Fig. 3.20. Fig. 3.20 shows the following:

1. The data reveals that there is a correspondence between the equilibrium scour depth S/h_b and the Shields parameter. With increasing Shields parameter the scour depth increases until it attains a constant level according to the value of w_b/D_p. Approaching the critical value for initiation of motion on the bed as $\theta \rightarrow \theta_{cr}$ the scour depth reduces. The latter behavior is expected since the sediment transport close to the berm is low and the trend agrees with the findings of Petersen et al. (2014) and Fredsøe et al. (2001) which involved scour alongside a berm without a pile and scour at a riprap revetment respectively. In the present treatment this corresponds to $w_b/D_p \rightarrow \infty$.
2. The data implies that the equilibrium scour depth is increased when $w_b/D_p < 3$. Obviously as the w_b/D_p decrease the flow deviation and acceleration at the side of

pile will influence the flow alongside the perimeter of the berm, forcing an increase in scour depth. This effect is in accord with the amplification of the bed shear stress presented in Fig. 3.16, where $w_b/D_p < 2.5-3$ forced an increase in both the amplification of the bed shear stress and the plan view extent over which the bed shear stress is amplified. This behavior is expected when $w_b/D_p \rightarrow 1$, i.e. pile alone setup without scour protection, where the equilibrium scour depth should increase to about 1.3 D_p (Sumer and Fredsøe , 2002).

3. Only the data for $h_b/D_p > 0$ (ie. $h_b \neq 0$) has been included in Fig. 3.20. The results for the $h_b/D_p = 0$ tests are indicated in Table 3.1. Now, Petersen et al. (2014) experimented with a berm installed flush with the initial sediment level, and as previously mentioned found that the turbulence generated around the individual stones at the edge of the berm was responsible for the scour with an equilibrium scour depth $S/D_c \sim 0.8$. for the present study that corresponds to $S \rightarrow D_c$ when $h_b \rightarrow 0$.

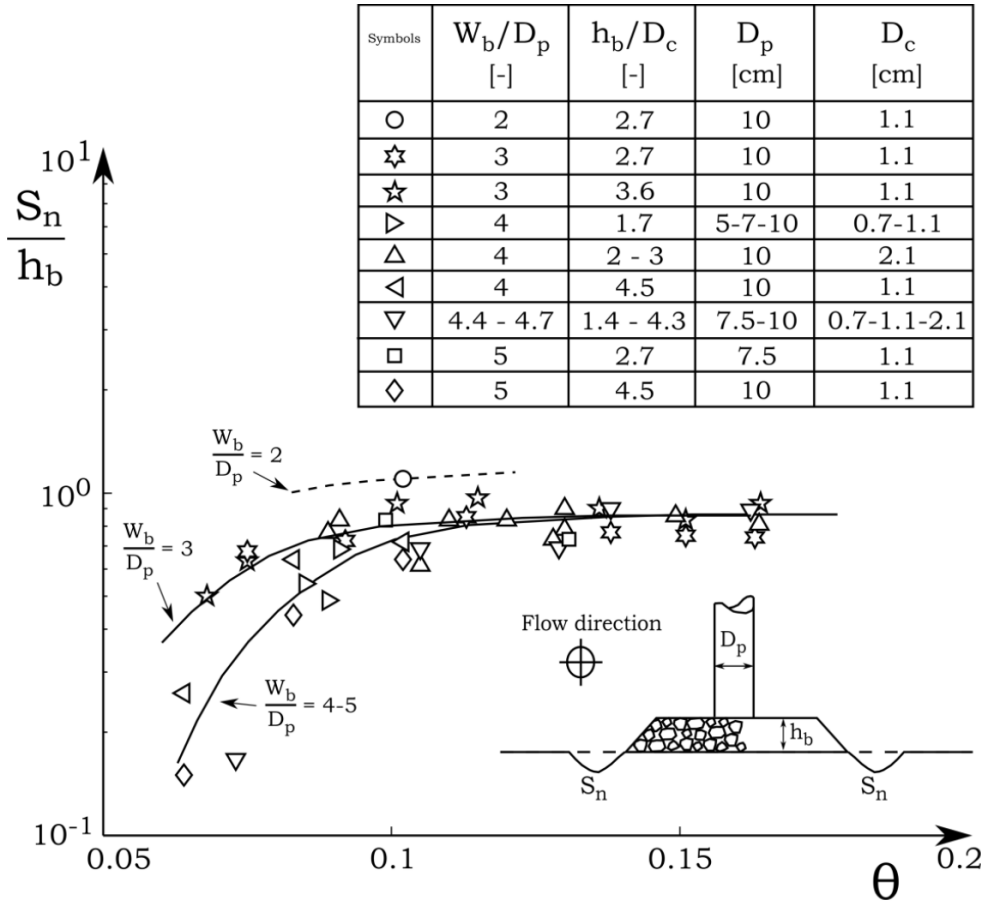

Figure 3.20. Normalized equilibrium near field scour depth at the transverse side of the scour protection in steady current (values are listed in Table 3.1). Live bed ($\theta > \theta_c$).

This agrees well with the present results for Test 17 -19, 22, 38 and 50-53 where S/D_c = 0.4 – 1.2. However the study of Petersen et al. (2014) comprised a two-dimensional setup, and for any practical treatment three-dimensional effects should be considered.

4. The data weakly indicates that there is a dependence to the parameter h_b/D_c. It is expected from the study of Petersen et al. (2014) that with $w_b/D_p \rightarrow \infty$ the surface roughness of the berm (D_c) should be the governing parameter for the scour process. This trend is observed in Fig. 3.20 for the data of w_b/D_p = 5 marked by squares and diamonds, here the scour depth slightly decreases from about $S_n/h_b \sim 0.8$ with $h_b/D_c = 2.7$ to $S_n/h_b \sim 0.65$ with $h_b/D_c = 4.5$. For the lower values of w_b/D_p there is no clear tendency to h_b/D_c and this supports the latter argument. However there is not enough data to support this conclusion.

The scour depth just upstream of the scour protection was measured in all the current experiments and the equilibrium scour depth here, S/h_b (see Fig. 3.1a), was between 0 and the values displayed in Fig. 3.20 for S/h_b. Note that these values are not represented in Table 3.1 for reasons of space.

Returning to the downstream scour the equilibrium scour depth on either side of the ridge can be expressed by following non-dimensional relationship between the governing parameters:

$$\frac{S}{D_p} = f(\theta, A_r, D_c/D_P) \tag{3.23}$$

In which S is the downstream scour depth, here normalized by the pile diameter D_p, $A_r = h_b/w_b$ is the berm-height-to-berm-width aspect ratio and D_c/D_p is the cover stone-size-to-pile-size ratio.

Regarding the independent variables in Eq. (3.23):

1. θ is involved as it controls the sediment transport rate in the scour process
2. A_r is involved since it scales the strength of the downstream counter-rotative vortices.
3. D_c/D_P represents the surface roughness of the berm

Fig. 3.21 displays the equilibrium scour depth S normalized by the pile diameter D_p is plotted against the Shields parameter and grouped according to the aspect ratio A_r.

1. The data presented in Fig. 3.21 show that the equilibrium scour depth S_d/D_p attains a constant level with increasing Shields parameters.
2. The data shown in Fig. 3.21 further implies a significant correlation between the equilibrium scour depth and the berm-height-to-berm-width ratio A_r. As A_r increases the scour depth increases as well. From the flow analysis made in the previous

sections it is obvious that both the berm and the pile strongly disturb the incoming flow with flow deviation and acceleration at the sides of the berm and the pile, and a recovery zone downstream. As A_r increases this effect becomes stronger and the near bed wake zone downstream of the structure is more developed. Hence the downstream convergence of the streamlines towards the centerline grows in strength supporting the two symmetric counter-rotative vortices. The increasing scour depth with A_r is in accord with previous studies on scour around an unprotected bottom-mounted pile with changing pile-height-to-pile-diameter ratio by DHI/Snamprogetti (1992) also presented in Sumer and Fredsøe (2002) and more recently in Zhao et al. (2010). Further in agreement with

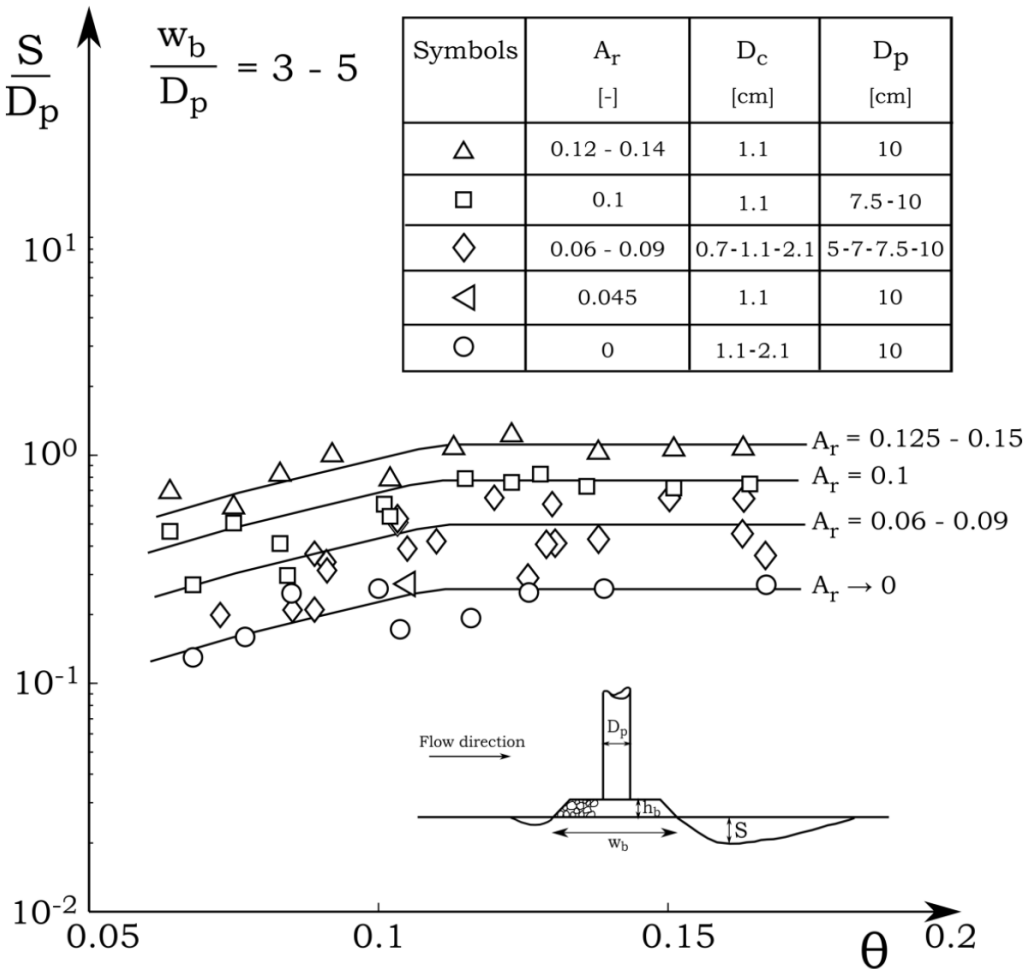

Figure 3.21. Normalized equilibrium scour depth downstream of scour protection in steady current (values listed in Table 1). Live bed ($\theta > \theta_c$). Here the aspect ratio $A_r = \frac{h_b}{w_b}$.

similar studies on spud can scour, considering an increase in the penetration of the spud can yields a lower scour depth (e.g. in Raaijmakers et al., 2013).

Fig. 3.21 does not indicate the influence of a change in the surface roughness of the berm here expressed by the parameter D_c/D_p. In Table 3.1 the test with A_r = 0.06 – 0.09 and D_c/D_p = 0.24 show a slightly lower equilibrium scour depth than those for A_r = 0.06 – 0.09 and D_c/D_p = 0.11. The latter behavior is caused by two effects: (1) the retardation of the converging flow downstream of the structure with increasing surface roughness, which in turn results in a lower vorticity for the downstream vortex pair. Visual observations and the corresponding measured bed-profile for the equilibrium stage of the scour tests show that the width of the ridge at the foot of the scour protection increases with D_c/D_p, which supports the latter statement; and (2) the deformation and sinking of the stones in the upstream side of the pile base explained by Nielsen et al. (2011) causes a slight elevation of the counter-rotating vortex pair, and in turn a reduction in the equilibrium scour depth. Obviously the latter effect diminishes if the upstream sinking of the stone layer is reduced by an properly designed filter layer, in Test 82 (with D_c/D_p = 0.24, see Table 3.4) a filter layer is installed beneath the cover stones and the equilibrium scour depth reaches a maximum which are comparable with test with a lower D_c/D_p for the same A_r plotted in Fig. 3.21. The latter argument suggests that the effect of (2) has a stronger influence on the formation of the counter-rotating vortices, however both effects have been observed in the present study.

3.4.2.3. Length of the Scour Hole in Steady Current

Fig. 3.22 presents the equilibrium downstream scour hole length L_s associated with the scour experiments presented in the previous paragraph. In which L_s is the length measured from the center of the pile to the end of the scour hole (see Fig. 3.1a and the definition sketch in Fig. 3.22). The equilibrium scour hole length can be expressed by following non-dimensional relation:

$$\frac{L_s}{w_b} = f(\theta, A_r) \tag{3.24}$$

The following is true in Eq. (3.24): (1) θ (or U_f) is involved because it controls the streamwise lifespan of the downstream counter-rotating vortices in the near bed domain and (2) A_r is involved because it controls how much the berm obstructs the flow. As seen from Fig. 3.22 the length of the scour hole increases monotonously with increasing θ until it attains a constant level of about 3.2 – 3.5w_b. The figure further shows that the data for L_s/w_b practically collapse onto a line when $A_r > 0$ (which in the present treatment corresponds to $h_b > 0$ with $w_b/D_p = 2 - 5$), and when $A_r = 0$ ($h_b = 0$) the scour hole length L_s/w_b attains a somewhat lower level. The latter effects are caused by the berms influence to the downstream vortices as mentioned in the previous section on scour depth.

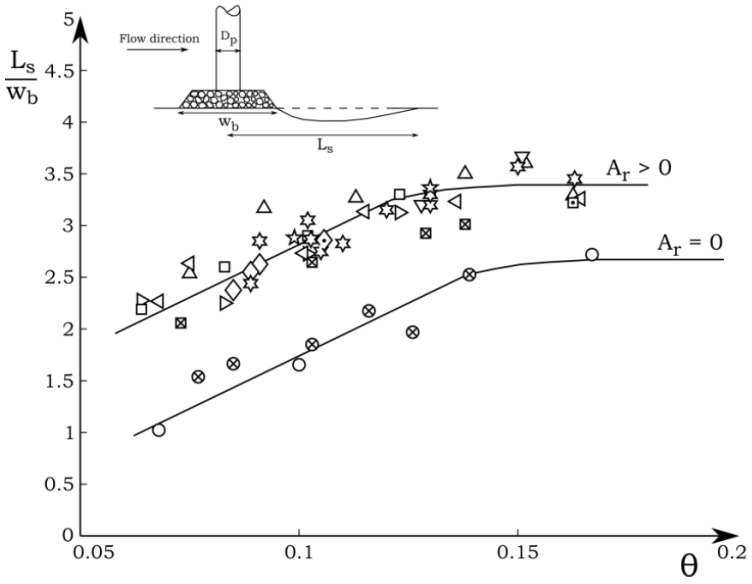

Symbols	A_r [-]	w_b/D_p [-]	D_p [cm]	D_c [cm]
△	0.13	3	10	1.1
▷	0.13	4	10	1.1
◁	0.1	3	10	1.1
▽	0.1	4	7.5-10	1.1
□	0.1	5	10	1.1
⊠	0.09	4.7	7.5	0.7 - 2.1
◇	0.09	4	10	2.1
☆	0.08	5	7.5	1.1
✡	0.08	4	5-7-10	1.1
⊡	0.07	4.4	10	1.1
◈	0.05	4.4	10	1.1
○	0	4.6	10	1.1
⊗	0	4	7.5-10	1.1 - 2.1

Figure 3.22. Normalized length of the downstream scour hole in steady current. Live bed ($\theta > \theta_c$).

3.4.2.4. Time Scale of the Scour Process in Steady Current

Fig. 3.23a displays the time series of the depth of the scour hole monitored at in the downstream scour hole where the maximum scour depth is experienced in concurrence with Fig. 3.17 (Test 23). As seen from Fig. 3.23 the scour depth attains its equilibrium value, *S*, through a transitional period. It is seen that for a substantial amount of scour to happen a certain amount of time must elapse. The following definition will be adopted in the present treatment

$$S_t = S\left(1 - exp\left(-\frac{t}{T}\right)\right) \tag{3.25}$$

in which T is termed the time scale of scour, and the time scale in Eq. (3.25) may be defined by following equation:

$$T = \frac{1}{S}\int_0^\infty (S - S_t)\, dt \tag{3.26}$$

In Fig. 3.23b the corresponding time series of scour depth at the transverse side of the scour protection is illustrated. As previously mentioned the time scale of scour for near-filed domain reaches its equilibrium in O(½T), in which T is taken from the time development of the downstream scour hole. The time development of the scour hole in the near-field domain was only monitored for the first 23 tests and no further remarks are made with respect to the time development of scour in the near-field domain.

As seen from Fig. 3.23a-b the motion of ripples over the measurement area, as mentioned previously, causes fluctuations as the scour process develops towards the equilibrium stage, where the fluctuations continue. This trend was also observed in edge scour alongside a submerged berm by Petersen et al. (2014). In accord with this study the time scale of the scour process was obtained from the scour-depth-versus-time series, using the area method according to the definition in Eq. (3.25) and Fig. 3.23. The data are included in Table 3.1.

On dimensional grounds the time scale can be written in the following non-dimensional functional form:

$$T^* = f(\theta, A_r) \tag{3.27}$$

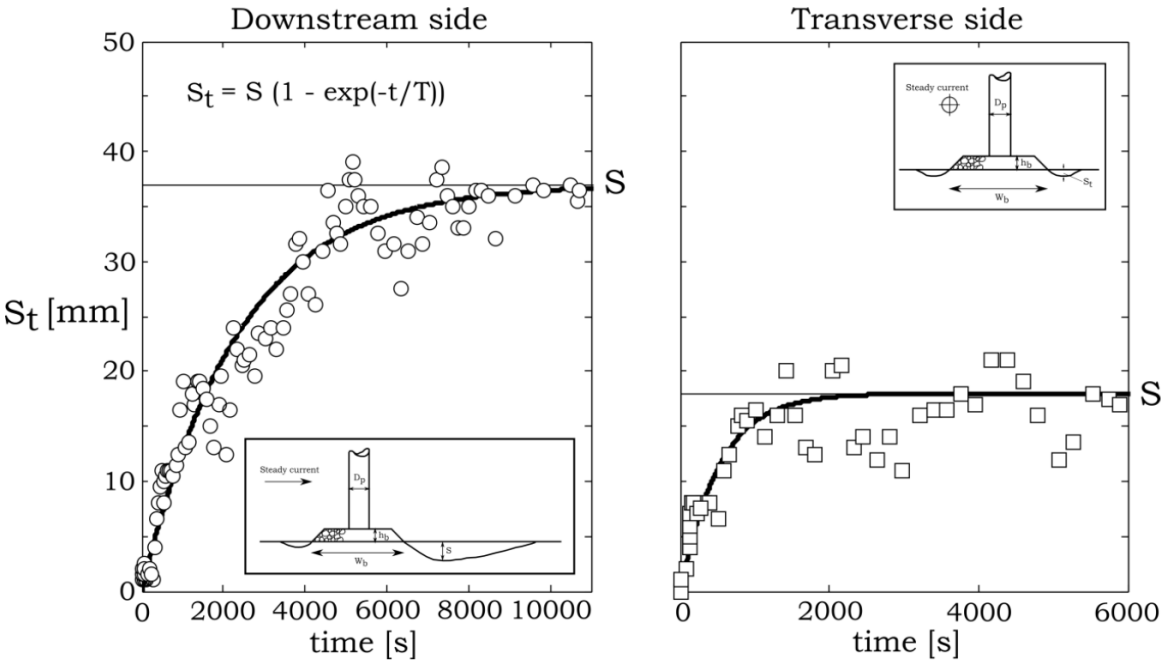

Figure 3.23. Time series of the scour depth monitored at the following positions: (a) at the maximum point of the downstream scour hole; (b) 5cm off the edge at the transverse side of the scour protection (Test 23).

in which T^* is the normalized time scale defined by Eq. (3.7), θ is involved because the time scale is governed by the sediment transport in the scour process in agreement with previous works on scour at berms (Petersen et al.,2014) and at unprotected piles (Sumer et al., 1992), and A_r is involved as it controls the strength of the counter-rotating vortices in the near-bed wake zone.

The time scale data corresponding to the scour process downstream are plotted in Fig. 3.24. First of all, Fig. 3.24 show that the time scale decreases with increasing θ. This is because, the larger the value of θ, the larger the sediment transport rate, and therefore the scour process happens faster. Secondly, from the data given in Fig. 3.24 collocated with that given in Fig. 3.21, one should expect an increase in the time scale T^* with increasing A_r. The latter effect attributed to the fact that the volume of sediment to be eroded increases with increasing A_r.

However, from the data given in Fig. 3.24 no clear influence of A_r on the time development of scour is observed, and this is attributed to the nature of the semi-dynamic pile and scour protection setup, where the scour protection at the base of the pile is allowed to deform during the scour process. Obviously, the latter effect disturbs the

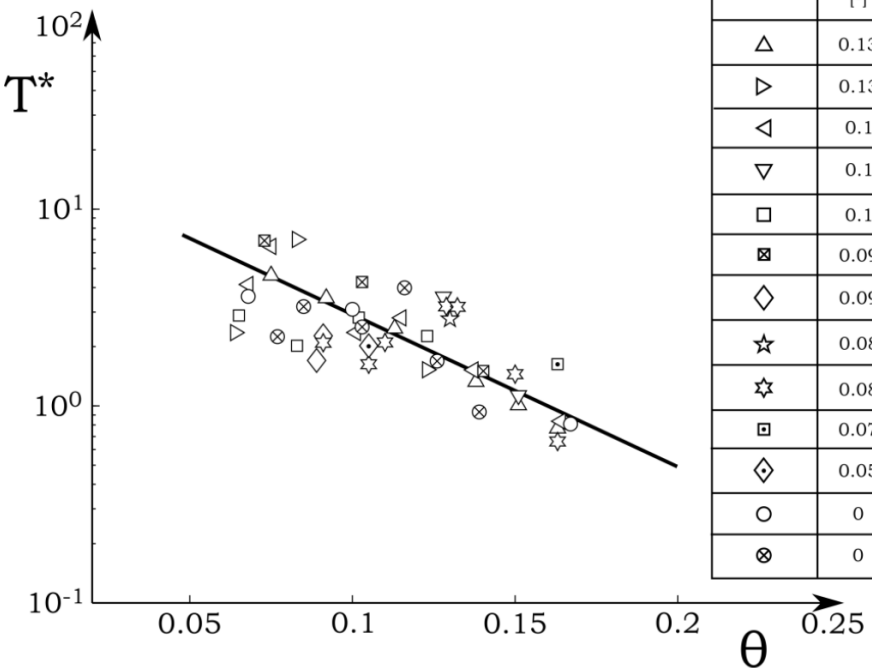

Symbols	A_r [-]	w_b/D_p [-]	D_p [cm]	D_c [cm]
△	0.13	3	10	1.1
▷	0.13	4	10	1.1
◁	0.1	3	10	1.1
▽	0.1	4	7.5-10	1.1
□	0.1	5	10	1.1
⊠	0.09	4.7	7.5	0.7 - 2.1
◇	0.09	4	10	2.1
☆	0.08	5	7.5	1.1
✡	0.08	4	5-7-10	1.1
⊡	0.07	4.4	10	1.1
⨀	0.05	4.4	10	1.1
○	0	4.6	10	1.1
⊗	0	4	7.5-10	1.1 - 2.1

Figure 3.24. Normalized time scale of scour downstream of the bottom-mounted cylinder with scour protection. Live bed ($\theta > \theta_c$).

collection of data, as the downstream scour pattern is heavily influenced by the shape of the scour protection with respect to the exact location of the maximum scour. Ideally, the exact location of the maximum scour should be identified for each time step and logged to determine the time scale of scour. This was practically impossible to achieve with the given setup, were the measuremenst of the scour depth time series was made on fixed pins, as described previously. Still, Fig. 3.24 indicates the O(T^*) which can be used to estimate the time development for practical purposes.

3.4.2.5. Equilibrium Scour Depth in Combined Current and Waves

The equilibrium scour depth obtained from the present experiments in combined waves and current is plotted in Fig. 3.25 as function of the parameter U_{cw}. Note that tests have not been reported for $U_{cw} <$ O(0.35) because of experimental constraints. Firstly, in the fundamental case of waves alone ($U_{cw} = 0$) the mechanism causing the edge scour was flawed by the nature of the wave flow environment in the flume facility. Here the steady streaming in the wave boundary layer and the wave drift (both are in the streamwise direction) enforce an equal return current (opposed to the streamwise direction), and the latter behavior showed to have an effect on the scour mechanism and in turn the measured scour patterns. Obviously,

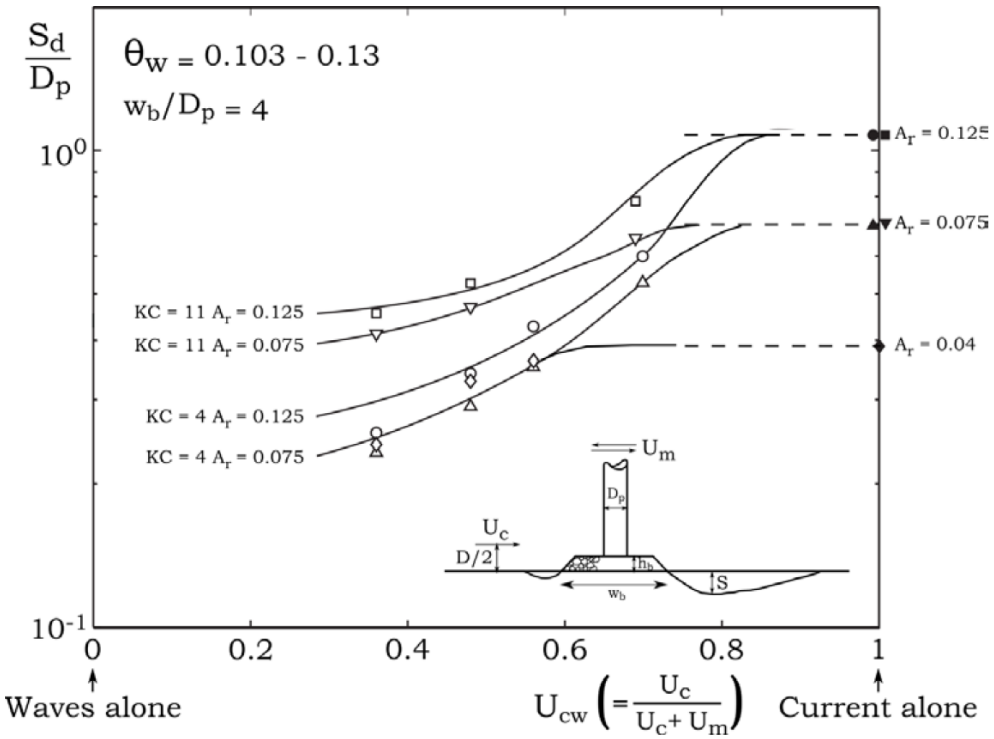

Figure 3.25. Normalized equilibrium scour depth downstream of scour protection in combined current and waves. Test 56 - 75, Table 3.2. Live bed ($\theta > \theta_c$).

such a return current is not observed in practical applications where the three-dimensionalities of the surrounding environment in most cases diminish any return current. Secondly, for tests with values of O(0.1) < U_{cw}< O(0.35), very small current velocity was required, which in the given setup was impossible to achieve and maintain.

The following conclusions can be inferred from the data plotted in Fig. 3.25:

- The equilibrium normalized scour depth S_d/D_p goes the values indicated by the filled markers (current alone values taken from Fig. 21) as the parameter $U_{cw} \to 1$, whereas it decreases significantly when $U_{cw} \to 0$.

- It is seen from Fig. 3.25 that the effect of A_r on the equilibrium scour depth in the current alone case, is also observed for lower values of U_{cw}, however the effect is not as dominant as for the current alone case, implied on the right vertical axis.

- The data in Fig. 3.25 indicates that even for larger values of U_{cw} even a slight wave superimposed on the current will reduce the scour depth. Also implied in the figure is the effect of the KC number (where the KC number is defined for the wave alone case by Eq. (3.11). Clearly, for the narrow range of KC numbers given in the figure (note w_b/D_p = 4), the vortex shedding from the pile has little implications for the sediment transport at the edge of the scour protection. Hence the KC number, for the present treatment, is interpreted as a scalar for the disturbance of the downstream wake and the counter-rotating vortices by the oscillatory motion imposed by the waves. The latter effect is in accord with the data given in Fig. 3.25 which shows an increasing scour depth with increasing KC number. Further the effect of the KC number diminish for large values U_{cw} > 0.7 where the downstream wake seems unaffected by the wave motion. The latter effect is in accord with previous studies on scour around a pile in combined wave and current by Sumer and Fredsøe (2001), Petersen et al. (2012b) and in the case of backfilling of scour holes around piles by Sumer et al. (2013).

Note that the present studies comprise waves propagating unidirectional with the current, and changes with respect to the footprint of the scour hole might occur if the direction of the waves are altered. Remark the selection of U_c taken at y = D/2 from the bed (in favor of the depth-averaged-velocity V or the bed friction velocity U_f) is made in accord with previous studies of the account (Sumer et al. (2001), Petersen et al. (2012b) and Sumer et al. (2013)), to give the best representation of the near-bed current velocity at various water depth. However, in the recent study by Sumer et al. (2013) for large piles the U_c at y = D/10 from the bed was chosen as an adequate measure. From Fig. 10 in the latter mentioned study the two approaches seem to conform, and hence the exact definition of U_c is considered to be a matter of convention.

3.4.2.6. Equilibrium Scour Depth in Simulated Tidal Current

Now, the present experiments with the edge scour generated by tidal current are discussed. Note that the half-period of the tidal cycle (see Fig. 3.5) was smaller than the time scale of scour ($T_{tidal}/2 \ll$ T, in which T is the time scale of scour indicated in Table 3.3), and the Shields parameter for each half-period is uniform. The aforementioned effects will have the following observed implications for the scour development:

1. The inversion of the current happens before the scour hole on the downstream side reaches its equilibrium, and at every reversal of the current downstream side scour and upstream accretion by backfill was observed. Clearly, with this behavior, the scour hole will attain its equilibrium over a number of tide cycles.

2. The equilibrium scour hole upstream and downstream is practically symmetrical with respect to depth and plan view extent, and the previously mentioned two-legged scour hole with the ridge in-between appears on both sides of the scour protection. This is attributed to the fact the time scale of scour is long compared with the half period of the tide cycle. It is expected that an asymmetric scour pattern will be more pronounced in the case where $T_{tidal}/2 \gg$ T. The latter two statements are in accord with the conclusions made in the study of Margheritini et al. (2006).

3. The designated near-field- and downstream scour hole (in the previous section on scour in steady current) coalescence; the downstream scour hole is "pushed" closer to the edge of the scour protection and the lateral scour hole grows as the current reverses. Now the radial distance to the deepest point of the scour hole r = [3.1 3.1 3.4] $\cdot D_p$ respectively for Test 76, 77 and 78.

4. The length of the scour hole (indicated in Table 3.3) decreases slightly from the estimated values in Fig. 3.22 which is expected from the nature of the scour development described in bullet item 1 and 3.

Fig. 3.26 displays the equilibrium normalized scour depth S_d/D_p in the simulated tidal current, comprising a range of KC number from 468 - 3744 (with the KC number defined in Fig. 3.5 and Eq. (3.2)). The following conclusions can be deduced from Fig. 3.26 and the listed values in Table 3.3:

- The present data in Fig. 3.26 reveals that the S_d/D_p for the tidal current scour depth attends to the values for steady current shown by the filled marker (steady current values taken from Fig. 3.21) irrespective of the KC number. This result is attributed to the constant presence of the counter-rotating vortices at the downstream side of the pile and scour protection. Clearly the trailing vortex pair remains unaffected in each half-period of the tide motion, scouring the adjacent sea bed with equal potential on the downstream side of the scour protection. The agreement in scour depth obtained in a steady current or tidal current flow climate has also been observed in the case of an unprotected monopole in the study of Margheritini et al. (2006) and indicated by Sumer and Fredsøe (2002).

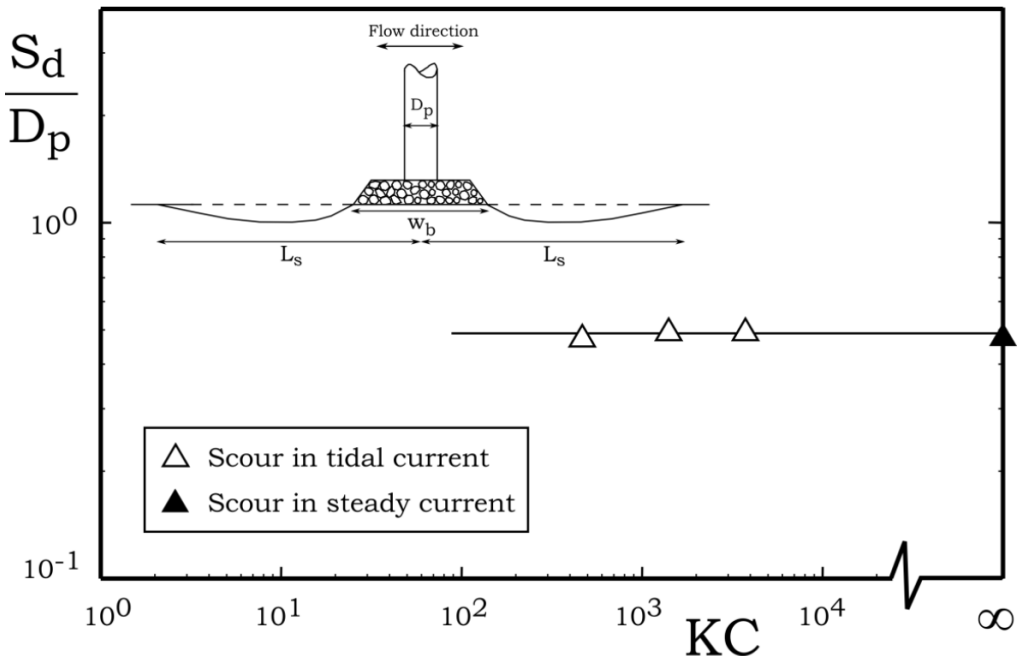

Figure 3.25. Normalized equilibrium scour depth downstream of scour protection in combined current and waves. Test 56 - 75, Table 3.2. Live bed ($\theta > \theta_c$).

3.4.2.7. Equilibrium Scour Depth with Elongated Filter Layer

A well-known principle, to reduce the edge scour and/or stabilize the scour hole, is to install a filter layer with an exposed part extending beyond the perimeter of the armour layer (Sumer and Fredsøe, 2002). As the edge scour develops the stones in the exposed filter slump into the scour hole and forms a protective slope, a falling apron.

The effect of applying a partial and asymmetric falling apron is investigated in the present study, with the exposed filter layer mainly in the downstream direction according to the definition sketch in Fig. 3.7 and Fig. 3.27. The expected reduction in the edge scour depth is achieved by a two-fold reason : (1) the exposed filter layer covers and protects the previously erodible sea bed downstream of the scour protection; (2) the erodible part of the downstream sea bed are located further downstream in the wake, where the counter-rotating vortices are weaker (the flow has recovered to a greater extent), in accord with Fig. 3.13.

Now, Fig. 3.27 shows the equilibrium scour depth S_d downstream of the pile and scour protection plotted against the exposed length of the filter layer. The following can be deduced from Fig. 3.27:

- The equilibrium downstream scour depth reduces with increasing L_f/D_p. The reduction is in accord with item 1 and 2 in the above description, and further in accord with the decreasing scour depth with the A_r described in conjunction with Fig.

3.21 and scour in steady current. Clearly, extending the filter beyond the armour in the present setup has the same effect as a decreasing A_r with a wider armour layer.

- The largest reduction in the equilibrium scour depth is achieved for $L_f/D_p < 1.5$, for larger values of L_f/D_p the S/D_p show an asymptotic behavior.
- The filter layer has no effect on the edge scour when $L_f/D_p \to 0$, here the scour depth collapses with value taken from Fig. 3.21 (filled marker on the vertical axis in Fig. 3.27).

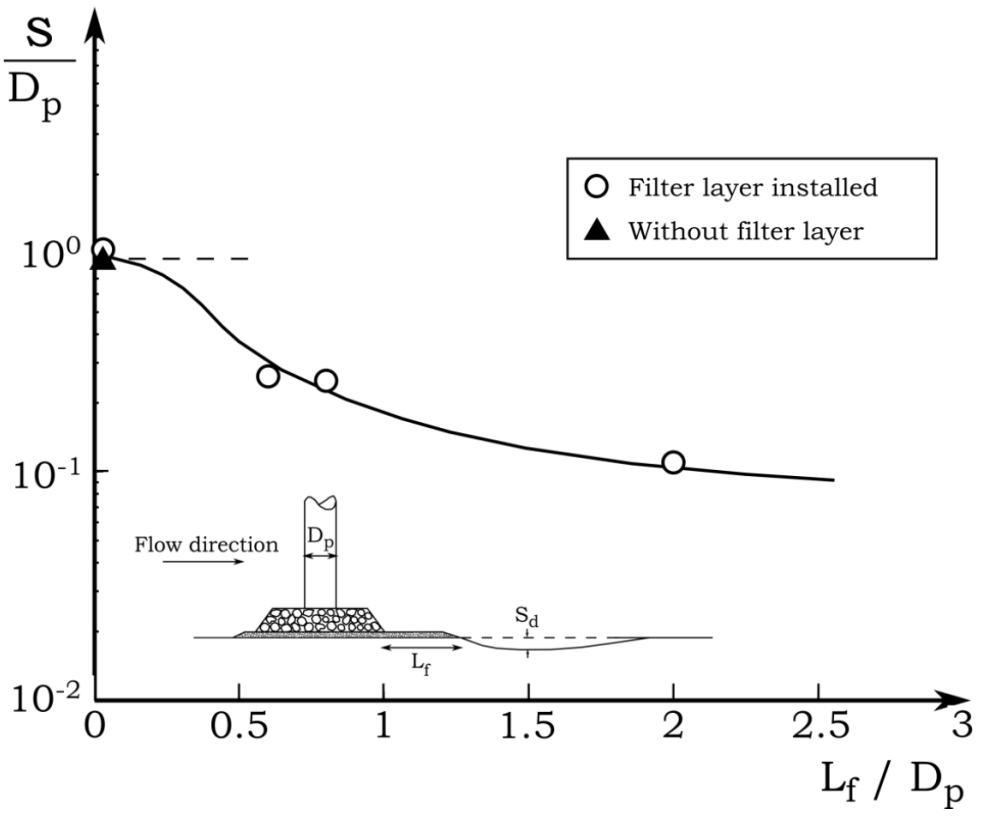

Figure 3.27. Normalized equilibrium scour depth downstream of scour protection with filter layer extending beyond the armour layer in steady current. Test 79 – 82, Table 3.4. Live bed ($\theta > \theta_c$).

3.5. Experience from Sites with Scour Protection Installed

Scour protection with rock armour are almost invariably installed at offshore wind turbine foundations; Horns Rev 1 OWF (Hansen et al., 2007), Egmond aan Zee OWF (Raaijmakers et al., 2007 and Louwersheimer et al., 2009), Scroby Sands OWF and Arklow Bank OWF (Whitehouse et al., 2011) to mention a few examples. (We may note an installation with no rock protection is also a viable option, Wittrup, 2012).

Two approaches of installing the scour protection systems are prevailing in these windfarms: (1) rock armour is placed around the foundation on top of a pre-installed filter layer; and (2) rock is placed in a previously generated scour hole around the foundation, a method preferred, for the most part, for very shallow waters to avoid "blockage" caused by the installed protection structure. It seems from previous reports that secondary scour or edge scour is experienced for both types of applications, and a detailed account on the topic is given in Whitehouse et al. 2011.

In the present investigation the authors selected to focus on two wind farms: (1) Egmond aan Zee OWF where the installed scour protection was made of rock armour on top of a pre-installed filter layer; and, to a smaller extent, (2) Scroby Sands OWF where rock is placed in a previously generated scour hole. Focus will be on the edge scour development and the magnitude of the edge scour depth.

3.5.1. Offshore Windpark Egmond aan Zee

3.5.1.1. Local Conditions and Installed Scour Protections

Several studies, such as Raaijmakers et al. (2007), Raaijmakers et al. (2010) and Whitehouse et al (2011), have reported on scour development at the Offshore Windpark Egmond aan Zee (OWEZ), and this section describes the local conditions and installed scour protections and the edge scour development in the period 2006-2013.

OWEZ is the first offshore wind farm in The Netherlands constructed in 2006, located about 10 to 18 km off the coast of Egmond aan Zee. OWEZ consists of 36 wind turbines with a distance in between from 140 D_p to 220 D_p (Simoons, 2012), and with a water depth range of 16 m to 21 m over the site. The turbines are founded on monopiles with a diameter D_p = 4.6 m (see Fig. 3.28), driven into the seabed consisting of fine sands with d_{50} = 0.25 mm. The scour protection comprises two layers of stone material; (1) a filter layer with a thickness of 0.4 m consisting of stones the size $D_{f,50}$ = 0.05 m; and (2) an amour layer on top of the filter layer with a minimum thickness of 1.4 m comprising cover stones the size $D_{c,50}$ = 0.4 m. From design the filter layer was installed in a circular shape with a berm width (expressed as diameter) $w_b \sim 5.2D_p$, subsequently the monopile was driven through the filter layer and lastly the armour layer was applied by a grab crane to a berm width $w_b \sim 4D_p$ (measured at the top). A detailed description of the design and installation is given in Raaijmakers (2009) and Raaijmakers et al. (2010).

Since edge scour development is obviously not dependent on the design of the scour protection, but on the actual as-built scour protection, the presently available layout of the

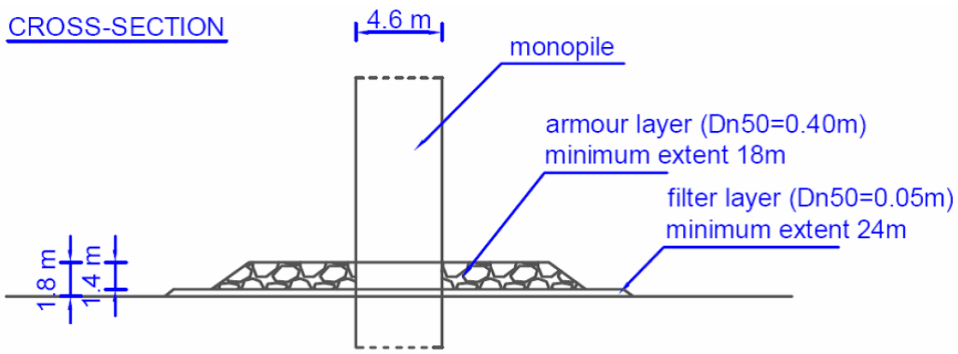

Figure 3.28. Design sketch of the scour protection system of OWEZ.

scour protection is plotted in Fig. 3.29. This figure shows that the present scour protection still meets the design requirements (while a gradual degradation of the scour protection each year was accounted for in design). The average armour layer thickness is estimated at 0.40-0.45D_p and the average filter layer thickness at 0.1D_p, although differences in filter layer thickness occur between the different radial sectors due to the materializing falling apron effect (see below).

The environmental conditions at OWEZ are dominated by tidal current with a main tidal direction of north-northeast (23˚N) during flood and south-southwest (203˚N) during ebb, see the actual tidal current rose for OWEZ in Fig. 3.30. The tide is characterized by a tidal asymmetry with a mean depth-averaged amplitude of the flood velocity of about 0.5m/s against an ebb velocity of 0.43 m/s, resulting in a tidal asymmetry factor of 1.15. The maximum recorded amplitude of the depth-averaged velocity in the direction of the flood current is 1.31m/s against 0.91m/s in the direction of the ebb current, resulting in a factor of 1.44.

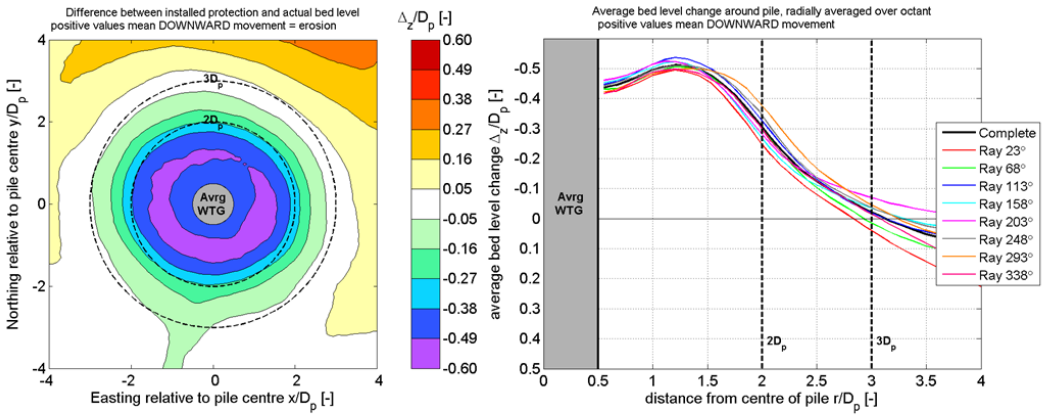

Figure 3.29. (Left) A filled contour plot of the average bed level change between 2013 and 2006, illustrating the present scour protection layout; (right) radially averaged rays over 45°-sectors, showing the armour layer within $r \leq 2D_p$ and the filter layer extending beyond the armour layer between $2D_p \leq r \leq 3D_p$. Courtesy of Nordzeewind, a 50/50 joint venture of Shell and NUON.

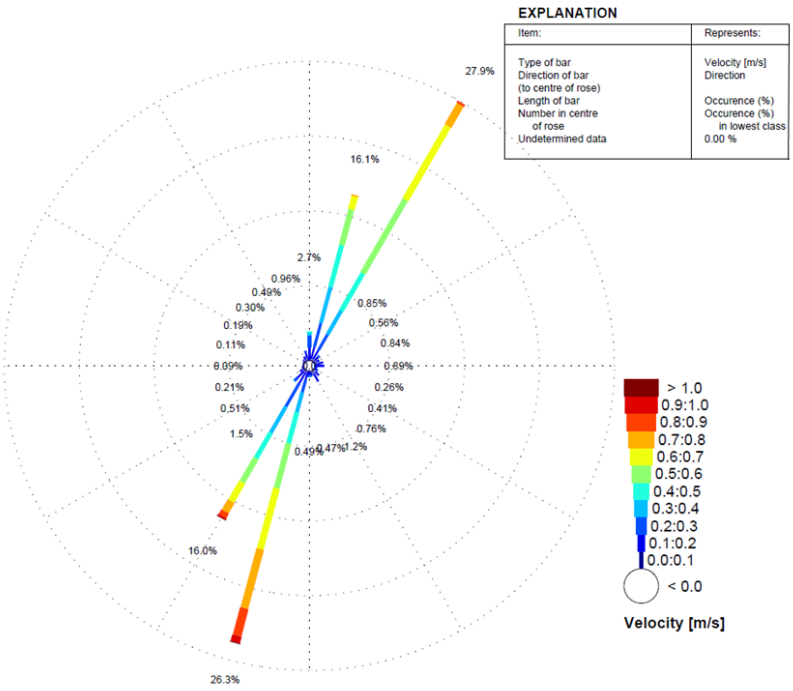

Figure 3.30. Environmental conditions at OWEZ, current rose.

Clearly, OWEZ is experiencing waves coming in from the North Sea (from southwest to north-northwest direction), and especially during large storms the effect of waves cannot be omitted in the developing edge scour. However, for the present treatment the effect of waves and/or combined waves and current is neglected, as they are considered mainly to decrease the edge scour depth caused by the tidal current. This is further confirmed by the fact that the edge scour patterns perfectly align with the direction of the tidal current and show almost perfect symmetry along the tidal current axis. Since the governing direction of the bigger waves shows a clear difference from the tidal axis, the edge scour patterns would not be symmetrical in case effect of the wave action on the edge scour patterns would be considerable. It should, however, be noted that most survey campaigns are performed during the calmer summer months and that temporary distortion of the tidal-current-driven edge scour patterns by storm action cannot be excluded.

3.5.1.2. Edge Scour Development at OWEZ

Before, during and after construction bathymetrical surveys were conducted to accurately determine the as-built layouts. Since construction annual surveys were performed to evaluate the performance of the scour protection and to quantify the edge scour development. At

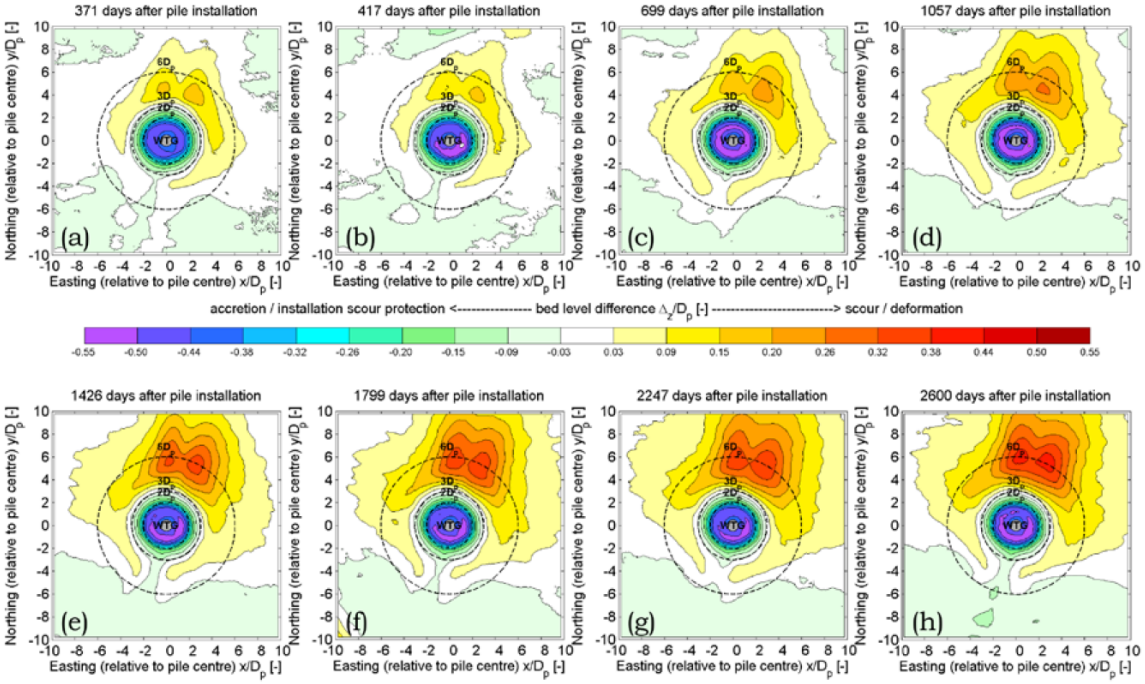

Figure 3.31. A filled contour plot of the average bed level change between 2006 and 2013, illustrating the developing edge scour (on average) through image a-h. Courtesy of Nordzeewind, a 50/50 joint venture of Shell and NUON.

present, the survey database contains a total of 403 surveys. The present section only details the average bed level changes around the scour protection (edge scour) over the aforementioned survey campaign running from 2006 - 2013.

The edge scour development will be described in reference to Fig. 3.31, which displays a sequence of the average bed level change following the installation of the armour layer in successive order. In this figure, the results of the 6^{th} to 13^{th} survey campaign are incorporated. Each subplot is computed by translating the horizontal survey coordinates to the pile centre and the vertical coordinates to the initial seabed level for each individual survey. Subsequently, the 36 surveys are normalized by dividing by the pile diameter and averaged, resulting in an average edge scour pattern for each year. In these figures downward movement (scour) is indicated by positive values. Note that the negative values close to the pile centre (within a circle of $3D_p$) represent the installed scour protections. The average number of days between pile installation and the survey is indicated in the title of each subplot.

The edge scour development around the perimeter of the scour protection is clearly visible in Fig. 3.31a-h in the region outside $3D_p$, and shows the following three distinct features, described below. (Note that these averaged plots clearly illustrate the patterns, but do not provide information on the edge scour distribution over the individual monopiles. Besides,

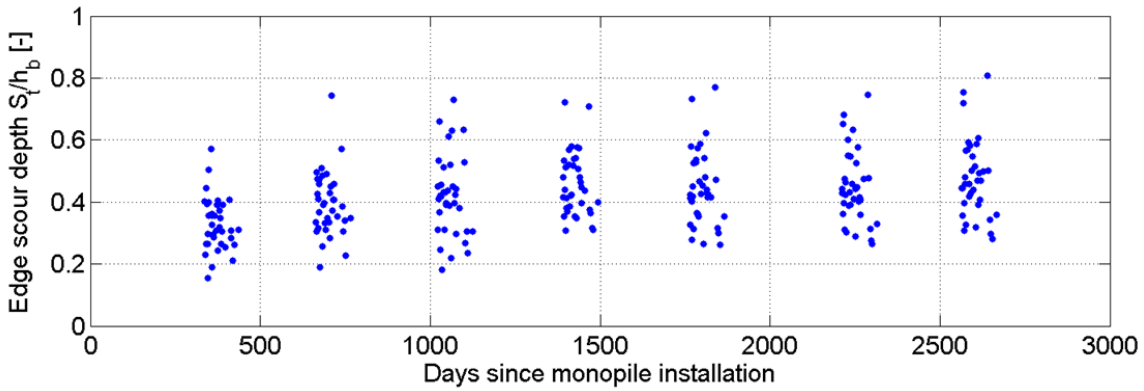

Figure 3.32. Maximum edge scour depth (local maxima) at the transverse sides for all 36 monopiles, normalized by h_b . Courtesy of Nordzeewind, a 50/50 joint venture of Shell and NUON.

the deepest edge scour depths are leveled out. Next, the individual edge scour values at the transverse and downstream sides will be discussed.):

(1) Edge scour happens from the upstream point to the transverse sides of the scour protection relative to the main tide direction (flood). Fig. 3.32 shows the time development of edge scour at the transverse side in Fig. 3.31 normalized by the berm height for the entire wind farm, with indices for each turbine (36 indices). Here the maximum edge scour depth is about $S = 0.3 – 0.8h_b$ (or 0.6 – 1.6 m) with an average scour depth about 0.5 h_b, the considerable scatter in Fig. 3.32 is attributed to the varying water depth over the site and in turn the varying current velocity. Obviously, as the edge scour seen at the transverse sides appears quite close the edge of the scour protection, some of the scatter in Fig. 3.32 also originates from the falling apron behaving differently for each turbine. From Fig. 3.20 the maximum edge scour depth at the transverse side can be estimated to be $S = 0.6 - 0.8h_b$ (with w_b/D_p = 4-5). Note, that a reduction in the edge scour depth is expected with an extension of the filter layer beyond the armour stones, which in OWEZ is $L_f/D_P \sim 0.65$, considering the knowledge obtained from Fig. 3.27. With this information it is concluded that the edge scour depth at the transverse sides is well predicted by Fig. 3.20. Further, note that the edge scour depth experienced (in Fig. 3.31a-h and Fig. 3.32) at the transverse side reaches its equilibrium stage relative faster than the downstream edge scour, which is in accord with the present experimental findings.

(2) A “two-legged” scour hole forms downstream to the main tide direction (flood) originating from the transverse sides of the scour protection (see Fig. 3.31). Fig. 3.33 shows the time development of scour in the downstream edge scour hole, similarly to Fig. 3.32 as explained previously, here normalized with the pile diameter. The deepest part of the (averaged) edge scour hole in Fig. 3.31 shown in Fig. 3.33 for each turbine reaches $S = 0.35 – 0.6D_p$ (or 1.6 – 2.8 m). From Fig. 3.21 the equilibrium edge scour depth in the downstream area is estimated $S/D_p = 0.95 – 1.1$ with $A_r \sim 0.12$ (A_r from Eq. (3.4)). From Fig. 3.27 a reduction of 0.45 S/D_p is

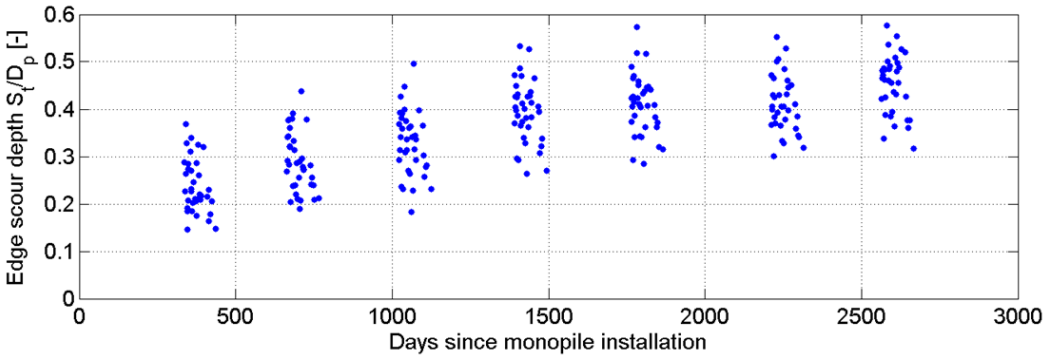

Figure 3.33. Maximum edge scour depth at downstream side for all 36 monopiles. Courtesy of Nordzeewind, a 50/50 joint venture of Shell and NUON.

obtained yielding an equilibrium scour depth $S/D_p = 0.4 – 0.5$ and this agrees well with the results displayed in Fig. 3.31g and Fig. 3.33. Note that the maximum equilibrium scour depth in Fig. 3.31 and Fig. 3.33 (downstream flood) remains practically unchanged in comparison with Fig. 3.17 and Fig. 3.21, while the plan view extent of the scour hole is highly affected by the asymmetrical tidal current experienced in practice. The first argument is supported by the explanations made in conjunction with Fig. 3.26, while the latter is expected from considerations on the sediment transport during each half cycle of the tidal motion. During flood the relatively higher velocities than during ebb, imply a far larger rate of general sediment transport in the far field of the pile, likewise in the near field where scour occurs. The latter effect has two governing implications on the formation of the edge scour hole: (a) the scour downstream of the flood direction happens faster, and therefore reaches a deeper scour during the half cycle of the flood; and (b) during flood the sediment from the far field backfills the upstream edge scour hole to a greater extent, than backfill experienced upstream during ebb. The latter remark is supported by the findings of Sumer et al. (2013, Fig. 11) which clearly show the decrease in the time scale of backfill for scour around piles with increasing Shields parameter and in turn the increased rate of sediment transport. Fig. 3.33 further indicates the time scale of the scour, and the scour process to be close to or at equilibrium during the last surveys. Comparing Fig. 3.32 and Fig. 3.33 one can observe the time scale of scour is relatively faster at the transverse side than in the downstream scour process, which is in agreement with the experimental findings.

(3) A ridge forms in the downstream (flood) edge scour hole, and shows in Fig. 3.31a-h as an elevated area in the scour hole along the right downstream centerline (flood). Note that the edge scour hole is practically symmetric about this line, which agrees with the experimental findings discussed in conjunction with Fig. 3.17. The sequence of images in Fig. 3.31a-h displays the average bed displacement over the ensemble of 36 wind turbines, and the indication of the ridge is somewhat leveled out for that reason. Therefore, also the three-dimensional bathymetry is plotted for an individual monopile in Fig. 3.34 which shows a typical edge scour pattern observed at OWEZ.

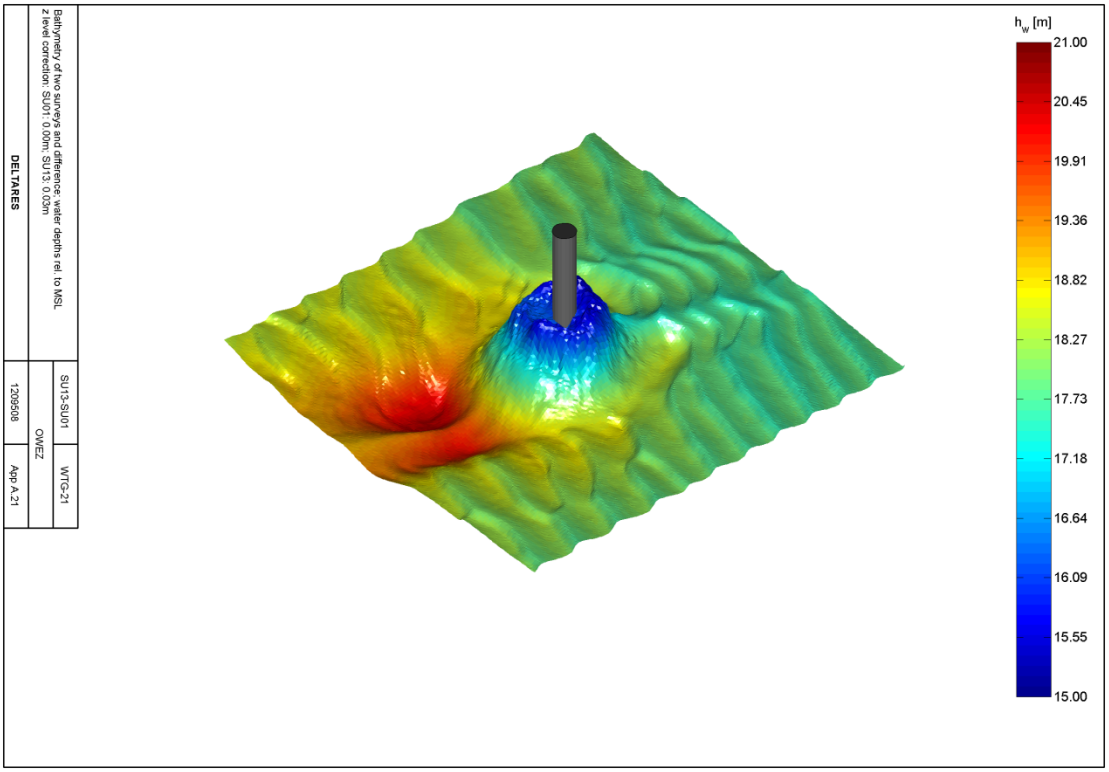

Figure 3.34. 3D-bathymetry around an individual monopile. In order to more clearly show the bed level elevations, the vertical axis is five times stretched, relative to the horizontal axis. Courtesy of Nordzeewind, a 50/50 joint venture of Shell and NUON.

This figure shows the water depth, obtained with multibeam, around the scour protection for a single monopile, and here the ridge is clearly visible on both sides of the scour protection. The latter statement supports the formation of the counter-rotating vortices for each half cycle of the tide motion, leaving the footprint as the two-legged scour hole with the ridge in between. Clearly, the tidal asymmetry causes the difference with respect to scour depth and plan view extent on either side of the scour protection, as previously mentioned.

Note that from the traces of the mega-ripples along the edge scour patterns in Fig. 3.34, one can observe the ripple crest bending towards the ridge. This is agreement with the experimental findings discussed in relation to Fig. 3.17 – 3.18. The shape of the mega ripples, with a steep and gentle side slope, indicates the direction of the dominant current, which is also the migration direction of the ripples: in this case the flood current is flowing from the top right to the bottom left of the figure. Further, note that due to the output resolution of the multibeam data (0.5x0.5m), the individual filter and armour rocks cannot be observed.

The downstream edge scour development in time is also demonstrated in Fig. 3.35. In this figure rays are plotted that have been calculated by radially averaging the bed levels in the

north-northeastern "octant" (between 0°N and 45°N, where edge scour is most severe) and averaging over all 36 monopiles in OWEZ. This plot nicely shows that in June 2006 all filter layers were installed, which did not yet have any effect on the surrounding seabed. Then shortly after another, the monopiles and the armour layer were installed and the survey of October 2006 shows a very small onset of edge scour at an extent between 3 and $6D_p$ from the pile centre. The next year, the initially loosely packed armour layer settled and the soil below compacted. Outside the scour protection edge scour development clearly started to develop with the deepest spot located at a distance of about $4.5*D_p$ from the pile centre (June 2007). In 2007 some additional armour rock was installed at a few monopiles, resulting in a slight increase of the average scour protection level (within $0.5\text{-}2.5D_p$) and from then on remaining at a rather constant level. Outside the scour protection, however, edge scour is continuously progressing. Although the increase in edge scour depth is slowing down.

In the previous figure, it was demonstrated that the maximum edge scour depth at the downstream side has more or less reached equilibrium. Since the filter material is launched by edge scour development (falling apron behavior) and will gather at the deepest location of the edge scour hole, and further increase of the scour hole mainly occurs in horizontal direction.

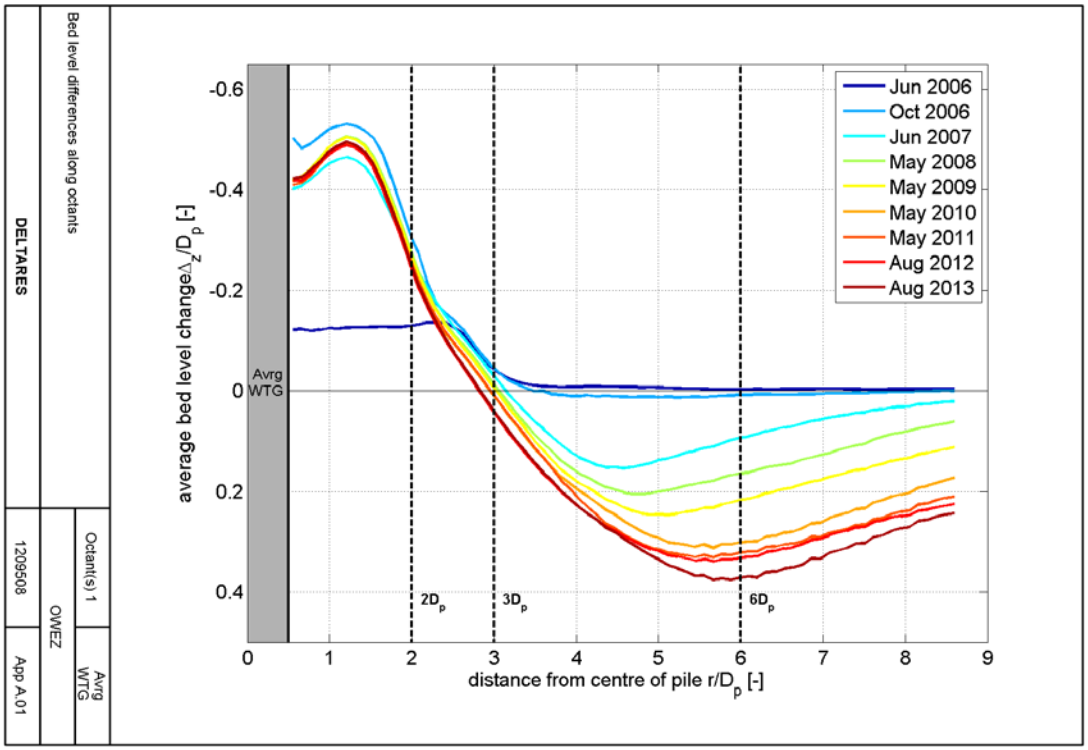

Figure 3.35. Edge scour development in time in NNE-octant (radially averaged over the area between 0°N and 45°N and averaged over all monopiles; normalized by the pile diameter)

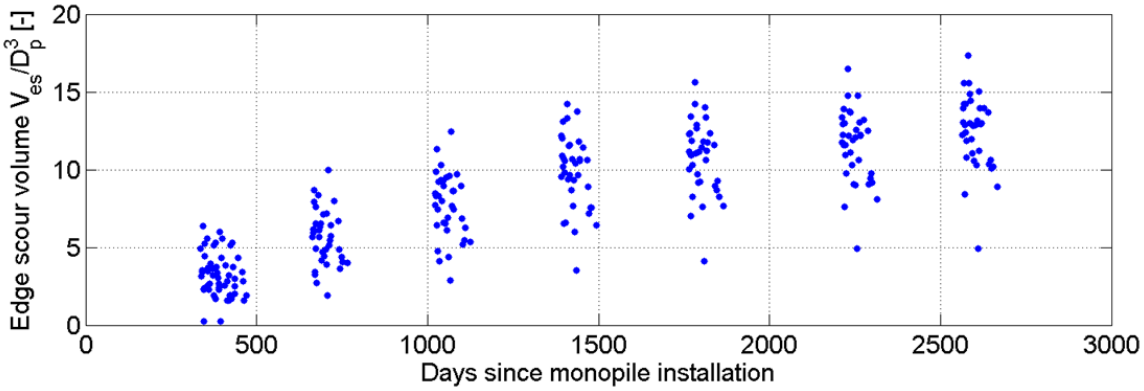

Figure 3.36: Edge scour development in time in NNE-octant (radially averaged over the area between 0°N and 45°N and averaged over all monopiles; normalized by the pile diameter)

Therefore, it is also relevant to know the volume of eroded seabed material in the sector between 315-45°N (clockwise) at a distance between 4-8D_p (note that the edge scour holes extend beyond r = 8D_p, but the multibeam surveys did not extend farther). The downstream scour volumes are normalized by D_p^3 (an equivalent cube with sides D_p) and plotted in Fig. 3.36. This figure shows that the downstream edge scour volume is still increasing, although the scour process is slowing down. Note that this "apparent" slowing down is partially caused by the chosen boundaries to compute the edge scour volume (both radially and the maximum distance from the pile of 8D_p). Since the main increase of the downstream edge scour hole occurs radially around the scour protection and farther away from the pile centre (r > 8D_p), it is very likely that the edge scour hole volume has not yet reached equilibrium. The clear outlier below the point cloud is related to a different extent of the filter layer and will be discussed below.

The edge scour depth at the transverse sides of the monopile is plotted in Fig. 3.37. Now the rays are calculated by radially averaging over the east-southeastern and west-northwestern octant (respectively between 90°N and 135°N and between 270°N and 315°N), which are located more or less perpendicular to the main tidal axis. The vertical values are now normalized by the average height of the scour protection between r = 0.5-2D_p (the area in which the armour layer is installed). This figure clearly shows that the transverse edge scour is not only less deep (about 0.2·h_b on average), but also that the development occurred faster with the profiles after 2009 almost collapsing to one line, as previously mentioned.

The development of the maximum transverse edge scour depths in these sectors with time was illustrated for all individual piles in Fig. 3.32. For all piles the averaged scour protection layer thickness was calculated (μ_{hb} = 2.06m; σ_{hb} = 0.12m). The maximum transverse edge scour depths range between 0.3 and 0.8h_b; the latter value was reported above to be the maximum value observed in the model tests (see Fig. 3.20 for w_b/D_p = 4). Note that the maximum transverse edge scour depths appear to be larger than the averaged profiles in Fig. 3.37. This is caused by the fact that maximum transverse edge scour depths occur very

locally and at different locations for all piles; these local maxima are leveled out in the averaging process.

A more accurate explanation of the edge scour depth variations at the individual monopiles can only be obtained by more extensive modeling of the current (the distribution over the OWEZ-area and the local details of the tidal asymmetry), the geology (the exact sediment parameters over the first few meters) and by including the falling apron behavior in more detail.

3.5.1.3. Effect of Elongated Filter Layer on Edge Scour Depth at OWEZ

To validate the effect of an elongated filter layer in the direction of the main tidal axis, a monopile is considered at which, erroneously, filter material was installed at the downstream side relative to the flood direction (see middle plot in Fig 3.38). To compare the effect of the elongated filter layer, the two neighbouring monopiles are also plotted. It can clearly be observed that the filter layer (with an average layer thickness of $0.13D_p$)

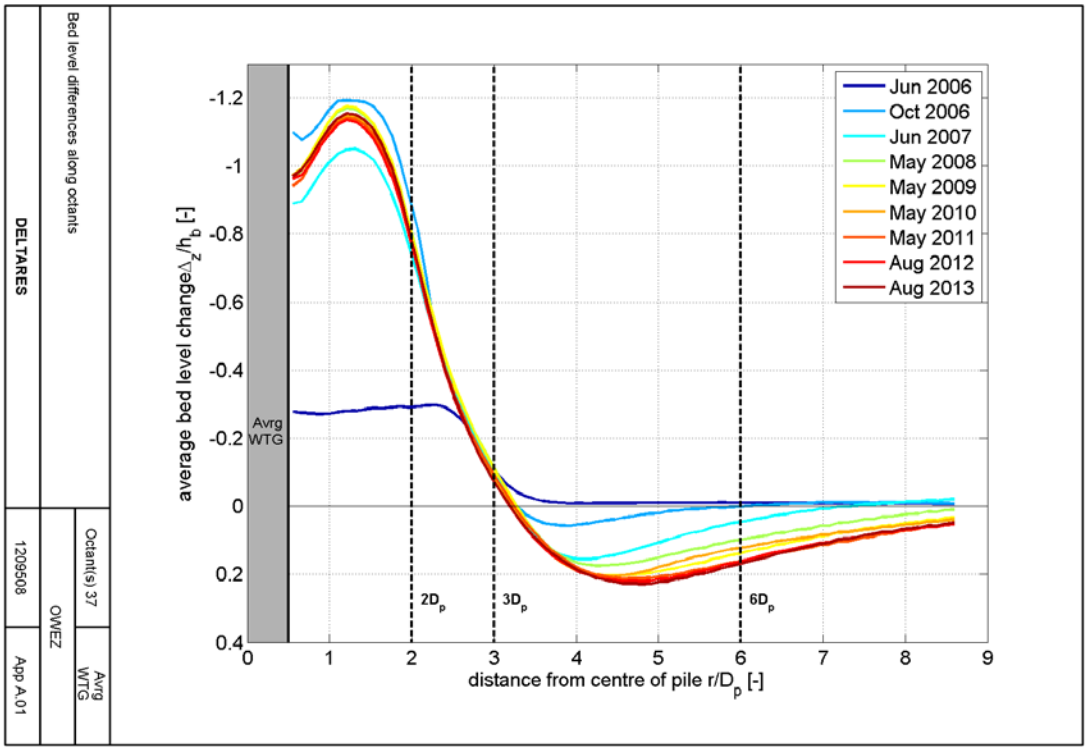

Figure 3.37. Edge scour development in time in NNE-octant (radially averaged over the area between 90°N and 135°N and between 270°N and 315°N and averaged over all monopiles; normalized by the average scour protection thickness within r = 0.5-2.0D_p)

extends to approximately $5D_p$ from the pile centre. Note that the filter layer was corrected before installation of the armour layer and that this monopile actually is equipped with the most effective scour protection against possible threats caused by edge scour development.

About 2600 days (just over 7 years) later, the effect on the downstream edge scour can clearly be seen in Fig. 3.39. The edge scour hole is smaller and less deep. At the transverse sides, also differences can be observed. At the eastern side where the filter layer blocked the flow, negligible scour occurred, while at the western side the transverse edge scour is similar to the neighbouring piles.

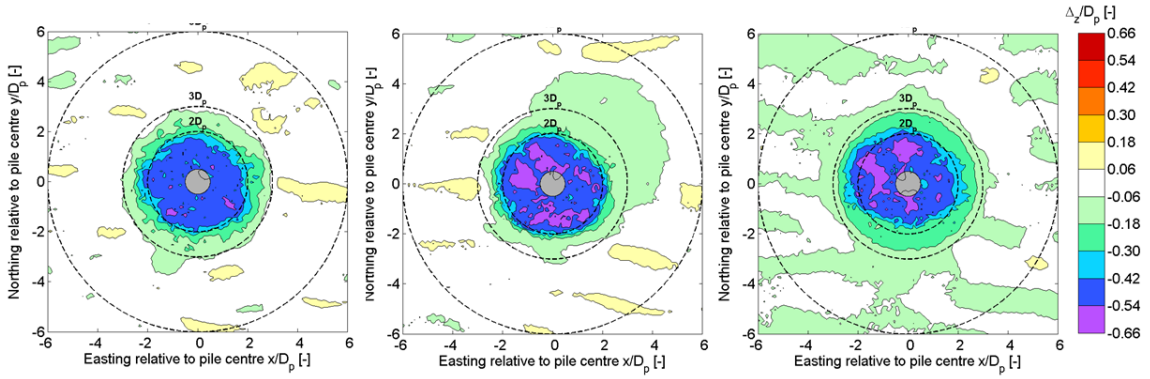

Figure 3.38: Installed scour protections at three neighbouring piles, showing a too large extent of the filter layer at the north-east side of the middle monopile.

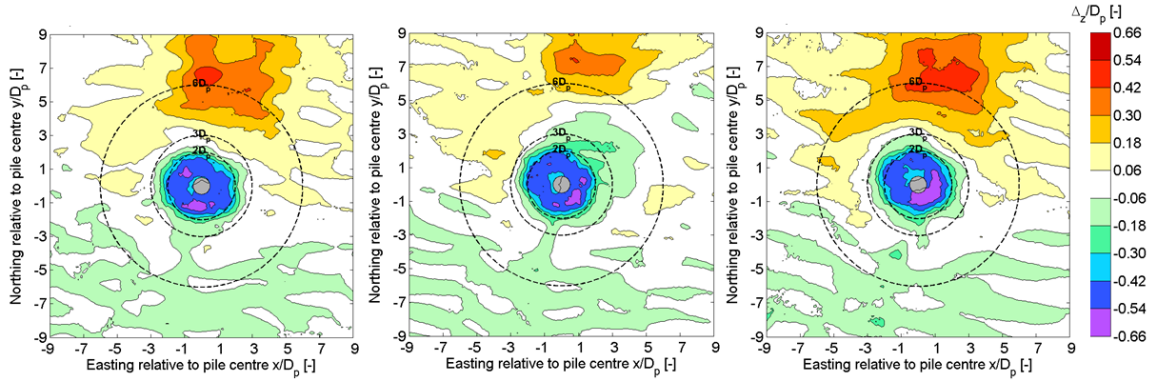

Figure 3.39: Edge scour pattern at one monopile with an elongated filter layer at the NNE-side (middle plot) and the two neighbouring monopiles; situation in 2013, 7 years after monopile installation.

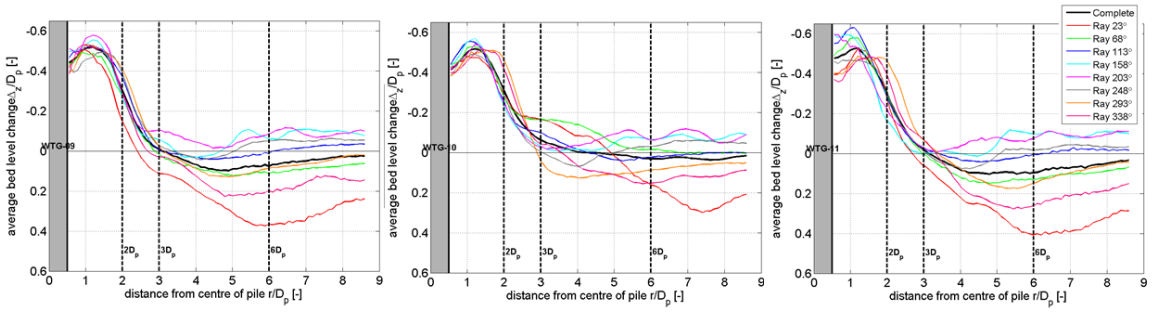

Figure 3.40: Cross-sectional profiles of the different octants (radially averaged over 45°-sectors) for the monopile with the elongated filter layer in NE-direction (middle plot) and the two neighbouring monopiles with "normal" scour protections. The red line (Ray 23°N) shows the effect of the extended filter layer.

The cross-sectional profiles of the different octants are plotted in Fig. 3.40. These three plots show that with a "normal" layout of the filter layer the maximum edge scour depth (radially averaged over 45°-sectors) is approximately $0.4D_p$ for the NNE-sector (represented by the red line, indicated as "Ray 23°N"), whereas this reduces to about $0.3D_p$ when the filter layer is about $2D_p$ longer. Moreover, the edge scour hole is significantly smaller and the deepest location is about $1.5\text{-}2.0D_p$ farther away from the pile, thereby reducing the risk on falling apron effects in the armour layer. If the shape of the edge scour hole is considered from a distance of $r = 7.5D_p$ from the pile centre, the edge scour holes look almost similar. This is a clear indication that relatively small rocks applied in a filter layer can effectively protect the surrounding seabed against edge scour.

The remaining edge scour hole will not just be pushed away from the pile, but will also be smaller and less deep. This can be an effective mitigating measure, if the electricity cables have to be installed in an edge scour prone area.

3.5.2. Edge Scour Development at Scroby Sands

For the installation procedure, where rock (scour protection) is placed in a previously generated scour hole around the foundation, Whitehouse et al. (2011) presented and discussed the edge scour development at Scroby Sand OWF located off the east coast of England. Fig. 3.41 (reproduced with permission from Fig. 4b in Whitehouse et al.,2011) shows typical edge development around the scour protection system for the specific wind farm, which has the following similarities to the edge scour development experienced in the present experimental campaign and at OWEZ:

(1) Scour happens at the transverse sides. However, the distinction of the scour development from the upstream point to the transverse side is not clear in Fig. 3.41. This could be caused by the scour protection being installed in the previously generated scour hole, and therefore the initial conditions for the scour is not identical for this case.

(2) A “two-legged” scour hole forms on either side of the scour protection along the flow direction of the tide, though the scour pattern observed is most notable on one side. The deviance in the observed edge scour patterns on either side of the scour protection can be caused by any asymmetries in the tidal current, as explained previously.

(3) A ridge forms in between the two legged scour hole extending from the periphery of the scour protection through the scour hole. It is not evident in Fig. 41 if the ridge extends to the base of the monopile. Note that from the traces of the ripples in Fig. 3.41, again the crest of the ripples in the two-legged scour hole bends towards to ridge.

Note that the edge scour patterns observed at Scroby Sands OWF, are affected by the scour protection being installed in a previously generated scour hole. Thereby, some remains of the initial scour hole generated around the unprotected monopile might be present and/or affect the edge scour development as explained in conjunction with the aforementioned item 1.

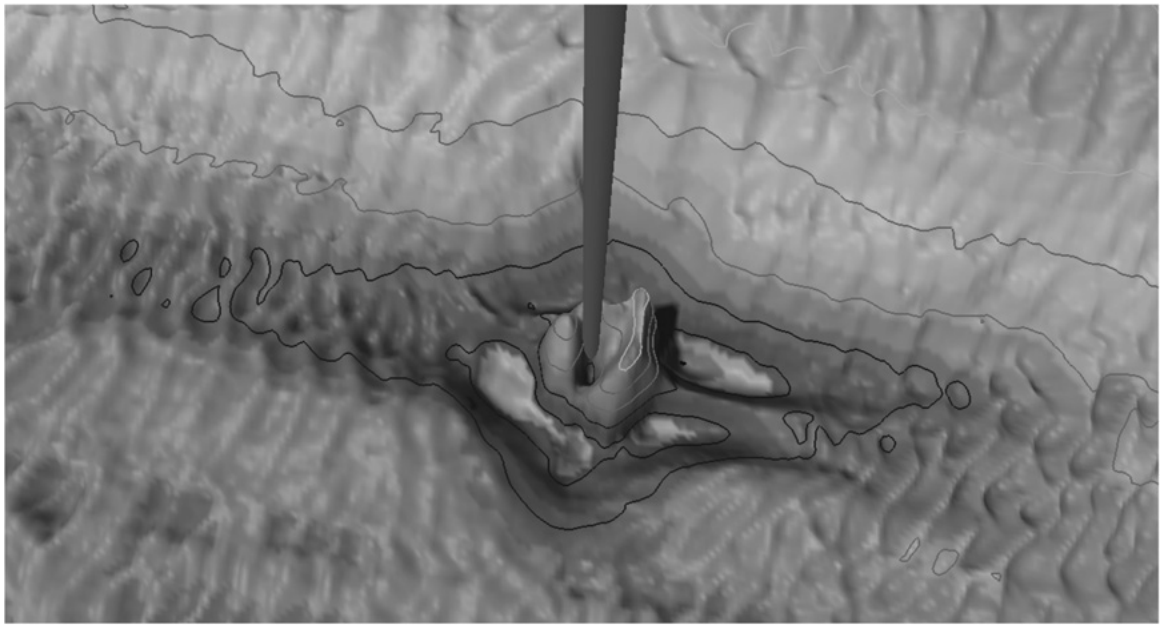

Figure 3.41. Typical scour hole with scour protection installed. Scroby Sands OWF, view looking east with depth contours at 1 m intervals (vertical exaggeration x 10). Reproduced with permission from Whitehouse et al. 2011.

3.6. Remarks on Practical Applications

The present study comprises a range for the Shields parameter of $\theta = 0.06 - 0.23$ and the sediment transport is mainly considered where bed load is dominant. Clearly for larger values of the Shields parameter and higher contributions of the suspended load caution must be exercised when extrapolating the data.

Small scale ripples were present throughout the live-bed test series, and the ripple size relative to the scour hole dimensions is obviously an order of magnitude larger than encountered in practice. The effect of this is mainly observed in the time development of the edge scour hole, and the implication is discussed in the section regarding time scale of scour. From the traces of the ripple patterns in Fig. 3.34 collocated with the information on the edge scour depth in Figs. 3.32 – 3.33 it seems the ripples do not affect the scour process to a great extent.

Note that the present tests simulate the scour process in tidal current with the time scale of the scour process relatively large compared with the tidal period ($T \gg T_{tidal}$) and a uniform Shields parameter during each half-cycle of the tide cycle. In practical applications deviations from both are expected, however from the discussion in the section on scour in tidal current, the latter deviations will mainly affect the plan-view extent and asymmetry of the scour hole, and only smaller deviations from the equilibrium scour depth are expected.

3.7. Conclusion

The present study presents and discuss an experimental research campaign completed to determine the governing flow mechanisms causing edge scour around scour protections at monopile foundations in current, simulated tidal current and combined waves and current. Subsequently a parametric study of the scour process comprising the latter flow climates was carried out, and the following conclusions can be drawn:

1. Scour happens alongside the upstream- and transverse perimeter of the scour protection, caused by the combined action of the horseshoe-vortex generated in front of the scour protection, the contraction streamlines and acceleration of flow at the transverse sides of the scour protection. Design guidelines are provided in Fig. 3.20 to determine the equilibrium scour depth in current, given the approach velocity and the thickness- and the width of the scour protection in relation to the pile diameter.

2. Mapping of the three-dimensional flow field downstream of the pile and scour protection by particle image velocimetry, together with flow visualizations and bed shear stress tests, have shown a pair of symmetrical counter-rotating vortices emerging in the wake of the monopile and scour protection. These vortices show a significant potential to scour the downstream wake area, and design guidelines are given in Fig. 3.21 and Fig. 3.22 to determine the equilibrium depth and length of the scour hole, given the approach flow, pile diameter and the aspect ratio of the thickness- and width of the scour protection layer.

3. It is found that the equilibrium edge scour depth remains unaffected from a steady current changed to a tidal current. However, this is not so for the plan-view extent of the scour, where the scour holes at the transverse sides and that downstream coalescence. The deepest part of the scour holes appears closer to the edge of the scour protection in the case of a tidal current.

4. The transverse side- and downstream scour can effectively be reduced by elongating the filter layer beyond the armour layer. The edge scour reduces considerably even for slightly elongated filter layers, as can be seen in Fig. 3.27.

5. The described mechanisms causing the edge scour have been investigated in practice for two wind farms. In both cases the appearance and magnitude of the edge scour seem to conform well to the experimental findings, supporting the conclusions of the present investigation.

Acknowledgement. This study is supported partially by: (1) Danish GTS-university-cooperation project “Future Marine Structures”; (2) EU FP7-project, MERMAID 28870; (3) Statkraft through the Ocean Energy Research Programme (SOERP); and (4) FORSKEL. Some of the tests presented in this study were conducted by MSc. Thomas Probst, MSc. Zahra Waisi and MSc-candidate Pierre Breard under the supervision of the authors.

Acknowledgements are also directed to Philippe de Garder and Johan Rasing from BASF for providing material and information on the procedure to apply Elastocoast®.

The authors would also like to acknowledge Noordzeewind, a 50/50 joint venture of Shell and NUON, for the use of the field data of Offshore Windpark Egmond aan Zee.

Chapter 4

Backfilling of a scour hole around a pile in waves and current

This chapter is published in Journal of Waterway, Port, Coastal and Ocean Engineering, ASCE. Vol. 139, No. 1, pp 9-23, January 1, 2013.

B. M. Sumer[1], T. U. Petersen[2], L. Locatelli[3], J. Fredsøe[4] , R. E. Musumeci[5] & E. Foti[6]

[1]Professor, [2]Ph.D. – candidate, [3]Research Engineer, [4]Professor, Technical University of Denmark. Section for Fluid Mechanics, Coastal and Maritime Engineering. Kgs. Lyngby, Denmark.

[5]Assistant Professor, [6]Professor, Department of Civil and Environmental Engineering, University of Catania, 95125 Catania, Italy

Abstract: This paper presents the results of an experimental investigation of backfilling of scour holes around circular piles. Scour hole around the piles is generated either by a current, or by a wave. Subsequently the flow climate is changed from current to wave, or to combined wave and current; or from wave to a smaller wave, leading to backfilling of the scour hole. The investigation has shed light onto the mechanism behind the backfilling process. The results show that the scour depth corresponding to the equilibrium state of backfilling is the same as that corresponding to the equilibrium state of scour around the pile for the same wave (or combined wave and current) climate. The time scale of backfilling has been determined as a function of three parameters, namely (1) the Keulegan-Carpenter number of the initial wave or the current (which generates the initial scour hole); (2) that of the subsequent wave which backfills the scour hole; and (3) the Shields parameter associated with the latter wave, for live-bed conditions. In the case of combined wave and current, the current-to-wave-velocity ratio is also involved. The time scale of the backfilling process is completely different from that of scour. The time scale of backfilling is much larger than that of scour when the Keulegan-Carpenter number associated with the backfilling is $KC_f < O(10)$ (typical wind farm application), while the trend is opposite when $C_f \gg O(10)$.

CE Database subject headings: Scour, piles, offshore structures, currents.

Keywords: Backfilling, scour, pile, offshore windfarm, offshore wind turbine, waves, current, time scale.

4.1. Introduction

Observations show that, when the correct conditions exist, a previously generated scour hole around a pile (Fig. 4.1, Panel 1) may be backfilled (Fig. 4.1, Panel 2); e.g., a scour hole generated by a steady current is backfilled when the flow conditions change from steady current to waves, as will be detailed in the paper.

A great many works have been devoted to scour around piles. A detailed account of the topic has been given in the books of Whitehouse (1998), Melville and Coleman (2000) and Sumer and Fredsøe (2002), and more recently in Roulund et al. (2005), Sumer (2007) and Sumer et al. (2007).

While much has been written on scour, relatively few studies have been reported on backfilling. The backfilling process comes into focus when the time variation of scour depth in a continuously changing flow climate (currents, waves, and combined waves and current) is considered. Scour around offshore wind turbine foundations is a typical example; the bed around an offshore wind turbine foundation continuously experiences scour and backfilling in an alternating fashion under the ever changing wave and current climate.

Engineering models have been developed with the purpose of predicting the time history of scour and backfilling for large times (weeks, months, or years), Nielsen and Hansen (2007), Raaijmakers and Rudolph (2008 a and b), and Harris et al. (2010). These models have essentially two components: scour and backfilling. The existing information on scour has been successfully incorporated in the models. This is not the case, however, for backfilling because of the lack of knowledge on this topic.

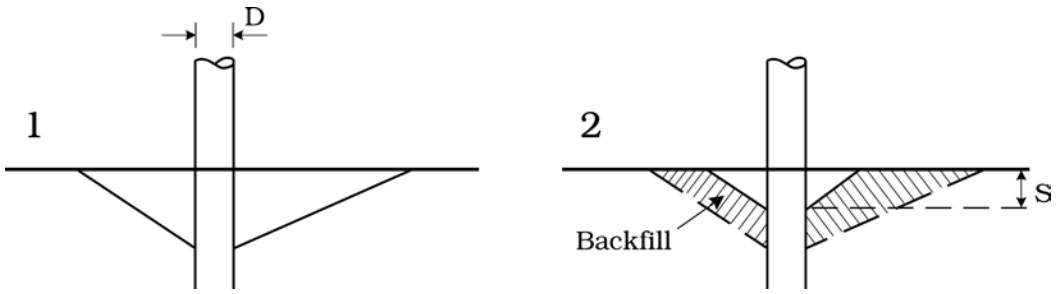

Figure. 4.1. Definition sketch (schematic). Panel 1: Scour hole generated by a current (or a wave). Panel 2: Scour hole after the initially generated scour hole is backfilled. S is the depth of the scour hole after the backfilling process attains its equilibrium.

To the authors' knowledge, no study is yet available investigating, in a systematic manner, backfilling around structures. Previously, Fredsøe et al. (1992) studied backfilling in the case of a pipeline in a limited experimental program. Likewise, Hartvig et al. (2010) studied backfilling in the case of a pile, again, with a limited coverage. Although both studies have specifically focused on backfilling (the first one in a 2-D environment while the second in a 3-D environment) and collected some but limited data, no clear understanding of the backfilling process was offered in these publications. There is also a complete lack of data on various properties of the backfilling process, particularly for the time scale, a crucially important quantity used in the development of engineering models such as those mentioned in the preceding paragraph.

The purpose of the present study is twofold. One is to gain an understanding of the backfilling process around a pile when the pile is exposed to a changing flow environment (the flow environment changing from, for example, a steady current, to a wave; or from a steady current to a combined wave and current; or from a wave to a smaller wave; etc.) The second purpose is to collect data for various characteristics of the backfilling process, including the time scale, for the purpose of establishing design diagrams.

4.2. Experimental Setup

The experiments were, for the most part, conducted with piles with diameters of D = 15 mm, 25 mm, 40 mm and 75 mm. However, some supplementary experiments were also conducted with a large pile with D = 310 mm. The former experiments were designated as small-pile experiments, and the latter experiments as large-pile experiments.

4.2.1.Experiments with small piles

Wave flume

These experiments were conducted in a wave-current flume (26.5 m in length, 0.6 m in width and 0.8 m in depth), equipped with Active Wave Absorption Control System (AWACS) and Danish Hydarulic Institue (DHI) Wave Synthesizer 2.40, which has been developed by DHI Water & Environment for control of wave generators in wave flumes, Schäffer et al. (1994). This made it possible simultaneous generation of desired incident waves, and absorption of the associated reflected waves.

A honey-comb type of wave filter, 0.6 m in length, and extending over the entire width and depth of the flume was placed in the flume, 2.7 m from the wave generator, to avoid unevenness of the surface elevation across the width.

Irregular waves were used in the experiments; they were generated by a programmable piston-type wave generator. Irregular waves were used in favour of regular waves to avoid bed undulations associated with very large test durations, up to 85 hours. (The generation mechanism of these bed formations is similar to that of alternating scour and deposition pattern induced by (partial) standing waves, reported in e.g., Sumer and Fredsøe, 2000.) The test durations were very large in order to capture large time scales involved in the backfilling process, as will be detailed later. In the wave generation, a measured in-situ water surface elevation spectrum for the North Sea storm conditions was used as the control spectrum to

generate wave-generator displacement signal, similar to our previous studies Kozakiewicz et al. (1994) and Sumer and Fredsøe (2000).

A sediment section in the form of a sand pit with two ramps at the two ends was formed in the flume. The sand pit was 0.6 m wide, 0.2 m deep and 6 m long, the distance from the offshore end of the sand pit to the wave generator being 13 m. The two end ramps (with 1:15 slope) were made from crushed stones the size 4 cm.

The grain size of the sediment (fine sand) used in the experiments was $d_{50} = 0.17$ mm with a geometric standard deviation of $\sigma_g = d_{84}/d_{50} = 1.3$.

A wave absorber, made of perforated plastic plates with an arch shaped cross-sectional profile, was placed at the onshore end of the flume to handle the reflection. The water depth in the experiments (wave; current; and combined wave and current experiments) was maintained at 40 cm at the sand pit section. It may be noted that, in the case of the combined wave and current experiments, the water depth was adjusted so that it was initially smaller than 40 cm (0.4-9.1% smaller, depending on the current velocity); and, with the introduction of the current, it increased to 40 cm.

Three conventional resistance-type wave gages were used to monitor the water surface elevation, one at the midway between the filter and the sediment section, the second one at the junction between the sediment section and the offshore ramp section, and the third one at the pile section.

4.2.2. Model piles and monitoring scour and backfilling

The model pile was embedded vertically in the sediment bed at the center of the sediment section. It was rigidly fixed, extending down to the base bottom of the flume.

Model piles with diameters $D = 15$ mm, 25 mm, 40 mm and 75 mm were implemented in the tests, as mentioned previously. This range of pile diameters was selected to adjust the range of the Keulegan-Carpenter number, one of the key parameters of the study. The 40 mm and 75 mm diameter piles were transparent. This enabled the scour and backfilling processes to be monitored by a mini video camera placed inside the pile with the help of a 45^0 mirror (Fig. 4.2), similar to Sumer et al. (2007). The overall time development of the scour hole was monitored by a second camera placed outside the pile (Fig. 4.2). The latter camera was used to monitor the scour depth in the case of 15 and 25 mm piles as these piles did not have the 45^0-mirror arrangement.

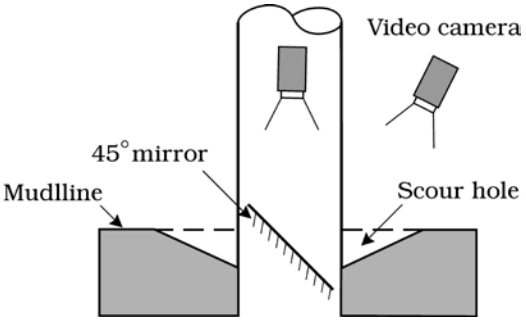

Figure. 4.2. Test setup to monitor the development of scour of backfilling.

With this setup, the scour and backfilling process was videotaped at the offshore side of the pile with a viewing area of approximately 100^0 in plan view. The time resolution of the video recording was 1/25 of a second, enabling the time scale of the backfilling processes, one of the key quantities, to be determined with a very large accuracy. This is particularly important when the time scale of the backfilling process is determined using the so-called tangent method (where the time scale is predicted by calculating the slope of the line tangent to the scour-depth-versus-time curve at time $t = 0$, Sumer and Fredsøe, 2002, p. 69), as will be detailed later.

4.2.3. Velocity measurements

In the case of waves and combined waves and current, the orbital velocity of water particles at the bed was measured, using a Laser Doppler Anemometer (LDA), a Dantec LDA-04 system (Dantec Dynamics, Denmark) comprising a 5 mW He-Ne laser and a Dantec 9057X0181 photomultiplier, the measurements being conducted in forward-scatter mode. The system was equipped with a Dantec 9055N0124 frequency shifter and a Dantec 9055N0214 frequency tracker. The measurement point was located at the pile section at 10 cm from the bed and at 20 cm from the side wall.

The orbital velocity was constantly monitored during the course of the experiment, and the data collected was used to calculate the spectrum of the orbital velocity. The latter was utilized to determine the velocity to calculate the quantities such as the Shields parameter and the Keulegan-Carpenter number (Eqs. (4.1) and (4.5), respectively), two major quantities

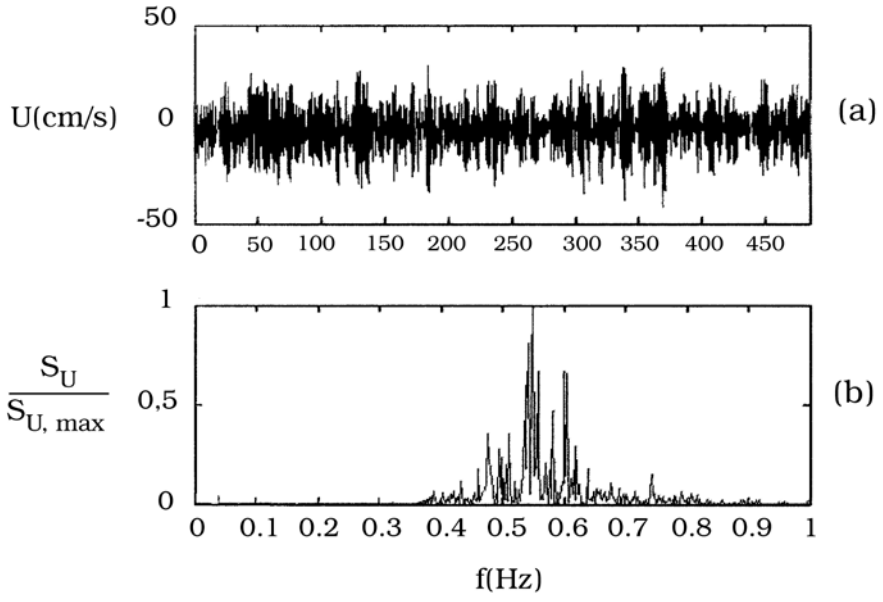

Figure. 4.3. (a): Time series of velocity and (b): Normalized spectrum. Test 58.

governing the backfilling process, as will be detailed later. A sample time series and a sample spectrum of the orbital velocity are presented in Fig. 4.3.

In the case of the current, the same LDA equipment was used to measure the velocity profile across the depth.

The sampling frequency was 140 Hz in both the wave and the current experiments.

4.2.4. 3D optical technique

The development of backfilling was monitored in a few experiments, using a 3D optical technique developed at the University of Catania (Baglio et al. 2001, Foti et al. 2011). This technique allows us to obtain metric information about 3D morphological evolution of the bed. Measurements are taken in a dynamic and non-intrusive way.

In the present experiments, two UI-2250RE-M CCD monochrome cameras, located outside the wave flume were used to monitor the bed evolution from an initially flat bottom, up to the current- or wave-induced equilibrium scour. In the backfilling tests, measurements of the bottom morphology were repeated until the equilibrium wave-generated backfilling was reached.

To visualize the position of the even sandy bottom within the images, a regular pattern of light markers was projected precisely onto the part of the bed which would be exposed to scour and backfilling in the test. The pattern was obtained by using two 20mW Lasiris SNF 660 nm laser generators coupled with two GMN31614MCN-1 Goyo Optical Inc's diffractive lenses having 1.6 mm focal length.

The location of all the components of the optical equipment is shown in Fig. 4.4. Due to the presence of a steel bar which interfered with the image formation, both cameras had to be placed on the upstream side of the flume (Fig. 4.4).

A calibration of the images was obtained by taking images of a 3D "tool" made up by the Lego® blocks, the dimensions of which are known with very high precision, within O(0.1mm). The size of the calibration tool was 25.52 cm in the flow direction, 15.96 cm in the transverse direction and 15.28 cm in the vertical direction. In particular, the geometrical camera calibration was carried out by implementing a new nonlinear algorithm, based on the four-step camera calibration of Heikkilä and Silvén (1997) which incorporates lens distortion. By recovering the deformation of the position of the grid points compared to the initial flat bottom, the 3D characteristics of scour/backfilling processes could be measured. Details on the methodology for image treatment, camera calibration and stereo matching can be found in Musumeci et al. (2013) and Appendix B.

4.2.5. Particle-tracking experiments

The purpose of these experiments was to get a picture of sediment particle trajectories near the bed over a long period of time. To this end, plastic particles the size $d = 3.1$ mm were used as tracers. The size of the particles was chosen relatively large to make it possible to trace the trajectory of the particle by video. The specific gravity of these particles was $s = 1.38$, and the fall velocity was $w_s = 15.4$ cm/s. This ensured that the particles travelled near the bed.

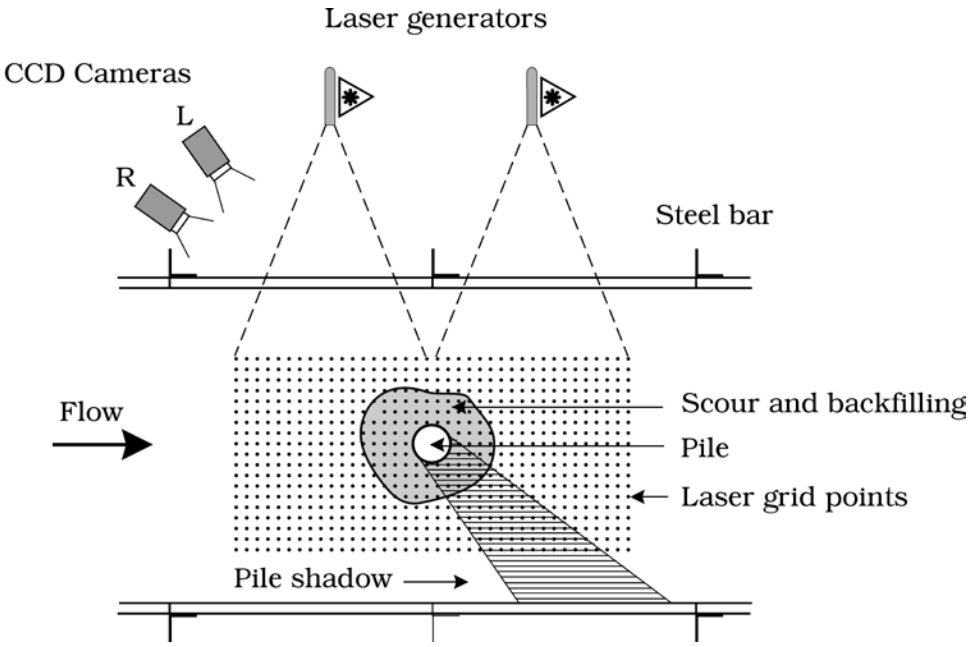

Fig. 4.4. Plan view of the 3D optical system to monitor scour/backfilling development.

In the experiments, the particles were released from different positions in plan view, and their trajectories were videotaped by a camera placed at multiple positions, covering a viewing area of 360° around the pile, approximately 0.5 m in the offshore-onshore direction and 0.6 m in the transverse direction.

Regular waves were used in the particle-tracking experiments. This was to get a better insight into the process of particle movement. Using regular waves was not a problem because the length of a typical test was not excessive and therefore the problem of bed undulations in the actual backfilling tests with regular waves was not existent. The particle-tracking experiments were conducted for the following wave parameters: The maximum value of the orbital velocity at the bed level was U_m = 0.22 m/s, the wave period T_w = 2 s and the Keulegan-Carpenter number $KC_f = (U_m T_w)/D = 11$.

4.2.7. Experiments with large piles

Wave flume

These experiments were conducted with a pile of D = 310 mm in another wave/current flume, 28 m in length, 4 m in width and 1 m in depth. Similar to the small pile experiments, a honey-comb type of wave filter, 0.9 m in length, and extending over the entire width and depth of the flume was placed in the flume at 3 m from the wave generator. Irregular waves, generated in the same way as in the small pile experiments, were used in the experiments.

The water depth in the experiments was maintained at 40 cm. Again, similar to the small pile tests, the water depth in the combined wave and current experiments was adjusted so that it

was initially smaller than 40 cm (2.5-4.5% smaller, depending on the current velocity); and, with the introduction of the current, it increased to 40 cm, the desired value of water depth.

The flume had a sand pit from an earlier experiment, with two ramps (made from crushed stones) at the two ends with a slope of 1:10. The sand pit was 4 m wide, 0.4 m deep and 8 m long, the distance from the offshore end of the sand pit to the wave generator being about 12 m. A scour protection with an extent of 50 cm was placed at the upstream end of the sand pit to protect the junction between the sand section and the ramp against scour caused by the current.

The same sand as in the small-pile experiments, with d_{50} = 0.17 mm and $\sigma_g = d_{84}/d_{50}$ = 1.3, was used in the experiments.

Likewise, the same arrangement as in the small pile experiments was made for the wave gages, one placed at the midway between the filter and the sediment section, the second one at the junction between the sediment section and the offshore ramp section, and the third one at the pile section.

4.2.8. Velocity measurements

The orbital velocity of water particles at the bed was measured, using a Laser Doppler Anemometer (LDA), a Dantec 2D LDA system (Dantec Dynamics, Denmark) comprising a 14 mm "pen-size" submersible probe, the measurements being conducted in the back-scatter mode. The system was equipped with a Dantec 9055N0124 frequency shifter and a Dantec 9055N0214 frequency tracker. The measurement point was located at the pile section at 10 cm from the bed and at 100 cm from the side wall. The way in which the velocity measurements were conducted was similar to the small pile experiments.

4.3. Test procedure and test conditions

4.3.1. Test procedure

The test procedure was typically as follows:

1. Run a scour test with an initially flat bed until the scour attains its equilibrium state (Panel 1 in Fig. 4.1). These tests are designated as scour tests.
2. Stop the flume.
3. Subsequently, run a test where the flow conditions are such that the scour hole is backfilled (Panel 2, Fig. 4.1). Run the test until the backfilling reaches its equilibrium state. These tests are designated as backfilling tests.

4.3.2. Test conditions for scour tests

Tables 4.1, 4.2 and 4.3 summarize the test conditions for the scour tests, Table 4.1 for scour tests in current, Table 4.2 for scour tests in waves alone, and Table 4.3 for scour tests in combined waves and current. Tables 4.4, 4.5 and 4.6, on the other hand, summarize the test conditions for the backfilling tests.

In Table 4.1, V is the depth averaged flow velocity, and U_c is the velocity measured at $D/2$

from the bed in the case of the small pile tests (following Sumer and Fredsøe, 2001 a). In the case of the large pile test, U_c is the velocity measured at D/10 from the bed. The reason why U_c was taken at D/10 (rather than D/2) is that the former is more representative for near-bed velocities for large pile diameters. (Clearly, in the implementation of the present large pile results in practice, the same quantity, namely, U_c at D/10 from the bed, should be used.)

The quantity U_f in Table 4.1 is the undisturbed friction velocity, obtained from the measured velocity distribution, using the familiar log-fit exercise. The obtained values were checked against the values found from the Colebrook-White formula (e.g., Schlichting, 1979). The Shields parameter, θ, in the table is defined by

$$\theta = \frac{U_f^2}{g(s-1)d_{50}} \tag{4.1}$$

in which g is the acceleration due to gravity, s the specific gravity of sand grains (=2.65).

The equilibrium scour depths normalized by the pile diameter are also indicated in Table 1 (last column). The small pile results agree with the existing data (see, e.g., Sumer et al., 1992, or Sumer and Fredsøe, 2002, Fig. 3.35). The large pile result also agrees with the existing data, corresponding to a flow-depth-to-pile-diameter ratio of $h/D = (40\,cm)/(31\,cm) = 1.3$, Melville and Sutherland (1988), also reproduced in Sumer and Fredsøe (2002, Fig. 3.26).

In Table 4.2, U_m is the orbital velocity at the bed level, calculated from the spectrum function of U:

$$U_m = \sqrt{2}\,\sigma_U \tag{4.2}$$

with σ_U

$$\sigma_U{}^2 = \int_0^\infty S_U(f)\,df \tag{4.3}$$

Here $S_U(f)$ is the spectrum function of the measured orbital velocity at the bed U, and f the frequency. Note, that $U_m = \sqrt{2}\,\sigma_U$ becomes identical to the maximum value of the bottom orbital velocity in the case of small-amplitude sinusoidal waves (Sumer and Fredsøe, 2001a). The quantity U_{fm} in Table 4.2 is the undisturbed friction velocity, calculated from

$$U_{fm} = \sqrt{\frac{f_w}{2}}\,U_m \tag{4.4}$$

in which f_w is the wave friction factor, calculated from the laminar wave boundary layer friction factor, as the boundary-layer flow was in the laminar regime, considering the wave boundary layer Reynolds number and the grain Reynolds number (see, e.g., Fredsøe and Deigaard, 1992). The Shields parameter in the table is defined in the same way as in Eq. (4.1), with U_f replaced with U_{fm}. Furthermore, KC, the Keulegan-Carpenter number, is defined by

$$KC = \frac{U_m T_p}{D} \tag{4.5}$$

in which T_p is the wave period corresponding to the wave peak frequency:

$$T_p = \frac{1}{f_p} \tag{4.6}$$

Similar to Table 4.1, the measured equilibrium scour depths normalized by the pile diameter are also indicated in Table 4.2 (last column). These values agree with the data of Sumer et al., 1992, also reproduced in Sumer and Fredsøe, 2002, Fig. 3.35), as will be discussed later.

In Table 4.3, where the test conditions are summarized for the combined wave and current conditions, the quantities are given for the two fundamental cases, i.e., the current-alone case, and the wave-alone case, which, when combined, form the corresponding combined wave and current climate. The quantity U_{cw} in Table 4.3 is defined by

$$U_{cw} = \frac{U_c}{U_c + U_m} \tag{4.7}$$

in which U_c is the current velocity, set equal to the velocity at D/2 from the bed in the current-alone fundamental case (following Sumer and Fredsøe, 2001 a), and U_m is the orbital velocity at the bed, calculated from Eq. (4.2), in the wave-alone fundamental case. Similar to Tables 4.1 and 4.2, the measured equilibrium scour depths normalized with the pile diameter are also given in the table (last column). These values are in good agreement with the corresponding data of Sumer and Fredsøe (2001 a), as will be discussed later.

4.3.3. Test conditions for backfilling tests

Table 4.4 gives the test conditions for the backfilling experiments conducted under waves.

There are two kinds of backfilling experiments in Table 4.4:

1. Tests 27-47 where the initial scour hole was generated by a current; and
2. Tests 48-61 where the initial scour hole was generated by a wave.

The current test conditions associated with the initial scour hole in item 1 above are given in Table 1, while the wave conditions associated with that in item 2 are given in Table 2.

The two KC numbers indicated in Table 4.4, KC_i and KC_f, are: KC_i is the Keulegan-Carpenter number for the test where the initial scour hole was generated, while KC_f is the Keulegan-Carpenter number corresponding to the actual backfilling test. (The sub-indices i and f stand for initial and final, respectively.) Clearly, if the scour hole was generated with a current, KC_i will be $KC_i = \infty$. Other quantities in Table 4.4, namely the peak frequency, f_p, the orbital velocity U_m, the friction velocity U_{fm}, and the Shields parameter, θ_f, are all those corresponding to the wave used in the actual backfilling test.

The quantity S in Table 4.4 is the depth of the scour hole corresponding to the stage when the backfilling process has attained its equilibrium state (Panel 2, Fig. 4.1) while the quantity T is the time scale of the backfilling process, and T^* the non-dimensional time scale defined by

$$T^* = \frac{(g(s-1)d_{50}{}^3)^{1/2}}{D^2} T \tag{4.8}$$

Note that the time scale is normalized in the same way as in scour processes (see, Sumer and Fredsøe, 2002).

Table 4.5 summarizes the test conditions for the backfilling experiments conducted under combined waves and current with the 40 mm diameter pile. In these experiments, the initial scour hole was generated by the current in Test 1 (Table 4.1). In the table, the quantities are given for the two fundamental cases, i.e., the current-alone case, and the wave-alone case, which, when combined, form the corresponding combined wave and current case.

Table 4.6 summarizes the test conditions for the backfilling experiments conducted under combined waves and current with the 310 mm diameter pile. In these experiments, the initial scour hole was generated by the current in Test 4.5 (Table 4.1). In addition to the parameters given in the previous table, one more parameter is also included in Table 4.5, namely the diffraction parameter, D/L, considering that the pile was large, and therefore the diffraction effect was not nil (Sumer and Fredsøe, 2001b and 2002).

Finally, we note that the Shields parameter in all the experiments (the scour experiments, Tables 4.1-4.3; or the backfilling experiments, Tables 4.4-4.6) was larger than the critical value corresponding to the initiation of the motion on the bed, meaning that both the scour experiments and the backfilling experiments were conducted in the live-bed regime. The latter was revealed by the visual observations that ripples prevailed on the sediment bed in all the experiments. Clearly, the live-bed regime in the backfilling experiments ensures backfilling to take place.

Table 4.1. Scour in steady current

Test number	Pile Diameter D [mm]	Undisturbed Depth-averaged current velocity V [cm/s]	Undisturbed velocity near the bed U_c [cm/s]	Friction velocity in steady current U_f [cm/s]	Shields parameter θ [-]	Measured Non-dimensional equilibrium scour depth S/D [-]	Time scale of scour process T [s]	T^* [-]
1	40	38.6	30.2	1,9	0.131	1.53	41	0.23
2	25	38.6	28.9	1,9	0.131	1.48	26	0.37
3	15	38.6	26.0	1,9	0.131	1.47	15	0.61
4	75	38.6	32.1	1,9	0,131	1,41	85	0.13
5	310	35.1	26.3	1.6	0.093	1.13	2050	0.19

Note: U_c was measured at D/2 from the bed for the small pile case (Test 1-4) and at D/10 for the large-pile case (Test 5)

Table 4.2. Scour in waves

Test number	Pile Diameter D [mm]	Peak Frequency of Waves f_p [Hz]	Maximum orbital velocity at the bed U_m [cm/s]	Maximum value of friction velocity U_{fm} [cm/s]	Keulegan-Carpenter number KC [-]	Shields parameter θ [-]	Measured non dimensional equilibrium scour depth S/D [-]	Time scale of scour process T [s]	T^* [-]
6	40	0.25	19.8	1.6	20	0.09	0.45	400	2.20
7	40	0.25	15.5	1.4	16	0.07	0.43	750	4.20
8	40	0.4	17.5	1.7	11	0.10	0.36	170	1.00
9	40	0.56	22.5	2	10	0.15	0.28	90	0.50
10	40	0.4	12.7	1.4	8	0.07	0.16	-	-
11	40	0.67	13.58	1.7	5	0.101	0,11	-	-
12	75	0.25	19.8	1.6	11	0.09	0,16	705	1.10
13	75	0.40	20.2	1.8	7	0.117	0,023	138	0.22
14	75	0.40	17.5	1.7	6	0.101	0,14	130	0.21
15	75	0.40	12.7	1.4	4	0.073	0,03	71	0.11
16	40	0.40	12.4	1.4	8	0.07	0,15	242	1.35
17	40	0.40	16	1.6	10	0.09	0,2	250	1.39
18	40	0.67	20.2	2	8	0.15	0,19	90	0.50
19	75	0.4	12.4	1.4	4	0.07	0,01	75	0.12
20	75	0.4	16	1.6	5	0.09	0,01	115	0.18
21	75	0.4	17.5	1.7	6	0.101	0,03	130	0.21

Table 4.3. Scour in combined waves and current

Test number	Pile Diameter D [mm]	Peak Frequency of waves f_p [hz]	Maximum orbital velocity at the bed U_m [cm/s]	Maximum value of friction velocity U_{fm} [cm/s]	Depth Averaged Current Velocity V [cm/s]	Undisturbed Current velocity at D/2 U_c [cm/s]	Shields parameter in steady current alone θ [-]	Keulegan-Carpenter number KC_f [-]	Shields parameter in waves alone θ [-]	U_{cw} [-]	Measured non dimensional equilibrium scour depth S/D [-]	Time scale of scour process T [s]	T^* [-]
22	40	0.4	12.4	1.4	12.4	9	0.02	8	0.07	0.42	0.69	2638	14.70
23	40	0.25	15.5	1.4	38.6	30.2	0.131	16	0.07	0.66	1,43	99	0.55
24	40	0.25	15.5	1.4	20.9	15.6	0.04	16	0.07	0.50	1,13	750	4.20
25	40	0.25	15.5	1.4	12.4	9	0.02	16	0.07	0.37	0.90	1350	7.5
26	40	0.67	20.2	2.0	38.6	30.2	0.131	8	0.15	0.60	1.21	60	0.33

Table 4.4. Backfilling in waves alone from a preformed current or wave-generated scour hole

Test no.	Pile Diameter D [mm]	Initial Keulegan-Carpenter number KC_i [-]	Peak Frequency of Waves f_p [Hz]	Maximum orbital velocity at the bed U_m [cm/s]	Maximum value of friction velocity U_{fm} [cm/s]	Final Keulegan-Carpenter number KC_f [-]	Final Shields parameter θ_f [-]	Measured non dimensional equilibrium depth of hole around pile S/D [-]	Time scale of backfill T [s]	T_* -
27	40	∞	0.25	19.8	1.6	20	0.090	0.45	1974	11
28	40	∞	0.25	15.5	1.4	16	0.070	0.43	6818	38
29	40	∞	0.4	17.5	1.7	11	0.100	0.42	4127	23
30	40	∞	0.4	12.7	1.4	8	0.070	-	20633	115
31	40	∞	0.4	12.7	1.4	8	0.070	0.17	17045	95
32	40	∞	0.56	22.5	2.0	10	0.150	0.37	1202	6.7
33	25	∞	0.25	19.8	1.6	32	0.090	0.52	399	5.7
34	25	∞	0.25	15.5	1.4	25	0.070	0.52	1304	18.6
35	25	∞	0.4	17.5	1.7	18	0.100	0.42	1100	15.7

36	25	∞	0.4	12.7	1.4	13	0.070	0.39	5186	74
37	25	∞	0.56	22.5	2.0	16	0.150	0.53	350	5
38	25	∞	0.67	15.3	1.8	9	0.110	0.24	1682	24
39	15	∞	0.25	19.8	1.6	53	0.090	0.97	81	3.2
40	15	∞	0.25	15.5	1.4	41	0.070	0.9	757	30
41	15	∞	0.4	17.5	1.7	29	0.100	0.72	260	10.3
42	15	∞	0.56	22.5	2.0	27	0.150	0.7	73	2.9
43	15	∞	0.67	15.3	1.8	15	0.110	0.37	-	-
44	40	∞	0.67	13.6	1.7	5	0.101	0.11	14150	78.9
45	40	∞	0.4	16.0	1.6	10	0.090	0.35	3750	20.9
46	40	∞	0.67	16.5	1.8	6	0.120	0.03	3550	19.8
47	40	∞	0.4	17.5	1.7	11	0.100	0.42	2350	14.3
48	25	32	0.25	15.5	1.4	25	0.070	0.49	343	4.9
49	25	32	0.4	17.5	1.7	18	0.100	0.41	252	3.6
50	25	32	0.4	12.7	1.4	13	0.070	0.19	1198	17.1
51	25	32	0.67	15.3	1.8	9	0.110	0.18	715	10.2
52	40	20	0.25	15.5	1.4	16	0.070	0.33	700	3.9
53	40	20	0.4	17.5	1.7	11	0.100	0.24	807	4.5
54	40	20	0.56	22.5	2.0	10	0.150	0.21	287	1.6
55	40	20	0.4	12.7	1.4	8	0.070	0.16	2494	13.9
56	40	20	0.67	13.6	1.7	5	0.101	0.04	3150	17.6
57	75	11	0.4	20.2	1.8	7	0.120	0.015	1225	1.9
58	40	20	0.56	15.7	1.7	7	0.107	0.02	1620	9.02
59	40	20	0.67	16.3	1.4	6	0.123	0.05	1225	6.8
60	40	20	0.67	13.6	1.3	5	0.101	0.08	1975	11.0
61	40	20	0.67	10.6	1.2	4	0.080	0.000	3550	19.8

Table 4.5. Backfilling by combined wave and current case

Test no.	Pile diameter D [mm]	Peak frequency of waves f_p [hz]	Maximum orbital velocity at the bed U_m [cm/s]	Maximum value friction velocity in waves U_{fm} [cm/s]	Depth averaged current velocity V [cm/s]	Undisturbed current velocity at D/2 U_c [cm/s]	Shields parameter in steady current $\theta_{curr.}$ [-]	Final Keulegan - Carpenter Number KC_f [-]	Shields Parameter in waves θ [-]	U_{cw} [-]	Measured non-dimensional equilibrium scour depth S/D [-]	Timescale of backfill T [s]	Timescale of backfill T_* [-]
62	40	0.25	19.8	1.6	38.6	30.2	0.131	20	0.09	0.60	1.41	1300	7.2
63	40	0.25	15.5	1.4	38.6	30.2	0.131	16	0.07	0.66	1.45	600	3.3
64	40	0.4	17.5	1.7	38.6	30.2	0.131	11	0.101	0.63	1.31	650	3.6
65	40	0.4	12.7	1.4	38.6	30.2	0.131	8	0.07	0.70	1.44	350	2.0
66	40	0.4	17.5	1.7	20.9	15.6	0.04	11	0.101	0.47	1.1	2000	11.1
67	40	0.25	19.8	1.6	20.9	15.6	0.04	20	0.09	0.44	1.12	1200	6.7
68	40	0.25	15.5	1.4	20.9	15.6	0.04	16	0.07	0.50	1.23	1500	8.4
69	40	0.4	12.7	1.4	20.9	15.6	0.04	8	0.07	0.55	1.13	5900	32.9
70	40	0.25	19.8	1.6	12.4	9	0.02	20	0.09	0.31	0.82	1500	8.4
71	40	0.25	15.5	1.4	12.4	9	0.02	16	0.07	0.37	1.0	3100	17.3
72	40	0.4	17.5	1.7	12.4	9	0.02	11	0.101	0.34	0.83	2500	13.9
73	40	0.4	12.7	1.4	12.4	9	0.02	8	0.07	0.41	0.75	11550	64.4
74	40	0.67	10.5	1.5	20.9	15.9	0.04	4	0.08	0.60	0.85	37550	209.
75	40	0.4	16.0	1.6	20.9	15.9	0.04	10	0.09	0.49	1.03	2450	13.7
76	40	0.4	16.0	1.6	12.4	9	0.02	10	0.09	0.36	0.82	3070	17.1
77	40	0.4	16.0	1.6	38.6	30.2	0.131	10	0.09	0.65	1.3	825	4.6

Note: Initial scour hole was generated by the current in Test 1, thus $KC_i = \infty$.

Table 4.6. Backfilling by combined wave and current case from a preformed current-generated scour hole

Test no.	Pile Diameter D [mm]	Peak Frequency of waves f_p [hz]	Bed Orbital Velocity U_m [cm/s]	Depth Averaged Current Velocity V [cm/s]	Undisturbed Current velocity at D/10 U_c [cm/s]	Shields parameter in steady current $\theta_{curr.}$ [-]	Final Keulegan - Carpenter Number KC_f [-]	Shields Parameter in waves θ [-]	U_{cw} [-]	Diffraction parameter D/L [-]	Measured non dimensional equilibrium scour depth S/D [-]	Timescale of backfill T [s]	Timescale of backfill T^* [-]
78	310	0.4	17.3	-	-	-	1.4	0.101	0	0.07	-	40000	3.9
79	310	0.4	17.1	35.1	26.3	0.093	1.4	0.101	0.61	0.07	0.92	3550	0.33
80	310	0.4	18.4	25.5	16.8	0.05	1.5	0.101	0.48	0.07	0.72	15750	1.46
81	310	0.67	13.2	35.1	26.3	0.093	0.7	0.104	0.67	0.12	1.07	3400	0.316
82	310	0.67	14.0	25.5	16.8	0.05	0.7	0.104	0.55	0.12	0.78	37550	3.5
83	310	0.67	14.0	-	-	-	0.7	0.104	0	0.12	-	250000	23.2

Note: Initial scour hole generated by the current in Test 5. Large pile experiments

4.4. Backfilling process

The backfilling process will be described by reference to Figs. 4.5 and 4.6. Fig. 4.5 displays a sequence of pictures of the bed morphology obtained in Test 47 using the previously mentioned 3D optical technique. Fig. 4.5a depicts the equilibrium scour hole generated by the current in Test 1 (Table 4.1). Upon the completion of the scour process, the current was stopped, and then the waves (Test 47, $KC_f = 11$) were switched on. With this, the scour hole was backfilled, Fig. 4.5b-d, illustrating the time evolution of the backfilling process.

Fig. 4.6 displays the time series of the depth of the scour hole monitored at the offshore side of the pile during the backfilling described in conjunction with Fig. 4.5. The quantity S_i is the initial depth of the scour hole (the scour depth generated by the current in Test 1), and S_t is the depth of the scour hole during the backfilling process. As seen, the backfilling develops towards an equilibrium stage through a transitional period. The depth of the scour hole corresponding to this equilibrium stage is S (Fig. 4.6), to be termed the equilibrium scour depth for easy reference. (Fig. 4.1b gives the definition sketch for the latter quantity.)

It is seen that, for a substantial amount of backfilling to develop, a certain amount of time must elapse. This time is called the time scale of backfilling process. The latter can be defined in several ways, as in the case of scour process (e.g. Sumer and Fredsøe, 2002), the following definition will be adopted in the present treatment:

$$S_t = S + (S_i - S)\exp(-\frac{t}{T}) \tag{4.9}$$

in which T is the time scale of backfilling process, and corresponds to the time T indicated in Fig. 4.6; the dashed line in Fig. 4.6 is tangent to the scour-depth-versus-time curve at time t = 0.

The two quantities, namely, S, the equilibrium scour depth; and T, the time scale, are two major parameters of the backfilling process (Fig. 4.6). Each parameter will now be considered individually.

4.5. Equilibrium scour depth

4.5.1. Wave case

Fig. 4.7 displays the equilibrium scour depth plotted in the familiar form S/D versus the KC number (Sumer and Fredsøe. 2002). There are two kinds of experiments associated with the data plotted in Fig. 4.7: (1) Scour experiments with an initially flat bed (square symbols in the figure); and (2) Backfilling experiments with an initially scoured bed where the initial scour hole was generated either by current (circle symbols), or by waves (triangle symbols).

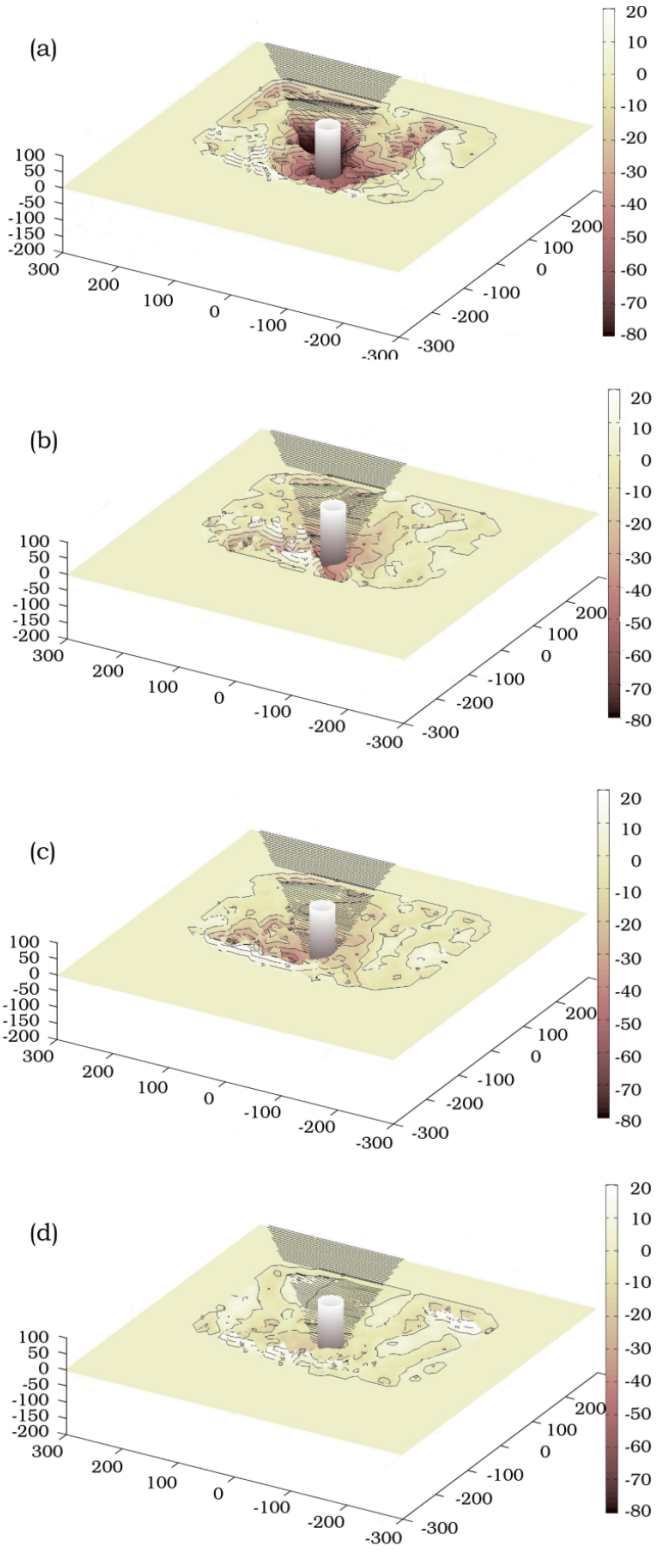

Fig. 4.5. Test 47: sequence of 3-D pictures illustrating the time evolution of backfilling: (a) t = 0; (b) t = T/2; (c) t = T; and (d) t ∼5T in which T is the time scale of the backfilling process equal to 2350 s (Table 4.4)

The scour-depth data plotted in Fig. 4.7 (the square symbols) compares well with Sumer et al.'s (1992) corresponding data, represented by

$$\frac{S}{D} = 1.3\left\{1 - \exp\left[-0.03(KC_f - 6)\right]\right\} \tag{4.10}$$

(the solid curve in Fig. 4.7), the empirical expression given in Sumer et al. (1992). Note that the latter expression is valid for the live-bed regime scour, $\theta_f > \theta_{cr}$. The Sumer et al. (1992) data is not plotted in Fig. 4.7 to keep the figure relatively simple.

Now, from Fig. 4.7, the scour-depth data obtained in the scour experiments (squares) and that obtained in the backfilling experiments (circles and triangles) practically coincide. This is an important result. It essentially implies that, regardless of the initial scour hole geometry (no matter whether the bed is initially flat, or scoured, or whether the initial scour hole is generated by steady current or by waves), the equilibrium scour depth of the backfilling process will be the same as that of the ordinary scour process for the same Keulegan-Carpenter number. This can be explained as follows.

Fig. 4.8 shows the result of a typical particle tracking experiment. As mentioned under Section 4.2.1. these tests were carried out in regular waves. With $KC_f = 11$. The particles were released at time $t = 0$, and their trajectories were videotaped for a time period of 20 minutes. As seen clearly from Fig. 4.8, the particles are brought into the scour hole from the areas offshore, onshore and the sides of the scour hole, in the way illustrated in Fig. 4.8. (Incidentally, the particle trajectories appear to be orthogonal to the perimeter of the scour hole, largely due to the fact that the perimeter of the scour hole acts as a "potential line", drawing an analogy to a sink flow in potential flow theory.) Fig. 4.8 implies that the actual sand particles are brought into the scour hole from outside, in all directions

Now, being in the scour hole, the sediment will subsequently be redistributed in the scour hole by the existing vortex flow around the pile. This is precisely the mechanism for the ordinary/familiar scour process around a pile, as described in Sumer et al. (1992. 1993), or see Sumer and Fredsøe (2002). Therefore, the equilibrium stage of the backfilling process should be governed by precisely the same mechanism as that experienced in the scour process. Hence, for a given Keulegan-Carpenter number, the equilibrium scour depth in the backfilling process should be the same as that of the scour process, as revealed by Fig. 4.7.

4.5.2. Combined wave and current case

Small pile experiments

Fig. 4.9 displays the results obtained in the case of combined wave and current. Again, the figure presents the results of two kinds of experiments: (1) Scour experiments with an initially flat bed (square symbols); and (2) Backfilling experiments with an initially scoured

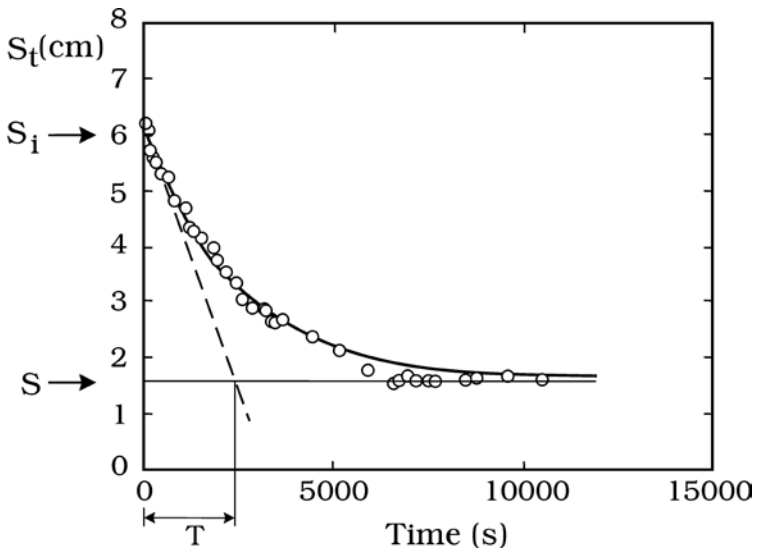

Fig. 4.6. Time series of depth of scour hole monitored at offshore side of pile during backfilling displayed in Fig. 4.5. Test 47.

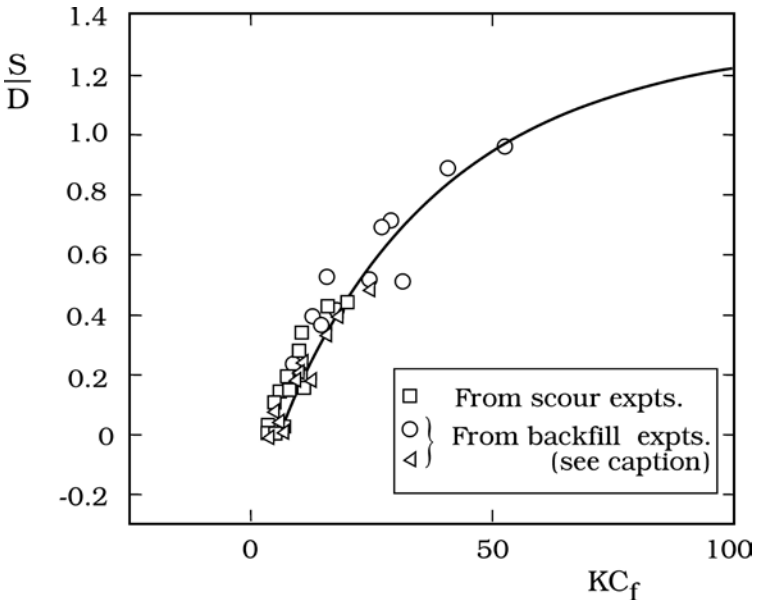

Fig. 4.7. Equilibrium scour depth; solid line: empirical equation given in Sumer et al. (1992) for the depth of scour hole generated by waves in the case of an initially flat bed Eq. (4.10). Squares: From present scour experiments (with an initially flat bed). Circles and triangles: From present backfill experiments (with initially scoured bed).

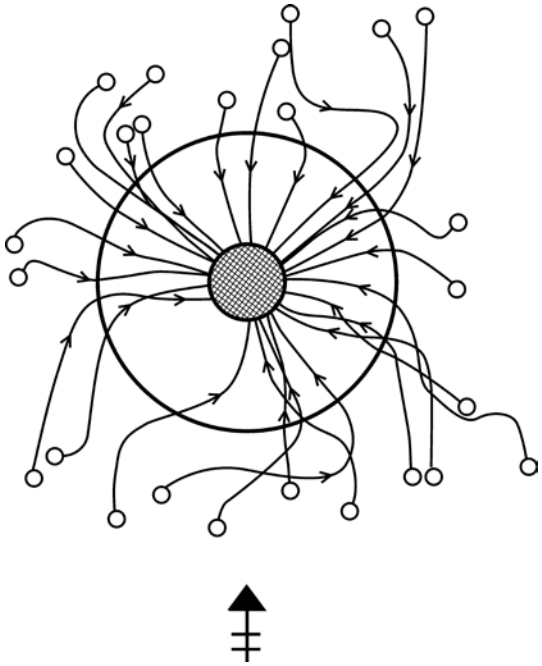

Fig. 4.8. Trajectories obtained in particle tracking experiment: regular waves with $KC_f = 11$. Circles are the points where particles are released.

bed (circle symbols). We note that the present scour data compares well with Sumer and Fredsøe's (2001 a) corresponding data (also reproduced in Sumer and Fredsøe. 2002). The solid lines in the figure represent the empirical expression given in Sumer and Fredsøe (2001 a) approximating the variation of S/D data as a function of KC and U_{cw}:

$$\frac{S}{D} = \frac{S_c}{D}\left[1-\exp\left\{-A\,(KC-B)\right\}\right]; \quad KC \geq B \tag{4.11}$$

in which S_c is the scour depth in the case of the current alone, and A and B are given as follows

$$A = 0.03 + \frac{3}{4}U_{cw}^{\;2.6} \tag{4.12}$$

and

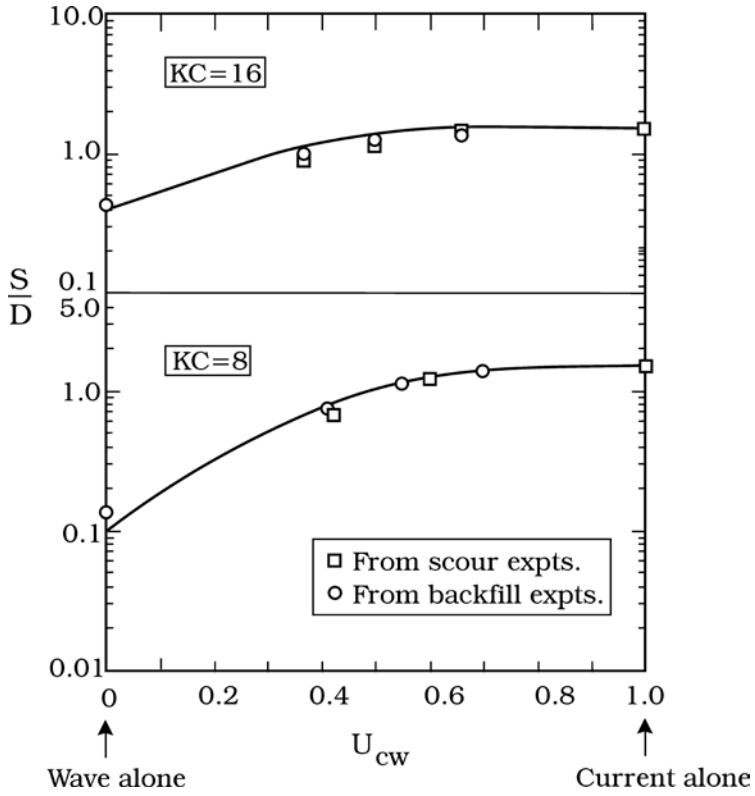

Fig. 4.9. Equilibrium scour depth. Solid line: Empirical equation given in Sumer and Fredsøe (2002) for the depth of scour hole generated by combined waves and current. Eq. (4.11). Squares: From present scour experiments (with an initially flat bed). Circles: From present backfill experiments.

$$B = 6\exp(-4.7U_{cw}) \tag{4.13}$$

by Sumer and Fredsøe (2002) note that caution must be exercised when the above equation is implemented for KC numbers larger than the upper bound of the tested range, namely for $KC \gtrsim 30$, and the equation is valid for the live-bed scour regime. Again, Sumer and Fredsøe's (2001 a) data are not plotted in Fig. 4.9 to keep the figure simple. Similar to Fig. 4.7, here, too, the scour depths obtained in the scour experiments and those obtained in the backfilling experiments practically coincide. This can be explained in the same way as in the wave case, namely, the final (equilibrium) scour depth in the backfilling process is essentially controlled by the same mechanism as that in the scour process.

Large pile experiments

The equilibrium scour-depth data obtained in the present backfill experiments are plotted in Fig. 4.10. In these experiments, the bed was initially scoured by the current in Test 5 (Table 4.1). Sumer and Fredsøe's (2002) empirical expression in Eq. (4.11) for small piles is also plotted in Fig. 4.10 for two KC numbers for reference purposes. It should be noted that the diffraction effect in Sumer and Fredsøe's (2001a) experiments was practically nil ($D/L \to 0$). The new data with the diffraction parameter being finite (yet not very large) appears to be

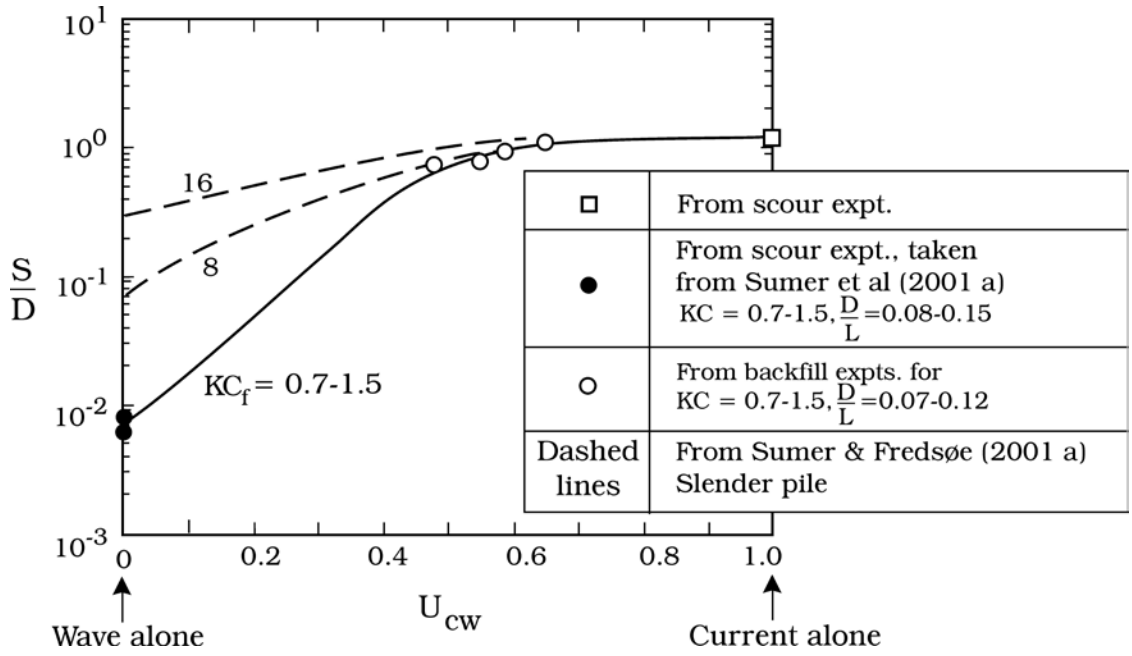

Fig. 4.10. Equilibrium scour depth in the case of large pile; dotted lines are plotted in the diagram as two reference lines.

consistent with the picture exhibited in Fig. 4.10. We note that, to our knowledge, no scour data exist in the literature for large piles exposed to combined waves and current.

The flume where the present experiments were conducted was available only for a limited period of time, and therefore no scour experiments in combined waves and current were carried out with an initially flat bed with the large pile. Thus we were unable to check whether or not the equilibrium scour depth in the present backfilling experiments is the same as that in scour experiments with the same wave and current conditions.

4.6. Time scale of backfilling process

4.6.1. Backfilling under waves

The time scale of the backfilling process T was obtained from the scour depth time series, using the tangent method according to the definition given in Eq. (4.9) and Fig. 4.6. The data are included in Tables 4.4-4.6.

On dimensional grounds, the time scale can be written in the following non-dimensional functional form:

$$T^* = f(KC_i, KC_f, \theta_f) \tag{4.14}$$

in which T^* is the nondimensional time scale defined by Eq. (4.8); KC_i is the

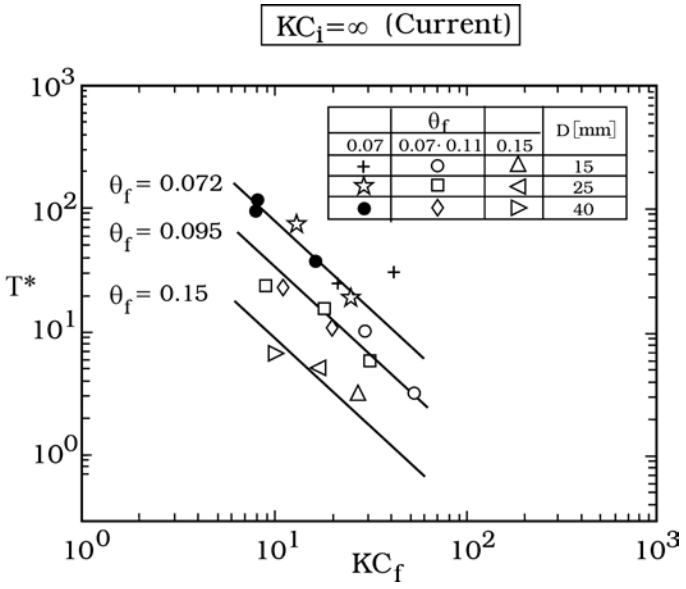

Fig. 4.11. Normalized time scale of backfilling where the initial scour hole is generated by a current with the initial scour depth corresponding to the equilibrium scour. This scour hole is subsequently subjected to waves to cause backfilling. Live bed $(\theta_f > \theta_{cr})$.

Keulegan-Carpenter number corresponding to the initial scour depth S_i (i.e. S_i is generated by a wave/current with the Keulegan-Carpenter number KC_i, with S_i corresponding to the equilibrium stage of the scour process); and KC_f and θ_f are, respectively, the Keulegan-Carpenter number and the Shields parameter corresponding to the wave which backfills the scour hole.

The following is true in Eq. (4.14): (1) KC_i is involved simply because it controls S_i, the initial scour depth, for the live-bed regime (Sumer et al. 1992; Sumer and Fredsøe, 2002); (2) KC_f is involved because it controls the equilibrium (or final) scour depth in the backfilling process; and (3) θ_f is involved because the time scale of the backfilling process, which is influenced by θ_f, similar to what occurs in the scour process (Sumer and Fredsøe, 2002).

It should be noted that all the above quantities, namely KC_i, KC_f and θ_f, correspond to the undisturbed flow, in the absence of the pile.

Now, in the case of the backfilling experiments with an initially scoured bed with the initial scour hole generated by current (i.e. $KC_i = \infty$), Eq. (4.14) reduces to

$$T^* = f(KC_f, \theta_f) \tag{4.15}$$

The time scale data corresponding to the $KC_i = \infty$ experiments are plotted in Fig. 4.11. First of all, the figure shows that the time scale decreases with increasing KC_f. This is because the larger the value of KC_f, the larger the equilibrium scour depth, and therefore the time needed for the waves to backfill the scour hole should be smaller. The figure also shows that the time scale decreases with increasing θ_f. This is because the larger the value of θ_f, the larger the sediment transport, and therefore the smaller the time scale of the backfilling.

The variation of the time scale, T^*, with KC_f and θ_f in Fig. 4.11 can be represented by the following empirical expression

$$T^* = (\theta_f^{\,2}\ KC_f)^{-1.45} \tag{4.16}$$

This equation is valid for the live bed conditions. i.e. $\theta_f > \theta_{cr}$. It should also be noted that the ranges of the parameters for which the data were collected are $8 \lesssim KC_f \lesssim 50$ and $\theta_{cr} \lesssim \theta_f \lesssim 0.15$, and therefore caution must be observed when extrapolating the preceding equation to areas outside the indicated ranges.

At this juncture, it will be interesting to compare the time scale of the backfilling process with that of scouring, although these are two entirely different processes (save the final stages of the backfilling process, however, see the previous discussion). Considering that, for example, for windfarm applications, the KC is of order KC < O(10); comparison of the present findings (Fig. 4.11) with the time scale of scour (Sumer et al. 1993; Sumer and Fredsøe, 2002) shows that the time scale of backfill is much larger than that of scour. For example, for $KC = 10$, the time scale for $\theta = 0.07$ is $T^* = 80$ (from Fig. 4.11) for backfilling, $T^* = 2$ for scour (Sumer et al. 1993); likewise, for θ = 0.15, $T^* = 9$ for backfilling and $T^* = 0.2$ for scour. However, for larger *KCs*, such as $KC \gg O(10)$, this exercise indicates that the time scale of scour can be larger than that of backfilling. This is also not unexpected, because the scour depth for such large *KCs* is very close to that generated by steady current, and therefore the time needed to backfill the scour hole will be substantially smaller.

Now, turning our attention to the case of the backfilling experiments with an initially scoured bed where the scour hole is generated by waves ($KC_i \neq \infty$) Eq. (4.14), the time scale data obtained in these experiments are plotted in Fig. 4.12 where the horizontal axis is selected to be the product $\theta_f^2 KC_f$, considering Eq. (4.16). The data presented in Fig. 4.11 is also plotted in Fig. 4.12 ($KC_i = \infty$. circle symbols). Line A in Fig. 4.12 represents the expression given by Eq. (4.16).

Fig. 4.12 indicates that the time scale decreases with decreasing KC_i, the Keulegan-Carpenter number corresponding to the flow climate generating the initial scour hole. This is because the smaller the value of KC_i. the smaller the initial scour depth; and therefore the time needed to backfill the scour hole should be smaller, as revealed by Fig. 4.12. The time scale data corresponding to the initially scoured bed generated by waves (Fig. 4.12) can be represented by the empirical expression (Lines B in Fig. 4.12)

$$T^* = (70\,\frac{KC_f}{KC_i}\,\theta_f^{\,2})^{-1.45} \tag{4.17}$$

Similar to Eq. (4.16), the above equation is valid for the live-bed regime, $\theta_f > \theta_{cr}$. Also, caution must be exercised when extrapolating Eq. (4.17) outside the ranges of the parameters for which the data were collected, namely, $4 \leq KC_f \leq 25$ and $\theta_{cr} \leq \theta_f \leq 0.15$. As previously mentioned, the live-bed regime in the backfilling experiments ensures that backfilling will take place.

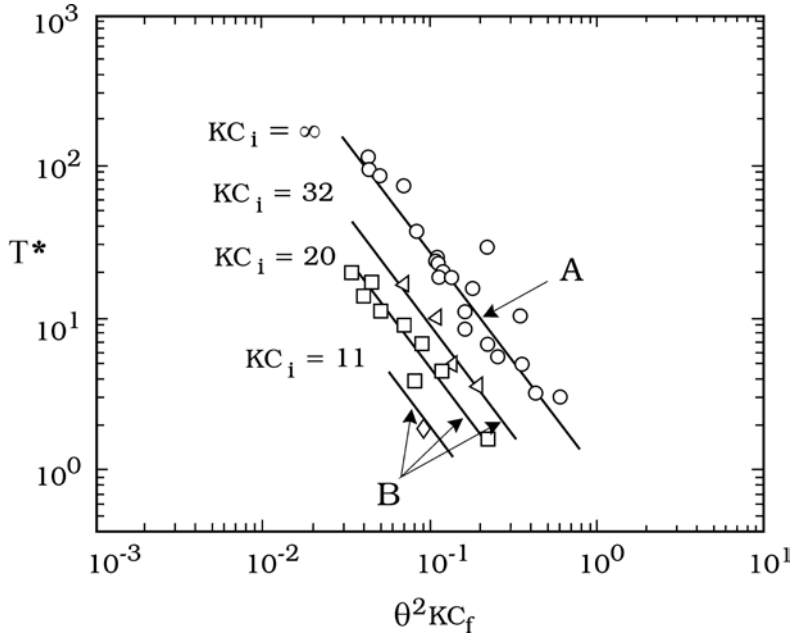

Fig. 4.12. Normalized time scale of backfilling where the initial scour hole is generated by a wave with the initial scour depth corresponding to the equilibrium scour. Live bed $(\theta_f > \theta_{cr})$.This scour hole is subsequently subjected to smaller waves to cause backfilling. $KC_i = \infty$ case corresponds to the current case displayed in Fig. 4.11. Line A: Eq. (4.16). Lines B: Eq. (4.17).

4.6.2. Backfilling under combined waves and current

Small pile experiments

The equilibrium scour depth in the case of combined waves and current has been discussed in conjunction with Fig. 4.9. Fig. 4.9 suggests that the equilibrium scour depth in the case of combined waves and current approaches the current values when the current-wave velocity ratio is $U_{cw} \gtrsim 0.7$, a result first revealed by Sumer and Fredsøe's (2001a) experimental data. Presumably, one would expect that, that for $U_{cw} \gtrsim 0.7$, no significant backfilling would occur in combined waves and current, where the initial scour hole is generated by current or waves (waves with very large KC_i, and therefore the initial equilibrium scour depth S_i is close to that generated by current). For that reason, the backfilling tests of the present experiments were designated in order for $U_{cw} \lesssim 0.7$ (Table 4.5). In these experiments, the initial scour hole was generated by the current of Test 1 (Table 4.1).

The time scale in the case of waves is given by Eq. (4.14). In the case of combined wave and current, there will be one additional parameter, U_{cw}, and therefore Eq. (4.14) in this case will read

$$T^* = f(U_{cw}, KC_i, KC_f, \theta_f) \tag{4.18}$$

and. in the case of the backfilling with an initially scoured bed with the initial scour hole generated by current ($KC_i = \infty$), the above equation will reduce to

$$T^* = f\left(U_{cw}, KC_f, \theta_f\right) \tag{4.19}$$

Now, the present combined wave and current data are plotted in Fig. 4.13 in the form of T^* versus U_{cw} for various pairs of KC_f and θ_f, with KC_f ranging from 4 to 20, and θ_f from 0.07 to 0.11. In Fig. 4.13, the plotted data on the vertical axis is that collected in the previously described wace-case backfilling experiments, except the data point corresponding to KC_f = 4; this latter data point was obtained from the empirical expression in Eq. (4.16).

For a given set of KC_f and θ_f, the time scale appears to decrease with increasing U_{cw}. This is because the larger the value of U_{cw}, the larger the scour depth (Fig. 4.8). This means that the time for the combined flow to backfill the scour hole will be relatively smaller with larger U_{cw}, as revealed by Fig. 4.13.

The limited data in Fig. 4.13 can be represented by the following empirical expression

$$T^* = 1.9 - C\,(U_{cw} - 0.7) \quad \text{with} \quad U_{cw} < 0.7 \tag{4.20}$$

in which the coefficient C is

$$C = \frac{0.65}{\left[\theta_f^{\,2}\; KC_f - 0.01\right]^{1.68} + 2} \tag{4.21}$$

The solid curves in Fig. 4.13 represent the above expression. Eqs. (4.20) – (4.21) while the horizontal lines (dashed lines) represent Eq. (4.16). The above equation is valid for the live-bed, regime, $\theta_f > \theta_{cr}$. Also, caution must be exercised when extrapolating Eq. (4.20) outside the ranges of the parameters for which the data were collected, namely $4 \leq KC_f \leq 20$ and $\theta_{cr} \leq \theta_f \leq 0.11$. It may be noted that the representation in Fig. 4.13 enables the time scale in the combined flow case to be predicted by the following procedure: (1) Calculate T^*, using the above equations, Eqs. (4.20)-(4.21); (2) If the T^* value exceeds the value calculated from Eq.(4.16), then adopt the value calculated from Eq. (4.16); (3) Otherwise, retain the value calculated from Eqs. (4.20)-(4.21).

Large pile experiments

Similar to the small pile case, the equilibrium scour depth in the case of combined current and waves approaches the current value when the current-wave velocity ratio is $U_{cw} \gtrsim 0.7$ (Fig. 4.10). Therefore, for $U_{cw} \gtrsim 0.7$ it is expected that no significant backfilling occur in combined waves and current in the backfilling experiments. The data (limited in size. as

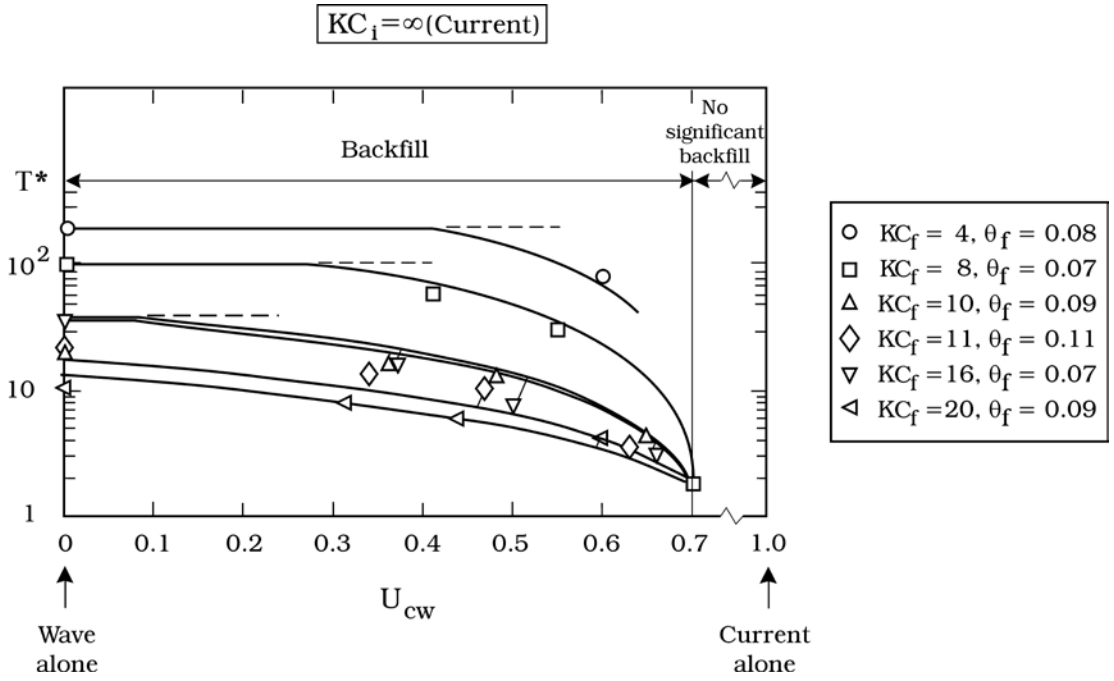

Fig. 4.13. Normalized time scale of backfilling where the initial scour hole is generated by a current with the initial scour depth corresponding to the equilibrium scour. Live bed $(\theta_f > \theta_{cr})$. This scour hole is subsequently subjected to combined waves and current to cause backfilling. No diffraction effect with D/L → 0. Solid curves: Eq. (4.20). Horizontal (dashed) lines: Eq. (4.16).

pointed out earlier) are plotted in Fig. 4.14. The variation in Fig. 4.14 is mainly due to the change in the Keulegan-Carpenter number, KC_f, as the values of the diffraction parameter, D/L, for the two cases plotted in the figure are rather close to each other, and therefore the time scale picks up the variation due to the change in KC_f. In this context, while the change in the flow pattern and in the resulting scour is not very significant when D/L changes from 0.07 to 0.12 (Sumer and Fredsøe, 2002, 2006), the opposite is true when KC_f changes from 0.7 to 1.5 (Sumer and Fredsøe, 2006, Fig. 3.2; Sumer and Fredsøe 2002, Fig. 6.18 and 6.19).

The variation of the time scale with U_{cw} can be explained in the same manner as in Fig. 4.13, and that with KC_f in the same manner as in Fig. 4.11.

Finally, the variation of the time scale with the parameters U_{cw} and KC_f can be represented by

$$T^* = -\frac{15.15}{KC_f^{\,2.38}}(U_{cw} - 0.7) \tag{4.22}$$

Eq. (4.22) is valid for the live-bed regime, $\theta_f > \theta_{cr}$. Also, similar to the previous cases, caution must be exercised when extrapolating Eq. (4.22) outside the ranges of the parameters for which the data were collected., namely, $0.7 \le KC_f \le 1.5$ and $\theta_{cr} \le \theta_f \le 0.1$.

4.7. Discussion

As previously mentioned, Fredsøe et al. (1992) studied backfilling below a pipeline, while Hartvig et al. (2010) studied backfilling around a pile. This section will discuss these studies as related to the present work.

The present findings agree with those of Fredsøe et al. (1992) in the sense that

- The depth of a backfilled scour hole for a given KC_f is the same as the scour depth obtained with an initially flat bed and with the same KC_f;
- The time scale of backfilling is a function of the initial KC. the final KC and the final Shields parameter, namely, KC_i, KC_f and θ_f, respectively; and
- The way in which the time scale of backfilling varies with these parameters is qualitatively the same in both studies

Regarding Hartvig et al.'s (2010) work. Hartvig et al. (2010) point out that the scour-depth development formula of Sumer et al. (1992) (also used in the present analyses) provides a fair fit to their test results.

Second, they report that initially, current-scoured beds, when subjected to waves, are

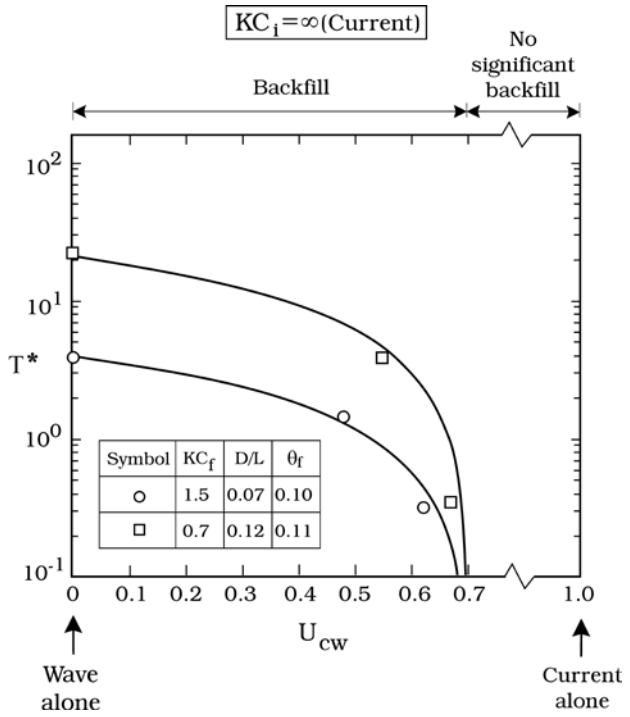

Fig. 4.14. Normalized time scale of backfilling where the initial scour hole is generated by a current with the initial scour depth corresponding to the equilibrium scour. Live bed $(\theta_f > \theta_{cr})$. This scour hole is subsequently subjected to combined waves and current to cause backfilling. Diffraction parameter. D/L, is finite; Solid curves: Eq. (4.22).

backfilled about 10 times slower than when they are scoured, a result similar to obtained in the current study for $KC < O(10)$.

Finally, the time resolution of the scour and backfilling measurements of Hartvig et al. (2010) is unfortunately too coarse to enable them to determine the time scale in a precise manner, and therefore their time-scale values are not conclusive. The experimental determination of the time scale (Sumer and Fredsøe. 2002) requires a very fine time resolution in monitoring the depth of the hole during the scour or the backfilling process (time resolution 0.04s of the present tests, see the discussion under the Wave Flume section and Fig. 4.6 to recall the formal definition of the time scale of backfilling. the quantity *T*). Hartvig et al. (2010) note that some of their test runs were impaired by one or more of the following uncertainties: few or short test runs, uncertain flow information, influence of standing waves, and global erosion. Hence, no direct comparison was made with the Hartvig et al. (2010) time scale data in the present paper.

4.8. Conclusions

1. Backfilling of a scour hole around a pile in the live-bed regime occurs when the flow climate changes from a steady current to a wave; or from a steady current to a combined wave and current; or from a wave to a smaller wave.
2. The scour depth corresponding to the equilibrium state of backfilling is the same as that corresponding to the equilibrium state of scour around the pile for the same wave (or combined wave and current) climate. Therefore the empirical equations developed from the previous research on scour can be used for the depth of the scour hole backfilled by the wave (or by the combined wave and current).
3. The time scale (normalized) is a function of: the initial Keulegan-Carpenter number associated with the initial scour hole (before the backfilling); and the Keulegan-Carpenter number, and the Shields parameter associated with the backfilling. This is for the case when the scour hole is backfilled with waves. Eq. (4.17). The time scale is a function of the same parameters as well as the current-velocity-to-wave-velocity ratio when the scour hole is backfilled with combined waves and current, Eqs. (4.20)-(4.21).
4. The time scale of the backfilling process is completely different from that of scour, because the scour process and the backfilling process are two entirely different processes. The time scale of backfilling is much larger than that of scour when the backfilling Keulegan-Carpenter number is $KC <$ O(10), while the time scale of backfilling can be smaller than that of scour when $KC \gg$ O(10).

Acknowledgement. This study was partially funded by the Danish Council for Strategic Research (DSF)/Energy and Environment Program "Seabed Wind Farm Interaction"; Statkraft AS (Norway) “SOERP - Statkraft Ocean Energy Research Programme”; and Danish GTS-universitetssamarbejde project “Fremtidens Marine Konstruktioner”.

Chapter 5

Time scale of scour around a pile in combined waves and current

This chapter is published in the Proceedings of the 6th International Conference on Scour Erosion, ICSE, Paris, France, August, 2012.

T. U. Petersen[1], B. M. Sumer[2] & J. Fredsøe[3]

[1]Ph.D. – candidate, [2]Professor, [3]Professor, Technical University of Denmark. Section for Fluid Mechanics, Coastal and Maritime Engineering. Kgs. Lyngby, Denmark.

Abstract: The time scale of the scour process around a circular vertical pile is studied in combined waves and current. A series of tests were carried out in a flume with pile diameters 40 mm and 75 mm, in both steady current, waves and combined waves and current. In the combined wave and current flow regime the waves and the current were co-directional. All the tests were conducted in the live bed regime. The time scale of scour in combined waves and current is governed by three parameters, namely the current-velocity-to-wave-velocity ratio (U_{cw}), the Keulegan–Carpenter number (KC) and Shields parameter (θ_w). The time scale of scour increases significantly when even a slight current is superimposing on a wave. The KC dependence of the time scale T is mainly observed for low values of U_{cw} in the wave dominated regime. For U_{cw} values larger than 0.4 no clear KC dependency was observed. The time scale decreases with increasing θ_w over the entire range of U_{cw}.

Key words: Coastal Structures, slender piles, offshore structures, pile, scour, time scale, vertical cylinder, steady current, wave, offshore wind farm.

5.1. Introduction

Many offshore wind farms are currently being planned, designed and constructed offshore in increasingly harsh environment. The pile foundations are often exposed to strong tidal currents and large waves individually and in combination. Scour around a circular vertical

pile has received a substantial amount of attention over the last decades, revealing many features of scour in steady current, in waves, as well as in combined waves and current. A detailed account has been given on the topic in the books of Whitehouse (1998) and Sumer and Fredsøe (2002), and in a recent review paper by Sumer (2007). Of particular interest is scour characteristics in a flow environment where waves and current are present concurrently. Although previous work reveals various features of scour processes (such as the scour depth) in combined waves-and-current environment (Sumer and Fredsøe, 2001a, Raaijmakers and Rudolph, 2008a, 2008b), no study is yet available, investigating in a systematic manner the time scale of the scour process, an important quantity needed to develop engineering models to predict scour history around piles for large times (months, years).

To this end, an experimental program of physical model tests has been carried out. The results show that the time scale of scour increases significantly when superimposing even a slight current on a wave flow regime. The results further show that the time scale of scour approaches the wave-alone time scale in the wave-dominated regime, and it approaches the current values in the current-dominated regime.

5.2. Experimental Setup

The experiments were carried out in a flume where the waves and current were co-directional. The flume was 0.6 m wide, 0.8 m deep and 28 m long. The water depth was maintained constant at h = 40 cm. Two plastic model piles were used with diameters D = 75 and 40 mm. The depth of the sand pit in the flume was 20 cm, the grain size of the sand was d_{50} = 0.17 mm and the sediment gradation $\sigma_g = \sqrt{d_{84}/d_{16}}$ = 1.3.

The development of scour depth over time was monitored by video in the same fashion as described by Sumer et al. (1992a, 1993). In the present experiments the objective was to examine the time scale of scour and therefore continuous video logging of the upstream scour depth was needed throughout every test series. The scour depth was measured at every 3 seconds for the first 5 minutes of each test, at every 10 min within the next 20 minutes, at every half hour for the rest of the test duration. A test lasted between 1 – 8 hours.

Three kinds of experiments were conducted: (1) Current-alone experiments, (2) Wave-alone experiments, and (3) Combined-waves-and-current experiments.

5.2.1. Current-alone experiments

The current was achieved by recirculating water in the flume. The velocity profiles in both vertical and transverse directions were measured by using a DANTEC laser Doppler anemometer (LDA) utilizing a forward scatter method.

5.2.2. Wave-alone experiments

Irregular waves were used throughout the test series to avoid large scale bed undulations, which were observed in regular wave test with test durations larger than O(2 hours). The waves were produced by piston-type wave generator. A measured in-situ water elevation spectrum for the North Sea storm conditions was used as the control spectrum to generate a displacement signal for the wave generator. The spectrum was well described by the JONSWAP wave spectrum. To handle the reflection an Active Wave Absorption Control System (AWACS) was applied. The AWACS system was developed by DHI Water & Environment for control of wave generators in wave flumes, Schäffer et al. (1994). To

further reduce the reflection a wave absorber was placed at the downstream end of the flume.

5.2.3. Combined-waves-and-current experiments

The velocity corresponding to the current part of the combined-waves-and-current flow climate ranged from V = 12.4 cm/s to V = 38.6 cm/s, where V is the depth averaged current velocity. The presence of the wave absorber at the downstream end of the flume demanded an increase in the water level (which was maintained constant in the wave-alone and current-alone experiments) when the steady current was initiated. The measurements showed an increase of the water level of approx 0.4 % at V = 12.4 cm/s, 1.7 % at V = 20.9 cm/s and 9.1 % at V = 38.6 cm/s. In order to accommodate this increase in water level with increasing current velocity, the initial water level was lowered in accordance with this. This procedure enabled a constant water level at h = 40 cm throughout every test.

The procedure used in the combined waves and current scour experiments:

1. Level off the bed
2. Introduce the wave
3. Introduce the current
4. From the obtained time series of scour depth, find the equilibrium scour depth and time scale (i.e. S_0 and T respectively Fig. 5.2).

5.3. Test Conditions

The test conditions and experimental results are shown in Table 5.1. In the table, f_p = peak frequency of the wave power spectrum and $U_m$is the orbital velocity at the bed given by

$$U_m = \sqrt{2}\sigma_U \tag{5.1}$$

in which σ_U is the root-mean-square (RMS) value of the orbital velocity U at the sea bed, calculated by

$$\sigma_U^2 = \int_0^\infty S_U(f)df \tag{5.2}$$

in which $S_U(f)$ defines the power spectrum of U and f is the frequency of the waves. Note that U_m becomes identical to the maximum value of the bottom orbital velocity for small amplitude sinusoidal waves.

The Keulegan-Carpenter number KC in the table is based on U_m and f_p:

$$KC = \frac{U_m}{Df_p} = \frac{\sqrt{2}\sigma_U}{Df_p} \tag{5.3}$$

This definition of the KC number has been adopted from Sumer and Fredsøe (2001) who made an analysis of how to define KC in irregular waves, and found that the combination of U_m and f_p in Eq. (5.3) gives the best representation.

The current velocity U_c in the table is taken as the undisturbed current velocity measured at the distance D/2 from the bed. U_c represents the characteristic velocity near the bed; the definition has been used previously by Sumer and Fredsøe (2001), and in Fredsøe et al. (1992) in the case of combined waves and current scour below pipelines.

Live-bed conditions prevailed throughout the test series. The Shields parameter of the wave component of the flow is described with range $\theta = 0.07 - 0.16$ whereas in the steady current alone test $\theta = 0.13$. The θ values are hence larger than the critical value of the Shields parameter for initiation of motion of the sediment particles at the bed. The formation of ripples on the sea bed in every test also revealed the live bed situation. The Shields parameter is defined by following relation

$$\theta = \frac{U_f^2}{g(s-1)d_{50}} \tag{5.4}$$

in which U_f is the undisturbed friction velocity in the case of steady current calculated by the Colebrook-White formula (Schlichting, 1979). In the case of waves U_f is replaced by U_{fm} which was calculated by the method of Fredsøe (1984).

For reasons of space the test conditions table (Table 5.1) is given in terms of ranges of the quantities. However detailed test conditions and test results are availbale from the first author.

5.4. Results and Discussion

5.4.1. Scour depth in current-alone and waves-alone cases

The scour process around piles occur due to increased sediment transport capacity in the vicinity of the pile, which in turn is a result of increased bed shear stress. In the case of current, the scour is caused by the combined action of the horseshoe vortex in front of the pile and the contraction near the sides.

The scour process reaches its equilibrium scour depth at $S/D = 1.3$ with $\sigma_{S/D} = 0.7$ (Sumer and Fredsøe, 2002). The present measurements agree well with the latter range.

In the case of waves the scour process is mainly governed by the vortex shedding mechanism which can be described as a function of the Keulegan-Carpenter number KC. Vortices formed behind the pile pick up the sediment, and when they are shed the sediment is convected away from the pile. This mechanism is governed by the KC number and Sumer et al. (1992a) give the following empirical expression for the equilibrium scour depth in waves:

$$\frac{S}{D} = 1.3\{1 - exp[-0.03(KC - 6)]\}; \quad KC \geq 6 \tag{5.5}$$

The present data agree well with the expression given in Eq. (5.5).

Table 5.1. Test conditions

Test number	Pile diameter D [mm]	Peak frequency of waves f_p [hz]	Bed orbital velocity U_m [cm/s]	Maximum value of bed friction velocity in waves U_{fm} [cm/s]	Depth averaged current velocity V [cm/s]	Undisturbed current velocity at D/2 U_c [cm/s]	Keulegan - Carpenter number KC [-]	Shields parameter θ [-]	U_{cw} [-]
1 - 12	40 - 75	0.25 - 0.4	12.4 - 15.5	1.4	0.0 - 38.6	0.0 - 30.2	4 - 16	0.07	0.0 - 0.72
13 - 34	40 - 75	0.25 - 0.4	16.0 - 19.8	1.6 - 1.7	0.0 - 38.6	0.0 - 30.2	5 - 20	0.09 - 0.10	0.0 - 0.67
35 - 42	40 - 75	0.67	20.2	2.0	0.0 - 38.6	0.0 - 32.1	4 - 8	0.15	0.0 - 0.61
43	40	-	-	-	38.6	30.2	-	0.13	1
44	75	-	-	-	38.6	32.1	-	0.13	1

5.4.2. Scour depth in combined waves and current case

The equilibrium scour depths found in the present combined waves and current experiments are plotted in Figure 5.1 as a function of the current-velocity-to-wave-velocity ratio U_{cw} defined by:

$$U_{cw} = \frac{U_c}{U_c+U_m} \tag{5.6}$$

We note that the test setup makes it impossible to cover the range of $U_{cw} < 0.3$. To cover this range very low current velocities would have been required, and this was practically impossible to achieve and control. We further note that the present scour data compares well with the data of Sumer and Fredsøe (2001). The solid lines in the figure represent the empirical expression given in Sumer and Fredsøe (2002, representing the data reported in Sumer and Fredsøe, 2001):

$$\frac{S}{D} = \frac{S_c}{D}[1 - exp\{-A(KC - B)\}]; \qquad KC \geq B \tag{5.7}$$

in which the KC number corresponds to the wave alone situation and S_c is the scour depth in current-alone, and the quantities A and B are given as follows:

$$A = 0.03 + \frac{3}{4}U_{cw}^{2.6} \tag{5.8}$$

$$B = 6\, exp(-4.7\mathrm{U_{cw}}) \tag{5.9}$$

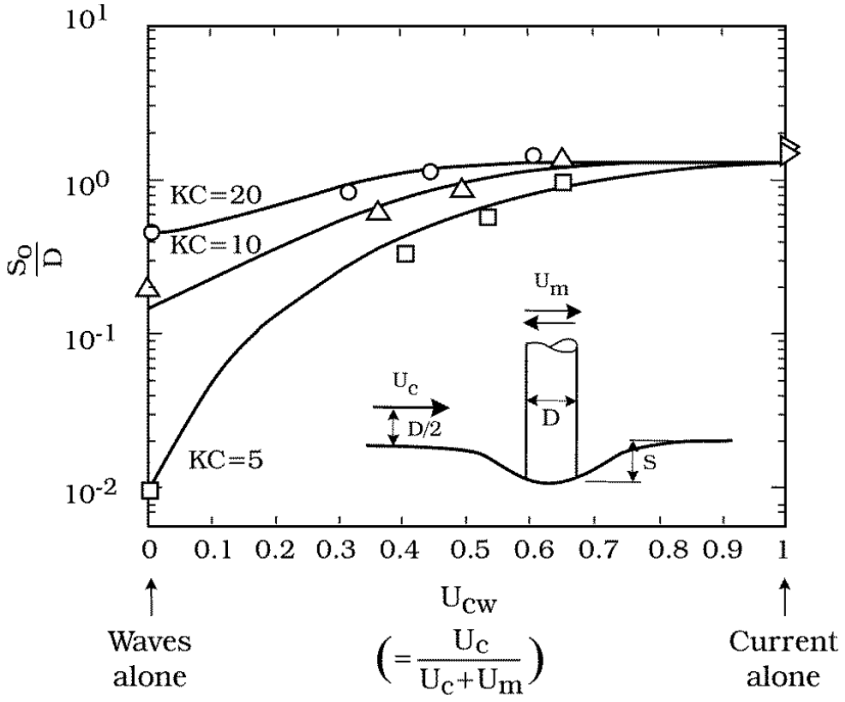

Figure 5.1. Observed equilibrium scour depth in combined waves and current. Live bed ($\theta > \theta_c$).

5.4.3. Time scale of scour in waves-alone and current-alone cases

When a pile is placed on an initially plane sediment bed, the scour will approach the equilibrium scour depth through a transitional period. The time development of scour in both steady current, waves and combined current and waves can be expressed by following relation:

$$S_t = S_0\left(1 - exp\left(-\frac{t}{T}\right)\right) \tag{5.10}$$

in which S_0 is the equilibrium scour depth for the scour process. Figure 5.2 displays a typical time series of the depth of a scour hole monitored at the upstream side of the pile. It is seen in Figure 5.2 that for a substantial amount of scour to occur, a specific amount of time must elapse. This time T is termed the time scale of the scour process and is defined as the time where the slope of the scour-depth-versus-time curve at t = 0 crosses the equilibrium scour depth.

In steady current Sumer et al. (1992a) expressed the time scale of scour with respect to the boundary-layer-thickness-to-pile-size-ratio, δ/D, and the Shields parameter:

$$T^* = \frac{1}{2000}\frac{\delta}{D}\theta^{-2.2} \tag{5.11}$$

in which T^* is the normalized time scale defined as:

$$T = \frac{D^2}{\left(g(s-1)d_{50}^3\right)^{1/2}}T^* \tag{5.12}$$

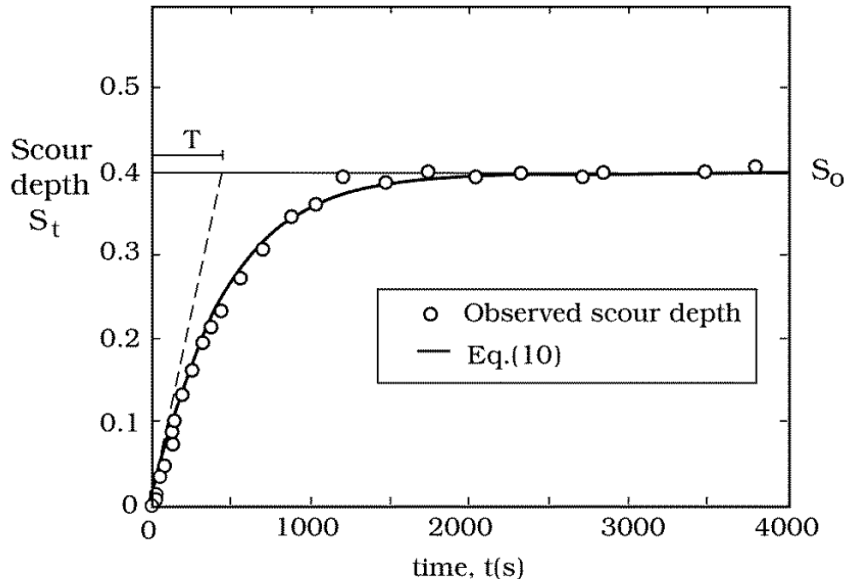

Figure 5.2. Observed time development of scour depth in combined current and waves. Live bed ($\theta > \theta_c$). KC = 4, U_{cw}= 0.47, θ_w = 0.15, S_0/D= 0.4, T = 445.

The time scale of scour in steady current increases with increasing δ/D and decreases with increasing θ. In the present experiments δ/D ranged from 2.7 to 5 and the Shields parameter was 0.13. The time scale of scour, T^*, in the present data corresponding to a current alone scour process agrees remarkably well with the estimated values found by Eq. (5.11).

In the case of scour process in waves, the KC number will also be involved in the non-dimensional formulation of the time scale:

$$T^* = 10^{-6}\left(\frac{KC}{\theta}\right)^3 \tag{5.13}$$

In the present experiments the KC number ranged from 4 – 20, and the θ value from 0.07 to 0.16. The present data agree well with the empirical expression stated in Eq. 5.13. The time scale of scour in waves increases with increasing KC number and decreases with increasing θ.

5.4.4. Time scale of scour in combined waves and current cases

In a scour process in combined current and waves the time scale varies with the KC number, the Shields parameter and the U_{cw} parameter. Therefore the normalized time scale can be written in following functional form:

$$T^* = f(U_{cw}, KC, \theta_w) \tag{5.14}$$

in which θ_w is the Shields parameter corresponding to the wave component of the flow.

In Figure 5.3 the time-scale data obtained in the present experiments are plotted according to Eq. 14. From Figure 5.3, the following conclusions can be drawn:

The normalized time scale approaches the wave alone values as $U_{cw} \to 0$.

For values of U_{cw} between 0 and 0.3 the normalized time scale increases significantly, and it becomes fairly constant in the range $0.3 < U_{cw} < 0.5$. The increase in time scale is attributed to the increased scour depth related to the formation of a horseshoe vortex in front of the pile when even a slight current is superimposed on a wave. The horseshoe vortex will mainly be present in the half period of the wave motion where the flow of the steady current and the waves are unidirectional. Further, the vortex shedding on the upstream side in waves is somewhat limited by the presence of the current. The combined effect of this is an increase in the normalized time scale.

For values of $U_{cw} \gtrsim 4$, the figure shows that the data for different KC numbers (in the present range, 4 - 20) practically collapse on a single curve.

Furthermore the steady current time scale plotted in Figure 5.3 indicate that the combined-wave-and-current time scales are in accord with the steady current data.

The normalized time scale decreases with increasing Shields parameter. This trend is observed over the entire interval $0 \leq U_{cw} \leq 1$.

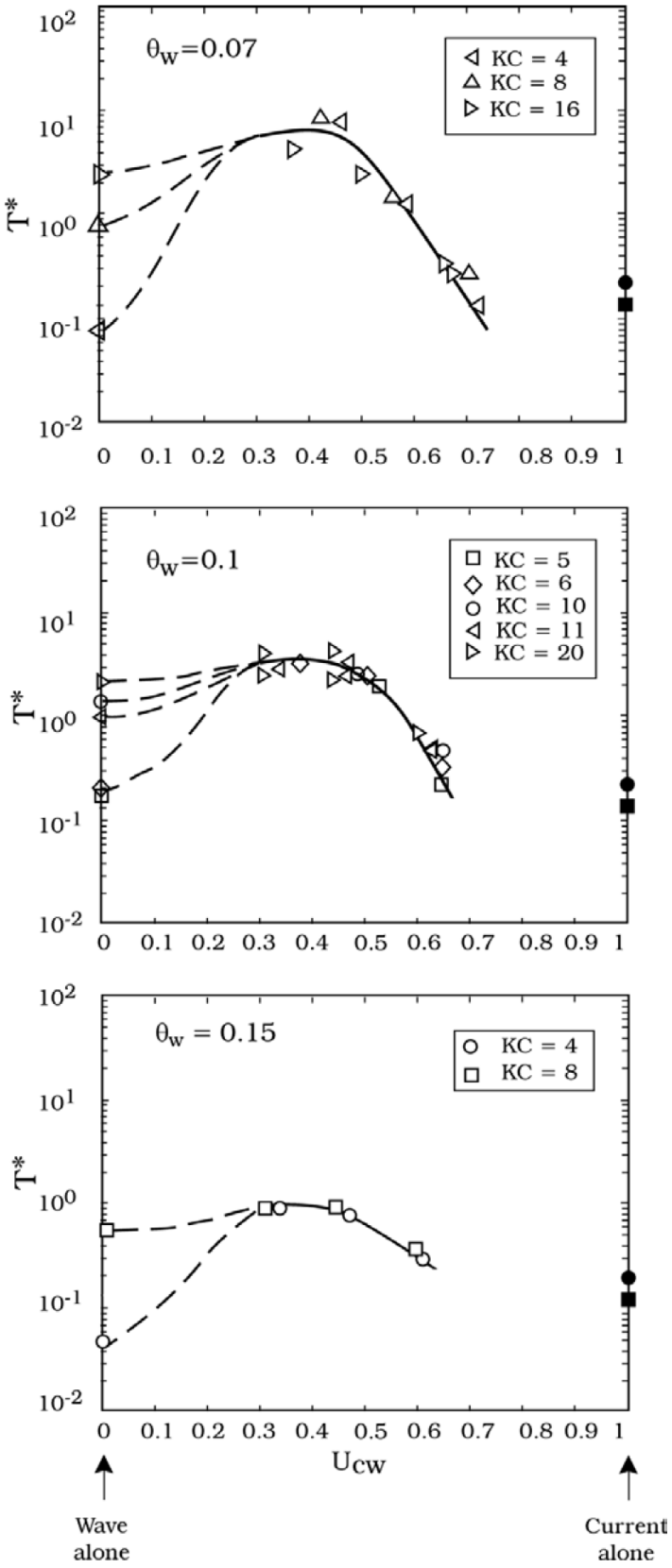

Figure 5.3. Time scale of scour around a circular cylinder in combined current and waves. Live bed ($\theta > \theta_c$). Circles represent the two current tests conducted with ■: $\delta/D = 2.7$, $\theta = 0.13$ and ●: $\delta/D = 2.7$, $\theta = 0.13$.

5.5. Conclusion

The time scale of scour in combined waves and current is governed by three parameters, namely U_{cw}, KC and θ_w. The present study indicate that:

1. The time scale of scour T increases significantly when even a slight current is superimposing on a wave.

2. The KC dependence of the time scale T is mainly observed for low values of U_{cw} in the wave dominated regime. For U_{cw} values larger than 0.4 no clear KC dependency was observed.

3. The time scale decreases with increasing θ_w over the entire range of U_{cw}.

Acknowledgement. This study was partially funded by (1) the Danish Council for Strategic Research (DSF)/Energy and Environment Program "Seabed Wind Farm Interaction"; (2) Statkraft thorugh Statkraft Ocean Energy Research Program (SOERP)(Norway); and (3) Danish GTS-university-cooperation project “Future Marine structures.” Some of the tests reported in the study were conducted by Mr. L. Locatelli, MSc.

Chapter 6

Overall Conclusions and Future Research

The mechanisms of edge scour, scour and backfill around piles and scour protections have been studied in the present thesis. Following paragraph presents the overall conclusions of the study which are detailed in the specific chapters.

Edge scour at stone covers or scour protections have been observed in the field at offshore wind turbine foundations. The edge scour can be caused by a transition in the surface roughness over the rough section of the stone layer to the smoother sand section on the side of the berm. Together with the side-slope of the berm this affects the immediate hydrodynamic field causing secondary current which in the 2D plane causes motion of the sediment away from the junction between the stone and the sand layer resulting in the edge scour. These secondary currents form longitudinal streamwise spirals along the length of the berm, redistributing the sediment agitated by the primary flow forming the edge scour hole alongside the berm. The stones at the edge of the berm are "undermined" and as result slump into the scour hole forming a protective slope. It was found that the scour depth attains a constant equilibrium scour depth at higher Shields parameters about the size of the cover stones. Design guidelines to estimate the equilibrium scour depth and the time scale of scour in current are provided in Chapter 2.

In the case of a stone layer placed around a monopile foundation the governing flow mechanisms causing the edge scour observed at the upstream-, transverse- and downstream sides of the side of the scour protection are as follows:

1. The edge scour at the upstream- to the transverse sides of the scour protection are caused by the combined action of the horseshoe-vortex generated in front of the berm and the contraction and acceleration of flow at the transverse sides of the scour protection. Design guidelines are provided in Chapter 3 to determine the equilibrium scour depth in current and in tidal flows.

2. From the transverse- to the downstream side of the pile and scour protection the edge scour is caused by a pair of counter-rotating vortices emerging in the wake area of the monopile and the berm. These vortices have shown a significant potential to scour the downstream wake area up to a level where the scour depth is about 1.1 times the pile diameter.

3. It is found that the maximum equilibrium edge scour depth remains unaffected from a steady current changed to a tidal current. This is, however, not the case for the plan view extent of the edge scour hole; here the tidal motion heavily affects the formation of the scour hole footprint, and the deepest part of the scour hole appears closer to the edge of the scour protection.

4. The edge scour can effectively be reduced by applying a falling apron, where the filter layer is extended beyond the armor layer. Design guidelines to determine the length and/or volume of the filter are provided in Chapter 3.

The above stated flow mechanisms causing edge scour has been investigated in the field for two offshore wind farms, and the edge scour observed in the experimental facility is found to be strikingly similar to that in the field, supporting the conclusions and results of the present experimental investigation on edge scour.

In the case of an unprotected monopile much research is available explaining the flow mechanisms causing scour and the time development of the scour process. However, there was a lack of knowledge in regards to the equilibrium scour depth as well as the time scale of the backfilling process. The present results, discussed in Chapter 4, have shown that backfilling of a previously generated scour hole may occur when the flow climate changes from a steady current to a wave; or from a steady current to a combined wave and current; or from a wave to a smaller wave. The scour depth corresponding to the equilibrium stage of backfilling is the same as that corresponding to the equilibrium stage of scour around a pile for the same wave or combined wave and current climate. The time scales of the backfilling process are provided in empirical equations and design diagrams in Chapter 4.

The time scale of scour around a pile in combined waves and current was studied in Chapter 5 and the results how that the time scale of scour increases when even slight current is superimposed on a wave. It is possible to estimate the time scale of the scour process using the presented design diagrams in Chapter 5.

Given the present information on the development of edge scour and in turn the implications to the stability and integrity of the stone cover several research areas are relevant to further expand the knowledge within design of scour protection systems. Following list are some possible areas of research which to the author's knowledge is relevant and where information is lacking:

- The migration of large bed forms (e.g. mega-ripples, dunes and sand waves) and the interaction with the scour protection system.
- Depravation of the general sea bed level and the implications to the scour protection system.
- Scour protection systems or stone covers consisting of one widely graded stone layer, i.e. omitting the classic design principle consisting of a filter- and an armor layer. The one widely graded stone layer is supposed to behave with a natural

armoring in the top layers, where the smaller size stones are winnowed out of the stone layer.
- The edge scour process at scour protections around offshore wind farms where the adjacent sea bed consists of cohesive sediments or stratified beds.
- Scour at a forward- and backward facing step of a porous stone layer in currents and waves.
- The effect of time scale of scour relative to the tidal period on the formation of edge scour at scour protections around offshore wind turbine foundations.
- Sinking of scour protections in waves or combined waves and current at offshore wind turbine foundations (Appendix C).

Further to this the research and discussions made in conjunction with scour and backfill mechanism around piles in Chapters 4 and 5 have shown several areas of interest which could be investigated further:

- The equilibrium stage of the scour process and the time scale of scour around an unprotected monopile in tidal current.
- The time scale of scour around a pile in combined waves and current, where the waves are propagating perpendicularly to the current.
- The effect of the counter-rotating vortices appearing in the near bed wake area downstream of the unprotected monopile in the scour process.
- The scour and edge scour process around gravity based type of foundations.
- The scour process and time scale of scour around jacket type of foundations.

Bibliography

Abdel-Aziz, Y.I., Karara, H.M. (1971) “Direct linear transformation into object space coordinates in close-range photogrammetry.” In: Proc. Symposyum in Close-Range Photogrammetry, pp.1–18. Urbana, Illinois

Allan, G. H., Serra, J (2001) “Morphological operators on the unit circle.” IEEE Transactions on image processing 10(12), 1842–1850

Astruc, D., Cazin,S., Cid., E., Eiff, O., Lacaze, L., Robin, P., Toublanc, F., Cáceres (2012) “A stereoscopic method for rapid monitoring of the spatio-temporal evolution of the sand-bed elevation in the wash zone .” Coastal Eng. 60(1), 11–20

Baglio, S., Faraci, C., Foti, E., Musumeci, R. (2001): “Measurements of the 3D scour process around a pile in an oscillating flow through a stereo vision approach”, Measurement, Elsevier Science Publication, 30(2), 145-164.

Baker, C. J. (1979): “The laminar horseshoe vortex.” Journal of Fluid Mechanics, vol. 95, part 2, 347-367.

Bayazit, M. (1976). “Free surface flow in a channel of large relative roughness.” Journal of Hydraulic Research, 14, no. 2, 1976, p. 155.

Bayazit, M. (1983). “Flow structures and sediment transport mechanics in steep channels.” In: Mechanics of Sediment Transport, Proc. Of Euromech 156, Istanbul, 12-14. July 1982, A.A. Balkema (Rotterdam), p.197.

Breusers, H. N. C. and Raudkivi, A. J. (1991): “Scouring.” Balkema. Hydraulic Structures design manual: 2.

Chiew, Y. M. (1995): “Mechanics of riprap failure at bridge pies.” Journal of Hydraulic Engineering, ASCE, vol. 121, No. 9, 635-643.

Chiew, Y. M. and Lim, F. H. (2000): “Failure behavior of riprap layer at bridge piers under live-bed conditions.” Journal of Hydraulic Engineering, Vol. 126, Issue 1, pp 43-55.

DHI/SNAMPROGETTI (1992): SISS Project. Sea bottom instability around small structures. Erodible bed laboratory tests (phase 1). Final report, text and drawings. DHI (Danish Hydraulic Institute) and Snamprogetti, Contract INGE91/SP/03060, june 1992.

Dixen, M., Sumer, B.M., and Fredsøe, J. (2013) "Numerical and experimental investigation of flow and scour around a half-buried sphere." Coastal Engineering, Vol. 73, March 2013, pp 84 – 105.

Elastocoast Webpage (2014). The innovative technology in coastal defence. http://www.polyurethanes.basf.de/pu/Coastal-Defense (31st of May 2014).

Faugeras, O.D., Toscani, G. (1987) “Camera calibration for 3D computer vision.” In: Proc. International Workshop on Industrial Applications of Machine Vision and Machine Intelligence, pp.240–247.Silken, Japan.

Fredsøe, J. (1984). “Turbulent boundary layer in wave/current motion.” Journal of Hydraulic Engineering, ASCE, 110(8), 1103-1120.

Fredsøe, J. and Deigaard, R. (1992): Mechanics of Coastal Sediment Transport. World Scientific, New Jersey, Singapore, London, Hong Kong.

Fredsøe, J., Sumer, B.M. and Arnskov, M.M. (1992): "Time scale for wave/current scour below pipelines". International J. Offshore and Polar Engineering. Vol. 2, No. 1, 13-17.

Fredsøe, J., Sumer, B. M, and Bundgaard, K. (1993). “Experimental investigation of wave boundary layers with a sudden change in roughness.” Journal of Fluid Mechanics, vol. 252, pp. 117-145.

Fredsøe, J., Sumer, B. M, Bundgaard, K. (2001). “Scour at a riprap revetment in currents.” Proceedings of 2nd IAHR Symposium on River, Coastal and Estuarine Morphodynamics. 2001, pp. 245-254.

Foti, E., Caceres Rabionet, I., Marini, A., Musumeci, R.E., Sanchez-Arcilla, A. (2011): “Experimental investigations of the bed evolution in wave flumes: performance of 2D and 3D optical systems”, Coastal Engineering, 58 (7), 606-622.

Fuhrman, D. R., Sumer, B. M., and Fredsøe, J. (2011). “Roughness-induced streaming in turbulent wave boundary layers.” Journal of Geophysical Research, vol. 116, C10002, doi:10.1029/2011JC007155.

Furieri, B., Russeil, S., Harion, J.-L, Turpin, C. and Santos, J. M. (2012): “Experimental surface flow visualization and numerical investigation of flow structure around an oblong stockpile.” Environmental Fluid Mechanics, Vol. 12, issue 6, pp 533-553.

Hansen, E. A., Simonsen, Nielsen, A. W., Pedersen, & Høgedal (2007) “Scour protection around offshore wind turbine foundations, full-scale measurements.” In Proceedings of EWEC, Milan, EWEA, pp. 4-6.

Hansen, N. E. O., Gislason, K. (2005) ”Movable scour protection on highly erodible sea bottom.” LICengineering A/S, Ehlersvej 24, DK-2900 Hellerup, Denmark.

Harris, J.M., Whitehouse, R.J.S. and Benson, T. (2010): “The time evolution of scour around offshore structures”. Maritime Engineering, vol. 163, March 2010 Issue MAI, 3-17.

Hartley, R., Zisserman, R. (2003) “Multiple view geometry in computer vision.” Cambridge University Press

Hartvig, P.A., Thomsen, J.M., Frigaard, P. and Andersen, T.L. (2010): “Experimental study of the development of scour and backfilling”. Coastal Engineering Journal, vol. 52, No. 2, 157-194.

Hayashi, T., Ohashi, M., and Kotani, Y. (1985) "River flow turbulence and longitudinal vortices." Recent Studies on Turbulent Phenomena, Tokyo Inst. of Tech., Japan, pp. 243-259.

Heikkilä, J., Silvén, O. (1997): “A four-step camera calibration procedure with implicit image correction”, IEEE Computer Society Conference on Computer Vision and Pattern Recognition, San Juan, Puerto Rico, 1106-1112.

Hjorth, P. (1975). "Studies on the nature of local scour." Ph.D. Thesis, Institutionen för teknisk vattenresurslära, Lunds Tekniska Högskola, Lunds Universitet.

Hoffmanns, G. J. C. M. and Verheij, H. J. (1997): “Scour manual.” Balkema.

Khosronejad, A., Kang, S. and Sotiropoulos, F. (2012), “Experimental and computational investigation of local scour around bridge piers,” Advances in Water Resources, Volume 37, pages 73-85.

Knight, D.W., and Shiono, K. (1990) "Turbulence measurements in a shear layer region of a compound channel." Journal of Hydraulic Research, Vol. 28, No. 2, pp. 175-196.

Knight, D.W., and Shiono, K. (1996) "River channels and flood plain hydraulics." Flood plain processes, edited by Anderson et al., Chapter 5, J. Wiley.

Kozakiewicz, A., Sumer, B.M. and Fredsøe, J. (1994): "Cross-Flow vibrations of a cylinder in irregular oscillatory flow", Journal of Waterway, Port, Coastal and Ocean Engineering, ASCE, Vol. 120, No. 6, 515-534.

Lauchlan, C. S and Melville, B. W. (2001): “Riprap protection at bridge pies.” Journal of Hydraulic Engineering, ASCE, vol. 127, No. 5, 412-418.

Liu, X. and Garcia, M. H. (2008): “Three-dimensional numerical model with free water surface and mesh deformation for local sediment scour.” Journal of Waterway, Port, Coastal and Ocean Engineering, 134 (4), 203-217.

Lowe, D.G.: Distinctive image features from scale-invariant key-points. International Journal of Computer Vision, 60(2), 91-110 (2004)

Louwersheimer, W. F., Verhagen, H. J., Olthof, J. (2009) ”Scour around offshore wind turbine.” Coastal structures 2007. Franco, L., Tomasicchio, G. R., Lamberti, A. (Eds.), Proceedings of the Fifth Coastal Structures International Conference, 2-4 July, 2007. World Scientific, Venice, Italy, pp. 1903-1912.

Margheritini, L., Martinello, M., Lamberti, A. and Frigaard, P. (2006): “Scour around monopile foundations for off-shore wind turbine in presence of steady and tidal currents.” Proc. Of the 30th International Conference on Coastal Engineering, San Diego, California, USA.

McLean, S.R. (1981). "The role of non-uniform roughness in the formation of sand ribons." Marine Geology, 42 :49-74.

Melling, A., Whitelaw, J.H. (1976). "Turbulent flow in rectangular duct." Journal of Fluid Mechanics., 78 : 289-315.

Melville, B.W. and Coleman, S. (2000): Bridge Scour. Water Resources Publications, LLC, CO, USA.

Melville, B.W. and Sutherland, A.J. (1988): “Design methods for local scour at bridge piers”, J. Hydraulic Engineering, ASCE, vol. 114, No. 10, 1210-1226.

Monin, A.S., and Yaglom, A.M. (1973) "Statistical Fluid Mechanics." Mechanics of Turbulence, MIT Press, Cambridge, Mass.

Musumeci, R.E., Farinella, G.M., Foti, E., Battiato, S., Petersen, T. U., and Sumer, B.M., (2013): "Measuring sandy bottom dynamics by exploiting depth from stereo video sequences." Proceedings of the 34th International Conference on Image Analysis and Processing, 2013, Paris, France.

Müller, A., Studerus, X. (1979) "Secondary flow in an open channel." Proceedings of the 18th IAHR Congress, Cagliari, Vol. 3, pp. 19-24.

Nakagawa, H., Nezu, I., and Tominaga, A. (1981) "Turbulent structure with and without cellular secondary currents over various bed configurations." Annuals, Disaster prevention Research Institute, Kyoto University, 24B : 315-338.

Naot, D., and Rodi, W. (1982) "Calculation of secondary currents in channel flows." Journal of the Hydraulics Division, ASCE, 108 :948 -968.

Naot, D. (1984). "Response of channel flow to roughness heterogeneity." Journal of Hydraulic Engineering, ASCE, 110 :1568-1587.

Newcombe, R. A., Izadi, S., Hilliges, O., Molyneaux, D., Kim, D., Davison, A. J., Kohli, P., Shotton, J., Hodges, S., Fitzgibbon, A.: KinectFusion: Real-Time Dense Surface Mapping and Tracking, IEEE International Symposium on Mixed and Augmented Reality, 2011

Nezu, I., Nakagawa, H., and Tominaga, A. (1985) "Secondary currents in straight channel flow and the relation to its aspect ratio." Turbulent Shear Flows 4. Springer-Verlag, pp. 246-260.

Nezu, I., and Rodi, W. (1985) "Experimental study on the secondary currents in open channel flow." Proceedings of the 21st IAHR Congress, Melbourne, vol. 2 :115-119.

Nezu, I., Nakagawa, H., (1993) "Turbulence in open-channel flows." A. A. Balkema, Rotterdam.

Nielsen, A. W. and Hansen, E. A. (2007): "Time varying wave and current-induced scour around offshore wind turbines". Proc. 26th International Conference on Offshore Mechanics and Arctic Engineering, OMAE 2007, June 10-15, 2007, San Diego, California, USA.

Nielsen, A. W., Sumer, B. M., Fredsøe, J. & Christensen, E. D. (2011) "Sinking of armour layer around a cylinder exposed to a current." Proceedings of the ICE-Maritime Engineering, ICE, vol. 164(4), pp. 159-172.

Nielsen, A. W., Liu, X., Sumer, B. M. & Fredsøe, J. (2013) "Flow and bed shear stresses in scour protections around a pile in a current." Coastal Engineering, ELSEVIER, vol. 72, pp. 20-38.

Perkins, H.J. (1970). "The formation of streamwise vorticity in turbulent flow." Journal of Fluid Mechanics, 44 :721-740.

Petersen, T.U, Sumer, B.M, Meyer, K.E., Fredsøe, J., and Christensen, E.D (2012a) "Edge scour in current adjacent to stone covers." Proceedings of sixth International Conference on Scour and Erosion, ICSE, Paris, France, 2012.

Petersen, T.U, Sumer, B.M., and Fredsøe, J. (2012b) "Time scale of scour around a pile in combined waves and current." Proceedings of sixth International Conference on Scour and Erosion, ICSE, Paris, France, 2012.

Petersen, T. U., Sumer B. M., Bøgelund, J., Yazici, A., Fredsøe, J. and Meyer, K. E. (2014) "Experimental investigation on flow and edge scour in current adjacent to stone covers." Submitted and under review in : Journal of Waterway, Port, Coastal and Ocean Engineering, February, 2014.

Offshore Center Danmark (2010): "OffshoreBook". http://www.offshorecenter.dk/log/bibliotek/OffshoreBook2010.pdf. Offshore Center Danmark, July 2010.

Offshore Center Danmark (2012): About Offshore. http://www.offshorecenter.dk/About-Offshore.asp (31st of June 2012).

Raaijmakers, T.C, Rudolph, D., Bergen, M.R.J.v, and Lieshout, H.v. (2007) "Offshore windpark Egmond ann Zee – Performance of scour protection and edge scour development." Proceedings European Offshore Wind Conference, December 4-6, 2007, Berlin, 10 pp.

Raaijmakers, T. and Rudolph, D. (2008 a): "Time-dependent scour development under combined current and wave conditions – laboratory experiments with online monitoring technique". Proceedings of the Fourth International Conference on Scour and Erosion, November 5-7, 2008, Tokyo, Japan, 152-161.

Raaijmakers, T. and Rudolph, D. (2008 b): "Time-dependent scour development under combined current and wave conditions – Hindcast of field measurements" Proceedings of the Fourth International Conference on Scour and Erosion, November 5-7, 2008, Tokyo, Japan, 340-347.

Raaijmakers, T. (2009): "Evaluation of performance of scour protection and edge scour development – Offshore Windpark Egmond aan Zee." Evaluation report, Deltares. Available through http://www.deltares.nl/en/publications.

Raaijmakers, T.C., Oeveren, M.C., Rudolph, D., Leenders, V., Sinjou, W. C. P., (2010) "Field performance of scour protection around offshore monopoles." Proceedings of the Fifth International Conference on Scour and Erosion, ICSE 2010, pp 428-439.

Raaijmakers, T.C., Joon, T., Segeren, M.L.A., Meijers, P. (2013), Scour: to protect or not to protect? That's the question. Feasibility of omitting scour protection. Proceedings EWEA Offshore 2013 Frankfurt.

Roulund, A., Sumer, B.M., Fredsøe, J. and Michelsen, J. (2005): "Numerical and experimental investigation of flow and scour around a circular pile". J. Fluid Mechanics, vol. 534, 351-401.

Sánchez-Arcilla, A., Cáceres, I., van Rijn, L., Grüne, J.: Revisiting mobile bed tests for beach profile dynamics. Coastal Eng. 58(7), 583–593 (2011)

Savitzky, A.; Golay, M.J.E. (1964). "Smoothing and Differentiation of Data by Simplified Least Squares Procedures". *Analytical Chemistry* **36** (8): 1627–1639.

Schäffer, H.A., Stolborg, T., Hyllested, P. (1994): "Simultaneous generation and active wave absorption of waves in flumes". Proc. Int. Symposium: Waves — Physical and Numerical Modelling. Univ. British Columbia, Vancouver, Canada, 90–99.

Schlichting, H. (1979): Boundary Layer Theory. Seventh Edition. McGraw Hill.

Shiono, K., and Knight, D.W. (1991) "Turbulent open-channel flows variable depth across the flow." Journal of Fluid Mechanics, Vol. 222, pp. 617-646.

Simoons, E. (2012): "Edge scour around an offshore wind turbine." MSc. Thesis, Delft University of Technology, January 2012.

Soille, P. (1999) "Morphological image analysis: Principle and Applications." Springer

Studerus, X. (1982). "Sekundärströmnungen im offenen Gerinne über rauhen Längsstreifen." Ph.D. Thesis, Institut für Hydromekanik und Wasserwirtschaft, ETH, Zürich, Switzerland.

Sumer, B.M., Fredsøe, J. and Christiansen, N. (1992): "Scour around a vertical pile in waves". Journal of Waterway, Port, Coastal and Ocean Engineering, ASCE, Vol. 118, No. 1, 15-31.

Sumer, B. M., Christiansen, N., Fredsøe, J. (1992). "Time Scale of Scour around a vertical pile." Proc., 2nd Int. Offshore and Polar Engineering Conference, International Society of Offshore and Polar Engineers, San Fransisco, California, Vol. 3, 308-315.

Sumer, B.M., Christiansen, N. and Fredsøe, J. (1993): "Influence of cross section on wave scour around piles". Journal of Waterway, Port, Coastal and Ocean Engineering, ASCE, Vol. 119, No. 5, 477-495.

Sumer, B. M., Christiansen, N. and Fredsøe, J. (1997): "Horseshoe vortex and vortex shedding around a vertical wall-mounted cylinder exposed to waves." Journal of Fluid Mechanics, vol. 332, 41-70.

Sumer, B.M. and Fredsøe, J. (2000): "Experimental study of 2D scour and its protection at a rubble-mound breakwater", Coastal Engineering, Vol. 40, Issue 1, 59-87.

Sumer, B.M. and Fredsøe, J. (2001a): "Scour around a pile in combined waves and current". Journal of Hydraulic Engineering, ASCE, vol. 127,, No. 5, 403-411.

Sumer B.M. and Fredsøe, J. (2001b): "Wave scour around a large vertical circular cylinder". Journal of Waterway, Port, Coastal and Ocean Engineering, ASCE, vol. 127, No. 3, 125-134.

Sumer, B.M. and Fredsøe, J. (2002): The Mechanics of Scour in the Marine Environment. World Scientific, New Jersey, Singapore, London, Hong Kong.

Sumer, B. M., Fredsøe, J., Lamberto, A., Zanuttigh, B., Dixen, M., Gislason, K., and Di Penta, A. F. (2005): "Local scour at roundhead and along the trunk of low crested structures." Coastal Engineering, Elsevier, Vol. 52, issue 10-11, pp 995-1025.

Sumer, B.M. and Fredsøe, J. (2006): Hydrodynamics Around Cylindrical Structures. World Scientific, New Jersey, Singapore, London, Hong Kong, First edition: 1997, Second/revised edition: 2006.

Sumer, B.M. (2007): "Mathematical modelling of scour: A review". J. Hydraulic Research, vol. 45, No. 6, 723-735.

Sumer, B.M., Hatipoglu, F. and Fredsøe, J. (2007): "Wave scour around a pile in sand, medium dense and dense silt". Journal of Waterway, Port, Coastal and Ocean Engineering, ASCE, vol. 133, No. 1, 14-27.

Sumer, B. M. & Nielsen, A. W. (2013) "Sinking failure of scour protection at offshore wind turbine foundation." Proceedings of the ICE-Energy, ICE, vol. 166(4), pp. 170-188.

Sumer, B.M., Petersen, T.U., Locatelli, L., Fredsöe, J., Musumeci, R.E., Foti, E. (2013) "Backfilling of a scour hole around a pile in waves and current." J. Waterway, Port, Coastal, Ocean Eng. 139(1), 9–23

Sumer, B. M. (2014) "Flow-structure-seabed interactions in coastal and marine environments." Journal of Hydraulic Research, Vol. 52, No. 1 (2014), pp. 1–13.

Tominaga, A., and Nezu, I. (1986) "Three-dimensional turbulent structure in a straight open-channel flow with vaying boundary roughness." Proceedings of the 3rd Asian Congress of Fluid Mechanics, Tokyo, pp. 608-611.

Tominaga, A., Nezu, I., Ezaki, K., Nakagawa, H. (1989) "Three-dimensional turbulent structure in open channel flows." Journal of Hydraulic Research, Vol. 27, 1989, No. 1.

Truelsen, C., Sumer, B.M., and Fredsøe, J. (2005). "Scour around spherical bodies and self-burial." Journal of Waterway, Port, Coastal and Ocean Engineering, Jan 2005, Vol. 131, No. 1, pp 1-13.

Tsai, R.Y. (1987) "A versatile camera calibration technique for hygh-accuracy 3D machine vision metrology using off-the shelf TV cameras and lenses." IEEE J. Robotics and Automation, RA-3(4), 323–344

van Driest, E. R. (1956): "On turbulent flow near a wall." Jounal of Aeronautical Sciences, Vol. 23, p.1007.

van Rijn, L. C. (2011) "Principles of fluid flow and surface waves in rivers, estuaries, seas and oceans." Aqua Publication.

Vos, L. D, De Rouck, J., Troch, P. and Frigaard, P. (2011): "Empirical design of scour protections around monopile foundations: Part 1: Static approach." Coastal Engineering, Elsevier, Vol. 58, issue 6, June 2011, pp 540-553.

Vos, L. D, De Rouck, J., Troch, P. and Frigaard, P. (2012): "Empirical design of scour protections around monopile foundations: Part 2: Dynamic approach." Coastal Engineering, Elsevier, Vol. 60, pp 286-298.

Wang, Z. Q. and Cheng, N. S. (2005): "Secondary flows over artificial bed strips." Advances in Water Resources, Vol. 28, issue 5, pp. 441 – 450.

Wang, Z. Q. and Cheng, N. S. (2006): "Time-mean structure of secondary flows in open channels with longitudinal bedforms." Advances in Water Resources, Vol. 29, issue 11, pp. 1634 – 1649.

Whitehouse, R. (1998): Scour at Marine Structures: A manual for practical applications. Thomas Telford.

Whitehouse, R., Harris, J.M., Sutherland, J., and Rees, J. (2011): "The nature of scour development and scour protection at offshore windfarm foundations." Marine Pollution Bulletin, 62(1), 73-88.

Wittrup, S. (2012): "Horseshoe vortex washes out the sediment around offshore wind turbines." An article published in Ingeniøren/energy&miljø, 16 January, 2012. Danish. http://ing.dk/artikel/hestesko-hvirvler-vasker-bunden-omkring-havvindmoller-vaek-125792

Zhao, M., Cheng, L. & Zang, Z. (2010). Experimental and numerical investigation of local scour around a submerged vertical circular cylinder in steady currents. Coastal Engineering, 57(8), 709-721.

4coffshore Webpage (2014). Welcome to the global offshore wind farm database http://www.4coffshore.com/windfarms/ (30th of May 2014).

Appendix A

Edge scour in current adjacent to stone covers

This chapter is published in Proceedings of the 6th International Conference on Scour Erosion, ICSE, Paris, France, August, 2012.

T. U. Petersen[1], B. M. Sumer[2], Knud Erik Meyer[3], J. Fredsøe[4] & Erik D. Christensen[5]

[1]Ph.D. – candidate, [2]Professor, [3]Associate Professor, [5]Professor, [5]Professor, Technical University of Denmark. Section for Fluid Mechanics, Coastal and Maritime Engineering. Kgs. Lyngby, Denmark.

Abstract: The present paper reports some early results of an experimental investigation of edge scour in currents. Two kinds of measurements are made (1) Particle Image Velocimetry (PIV) measurements of secondary currents that take place near a junction between the stone cover and the sand bed in a clear-water experiment; and (2) scour measurements in actual scour experiment in the live-bed regime.

The early results indicate that edge scour in a steady current propagating in-line with a stone layer is caused by the combined action of two effects; (1) Primary flow and (2) Secondary flow. The primary flow stirs up the sediment and puts into suspension, and the secondary flow carries it away from the junction between the stone layer and the sand bed, resulting in a scour hole forming adjacent to the toe of the stone layer.

Key words: Edge scour, cover stones, steady current, scour protection, coastal structures, offshore structures, scour, offshore wind farm.

A.1. Introduction

Scroby Sands wind farm located in the North Sea 2.5 km off the coast of Great Yarmouth, UK, utilized a scour protection system with rock dump around the monopiles. Surveys made in 2004-2005 show a strong deformation of the scour protection layer comprising both sinking of the stone layer and considerable edge scour (Whitehouse et al., 2011). The design principles of the scour protection implemented in the Scroby Sands wind farm have been described in Hansen and Gislason (2005).

Fig. A.1 illustrates the edge scour adjacent to a stone layer placed on a sandy bottom.

As pointed out by several investigators, e.g. Fredsøe et al. (2001) and Raaijmakers et al. (2010), edge scour is in fact expected from the design considerations, but so far the mechanisms causing edge scour have not been fully established.

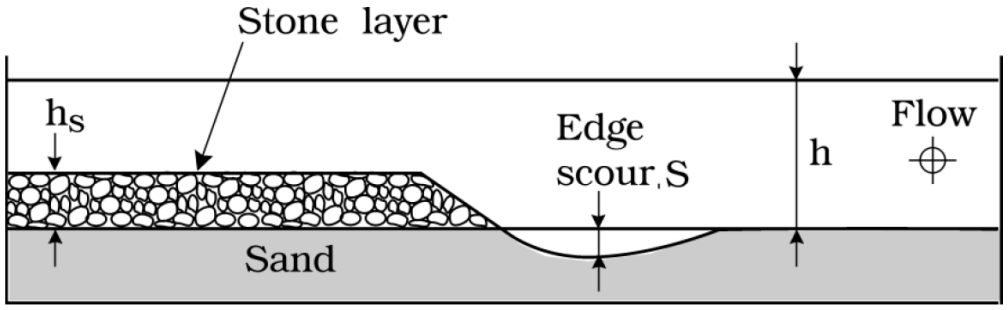

Figure A.1. Definition sketch

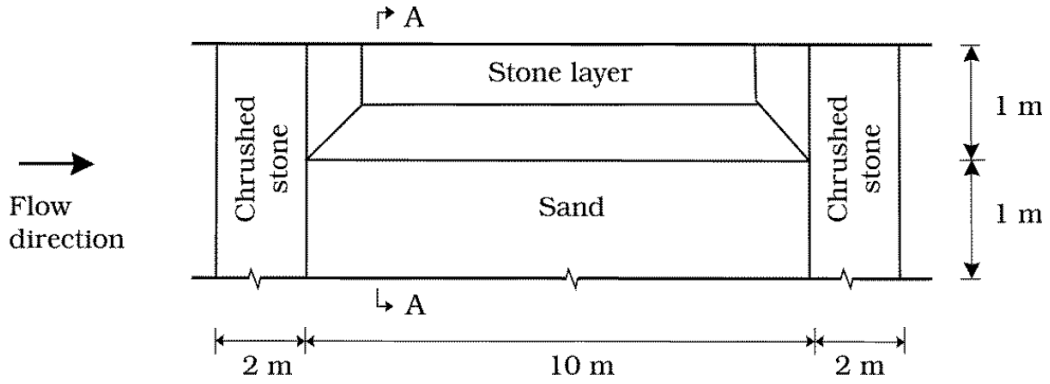

Figure A.2. Experimental setup, Plan view

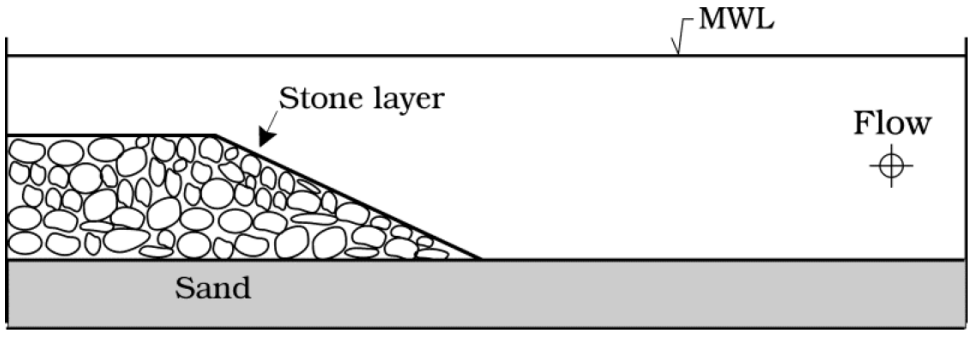

Figure A.3. Cross-sectional view, A-A in Fig. A.2.

To address this issue an extensive program of physical model tests is in progress. The purpose of the study is to gain an understanding of the stability of stone covers and the scour adjacent to the side edges. This paper presents some early results obtained in the aforementioned experimental campaign.

A.2. Experimental Setup

The experiments were carried out in a current flume. The flume was 2.0 m wide, 0.5 m deep and 28 m long. The water depth was h = 30 cm. The current was achieved by recirculating water in the flume.

A sediment section in the form of a sand pit with two ramps at the two ends was formed in the flume. The sand pit was 2 m wide, 0.15 m deep and 10 m long (see Figure A.2), the distance from the upstream end of the sand pit to the inlet section being 7.5 m. The two end ramps (with 1:15 slope) were made from round stones the size 4 cm. The grain size of the sediment (fine sand) used in the experiments was d_{50} = 0.17 mm with a geometric standard deviation of $\sigma_g = d_{84}/d_{50}$ = 1.3.

A stone layer was placed on top of the sand covering half of the flume width in the cross-sectional direction extending over the entire longitudinal direction of the sand pit. At the intersection of the stone layer with the sand a slope α of 1:3 was applied (Figure 3).This slope was adopted to match the stone layer design encountered in practice.

The stone layer was made of crushed angular stones with size D_s = 2.1 cm with a geometric standard deviation of σ_g= 1.2. The experiments were conducted with a stone layer thickness h_s = 18 cm corresponding to N ~ 9 layers of stones.

A mini underwater video camera videotaped the overall time development of the scour process at the toe of stone layer. The movement of the sand grains in the video recordings acted as flow tracers, visualizing the flow structures alongside the toe of the stone layer and the individual stones.

The experiments were run for sufficiently long period of time for the scour process to reach its equilibrium stage. Subsequently, the scour profiles in the cross-flow direction were measured by a laser rangefinder (leicaDisto™ D3a) with a precision of 1 mm and this operation was performed at 10 sections (about 10 cm apart) along the length of the working section.

A.2.1. Velocity measurements by LDA

The velocity profile across the water depth over the sand section was measured, using a Laser Doppler Anemometer (LDA), a Dantec 2D LDA system (Dantec Dynamics, Denmark) comprising a 14 mm “pen-size” submersible probe, the measurements being conducted in backward-scatter mode.

The measurement point was located 7 m away from the beginning of the sand pool and at 0.5 m distance from the side wall. The system was equipped with a BSA F60 Flow Processor and the data was logged in BSA Flow Software v4.50. The data was logged in burst mode which meant the sampling frequency ranged between 90 – 300 Hz.

The steady current velocity was constantly monitored during the course of the experiment, and the data collected was used to determine the velocity to calculate the quantities such as the depth averaged velocity and the bed friction velocity.

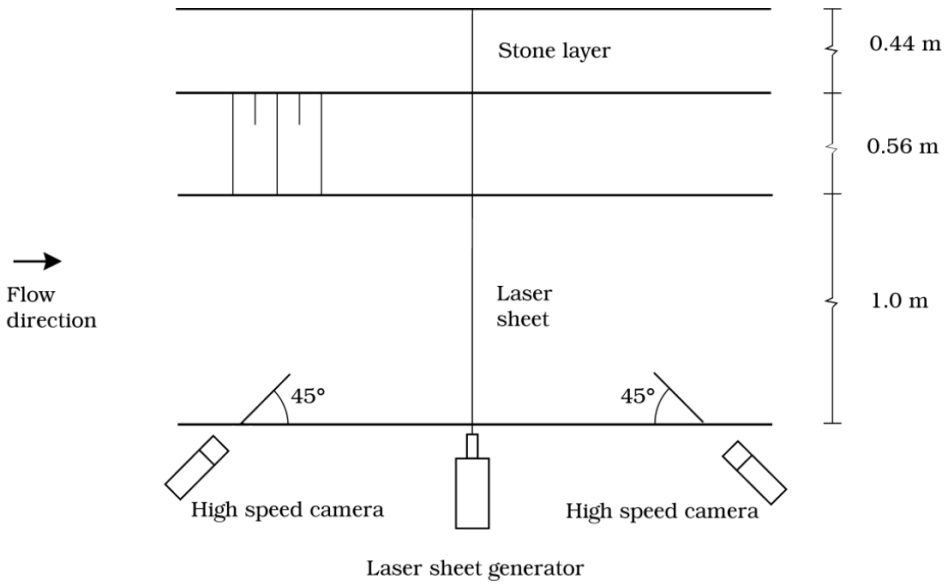

Figure A.4. Stereoscopic PIV setup plan view

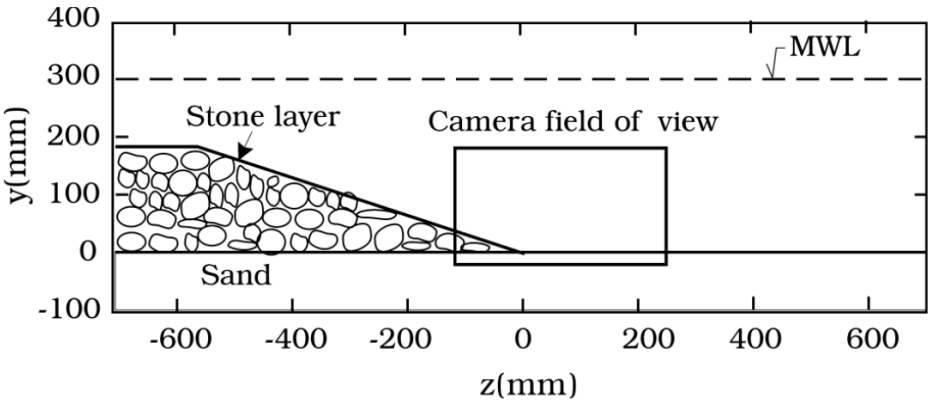

Figure A.5. Camera field of view

A.2.2. Velocity measurements by PIV

Particle Image Velocimetry (PIV) measurements were made to investigate the three-dimensional flow in cross-sectional plane at the junction between the sand and the stone layer. The objectives of the PIV study were twofold: to obtain the secondary currents, and to estimate the turbulence intensity field over the sand and the stone layer. The latter will not be reported in the present paper for reasons of space.

The measurements were made with a PIV system from Dantec Dynamics; the system consisted of two four megapixel cameras, double pulsed (1200 mJ/pulse) Nd:Yag laser, a synchronizer to facilitate system timing and frame grabbers to facilitate image acquisition. The PIV data logging was made in Dynamic Studio v2.50. As shown in Fig. A.4 the two cameras were mounted alongside the flume side wall viewing the measurement volume at a 45° angle. On the glass side wall for each camera a water prism with an orientation of 45° was mounted in order to eliminate refraction. The laser light

sheet was also introduced from the flume side wall aimed directly at the measurement volume.

The PIV measurements were made in the clear-water regime, where no sediment transport occurred (not even adjacent to the stone cover). This ensured that the sediment bed would not change during the execution time, and that larger sediment particles suspended from the bed would not disturb the data collection. This further allowed acquisition of large ensembles of data. Note that the scour experiment (Test 1 in Table A.1) was performed in the live-bed regime.

Given the appreciable amount of data storage and post-processing requirements of the PIV measurements, it was decided to focus on a single stone layer thickness and a specific depth-averaged-velocity flow scheme. The setup was prepared with a flat sediment bed and the experiment was carried out in the clear water regime, and no change in the bed morphology was observed.

For the given setup one camera field of view was measured, so that the flow in the vicinity of the stone layer toe was covered, as illustrated in Fig. A.5. The calibration images for the field of view were used to provide the dimensional position for the field of view in laboratory coordinates.

At the frame position an ensemble of 5400 image pairs were obtained. The image pairs were subsequently analyzed and interrogated using the Dynamic Studio v2.30. Images were interrogated with 32 x 32 windows, using a 50 % overlap. Typical vector removal rates ranged from 2 to 4 % with the bulk of removed vectors near the sediment bed and the stone layer. In both cases the moderate scattering of laser light from the sediment grains and the stones were responsible. This effect was inevitable despite the effort to minimize it with flat black paint.

A.3. Test Conditions

Table A.1 summarizes the test conditions for the scour tests. In the table the quantity V is the depth averaged current velocity. Note that for test no. 2 the velocity measurements were made within the camera field of view (Fig. A.5) extending up to h ~ 16 cm above the bed.

The quantity U_f denotes the bed friction velocity determined in the following two ways: (1) from the familiar log-fit exercise using the measured velocity profiles from the PIV measurements; (2) from the flow resistance relation

$$U_f = \sqrt{f/2}\,V \tag{A.1}$$

in which f is calculated from the Colebrook-White formula (e.g. Schlichting, 1979) and V was obtained from the LDA measurements described in the previous section. The Shields parameter θ in the table is defined by

$$\theta = \frac{U_f^2}{g(s-1)d_{50}} \tag{A.2}$$

Table A.1. Test conditions

	Stone size	Number of Stone Layers	Stone layer thickness	Depth Averaged Current Velocity	Friction velocity in steady current	Grain Reynolds number	Shields Parameter	Equilibrium scour depth
	D_s	N	h_s	V	U_f	$d_{50}U_f/\nu$	θ	S
	[cm]	[-]	[cm]	[cm/s]	[cm/s]		[-]	[mm]
1	2.1	9	18	30.5	1.4	2.4	0.072	10
2	2.1	9	18	10.6	0.45	0.76	0.007	-

n which g is the gravitational acceleration, s the specific gravity of the sediment grains (=2.65).

In the table the quantity *S* is the scour depth corresponding to the equilibrium stage of the scour process (Fig. A.1).

Note that the Shields parameter in Test 1 was larger than the critical value corresponding to initiation of motion at the bed, meaning that the scour experiments were conducted in the live-bed regime. This was also revealed by the appearance of ripples on the sediment bed. The Shields parameter in Test 2 was lower than the critical value and no motion on the bed was observed.

A.4. Results and Discussion

A.4.1 Secondary flow

Figure A.6 shows the secondary flow structures within the full camera field of view and Figure A.7 shows a close-up of the corner section. Previous studies show that secondary flow structures of channel flows can be caused by a sudden change in roughness and corner-induced effects. The sudden change in roughness forces a secondary current directed from the rough section into the smooth section due to mean flow deflection (Müller and Studerus, 1979). The corner induced secondary current is turbulence-driven (van Rijn, 2011 and Nezu and Nakagawa, 1993), where the flow goes from the main body of the flow towards the corner. The secondary flow very close to the bed in the sand section is directed away from the stone layer toe, and that over the stones are directed into the stone layer. The separation of the flow over the stones highly disturbs the measurements in the local field.

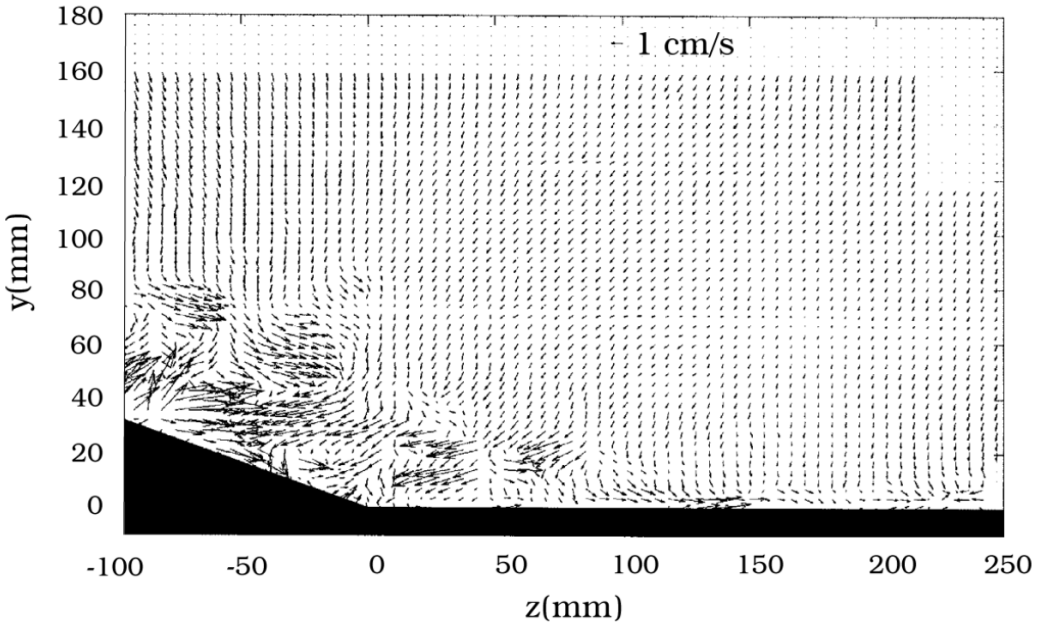

Figure A.6. Secondary flow structures in camera field of view. Test 1.

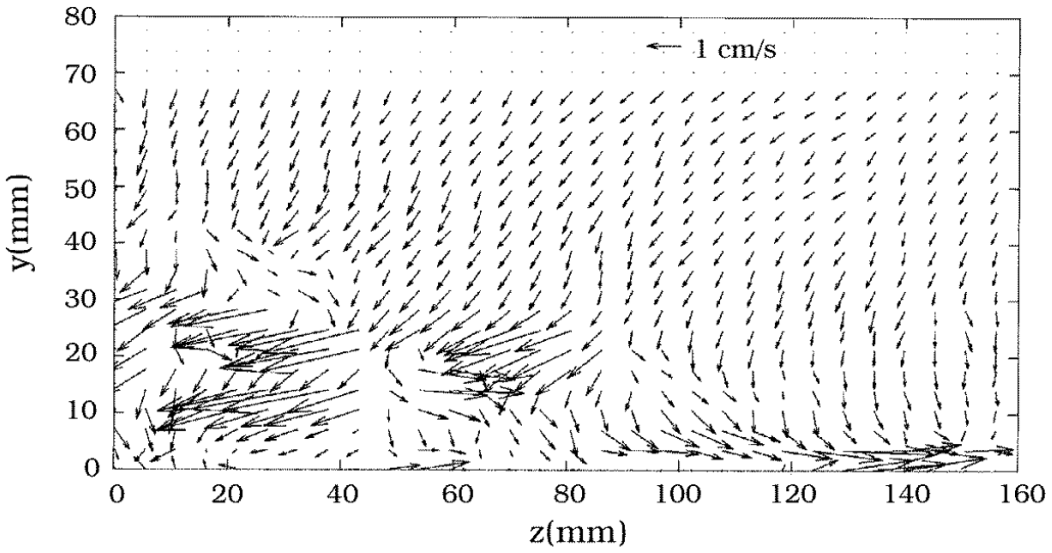

Figure A.7. Secondary flow structures close-up of corner section. Test 1.

A.4.2. Mechanism of edge scour

Figure A.8 shows the cross flow bed profiles measured at ten sections corresponding to the equilibrium stage of Test 1. The results show considerable scatter and is due to the ripples. Further to this, the ripples extend over the entire sediment bed. Figure A.9 displays the "space-averaged" cross-flow bed profile, averaged over the 10 profiles given in Fig. A.8. Fig. A.9 also includes the "time-averaged" profile, obtained at the last section (x = 900 mm). As expected, the mean profile obtained by space averaging and that obtained by time averaging practically collapse on a single curve.

Despite the scatter Figure A.8 and A.9 show following pattern:

1. Scour occurs at the edge of the stone layer (Area B)
2. Deposition occurs inside the toe of the stone layer (Area A)
3. A slight deposition of sediment outside area B (Area C)

Figures A.6 – A.9 suggest the governing mechanism of the edge scour as follows. The scour is caused by following two effects: (1) turbulence in the primary flow near the junction between the stone layer and the sand bed; and (2) the secondary flow described in the previous paragraph. Sediment is stirred up by the turbulence and brought up into suspension, and the secondary flow carries the sediment away from the junction between the bed and the stones, resulting in the edge scour.

With this, stones at the edge of the cover stones are "undermined", and as a result slump down into the scour hole.

There are two kinds of turbulence. One source of turbulence in the primary flow mentioned above is that generated in the fully developed turbulent boundary layer over the sand bed and the stone layer. The second source of turbulence, on the other hand, is

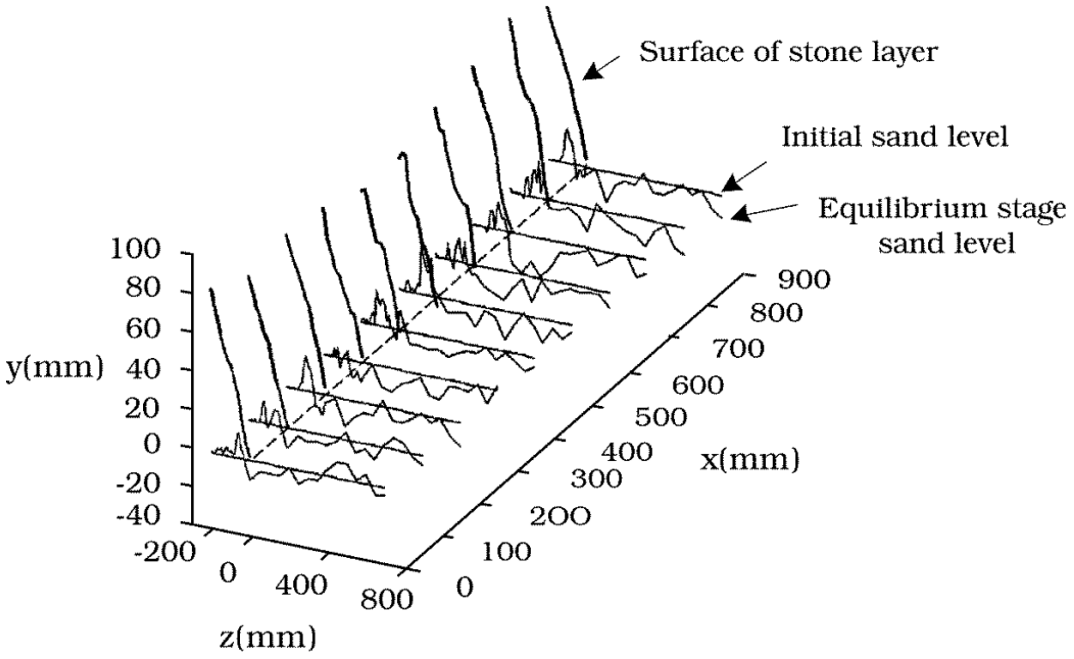

Figure A.8. Bed profiles measured at 10 sections across the longitudinal direction. The length of the working section was 1 m. Live-bed ($\theta > \theta_{cr}$). Test 1. Vertical scale is grossly exaggerated.

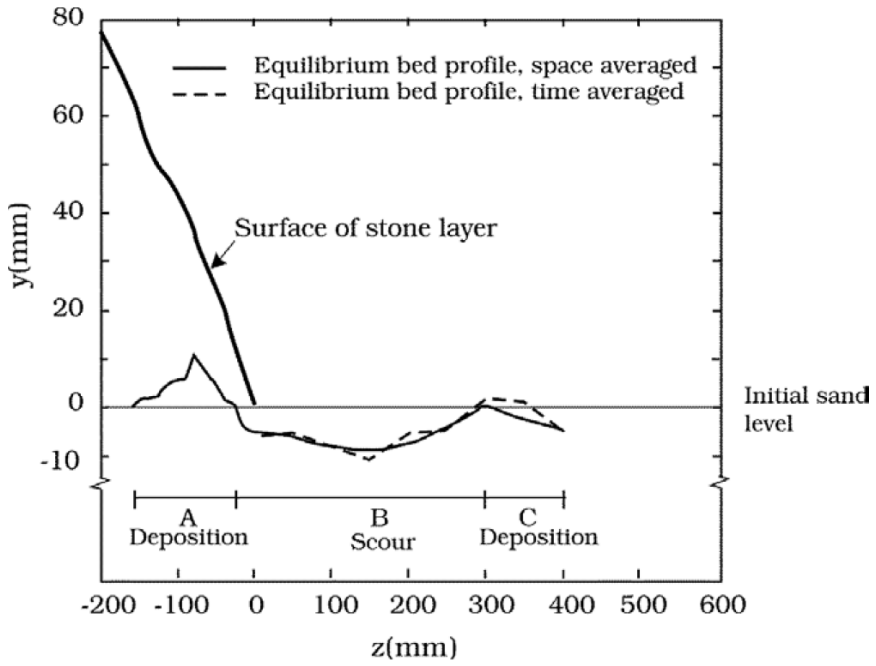

Figure A.9. Mean bed profile, space- and time averaged in cross-flow direction. Sketch of scour deposition pattern. Live-bed ($\theta > \theta_{cr}$). Test 1. Vertical scale is grossly exaggerated.

the turbulence generated locally around individual stones at the toe, in the form of horseshoe-vortex and lee-wake flow.

As the scour around the stones continues and the process removes sand beneath the stones, stability is lost and therefore the stones slump into the scour hole. In some cases the latter process was accompanied by sinking of the stones caused by shear failure of the sand beneath the stones. Here the sand loses its bearing capacity and the stones sink into the sediment bed.

The displacement of the stones at the edge causes the upper layers of stones to move as well. The stones located at the surface therefore move towards the edge. As a result of this the surface of the sloping stone layer stretches and settles. The observed settlement of the stone layer surface is O(0.3 - 0.5 D_s).

From the video recordings the detailed mechanism of the stone displacement at the toe was observed. The scour holes around the toe stones are caused by contraction of the streamlines at the side edge of the stone and the local enhancement in the turbulence intensity, caused by the horseshoe vortex and the vortex shedding. The formation of the horseshoe vortex and the vortex shedding was revealed by sediment which acted as flow tracers.

As seen clearly from Figures 8 and 9 that sand is infiltrated into the cover stone layer and as a result a substantial amount of deposition takes place inside the stone layer. This is, again, caused by the same mechanism as that causing scour, i.e. the sand stirred up by the turbulence and brought into suspension is carried into the stone layer by the secondary current and deposited there.

A.5. Conclusion

Edge scour in a steady current propagating in-line with a stone layer is caused by the combined action of two effects; (1) Primary flow and (2) Secondary flow. The primary flow stirs up the sediment and puts into suspension, and the secondary flow carries it away from the junction between the stone layer and the sand bed, resulting in a scour hole forming adjacent to the toe of the stone layer, Area B in Fig. A.9.

As a result of this mechanism the sediment is deposited in two locations, Area A and Area C in Fig. A.9.

Acknowledgements: This study was partially funded by (1) Danish GTS-university-cooperation project “Future Marine Structures”; (2) the Danish Council for Strategic Research (DSF)/Energy and Environment Program "Seabed Wind Farm Interaction"; (3) EU FP7-project, MERMAID 28870; and (4) Statkraft thorugh: Statkraft Ocean Energy Research Program (SOERP)(Norway).

Appendix B

Measuring sandy bottom dynamics by exploiting depth from stereo video sequence

This chapter is published in the Proceedings of The 17th International Conference on Image Analysis and Processing (ICIAP), September, 2013, Naples, Italy.

R. E. Musumeci[1], G. M. Farinella[2], E. Foti[1], S. Battiato[2], T. U. Petersen[3] & B. M. Sumer[3]

[1]Dept. of Civil and Environmental Engineering, [2]Dept. of Mathematics and Computer Science, University of Catania, Italy.

[3]Technical University of Denmark. Section for Fluid Mechanics, Coastal and Maritime Engineering. Kgs. Lyngby, Denmark.

Abstract: In this paper an imaging system for measuring sandy bottom dynamics is proposed. The system exploits stereo sequences and projected laser beams to build the 3D shape of the sandy bottom during time. The reconstruction is used by experts of the field to perform accurate measurements and analysis in the study of the final equilibrium conditions of sea bottoms in the presence of water flows. Results obtained by processing data acquired in hydraulic laboratory confirm the effectiveness of the system which makes simple and fast the understanding of the sandy bottom dynamics and the related equilibrium phenomena.

Keywords: Sandy bottom dynamics, Stereo system.

B.1. Introduction

The investigation of the three-dimensional morphological evolution of coastal sandy bottoms under the action of waves and currents is particularly relevant in the fields of physical oceanography and coastal engineering. For example, a detailed knowledge of scour processes at the foundation of coastal structures is fundamental to predict damages and failures potential of the structures themselves. Such a kind of studies are usually tackled by means of laboratory investigations, where all the complexity of the involved phenomena can be well controlled and reduced to simpler and reproducible conditions (Sumer and Fredsøe, 2002). A typical experimental setup is shown in Fig. B.1.

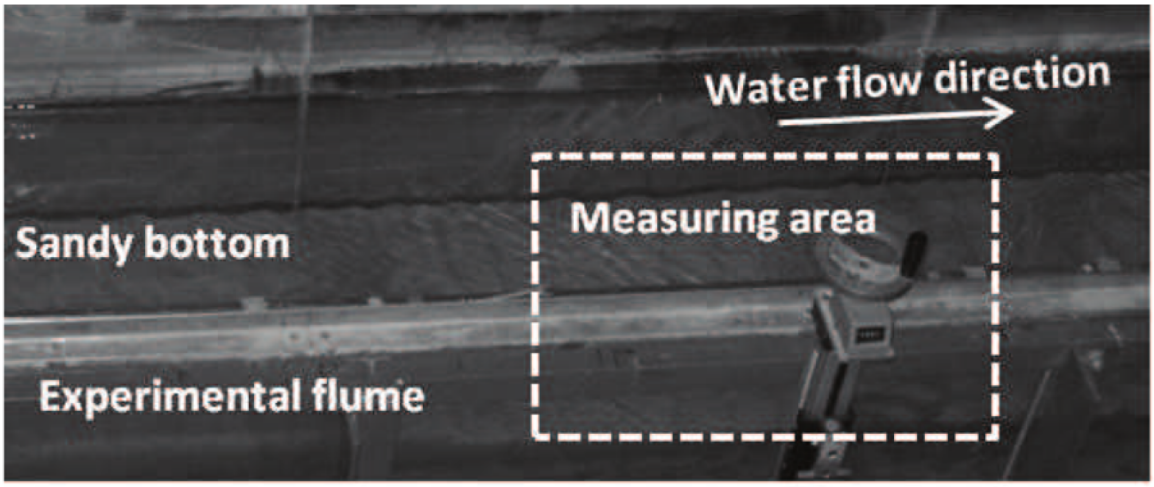

Figure B.1. View of the experimental setup.

In hydraulic wave flumes, mechanical instruments are often used to determine bottom evolution (Sánchez-Arcilla et al., 2011), however optical instruments are becoming more and more popular due to their noninvasiveness with respect to the experiments, i.e., the fact that it is possible to observe the dynamics of the bottom induced by the flow without generating spurious disturbance to the flow itself. This is one of the aims, for instance, of the approach proposed in Sumer et al. (2013) where the authors used a single mini waterproof camera coupled with a 45^o mirror located within a transparent pile to monitor at a single point the maximum scour depth at the basis of a vertical cylinder.
In order to gain knowledge of the three-dimensional characteristics of the coastal bottom morphology, several 3D based approaches have been recently proposed, ranging from commercial 3D laser scanners to more sophisticated stereo pairs techniques (Astruc et al., 2012; Baglio et al., 2001; Foti et al., 2011; Sumer et al., 2007). Unfortunately such optical methods are usually limited to measure the phenomena under consideration in dry condition, i.e., either the wave flume need to be stopped and drained either the measuring area is located in the dry part of the shore. Moreover the images of sandy bottom are structureless and it is difficult to find corresponding points in stereo pair images to be used to reconstruct the sandy bottom and to track interesting points and areas to understand their evolution in time. A recent study (Astruc et al., 2012) have proposed a stereoscopic technique able to measure in the dry part of the swash zone (i.e., in the part of the beach which is alternately wet and dry) rapid variations of the sandy bed elevation based on the use of Particle Tracking Velocimetry (PTV) algorithms. A grid of light dots (each dot was 2 cm wide) projected on the dry part of the swash zone has been employed to add some recognizable structure to be tracked in the images.
Obtaining 3D measurements of the bed morphology undewater is much more difficult, due to problems both in image formation and image aquisition (see Figure B.1). Indeed, due to the small size of the sand grains, $O(10^1 \mu m)$, and to the limited variability of colours, the images of sandy bottoms are “structure free”, hence making difficult the matching of the points of the different point of view (i.e., correspondence problem in stereo systems). On the other hand it is preferable that the cameras are located below the water level and relatively far from the observing area, to avoid variable refraction and reflection disturbances from the moving water surfaces and undesired localized effects due to the presence of the optical equipment. Notice that classic computer vision

techniques adopting interest feature points (like SIFT, Lowe, 2004) are not suitable to solve the matching problem in this context since the unstructured material observed into the scene (i.e., the sand) due to the high variability of the background induced by the water waves and the related reflection.
To deal with such problems, a stereoscopic technique with the cameras located in front of the glass wall of the flume below the still water level has been proposed in Baglio et al. (2001). A grid of laser dots projected on the sandy bottom has been used to allow manual correspondences (made by the experts) between points observed by the stereo pairs and hence to perform 3D measurements. The main advantage of the technique is the possibility to perform 3D dynamic measurements of the bottom evolution (i.e., 3D depth is generated from stereo video) without disturbing the water flow. Such a technique was extended in Foti et al. (2011) considering large scale applications in the swash zone region. In that case, not only a much greater number of dots was deemed necessary, but also longer time series were recorded up to equilibrium conditions. The technique has been also recently applied in Sumer et al. (2013) to investigate the backfilling process of a scour at the base of vertical cylinder. In this last work the possibility to measure the 3D dynamics of the bottom evolution has been fundamental to demonstrate that wave-induced scours and wave-induced backfillings of a current-scour lead to the same equilibrium conditions. However, although quite accurate from the measuring point of view, the procedure used in Baglio et al. (2001), Foti et al. (2011) and Sumer et al. (2013) to build the 3D maps is not easily applicable to the analysis of a large number of images (e.g. frames of long video pairs), required for an accurate analysis of the time evolution of the process. Indeed, both the automatic detection of hundreds of grid laser dots contained in each image and the matching of the stereo pairs are carried out manually by the experts. This process becomes impossible to do by considering hours of acquisition at 4 fps, as the experimental setting of this paper. Hence, in order to become an useful and versatile measurement instrument for sandy bottom evolution the aforementioned technique needs to be made automatic.
Building on previous works Baglio et al. (2001), Foti et al. (2011) and Sumer et al. (2013), in this paper an automatic system for measuring sandy bottom dynamics from stereo image sequences is proposed. After system calibration, the projected laser beams are detected on the stereo pair frames through an image processing pipeline. Exploiting the calibration parameters, the detected dots on the left image are matched with the ones on the right by projecting their coordinates and considering weak perspective assumption. Then the 3D maps are hence obtained by triangulation and the analysis is performed.
The paper is organized as follows: in Section B.2 the proposed system is described by focusing on (i) the automatic detection of the laser dots onto the gathered images of the sandy bottom, and (ii) the automatic stereo matching of the dots on the stereo pairs. Section B.3 discusses the experimental setting and summarize the results. Finally, conclusions and hints for future works are given in Section B.4.

B.2. Proposed System

As it is standard in stereo vision approaches, the proposed technique can be schematized in the following three stages: (i) stereo image acquisition; (ii) matching of the corresponding points;

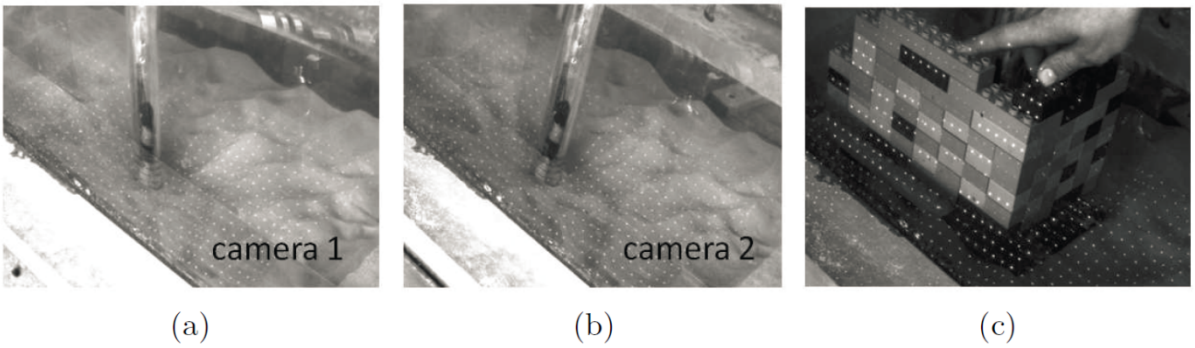

Figure B.2. (a) and (b): stereo pairs related to the experimental settings. The projected laser dots onto the sandy bottom and the the scour around a vertical pile are visible. (c) 3D rig used during calibration.

(iii) 3D measurement and analysis.

The main objective of the instrumental setting used in this work is to obtain "suitable" images to make correspondences of points of the sandy bottom morphology throughout the experiment. Moreover, to make accurate measurements of the bottom dynamics the depth of specific points (e.g., evolution of points around a vertical pile) should be reconstructed in time. This is achieved by projecting a grid of laser points onto the sandy bottom. Figure 1 shows a typical view of the experimental setup , while Figure 2*(a)* and *b* shows an example of a stereo images where the laser grid points are visible. The light dots become an optical well-defined point measuring stations on the sandy bottom, and also allows to add points to be matched between the stereo images.

In a previous work (Baglio et al., 2001), Gaussian lenses have been used during acquisition. Here we follow the protocol of Foti et al. (2011) where non-Gaussian lenses have been exploited to obtain an uniform density distribution of light with sharp ends. External lighting conditions of the hydraulic laboratory are also very important. In the ideal condition a dark room in which only the laser beams can be seen simplify the detection of the points. Unfortunately those conditions are difficult to be obtained in hydraulic laboratories, where for safety reason windows cannot usually be shaded to get complete darkness. Spurious reflections, due to the flume's glass walls or to the moving free surface of water, can also affect the quality of the images. It follows that the images must be carefully analyzed in order to reject points which do not belong to the laser grid projected onto the bed. As can be assessed by visual inspection of Figure 2*(a)* and *(b)*, there are many source of variability in the images which make difficult both, dots detection (e.g., there are many false positive dots coming from reflection) and matching.

Being a stereoscopic approach, the image acquisition is obviously performed by using two cameras which simultaneously record videos of the sandy bottom evolution. In order to avoid any disturbance to the flow, the cameras are located outside of the flume, in front of glass walls in the correspondence of the measuring area. Due to the fact that in hydraulic laboratories several optical obstacles are usually present (e.g., steel frames, structural elements, other measuring instruments, etc.), the technique has been developed in such a way that there are no constraints on the relative position of the two cameras. The only requirement is that both cameras should have a "vision" as much complete as possible of the phenomenon under investigation.

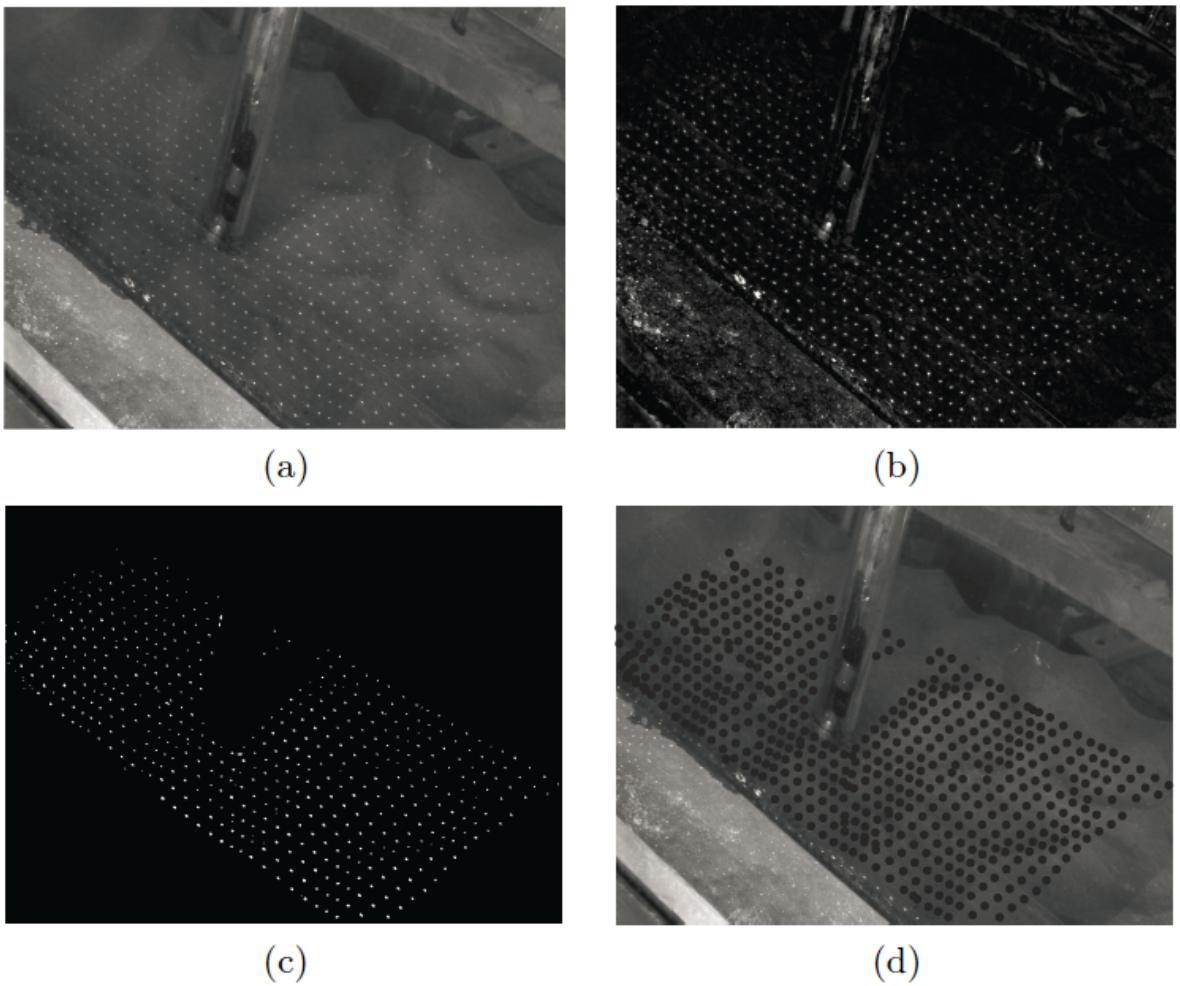

Figure B.3: Detection of laser dots. (a) Original image; (b) Filtered image; (c) Dots vs. other separation; (d) Detected laser dots

About the camera calibration, while Baglio et al. (2001) and Foti et al. (2011) used a direct linear transformation (DLT) (Abdel-Aziz and Karara, 1971; Faugeras and Toscani, 1987), in the present work a four-step camera calibration procedure is performed (Heikkilä and Silvé, 1997). Traditionally, several views of a 2D planar rig are adopted during calibration (Tsai, 1987). To facilitate the operations within the flume filled with water, the stereo images of a 3D calibration rig are used (see Figure B.2*(c)*). The rig has known dimensions, which can be modified according to the dimensions and shape of the investigated phenomenon to properly calibrate the stereo system in order to obtain the required accuracy in the measurements. Once, the calibration of the stereo system is done, the laser dots should be detected and matched in the image pairs to obtain the correspondences useful to build the 3D map of the sandy bottom at varying of time. The following subsections illustrate the techniques implemented for making automatic the laser dot detection and matching.

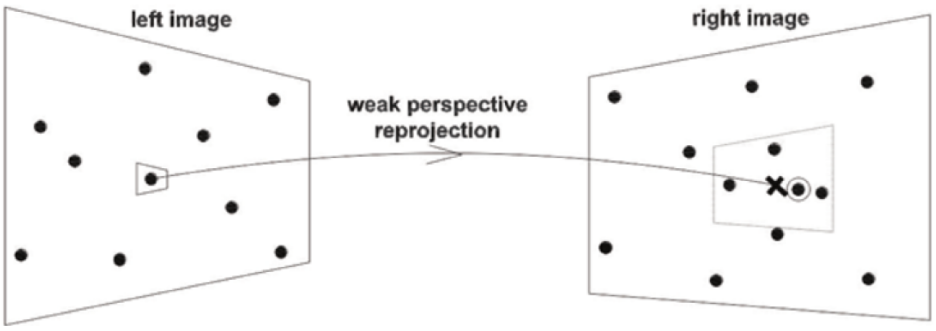

Figure B.4. Closest neighbour matching considering weak perspective.

B.2.1. Detection of laser dots

The automatic detection of the light dots position on the images is obtained by means of an image processing pipeline involving a sequence of filtering, morphological operations and foreground (i.e., dots) versus background separation procedures. An example of the images obtained at the various steps of the pipeline is shown in Figure B.3. Note that, due to the high variability and artifacts introduced by the reflection, noisy input, etc., this task is not so trivial as expected.

As first, each image is filtered by means of a Gaussian kernel to remove noise (see Figure 3*(b)*). Then, in order to correct uneven illumination and to enhance the intensity of the laser dots, a morphological top-hat transform (Allan and Serra, 2001) is carried out by means of a disk structuring element (see Figure B.3*(c)*). The results of such an operation is hence binarized through a thresholding procedure to separate dots (i.e., foreground versus background). Therefore a flood-fill operation (Soille, 1999) of the obtained binary image is applied to fill holes, (i.e., to fill the background pixels that cannot be reached by filling in from the edge of the images). Finally, the segmented spots (i.e., the connected elements on the image) are analyzed with respect to their shapes (through geometric constraints, such as area, etc.) in order to retain only the laser dots (see Figure B.3*(d)*). Then, the centroid coordinates of all the detected dots are determined and stored.

The parameters used in the aforementioned pipeline have been learned on the pair of images used for the stereo calibration procedure. Specifically, for those images a manual labeling has been performed and the parameters have been learned with a search procedure on a quantized version of the parameter space.

B.2.2. Stereo matching

In a previous work (Foti et al. 2011), it was shown how standard methods used for stereo matching (e.g., correlation) fail to properly recover the sandy bottom geometry, due to the lack of structures useful to deal with the correspondence problem. As we have experimented in this context, the classic approach to match invariant feature points (e.g., SIFT Lowe, 2004) in the pair images has problems due to the high variability and presence of artifacts generated by the reflection and to the periodic patterns and deformation present in the sandy texture and in the waves induced by the experiments.

At this stage we have the detected dots from the pipeline described in previous section. Also, since the cameras have been stereo calibrated, all the intrinsic and extrinsic parameters of the stereo system are known. Therefore, in the present work, the problem of

stereo matching is solved by means of a Closest Neighbour Method (CNM), i.e., through a purely geometric approach, based on the distance of the reprojected points and making the assumption of weak-perspective model (Hartley and Zisserman, 2003). A sketch of the proposed procedure is shown in Figure B.4. In our case, the approximation to a weak perspective model is possible and profitable since the dimension of the measuring area is relatively small compared to the distance of the cameras from it (i.e., the average variation of the depth of the measured area is very small with respect to the average distances of points). Hence, a constant size window is introduced to select a set of dots on the right image which are neighbours of the reprojection. Within such a set, the dot which is closest to the reprojection is chosen as the matching point. Subsequently, a series of checks are performed to guarantee a biunique correspondence of the matchings and hence remove false positive and wrong matchings.

B.2.3.3D sandy bottom reconstruction and analyses

Once the matching pairs are obtained the depth of the sandy bottom is reconstructed by using triangulation [15]. Moreover, in order to obtain a smooth 3D depth maps over time, a linear interpolation of the 3D dots coordinates related the sandy bed is carried out. The morphology of the sandy bottom surface is enlightened by means of contour lines. Since the depth map is built for each stereo pairs of the video streams, the 3D dynamics of the sandy bottom can be analyzed following the dots of interest for the specific experiment (e.g, points around the pile).

B.3. Experimental setting and results

In the present work, the proposed system has been applied to a laboratory analysis of the evolution of the scour which occurs at the foundation of an offshore structure due to marine currents and the refilling (or backfilling) of such a scour hole generated by the subsequent action of wind waves. From the engineering point of view, a throughout three-dimensional understanding of the phenomenon is particularly important for protecting the foundations of off-shore structures (e.g., wind turbines, oil platforms, etc.) from erosion.

The experiments have been carried out at the hydraulic laboratory of the Section for Fluid Mechanics, Coastal and Maritime Engineering of the DTU Mekanik of the Technical University of Denmark in a wave-current flume, which is $28m$ long, $0.6m$ wide and $0.8m$ deep. Fine sand was used during the experiments, having a median diameter $d_{50} = 0.17mm$ and gradation equal to 1.3. The water depth was $h = 0.4m$. The diameter of the plexiglass vertical circular pile used to investigate scour and backfilling was $D = 40mm$. In Fig. B.3*(a)* is possible to observe the aforementioned setting as seen from the right camera.

The evolution of the bottom morphology was recorded starting from flat bottom conditions up to current- or wave-induced equilibrium scour and backfilling by means of two UI-2250RE-M monochrome cameras, located outside of the wave flume (see Figure 2*(a)* and *(b)*). The grid of light points was obtained by means of two 20 mW Lasiris SNF 660-nm laser generators (in order to cover the measuring area) coupled with two GMN31614MNC-1 Goyo Optical Inc. diffractive lenses with 1.6 mm focal length. Each laser produced a square grid of 19×19 equally spaced laser beams, with a total of 722 dots projected onto the sandy bottom. Some of the laser dots were not visible due to the pile shadow.

A total of 137 video pairs were recorded at 4 fps, using an image size of 1600×1200

pixels. The duration of each video was in the range of 2 to 15 minutes. The longest video pairs were recorded at the beginning of the experiment to monitor the initial stages of the evolution which are the fastest, then video pairs were taken each 10 minutes up to an equilibrium condition was reached, after $2 \div 4$ hours. One of the main motivation of the present work is that, the manual treatment of the above data is extremely time consuming, since the analysis of one image of a single stereo pair may take up to 2 hour. Moreover, due to the small size of the light dots, the manual detection and matching are prone to material errors of the operator.
Here we report one case study related the investigation of the dynamics of sediment transport around a vertical cylinder by Sumer et al., 2013 (see Fig. B.5). The considered images have been chosen in such a way to be representative of several stages of the bottom evolution.
By defining T as the time scale of the backfilling process, the set of pairs related the case study refer to the following experimental conditions:

- Stereo Pair 1: initially flat bottom;
- Stereo Pair 2: current-induced scour at equilibrium;
- Stereo Pair 3: wave-induced backfilling after a time equal to $T/2$;
- Stereo Pair 4: wave-induced backfilling after a time equal to T;
- Stereo Pair 5: wave-induced backfilling at equilibrium;

To perform an objective evaluation of the proposed system, the dots in the images related the case study under evaluation were manually labeled and matched. The total number of manually labeled dots is 5610. The final number of manually labeled matchings is 2660. The overall detection rate obtained with the pipeline summarised in Section 2.1 was 0.83% with an average rate per image of 0.825%. The matching rate obtained considering the corrected detected points was 0.734% for the equilibrium condition state. The most important fact is that the interesting dots useful for the investigation of the dynamics of sediment transport around the pile were well detected and matched allowing the study of the flume at the equilibrium backfilling condition (Condition related Stereo Pair 5 in the list above). The results obtained can be considered satisfactory to perform the analysis, although further improvement is deemed necessary to reach better performances of the matching in the case of sandy bottom morphologies characterized by high steepness and high reflection noise and artifacts (e.g., condition related to the Stereo Pair 2 in the above list).
Once the matching is done, the 3D map of the sandy bottom is reconstructed. Examples of the 3D maps obtained from both manually labeled process (Sumer et al., 2013) and from proposed method are reported in Fig. B.5 for Stereo Pair 1 and Stereo Pair 5, which corresponds respectively to the flat bed conditions and the wave-induced backfilling at equilibrium. In Figure 6, the cross-sections of the sandy bottom along the central axis of the wave flume obtained by the manual reconstruction (Sumer et al., 2013) and the one performed with the proposed automatic procedure are compared. The data are referred to the equilibrium condition of wave-induced backfilling. The independent measurement of the position of the sandy bottom (i.e., the ground-truth) as been recovered by a waterproof minicamera coupled with a 45^o mirror (Sumer et al., 2013) is also reported in the plots (i.e., the red dot in Fig. B.6). This result shows how the proposed method is able to accurately reconstruct the 3D sandy surface and hence can be used to measure the interesting quantities of morphological

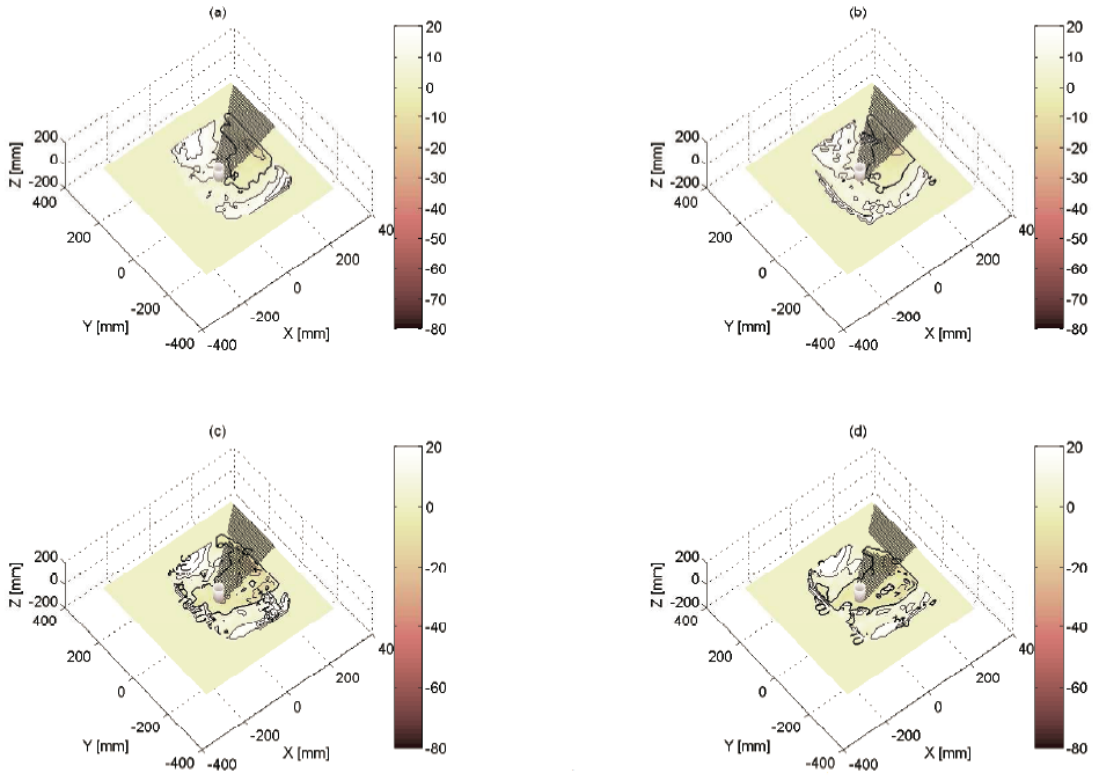

Figure B.5. 3D depth maps of the sandy bed: (a) flat bottom condition (Stereo Pair 1) as recovered manually (Sumer et al., 2013); (c) flat bottom condition (Stereo Pair 1) as recovered by the proposed automatic pipeline; (b) backfilling at equilibrium (Stereo Pair 5) as recovered manually (Sumer et al., 2013); (d) backfilling at equilibrium (Stereo Pair 5) as recovered by the proposed automatic pipeline.

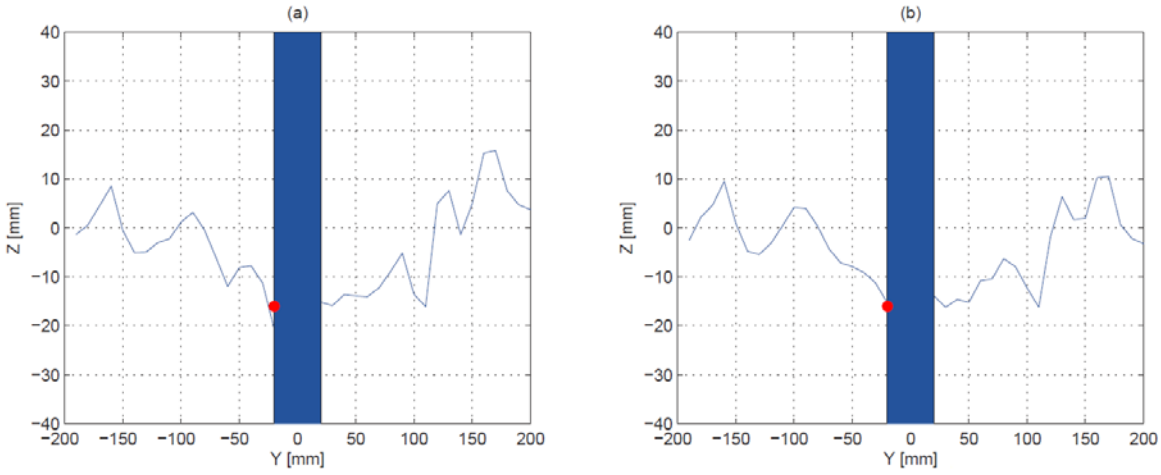

Figure B.6. Cross-section along the central axis of the flume at the equilibrium backfilling condition: (a) result recovered by using manual reconstruction (Sumer et al., 2013); (b) result obtained by the proposed automatic pipeline. The red dot indicates the ground-truth related the bed position (Sumer et al., 2013). The proposed method obtains the best result.

analyses, such as the measurement of the maximum scour depth. The results obtained with the proposed method outperforms the previous results obtained through manual approach (Sumer et al., 2013).

B.4. Conclusions and Future Works

In this paper a system for measuring quantities useful for sandy bottom morphological analyses over time has been presented. The system makes use of stereo vision and projected laser beams which are automatically detected and matched to find the correspondences useful for the 3D sandy surface reconstruction. The results obtained in measuring the final equilibrium conditions by processing data acquired in hydraulic laboratory confirm the effectiveness of the system which makes effortless for the expert the understanding of the sandy bottom dynamics phenomena. An improvement of the proposed method is under development to cope with the limits due to the weak perspective model assumption used here for reprojection. Moreover, future works will be devoted to test the performances of recent hardware (e.g., Kinect, Newcombe et al., 2011) for the 3D sandy bottom reconstruction.

Acknowledgments: The research described in this manuscript was supported by the EC project HYDRALAB IV (contract no. 261520) and by the Italian Ministry for Education, University and Research funded PRIN 2010-2011 HYDROCAR (Prot. no. 20104J2Y8M_003).

Appendix C

Sinking of scour protections at Horns Rev 1 offshore wind farm

This chapter is to be published in the book of abstracts of the 34th International Conference on Coastal Engineering, Seoul, Korea, June, 2014.

A. W. Nielsen[1], B. M. Sumer[2] & T. U. Petersen[2]

[1]DHI, Dep. for Ports and Offshore Technology (DK-POT), Agern Allé 5, 2970 Hørsholm, Denmark.

[2]Technical University of Denmark. Section for Fluid Mechanics, Coastal and Maritime Engineering. Kgs. Lyngby, Denmark.

C.1. Introduction

For more than a decade, an increasing number of offshore wind farms have been installed. This trend will continue for decades according to public plans. The development of offshore wind power has unveiled a number of unknowns in our knowledge of interaction between structures, waves, current, and seabed. One of the major surprises was observed at one of the first large offshore wind farms: Horns Rev 1 Offshore Wind Farm (installed 2002). The wind farm is located off the west coast of Denmark in the North Sea. The water depth in the area is shallow: 6 to 14 m MSL, and the seabed is dominated by fine sand. The area is exposed to relatively strong tidal current, up to 0.8 m/s, and large waves, including breaking waves. The turbines are founded on mono piles with a traditional scour protection. The scour protections consist of a fine filter layer and a cover layer of large stones; hence considered being non-movable. Due to the means of installation, the scour protections are rather irregular in shape and size. Although the scour protections were supposed to be non-movable, a survey in 2005 showed major sinking, up to 1.5 m, of the scour protections adjacent to the mono piles. This could not readily be explained by data available at that time.

C.2. Recent research and results

Since the 2005 survey, DHI and DTU have been researching on the topic to find an explanation for the sinking of the scour protections at Horns Rev 1 Offshore Wind Farm. Hansen et al. (2007) presented the surveys and a crude model showing that sediment transport underneath the scour protection could take place.
Nielsen et al. (2011, 2013) and Sumer and Nielsen (2013) presented results from physical and numerical model tests with current flow, showing that current flow can cause sinking adjacent to the pile, but it required strong currents rarely present during the period.
Most recently, DTU and DHI conducted tests of sinking of the scour protections under waves, and combined waves and current. These tests disclosed important mechanisms related to the sinking of scour protections adjacent to mono piles. The tests showed that the sinking under wave-dominated conditions is controlled by two different mechanisms: in-filling of sediment from the surrounding seabed into the scour protection (stabilizing) and suction of sediment through the scour protection at both sides of the pile (destabilizing). The in-filling mechanism is the strongest, but it had a time-delay, so a significant sinking could take place before in-filled sediment reached the pile and stopped the sinking. The time scale of the infilling process increased for thicker scour protections.
The surveys from Horns Rev 1 Offshore Wind Farm were analyzed with respect to these new findings, and the result indicates that a considerable part of the sinking took place during wave-dominated sea states.

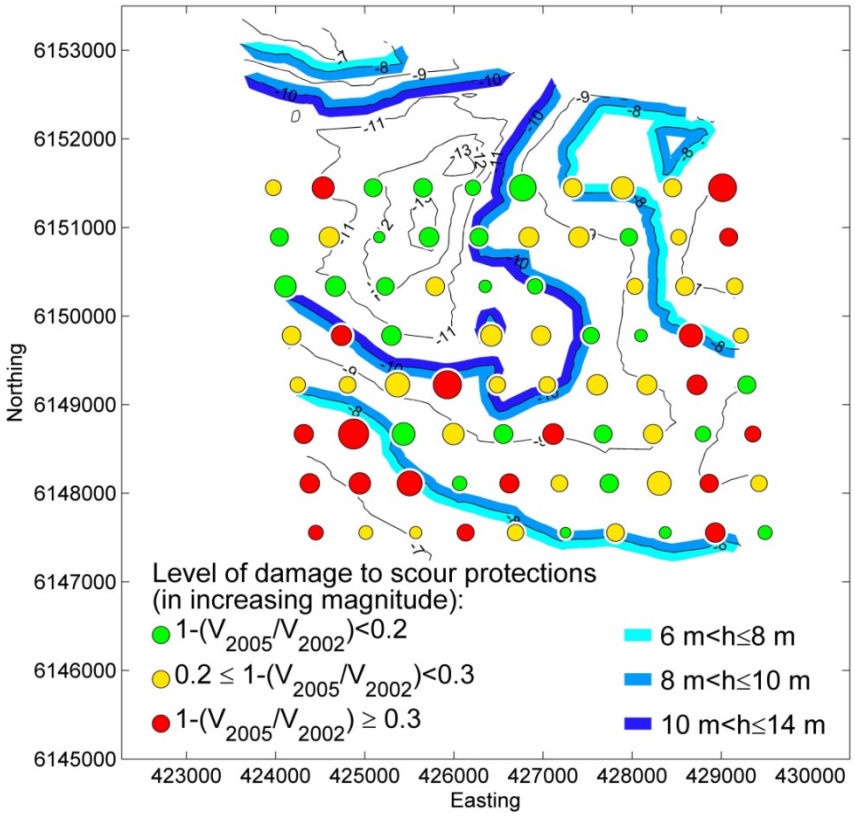

Figure C.1. Bathymetry of the Horns Rev 1 OWF with scour protections. The size of the circles scales with the installed volume of the scour protections.

Fig. C.1 shows the bathymetry of the Horns Rev 1 OWF and the scour protections as circles; the size of the circles scales with the installed volume of the scour protection, V_{2002}, and the colour gives the level of damage, $1-(V_{2005}/V_{2002})$. It is seen that the largest damage took place at low water depth and for the largest scour protections, in accordance with the recent results.

C.3. Conclusion

These observations indicate that waves had a significant role in the sinking as sinking would not increase for larger scour protections in the case of current-dominated situations. Furthermore, most damage was observed at the most wave-exposed low water depths.